



Analytical model for cellular beams made of hot rolled sections in case of fire

Olivier Vassart

► To cite this version:

Olivier Vassart. Analytical model for cellular beams made of hot rolled sections in case of fire. Civil Engineering. Université Blaise Pascal - Clermont-Ferrand II, 2009. English. NNT : 2009CLF21951 . tel-00860914

HAL Id: tel-00860914

<https://theses.hal.science/tel-00860914>

Submitted on 11 Sep 2013

HAL is a multi-disciplinary open access archive for the deposit and dissemination of scientific research documents, whether they are published or not. The documents may come from teaching and research institutions in France or abroad, or from public or private research centers.

L'archive ouverte pluridisciplinaire **HAL**, est destinée au dépôt et à la diffusion de documents scientifiques de niveau recherche, publiés ou non, émanant des établissements d'enseignement et de recherche français ou étrangers, des laboratoires publics ou privés.

N° d'ordre : D.U. 1951
EDSPIC : 444



UNIVERSITE BLAISE PASCAL - CLERMONT II

**ECOLE DOCTORALE
SCIENCES POUR L'INGENIEUR DE CLERMONT-FERRAND**

THESE

présentée par

Olivier VASSART

Ingénieur de l'Ecole Polytechnique de Louvain (Belgique)

pour obtenir le grade de

DOCTEUR D'UNIVERSITE

SPECIALITE : GENIE CIVIL

**ANALYTICAL MODEL FOR CELLULAR BEAMS MADE OF HOT
ROLLED SECTIONS IN CASE OF FIRE**

(Modèle analytique en situation d'incendie pour des poutres cellulaires
réalisées à partir de profilés laminés à chaud)

Soutenue publiquement à Clermont-Ferrand le 16 Septembre 2009 devant le jury :

M.	Hamid Bouchaïr	Président
M.	Louis-Guy Cajot	Examineur
M.	Jean-Marc Franssen	Rapporteur
M.	Jean-Pierre Muzeau	Directeur de thèse
M.	Ali Nadjai	Rapporteur
M.	Bin Zhao	Rapporteur

Doctorat Européen préparé au Laboratoire de Mécanique et Ingénieries (LaMI) de l'Université Blaise Pascal et au centre de recherche Produits Longs d'ArcelorMittal.

Abstract

This thesis allows developing an analytical model for the prediction of the critical temperature of cellular beams made of hot rolled sections subjected to fire.

This target is carried out through research focused on tests and simulations of isolated cellular beam submitted to fire. Based on this study a new analytical model is developed.

In order to ensure the reliability of the developed model, different steps are followed:

- realisation of large scale fire tests in laboratory
- implementation of a Finite Element model in the software SAFIR
- calibration of the FEM model in comparison with laboratory tests
- development of the simplified analytical model
- validation of this analytical method through a parametrical study using FEM software SAFIR.

The developed Finite Element and analytical models are able to reproduce with a satisfactory level of accuracy the complex behaviour of cellular beam in fire conditions.

Key words:

Construction, steel, composite, cellular beam, instability, fire resistance.

Résumé

Cette thèse a permis de développer un modèle analytique pour la prédiction de la température critique de poutrelles cellulaires fabriquées à base de profilés laminés en situation d'incendie. Ces résultats seront basés sur la mise au point d'un nouveau modèle analytique de poutrelle cellulaire isostatique soumise au feu. Pour assurer la fiabilité du modèle développé, les étapes suivantes ont été considérées :

- la réalisation de tests en grande échelle en laboratoire
- la mise au point d'un Modèle Éléments Finis dans le logiciel SAFIR
- la validation du Modèle Éléments Finis en comparaison des essais en laboratoire
- le développement du modèle analytique simplifié
- la validation de cette méthode analytique par une étude paramétrique utilisant le modèle Éléments Finis

Le modèle éléments finis et le modèle analytique qui ont été développés sont capables de reproduire le comportement complexe des poutrelles cellulaires en cas d'incendie avec un niveau de précision satisfaisant.

Mots clés :

Construction, acier, mixte acier béton, poutre cellulaire, instabilité, incendie.

Table of Contents

1. State of the art	23
2. Experimental test campaigns.....	31
2.1 Introduction.....	31
2.2 Experimental test data in cold conditions	31
2.2.1 Test specimen	31
2.2.2 Test setup and test procedure	32
2.2.3 Results of the test campaign	33
2.3 Experimental test campaign in fire condition	33
2.3.1 Characteristics of the cellular beam members.....	34
2.3.2 Composite floor.....	36
2.3.3 Fire protection of the cellular beam	38
2.3.4 Applied thicknesses of sprayed fire protection material.....	39
2.3.5 Loading and boundary conditions of the beam	39
2.3.6 Thermal measurements.....	41
2.3.7 Results of the test	42
2.3.8 Conclusion of the test in fire conditions	42
2.4 Conclusion on the existing test campaign	42
2.5 New experimental test program	43
2.5.1 Testing procedure of the beam at ambient temperature.....	50
2.5.2 Experimental results of tests at elevated temperature.....	51
2.6 Conclusion on test campaigns	58
3. Elaboration of a FEM model for cellular beams	61
3.1 FEM model for pure steel cellular beam.....	61
3.2 FEM model for composite cellular beam	64
3.2.1 Shear resistance of steel studs.....	69
3.2.2 Stiffness of a steel stud (k)	72
3.2.3 Torsional stiffness (GJ).....	73
3.2.4 Modelling of the steel stud using SAFIR BEAM Finite Element.....	73
3.3 Simulation of the test campaigns	78
3.3.1 Short span tests in cold conditions	78
3.3.2 Protected furnace test.....	82
3.3.3 Ulster test campaign	85
4. Analytical calculation model for cellular beam in fire conditions	97

4.1	Web post buckling analytical model	97
4.1.1	Position of the critical section in the web post	99
4.1.2	Principal compressive stress	100
4.1.3	Forces acting on a pure steel 'T' section	102
4.1.4	Repartition of the shear between the 'T' members	104
4.1.5	Forces acting on a 'T' shape composite section	107
4.1.6	Principal stress resistance	109
4.1.7	Principal stress resistance for instability	111
4.1.8	Post critical reserve of strength	115
4.2	Resistance of the net section at the location of a web opening (Vierendeel model)	117
4.2.1	Determination of the geometry	118
4.2.2	Geometry of the net section	120
4.2.3	Cross sectional characteristics of the members	122
4.2.4	Characteristics of an inclined section at the location of an opening	123
4.2.5	Calculation of forces considering Vierendeel action	125
4.2.6	Calculation of forces considering the thermal expansion of the flange and the web	127
4.2.7	Development of an analytical model for the evaluation of stresses due to thermal expansion	134
4.2.8	Cross section classification of a member at a web opening	141
4.2.9	Verification of the resistance of an inclined section	143
5.	Validation of the analytical model	151
5.1	Web post buckling model	151
5.1.1	Web post buckling in pure steel section	151
5.1.2	Web post buckling in composite section	154
5.1.3	Web post buckling in composite non-symmetrical section	156
5.1.4	Parametrical study	159
5.1.5	Implementation of a tool for the simplified model	165
5.1.6	Results of the parametrical study	166
5.2	Vierendeel bending	167
5.2.1	Parametrical study for Vierendeel bending	169
5.2.2	Results of the parametrical study	178
6.	Conclusion	181

List of Tables and Figures

List of Tables and Figures

List of Tables and Figures

List of Tables

Table 2-1 : List of specimen for testing	32
Table 2-2 : Results of the FEA	33
Table 2-3 : Measured thickness of the protection spray.....	39
Table 2-4 : Steel cellular beams detailing.	48
Table 3-1 : Results of the FEA	80
Table 4-1 : Characteristics of the elementary areas of a gross section	119
Table 4-2 : Characteristics of the elementary areas of the web of a net section.....	121
Table 4-3 : Characteristics of the elementary areas of an inclined section	124
Table 4-4 : Strength reduction factors for the design of class 4	144

List of Figures

Figure 1–1 : Oxycuting of the parent profile	23
Figure 1–2 : Separation and positioning of the two parts of the parent profile	24
Figure 1–3 : Welding of the two parts of the parent profile.....	24
Figure 1–4 : Final geometry of the cellular beam	25
Figure 1–5 : Asymmetric section	26
Figure 2–1 : Test arrangement.....	32
Figure 2–2 : Cross section of the tested cellular beam	34
Figure 2–3 : Span and Geometry of the tested cellular beam.....	35
Figure 2–4 : Composite steel deck on the cellular beam	37
Figure 2–5 : Spray material applied on the entire surface of the beam.....	38
Figure 2–6 : Position of the beam in the furnace and loading.	40
Figure 2–7 : Position of the different temperature measurements	41

Figure 2–8 : Temperature of the steel at different positions.....	41
Figure 2–9 : Shape of the beam after the fire test.....	42
Figure 2–10 : Profiles used for A1 section	44
Figure 2–11 : Profiles used for B1 section	45
Figure 2–12 : Furnace temperature time curve used in the experimental study	46
Figure 2–13 : ISO-834 curve	46
Figure 2–14 : Dimensions of the Holorib sheets HR 51/150	47
Figure 2–15 : Symmetrical composite cellular beam.....	48
Figure 2–16 : Characteristics of the beam A1	48
Figure 2–17 : Asymmetric composite cellular beam.....	49
Figure 2–18 : Characteristics of the beam B1	49
Figure 2–19 : Experimental set up / load introduction of test A1	50
Figure 2–20 : Web post buckling mode failure A1.....	51
Figure 2–21 : Typical Thermocouples locations.....	52
Figure 2–22 : Typical Thermocouples locations.....	52
Figure 2–23 : Thermal measurement in the upper flange along the beam	53
Figure 2–24 : Thermal measurement in the Lower flange along the beam.....	53
Figure 2–25 : Thermal measurement in the upper web along the beam.....	54
Figure 2–26 : Thermal measurement in the Lower web along the beam	54
Figure 2–27 : Furnace	55
Figure 2–28 : Time versus deflection of test A2.	56
Figure 2–29 : Time versus deflection of test B2.	57
Figure 2–30 : Web post buckling failure mechanism.....	57
Figure 3–1 : Definition of the geometry and local axes	61
Figure 3–2 : Definition of the integration point on the thickness of the element.....	62
Figure 3–3 : SHELL Finite Element model in SAFIR software	62
Figure 3–4 : Boundary conditions.....	63

Figure 3–5 : Initial deformation for the SHELL F.E. model.....	64
Figure 3–6 : BEAM element: (a) Local axes (b) Degrees of freedom at nodes.....	64
Figure 3–7 : Cross section of a BEAM Finite Element with concrete and rebars.....	65
Figure 3–8 : Numerical model taking into account a composite slab with full shear connection.....	66
Figure 3–9 : Description in detail of the connection between SHELL and BEAM element. ...	67
Figure 3–10 : Numerical model taking into account a composite slab with steel studs.....	68
Figure 3–11 : Description in detail of the connection between SHELL and BEAM elements forming the slab and the steel stud.....	68
Figure 3–12 : Failure of a steel stud by shear	69
Figure 3–13 : Failure of the concrete around the connection.....	70
Figure 3–14 : Scheme of a corrugated steel sheet perpendicular to the beam direction	71
Figure 3–15 : Stud's deformation model	72
Figure 3–16 : Steel stud composed of 4 squared fibres.....	74
Figure 3–17 : σ - ε relationships for Steel in EC3.....	79
Figure 3–18 : Load-Deflection Diagram (Beam 3).....	81
Figure 3–19 : Deformations at the end of the simulation (Beam 3).....	81
Figure 3–20 : Numerical model of the tested beam	83
Figure 3–21 : Numerical model of the tested beam	83
Figure 3–22 : Deformed shape of the structure after the test and at the end of the simulation	84
Figure 3–23 : Comparison between the deflections SAFIR/Test	84
Figure 3–24 : FEM model of test A and test B	85
Figure 3–25 : FEM vs test A1	86
Figure 3–26 : FEM vs test B1	86
Figure 3–27 : Membrane force in tension.....	87
Figure 3–28 : Displacements after 3000 sec of heating	87
Figure 3–29 : Displacements at the beginning of the web post buckling	88

Figure 3–30 : Displacements at the end of the test.....	88
Figure 3–31 : FEM vs test A2.....	89
Figure 3–32 : FEM vs test B2.....	89
Figure 3–33 : Cellular beam after the test B2.....	90
Figure 3–34 : Cellular beam after the numerical simulation of the test B2.....	90
Figure 3–35 : Comparison between the deformed shape of the test B2 (furnace test vs numerical simulation).....	91
Figure 3–36 : σ - ε relationships for steel in EC3	92
Figure 3–37 : Modified σ - ε relationships for steel.....	92
Figure 4–1 : Principle of the check of the web post stability.....	97
Figure 4–2 : Definition of critical section for stability of an intermediate web post	98
Figure 4–3 : Compression stresses in the cellular beam	99
Figure 4–4 : Out of plane displacement and position of the critical section	100
Figure 4–5 : Orientation of the face tangent to the border of the opening.....	101
Figure 4–6 : Stresses at point P (Mohr circle)	102
Figure 4–7 : Forces acting on 'T's	103
Figure 4–8 : Shear forces repartition.....	104
Figure 4–9 : Steel beam test 3a - Shear stresses comparison	105
Figure 4–10 : Form of the variable η as a function of α	106
Figure 4–11 : Shear area of a 'T' at the location of an opening	106
Figure 4–12 : Forces in the steel 'T's and the slab.....	107
Figure 4–13 : Shear force distribution between concrete slab and steel beam.....	108
Figure 4–14 : Curve ξ in function of α	110
Figure 4–15 : Instability mode of the 'T's.....	111
Figure 4–16 : Critical forces for a member	113
Figure 4–17 : Euler buckling forces.....	114
Figure 4–18 : Rectangular part of the web post	115

Figure 4–19 : Elongated opening	115
Figure 4–20 : Value of κ factor respecting to ψ value	116
Figure 4–21 : Standard panel.....	117
Figure 4–22 : Failure caused by Vierendeel effect.....	117
Figure 4–23 : Geometrical description of a transverse cross-section	118
Figure 4–24 : Net section location.....	120
Figure 4–25 : Decomposition of the net section	120
Figure 4–26 : Decomposition of the gross section	122
Figure 4–27 : Shear area of a 'T' at the location of a web post.....	122
Figure 4–28 : Inclined section at the location of an opening	123
Figure 4–29 : Decomposition of a 'T' section	124
Figure 4–30 : Section of an opening with angle ϕ_{\max}	126
Figure 4–31 : Forces acting on an inclined section	127
Figure 4–32 : Numerical model without loading	128
Figure 4–33 : Thermal stresses in cellular beam	129
Figure 4–34 : Concentration of thermal stresses in cellular beam	130
Figure 4–35 : ISO-834 curve	131
Figure 4–36 : Boundary condition of the SAFIR SHELL element.....	131
Figure 4–37 : Stresses results for the UB section	132
Figure 4–38 : Stresses results for the HD section.....	133
Figure 4–39 : Stresses results for the HEM section	133
Figure 4–40 : Simplified geometry.....	134
Figure 4–41 : Free thermal elongation	134
Figure 4–42 : Axial force due to fully restrained web and flange.....	135
Figure 4–43 : Elongation of the 'T' taking into account web and flange	136
Figure 4–44 : Geometrical description of the 'T' section	137
Figure 4–45 : Thermal stresses for UB section	138

Figure 4–46 : Thermal stresses for a critical HD section.....	139
Figure 4–47 : Decrease of the Young modulus with the temperature	140
Figure 4–48 : Strength reduction factors for the design of class 4 vs effective yield strength.....	144
Figure 5–1 : ISO 834-curve	151
Figure 5–2 : Displaced shape of a beam without web post buckling.....	152
Figure 5–3 : Displaced shape of a beam with web post buckling.....	152
Figure 5–4 : Out of plane displacement of the web post for symetric steel profile	153
Figure 5–5 : Out of plane displacement of the web post	153
Figure 5–6 : Displaced shape of a beam without web post buckling.....	154
Figure 5–7 : Displaced shape of a beam with web post buckling.....	155
Figure 5–8 : Out of plane displacement of the web post for composite section	155
Figure 5–9 : Out of plane displacement of the web post for composite section	156
Figure 5–10 : Displaced shape of a beam without web post buckling.....	157
Figure 5–11 : Displaced shape of a beam with web post buckling.....	157
Figure 5–12 : Out of plane displacement of the web post for composite hybrid section	158
Figure 5–13 : Out of plane displacement of the web post for composite hybrid section	158
Figure 5–14 : Thermal calculation of the SHELL element forming the web	159
Figure 5–15 : Web temperature	160
Figure 5–16 : Dimensions of the steel profile	162
Figure 5–17 : Geometry of the IPE500 with $w = 50\text{mm}$	163
Figure 5–18 : Geometry of the IPE500 with $w = 375\text{mm}$	163
Figure 5–19 : Delta between SAFIR and simplified model for the failure load in cold conditions.....	164
Figure 5–20 : Delta between SAFIR and simplified model for the failure load in cold and hot conditions.....	165
Figure 5–21 : Summary of the results for the parametrical study on the web post buckling.....	166
Figure 5–22 : Displaced shape of a beam without Vierendeel failure	167

Figure 5–23 : Displaced shape of a beam with Vierendeel failure	168
Figure 5–24 : Vertical displacement of the central part of the beam in function of the time .	168
Figure 5–25 : FEM model of a ‘T’ section using a BEAM element	169
Figure 5–26 : Temperature in the section after 1800 sec.....	170
Figure 5–27 : Temperature distribution equivalent to the SHELL FEM model	170
Figure 5–28 : Web and flange temperature distribution	171
Figure 5–29 : Bearing capacities in function of the temperature in the section.....	172
Figure 5–30 : Temperature in the different sections.....	173
Figure 5–31 : Example of ACB® beam with filled openings.....	174
Figure 5–32 : Example of ACB® beam with reinforced opening	174
Figure 5–33 : Measures to avoid buckling of the web post	175
Figure 5–34 : FEM model of the filled opening in SAFIR	176
Figure 5–35 : FEM model with one filled opening in SAFIR.....	177
Figure 5–36 : FEM model with three filled openings in SAFIR.....	177
Figure 5–37 : Summary of the results for the parametrical study on the Vierendeel bending	178

Acknowledgments

Acknowledgments

Acknowledgments

Acknowledgments

The work presented in this thesis has been accomplished in the Research Centre of ArcelorMittal in Esch sur Alzette (Luxembourg) and in the Laboratoire de Mécanique et Ingénieries (LaMI) de l'Université Blaise Pascal – Clermont II.

I acknowledge Prof. J-P Muzeau, from LaMI, for the direction of this thesis, and Prof. H. Bouchair for his investment. I want also to express my appreciation to Mr. Mike Hawes and Mr. Andy Holmes from Westok Limited and to Prof. Ali Nadjai from Firesert who kindly granted me access to the tests results of testing campaign performed at the University of Ulster.

I also wish to thank my colleagues of the ArcelorMittal Research Centre for their support in the realisation of this work, especially Ms. Renata Obiala and Mr. Marc Brasseur for their important input in this thesis.

I offer my regards to all those who supported me in any respect during the completion of the project.

Finally, deep and sincere gratitude goes to my family: these are only a few of the many chapters that I could complete with their love, trust and support.

Acknowledgments

Chapter 1
Sate of the art

1. State of the art

Echoing the new trends of modern construction design, the spans are becoming longer. Therefore, steel frame buildings must be optimised using elaborated prefabricated solutions.

In order to minimise sections' size and maximise economy of the structure, steel beams should be designed to act compositely with the floor slab. The monolithic composite section (steel profile and concrete slab) is also benefiting in case of fire. The increased use of long span composite beams leads to large open offices with minimal number of columns. However, the beam depth will increase together with the span. These long span beams can lead to increased storey heights. The use of cellular beams (CB) largely overcomes this problem because ducts, pipes and other facilities can pass through the openings in the web. In addition, as CB is constructed from hot rolled sections, the increased section depth results in added strength without additional material and thus tends to reduce the total weight of the steelwork.

The following series of figures (Figure 1–1 to Figure 1–3) show the different steps to follow in order to manufacture cellular beams from a rolled steel profile:

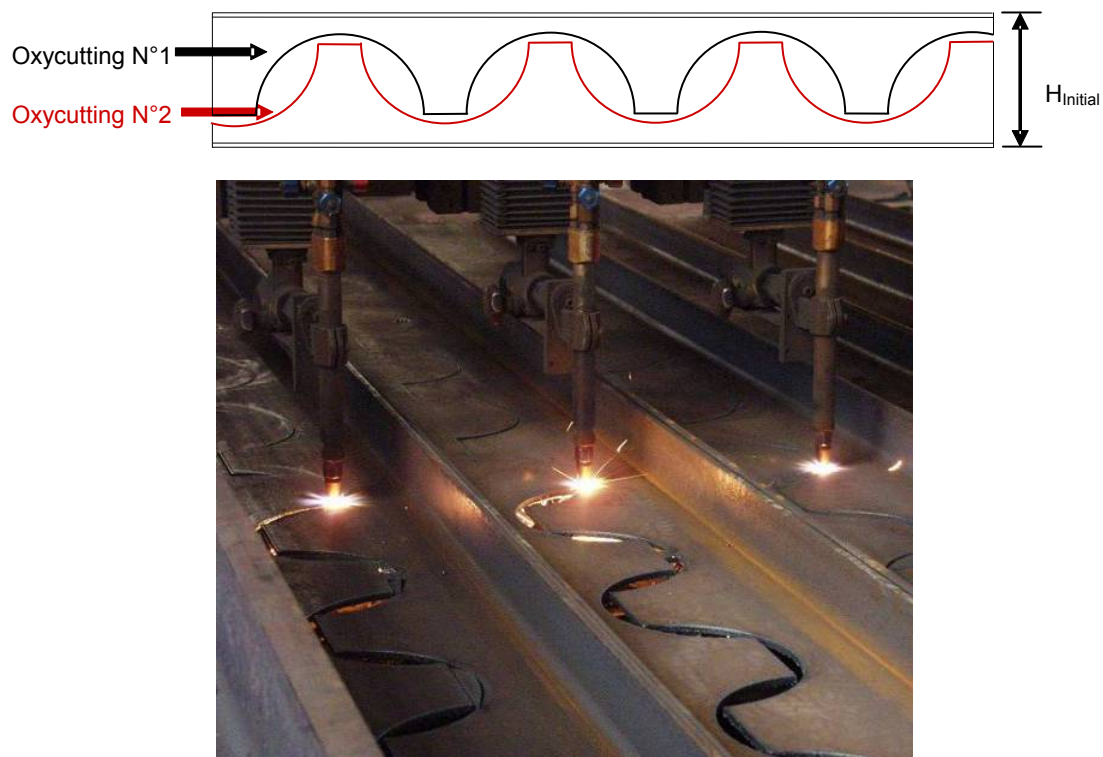


Figure 1–1 : Oxycutting of the parent profile

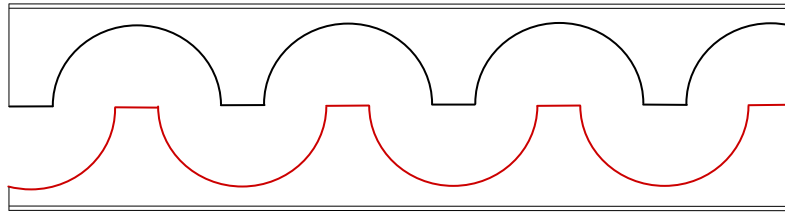


Figure 1-2 : Separation and positioning of the two parts of the parent profile

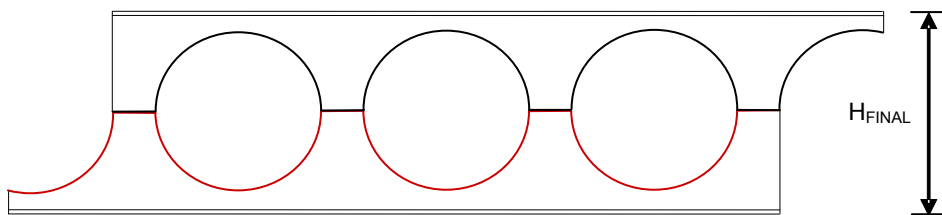


Figure 1-3 : Welding of the two parts of the parent profile

At the end of the process, for the approximately same weight of steel, the cellular beam could be 1.5 times as high as the parent profile (see Figure 1–4) with a second moment of inertia 2.5 as high as the parent profile.

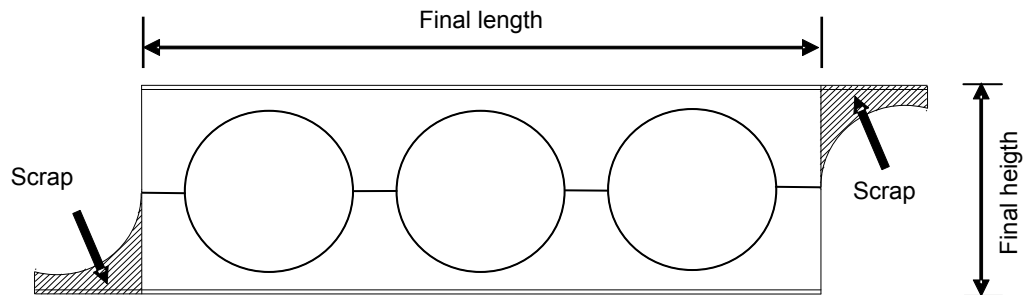


Figure 1–4 : Final geometry of the cellular beam

It is to be noticed that fire resistance is one of the main bottlenecks in the development of the steel construction for multi-storey buildings. But, the new fire engineering methods obtained from recent research ([1] to [15]) have demonstrated that it can be possible to accomplish fire safe steel structure without expensive passive fire protection, which ultimately leads to the reduction of steel competitiveness.

Moreover, efficient assessment of structures in fire conditions is becoming more and more relevant and it is commonly facilitated by the use of numerical models ([16] to [19]). However until now, no rigorous research about the performance of cellular beams in fire has been conducted in a systematic way. The design assumptions are still largely based on the performance of solid web beams in fire standard tests, which is obviously not rigorous enough and leads to a non economical design.

The fire resistance of cellular beams has been very controversial in recent years, with most of the debates focusing on the requirements for intumescent protection. That is why there is a clear need for improved understanding of the fire performance of the cellular beam itself in order to provide a clear design guidance and to promote cost effective design.

Throughout Europe, no widely-accepted agreement has yet been reached on how to assess the fire resistance requirements for cellular beams. In the UK, there is a rather rough prescriptive “rule” specified in BS5950 Part 8:1990 [20] for beams with web openings, stating that 20% extra coating thickness is required compared with solid-web beams. This rule has recently been subject to much scrutiny. Tests about some beams with large web openings have shown that the additional coating thickness is more often conservative than not unconservative, but these tests have been criticised because they only took one intumescent

product into consideration. The Steel Construction Institute in the UK published some simple advice in AD269 [21], where it is explained that increase of fire protection thickness depends on the geometrical properties of the beam. An updated document RT1006 [22] has been published recently, but it is simply an update to the traditional prescriptive fire protection rules. Both of these publications have been controversial, which indicates our limited knowledge and lack of uniformly accepted methods.

The investigation will also include the effects of asymmetry (see Figure 1–5). It is efficient to reduce the upper section profile when designing a composite cellular beam. In a composite section the large part of the compression is taken by the concrete slab and the tension forces by the steel profile. Depending on the geometry, the neutral axis can be located close to the upper flange. Consequently, a reduction of the upper flange section will not change the overall bearing capacity of the composite section. The economics of the beam is improved by only placing steel where it is required. Asymmetry causes changes in the stress patterns as well as distribution of temperature and strength. These effects will also be considered as part of the present research.

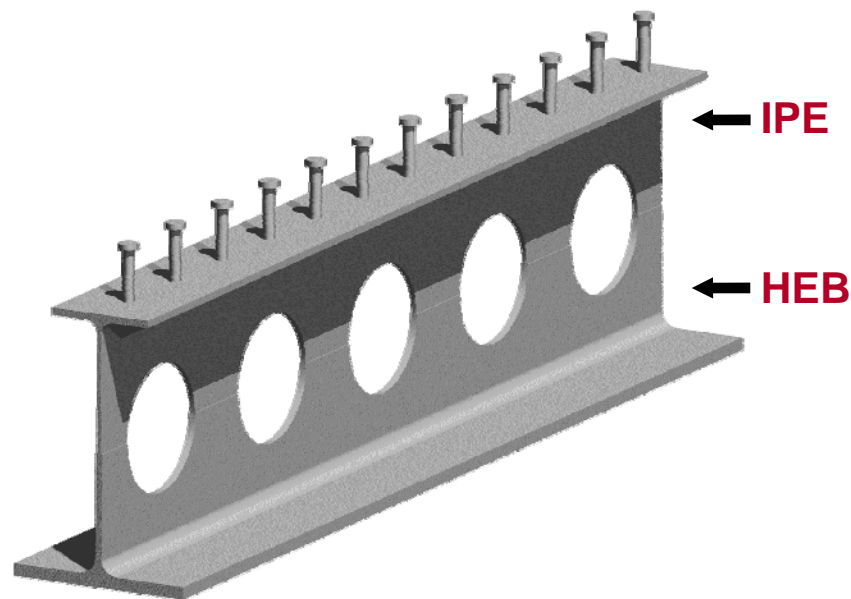


Figure 1–5 : Asymmetric section

Some previous research has been carried out in order to understand the behaviour of cellular beams in cold conditions. These researches led to some papers and design rules, of which the most recent rules are described in [23] [24] [25]. However, only one loaded and one unloaded fire test on cellular beams have been performed in the frame of these projects.

The conclusions were that further developments by calculation and testing are necessary to develop a design tool for cellular beams subjected to fire. This is the main aim of this work.

In order to ensure the reliability of the developed analytical model different steps were followed for the elaboration of the model.

A first step consists in experimental test campaigns. The available test data were summarised and a new test campaign was launched at the University of Ulster. The aim of this test campaign was to especially highlight the complex behaviour of unprotected cellular beams in case of fire. Two cold tests and four fire tests were realised and are reported in Chapter 2.

A second step was the elaboration of a FEM model for cellular beams ; this model was built in the Software SAFIR from the University of Liège. The model must be able to reproduce the complex behaviour of Cellular beam in case of fire taking into account instabilities.

A third step was the elaboration of the analytical calculation model for cellular beam in fire conditions. The aim of the model is to predict the critical temperature of each critical section for the main failure modes of cellular beams.

A last step was the validation of the analytical model against a parametrical study based on the finite element model developed and calibrated in step two.

Chapter 2

Experimental test campaigns

2. Experimental test campaigns

2.1 Introduction

Experimental test campaign on cellular beam are not really available in the literature due to the fact that each cellular beam producers perform their own test campaigns to develop their calculation procedure. In fire conditions, only one test was available in the literature.

Therefore, it was decided to first summarise the available test campaigns in cold conditions and extract the useful information for the calibration of the FEM Software SAFIR.

2.2 Experimental test data in cold conditions

The first test set that was used for the calibration of the model was performed by the Technische Universität Kaiserslautern in the scope of the RFCS Project Large Web Opening for Service Integration [25].

The next paragraph of this thesis briefly presents the test campaign. A complete report of this test campaign and the calibration of the SAFIR Finite Element model have been performed in the scope of the RFCS Project Valorisation of Large Web Opening for Service Integration (LWO⁺) [54]. All the tests data, results and FEM calculation can be found in this reference.

This test campaign was designed to investigate the web post buckling behaviour and the shear buckling in the welding between the two 'T' sections. The tests were performed on short span beams (app. 4.5m). With this testing procedure, the beams were mainly subjected to shear and not to bending.

2.2.1 Test specimen

A configuration for 10 tests has been defined. The idea was to cover the full range of web thickness available in I and H profiles for cellular beams. The following solutions have been retained.

The nominal steel grade is S235 for the whole sections (the measured values can be found in the reference [25]).

Specimen n°	Upper profile	Lower profile	Web thickness	Beam depth	Span length	Web post width	Diameter a_0	w/a_0 ratio
			[mm]	[mm]	[mm]	[mm]	[mm]	[-]
1-ss	IPE 400	IPE 400	8.6	558	1910	122	360	0.34
2-hs	HE 300 A	HE 300 M	8.5/21	477	1800	95	350	0.27
3-ss	HE 400 B	HE 400 B	13.5	599	1990	63	425	0.15
4-ss	IPE 400	IPE 400	8.6	600	1990	55	430	0.13
5-hs	IPE 300	HE 300 M	7.1/21	482	1690	55	355	0.15
6-ss	HE 300 M	HE 300 M	21	495	1590	50	335	0.15
7-hs	HE 300 B	HE 300 M	11/21	482	1870	123	350	0.35
8-hs	HE 300 A	HE 300 B	8.5/11	415	1800	147	300	0.49
9-ss	HE 400 B	HE 400 B	13.5	524	1846	150	310	0.48
10-ss	HE 300 M	HE 300 M	21	462	1800	147	300	0.49

ss corresponds to symmetric section; hs corresponds to hybrid section

Table 2-1 : List of specimen for testing

2.2.2 Test setup and test procedure

The statical system was a single-span beam submitted to three point bending, both ends were simply supported so that the system was statically determinated (see Figure 2–1). A concentrated load was applied by a hydraulic jack on the top flange at the middle of the beam.

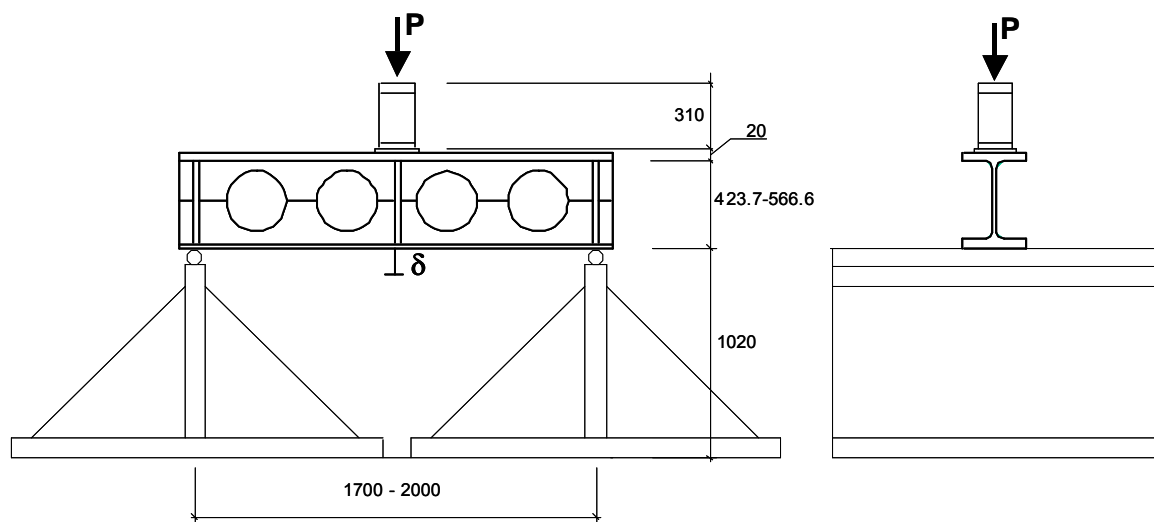


Figure 2–1 : Test arrangement

In the first step, the “displacements - controlled” load at low displacement rate was applied. It means that the velocity of the movement of the jack was controlled. In the second step, the load was applied stepwise by holding the displacement at each step in order to record the load relaxation effects. The tests were performed not only until the maximum load has been reached but until the structure was completely destroyed. This test procedure could highlight the post critical behaviour of small span cellular beam. It was possible to analyse the behaviour of the weld between the two ‘T’ sections after the web post buckling.

2.2.3 Results of the test campaign

The maximum load applied during the different tests was recorded and also compared to the analytical model. The results can be found in Table 2-2. In the LWO report [25]., test results were only available for the height first tests.

Specimen N°	Sections		Limit load [kN]	
	Upper part	Lower part	ACB 2.3	Test
1-ss	IPE400	IPE400	382	500
2-hs	HEA300	HEM300	320	606
3-ss	HEB400	HEB400	326	627
4-ss	IPE400	IPE400	165	252
5-hs	IPE300	HEM300	170	393
6-ss	HEM300	HEM300	421	971
7-hs	HEB300	HEM300	508	905
8-hs	HEA300	HEB300	248	685

ss corresponds to symmetric section; hs corresponds to hybrid section

Table 2-2 : Results of the FEA

It should be pointed out that the loads' limit in the experiment are always bigger than the limits given by the analytical model in cold condition. This tendency for small span has been also highlighted by Bitar in reference [24].

2.3 Experimental test campaign in fire condition

The only available test data was the furnace test performed in the scope of the RFCS project “Large Web Opening for Service Integration” [25]. This test was the only test in hot conditions available for such product.

2.3.1 Characteristics of the cellular beam members

The cellular beam was realised on the basis of different profiles:

- lower chord : HEB 340
- steel strength limit : 468 N/mm^2 (Flange)
- upper chord : IPE 300
- steel strength limit : 408 N/mm^2 (Flange)
 456 N/mm^2 (Web)

These two profiles were cut along the web and the two halves were welded in the web with a throat thickness $a = 5 \text{ mm}$.

Steel stiffeners were welded on each side of the web post at the level of the 3 concentrated loads (see Figure 2–6).

Dimensions of the cellular beam (see Figure 2–2 and Figure 2–3):

- upper flange : $150 \times 10.7 \text{ mm}$ ($I \times e$)
- lower Flange : $300 \times 21.5 \text{ mm}$ ($I \times e$)
- total height : 484.5 mm
- opening : $\varnothing 380 \text{ mm}$
- spacing between openings : 570 mm
- span : 6694 mm

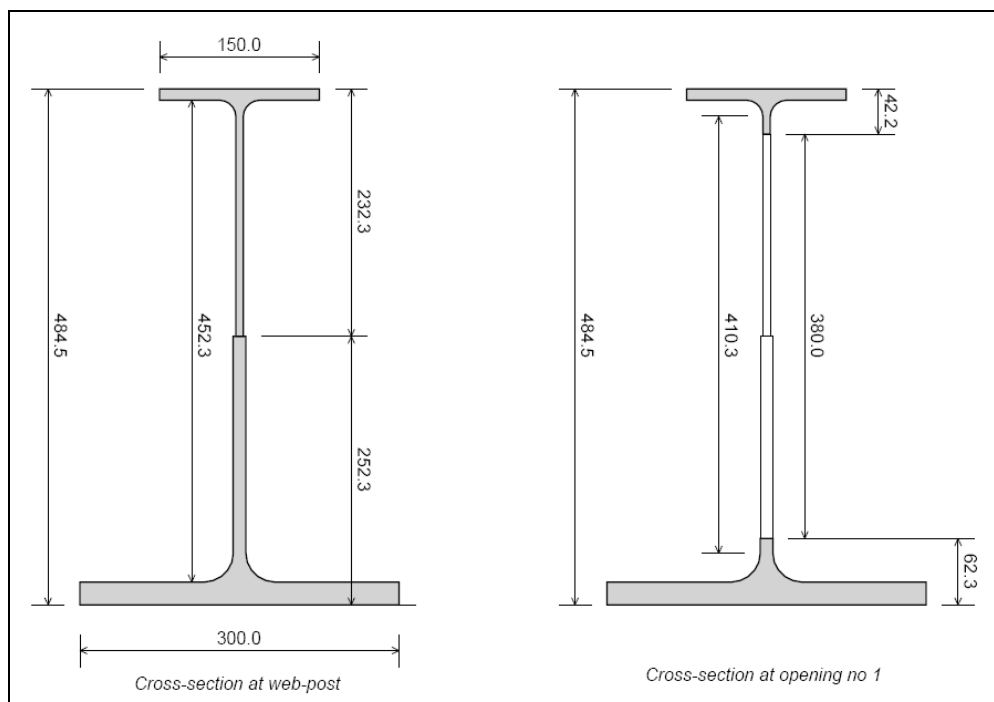


Figure 2–2 : Cross section of the tested cellular beam

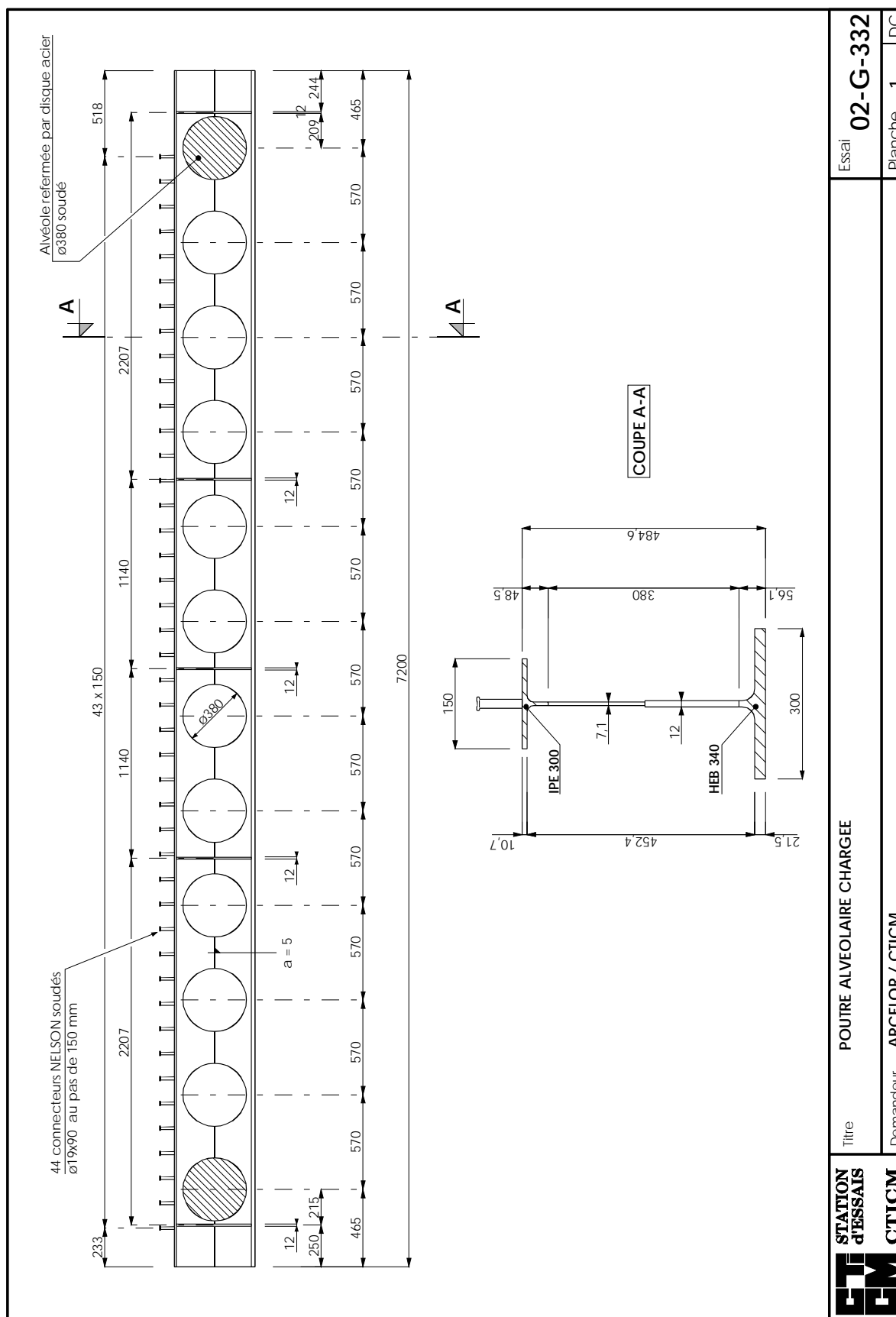


Figure 2–3 : Span and Geometry of the tested cellular beam

2.3.2 Composite floor

The cellular beam supported a composite slab made of a composite steel sheet and poured concrete. The connection between the beam and the slab was ensured by steel studs welded on the upper flange of the beam.

Characteristics of the composite steel sheet:

- reference of the steel sheeting : HI-BOND 55 - 750
- producer : MONOPANEL
- thickness of the steel sheet : 75/100 mm
- size of the rib : 150 mm
- spacing of the rib : 750 mm

Characteristics of the concrete slab:

- dimensions of the concrete slab : 1800 x 135 mm (l x e)
- concrete thickness over the ribs : 80 mm

The steel sheet HI-BOND 55-750 was fixed on the upper flange of the cellular beam using nails (HILTI) placed in each rib of the steel sheeting.

The welded steel mesh was positioned 20mm from the top of the concrete surface on the entire slab.

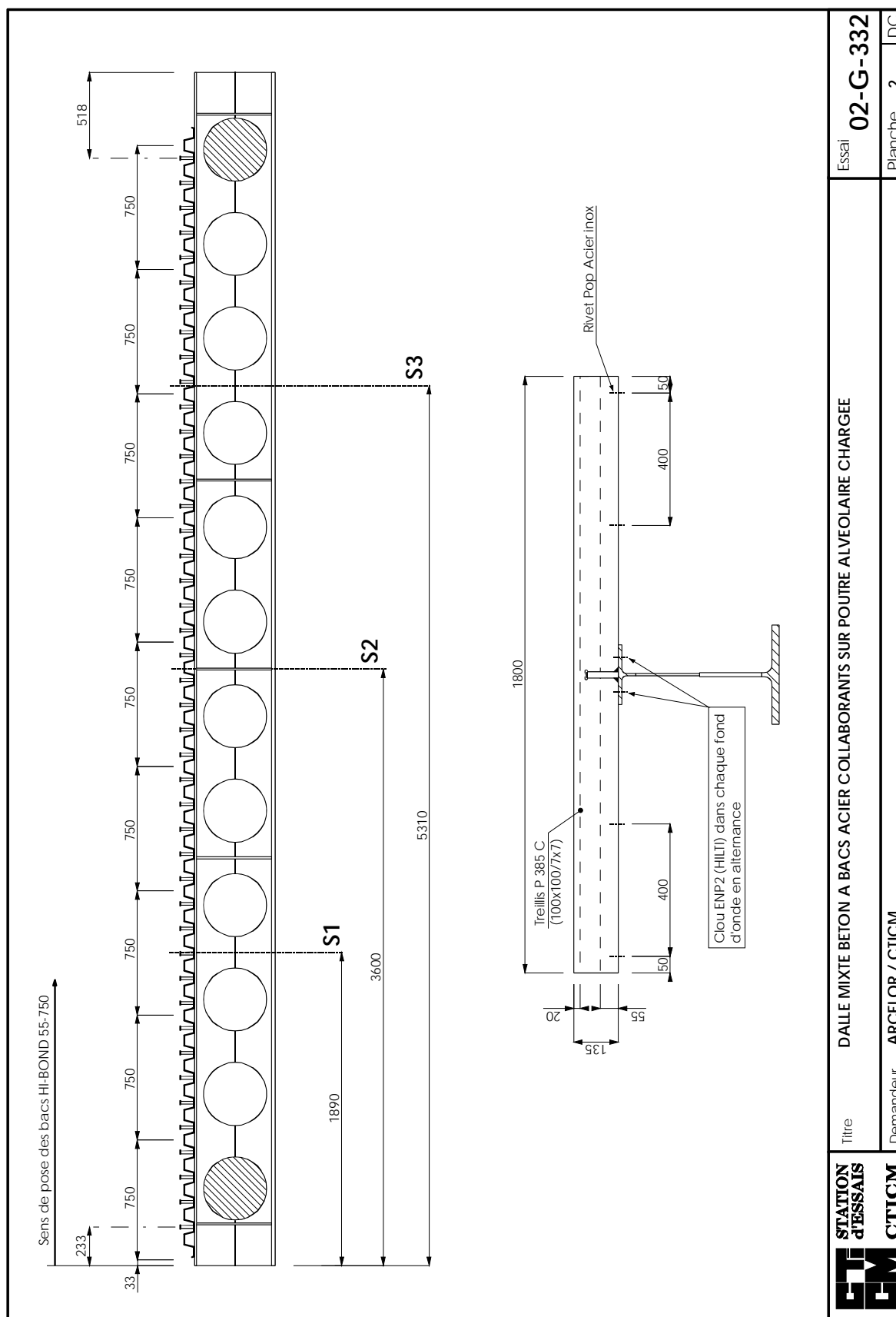


Figure 2-4 : Composite steel deck on the cellular beam

2.3.3 Fire protection of the cellular beam

In the analysed fire test, the cellular beam was protected against fire using a spray material NEWSPRAY (PROJISO).

The product was applied uniformly on the entire visible surface of the cellular beam (see Figure 2–5). The nominal thickness of the spray was 20 mm.



Figure 2–5 : Spray material applied on the entire surface of the beam

The thickness of the web at the openings diameter Ø380mm was protected applying the spray material NEWSPRAY in the continuity of the plain part of the web.

The holes between the upper flange of the beam and the ribs were fulfilled completely with the spray material in order to avoid any weak point of the upper flange's protection. This method is often used on site in order to avoid discussion on the temperature of the steel studs.

2.3.4 Applied thicknesses of sprayed fire protection material

The thicknesses of the sprayed protection material NEWSPRAY have been measured at 10 different positions. As it is shown in the Table 2-3, the thickness of the protection material really varied along the beam and the analysis of the tests results (temperature in the different sections) is really difficult. This variation in the thickness is an industrial reality and comes from the application procedure for spray materials.

Position	MEASURED THICKNESSES (mm)			
	Min	Mean	Max	Standard deviation
Lower flange	11	24	45	5
Web around the openings	20	27	40	7

Table 2-3 : Measured thickness of the protection spray

2.3.5 Loading and boundary conditions of the beam

The cellular beam was simply supported between two supports made of two circular bars Ø100mm with a span of 6694mm (see Figure 2–6).

Three concentrated loads were applied on the beam during the whole duration of the fire tests.

The loads were applied by 3 hydraulic jacks pushing on transverse steel profiles HEB240, L=600mm (see Figure 2–6)

- span between the supports : 6694 mm
- distance between the support and the first load : 2207 mm
- distance between the loads : 1140 mm
- loads applied by each hydraulic jack : 100 kN

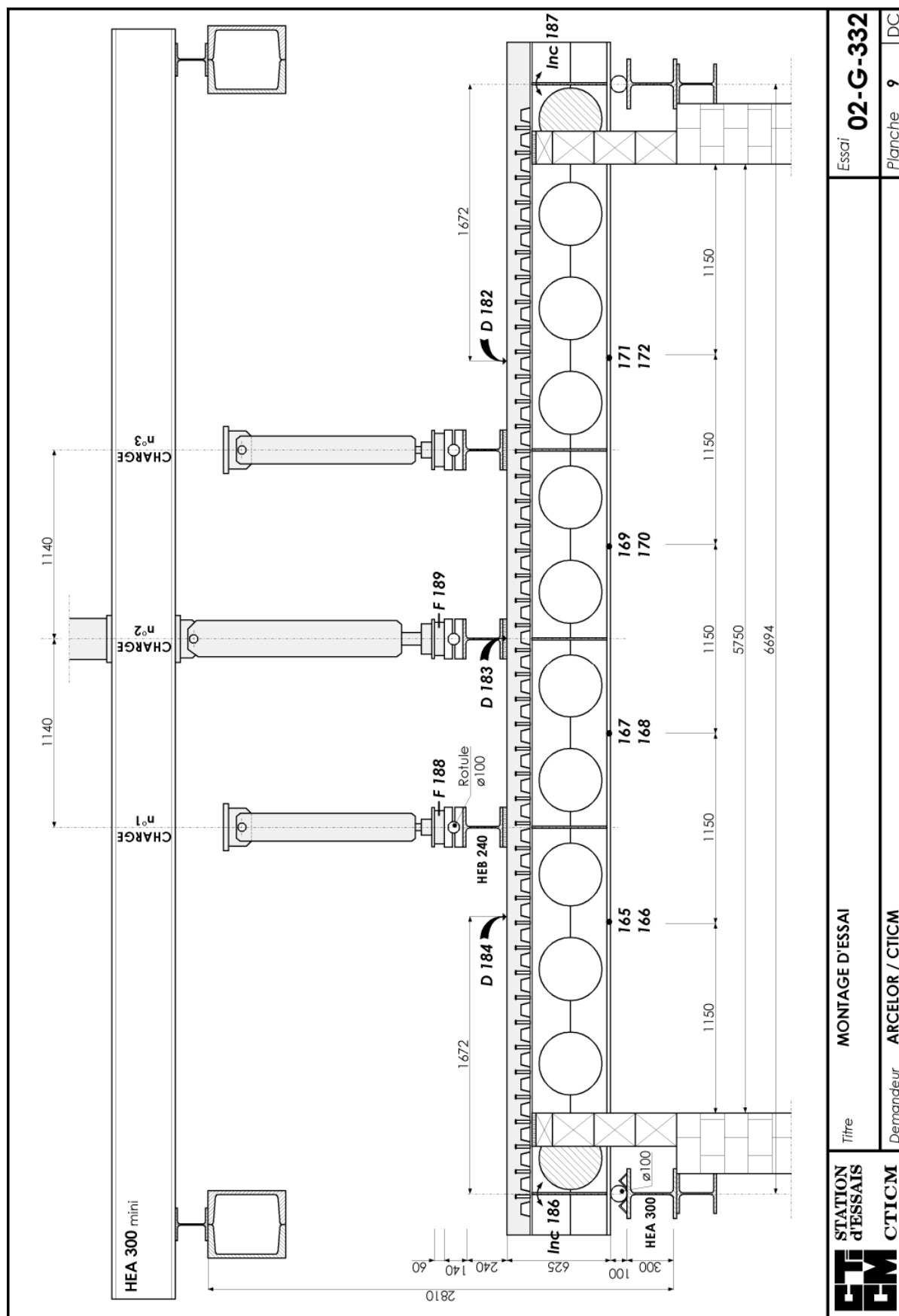


Figure 2–6 : Position of the beam in the furnace and loading.

2.3.6 Thermal measurements

As already explained in Chapter 2.3.4, the stability of the thermal results is not as accurate as expected. The thickness of the fire protection was so variant that the temperature diverges significantly for the same section at different positions along the length of the beam.

Moreover, the temperature of the web on the upper part of the opening (see Figure 2–7 and Figure 2–8) is really smaller than on the other parts (see Figure 2–8) due to the accumulation of the protection material in this area of the section.

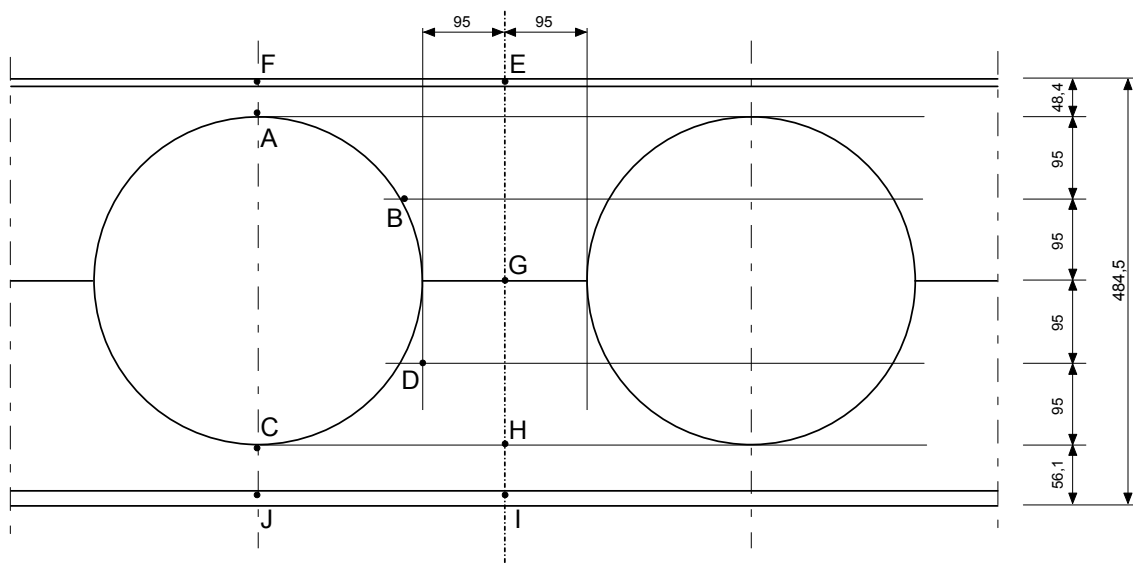


Figure 2–7 : Position of the different temperature measurements

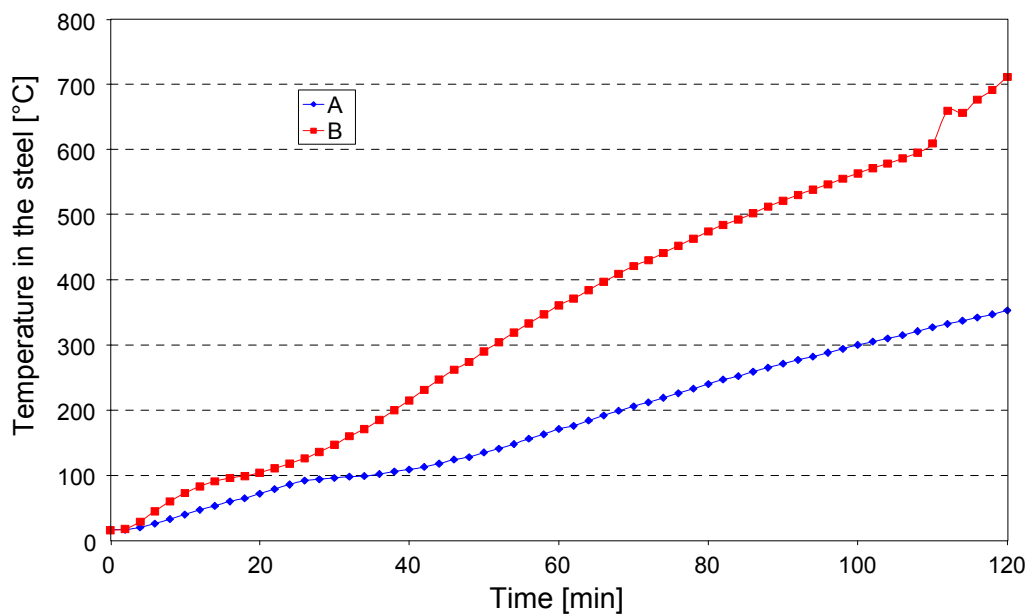


Figure 2–8 : Temperature of the steel at different positions

2.3.7 Results of the test

The complete set of results for this fire test are available in the “RAPPORT d'ESSAI n° 02-G-332” of the CTICM [57]. This information was also reported in the final report of the RFCS project “Large web openings for service integration” [25].

The beam failed by web post buckling after 120 minutes and the Figure 2–9 shows the shape of the beam after having removed the protection.



Figure 2–9 : Shape of the beam after the fire test

2.3.8 Conclusion of the test in fire conditions

As explained in Chapter 2.3.4, the stability of the thermal results obtained was not accurate, as expected, for this fire test. The reason is that the thickness of the fire protection was very variant and consequently the temperature varied a lot for the same section at different positions along the length of the beam.

2.4 Conclusion on the existing test campaign

In the first available test campaign, the load-deformation behaviour of short beams with large web openings has been investigated. Using this study, it was possible to simulate the test with the Finite Element model built in SAFIR as described in Chapter 3. But this test campaign was designed to focus on shear behaviour with small span beam and the tests were only performed in cold conditions.

Concerning the test in fire conditions, as explained in Chapter 2.3.4, the stability of the thermal results obtained was not accurate, as expected. The reason is that the thickness of the fire protection was very variant and consequently the temperature varied a lot for the same section at different position along the length of the beam.

In order to assess the behaviour of unprotected cellular beams, a new test campaign was launched.

2.5 New experimental test program

In order to better understand the complex behaviour of cellular beam in fire condition, a new series of full-scale tests on composite beams was performed at the University of Ulster. This series of tests was performed on unprotected cellular beams.

In case of unprotected cellular beams, additional parameters play a significant role:

- heating velocity
- thermal expansion
- thermal gradient between the different parts of the beam

The tests were carried out on two series of full-scale composite cellular steel beams with span of 4500mm subjected to one and two concentrated loads using two types of beams; symmetrical composite beams and asymmetric composite beams.

Symmetrical composite beams (Test A1):

The beam for Test A1 was produced on the basis of UB406X140X39 (see Figure 2–10) for the top 'T' section and UB406X140X39 for the bottom 'T' section with a finished depth of 575x140.

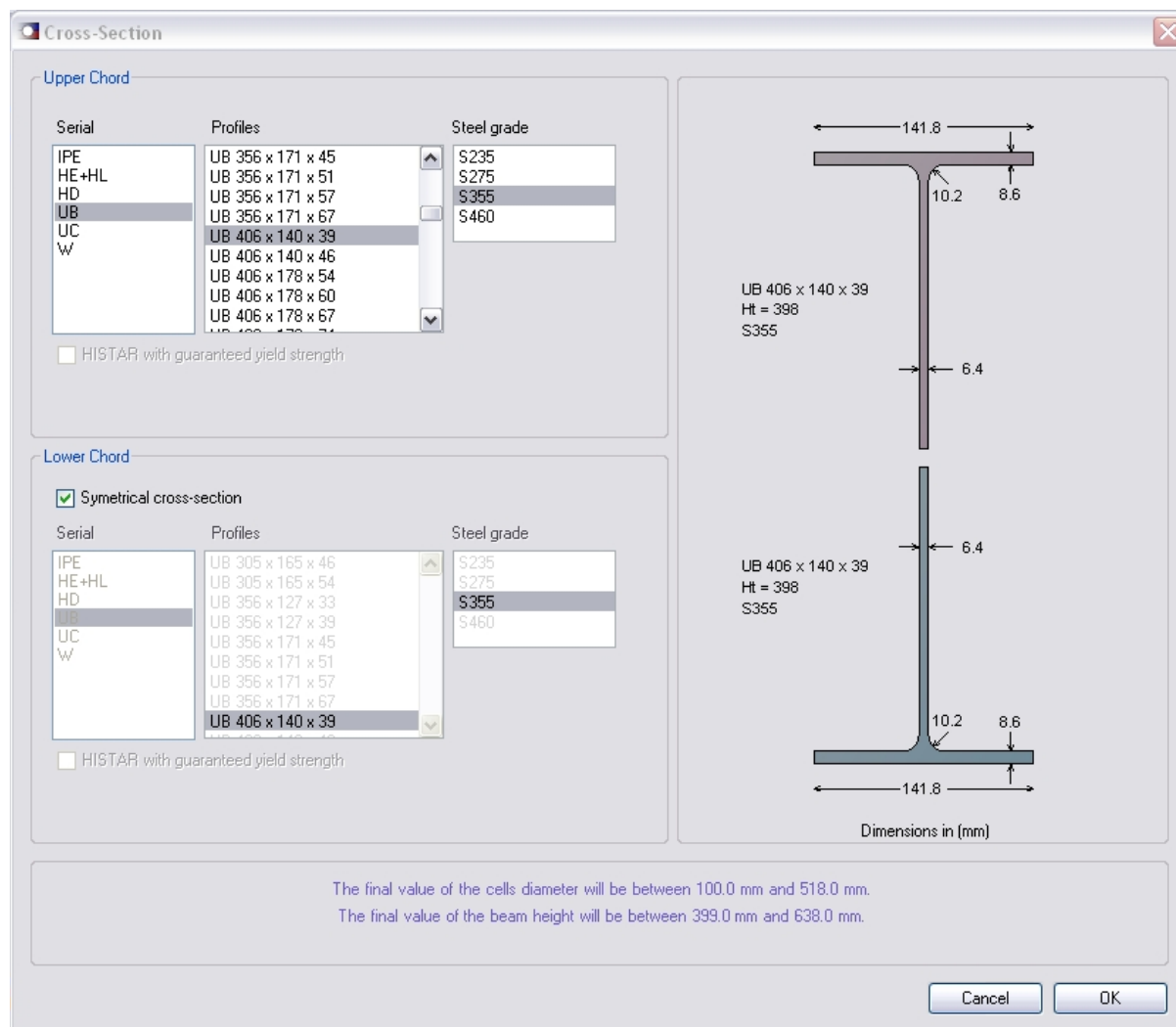


Figure 2–10 : Profiles used for A1 section

Asymmetric composite beams (Test B1):

The beam for Test B1 was produced on the basis of UB406X140X39 for the top 'T' section and of UB457X152X52 for the bottom 'T' section (see Figure 2–11) with a finished depth of 630mm.

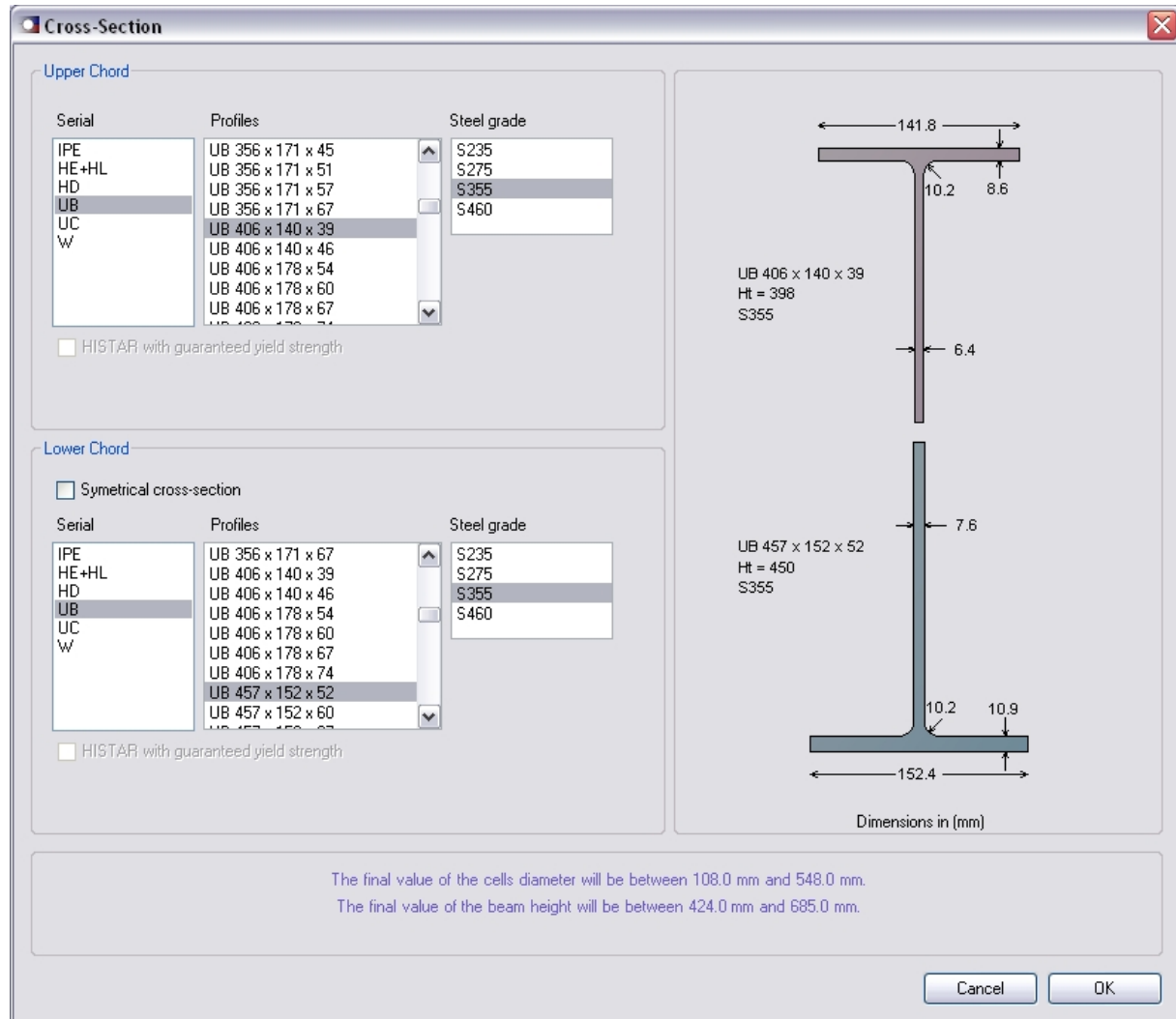


Figure 2–11 : Profiles used for B1 section

Each type of beam was tested:

- at ambient temperature up to failure.
- at elevated temperatures under load derived from cold test with a low heating velocity (10°C/min).

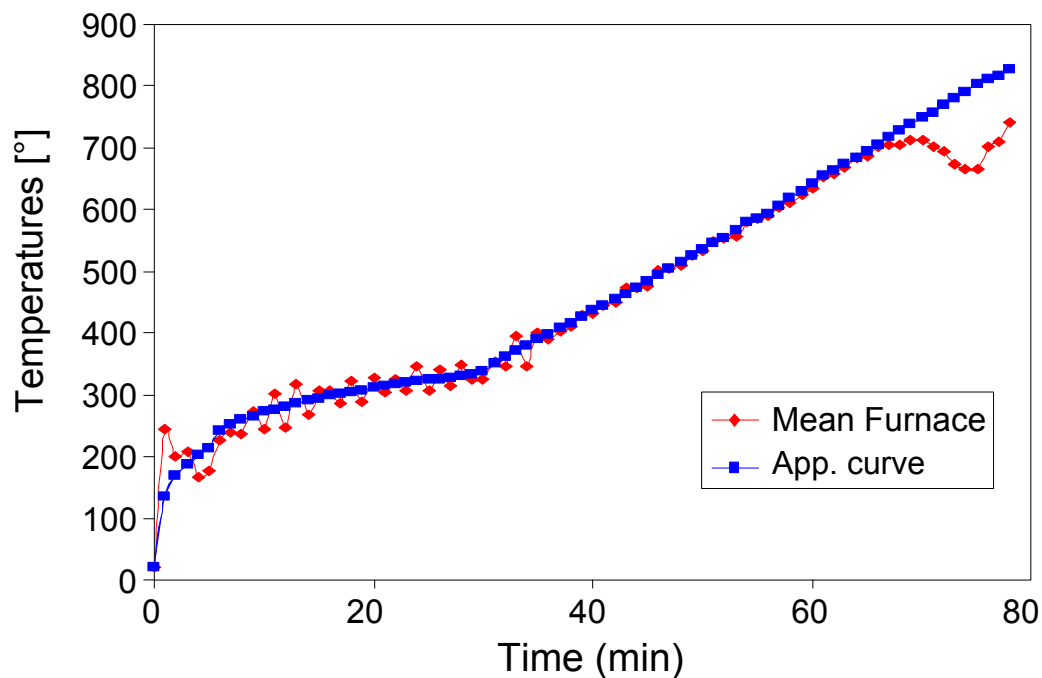


Figure 2–12 : Furnace temperature time curve used in the experimental study

- at elevated temperatures under load derived from cold test with a fire curve corresponding to the ISO-834 heating curve (see Figure 2–13).

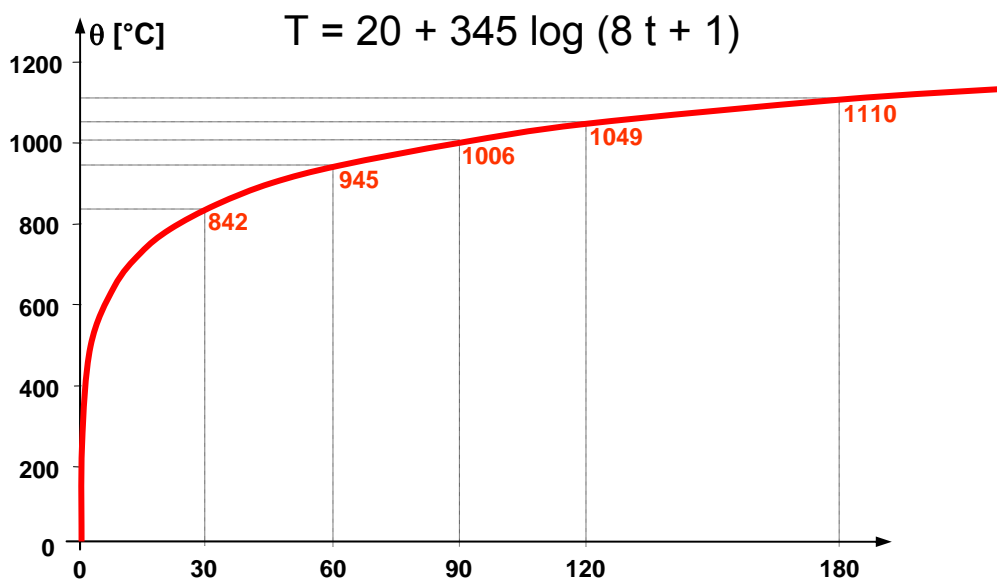


Figure 2–13 : ISO-834 curve

Specimens for the two series of 3 tests were fabricated on the basis of the same mother steel bare in order to guarantee exactly the same material properties for the 3 series of tests.

All the concrete slabs produced with normal-weight concrete (Grade 35N/mm²) had a nominal thickness 150mm and width of 1200mm. The slab reinforcement was composed of welded wire mesh reinforcement A142 with yield strength of 460N/mm². Full interaction between the slab and beam was ensured in all specimens by the use of highly-concentrated shear connectors of 19mm-diameter studs of a height 120mm. The shear studs were evenly distributed in one row with an interval of 150 mm along the beam length.

A Holorib sheet HR 51/150 with a thickness of 1.25 mm was used as sheeting (see Figure 2–14). The measured yield stress from a tensile test was $f_y = 327\text{N/mm}^2$.

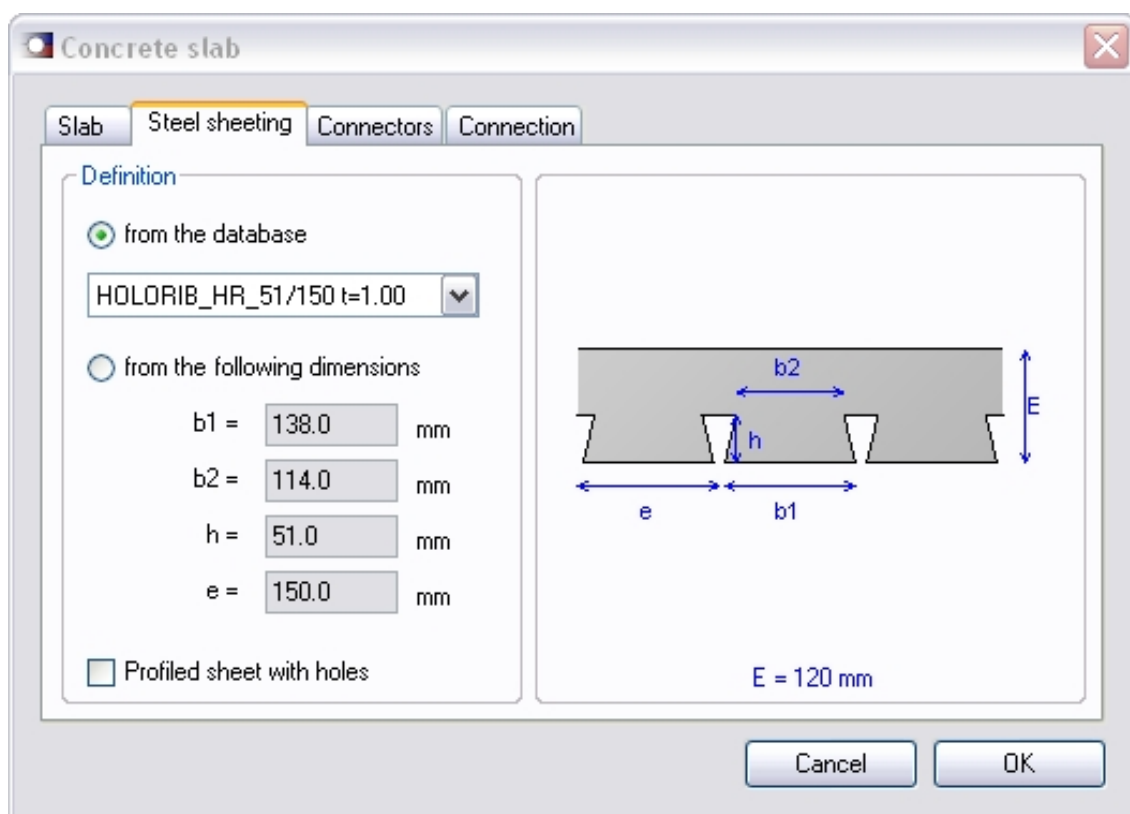


Figure 2–14 : Dimensions of the Holorib sheets HR 51/150

Concrete compressive strength was measured at different points of time, specifically after 2 weeks, 28 days and during the testing days.

Top 'T'	Bottom 'T'	a_o [mm]	W [mm]	W/ a_o	$a_o/t_w \epsilon$	e [mm]	e/ a_o	d/ t_w	A_{TB}/A_{TT}
UB406X140X39 S355	UB406X140X39 S355	375	125	0.33	59.60	500	1.33	83.9	1
UB406X140X39 S355	UB457X152X52 S355	450	180	0.4	59.21 70.31	630	1.4	84.3	1 1.43

Table 2-4 : Steel cellular beams detailing.

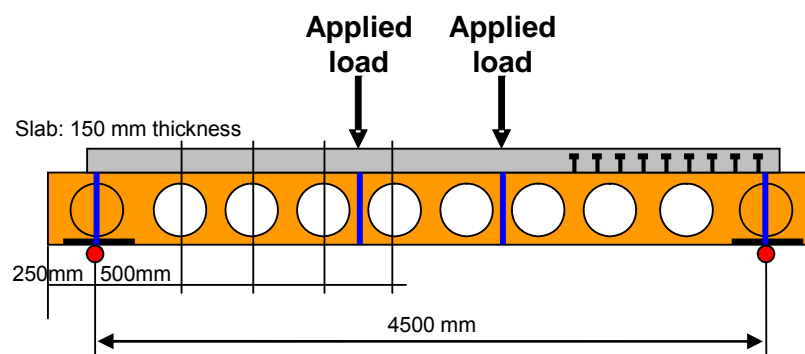


Figure 2-15 : Symmetrical composite cellular beam

Characteristics of the beam A1:

'T' section :

'T' depth = 287.4 mm

Flange width = 141.8 mm

Web thickness = 6.4 mm

Flange thickness = 8.6 mm

Root radius 10.2 mm

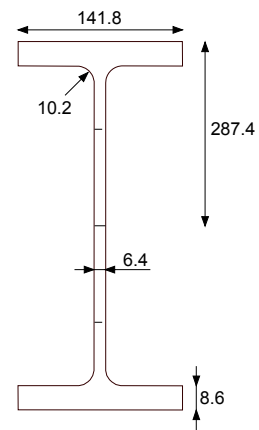


Figure 2-16 : Characteristics of the beam A1

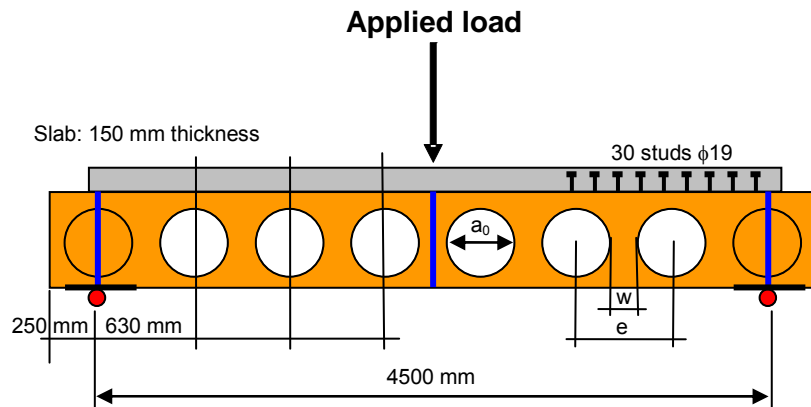


Figure 2-17 : Asymmetric composite cellular beam

Characteristics of the beam B1:

Top 'T' section:

'T' depth = 302.1 mm

Flange width = 141.8 mm

Web thickness = 6.4 mm

Flange thickness = 8.6 mm

Root radius 10.2 mm

Bottom 'T' section:

'T' depth = 328.0 mm

Flange width = 152.4 mm

Web thickness = 7.6 mm

Flange thickness = 10.9 mm

Root radius 10.2 mm

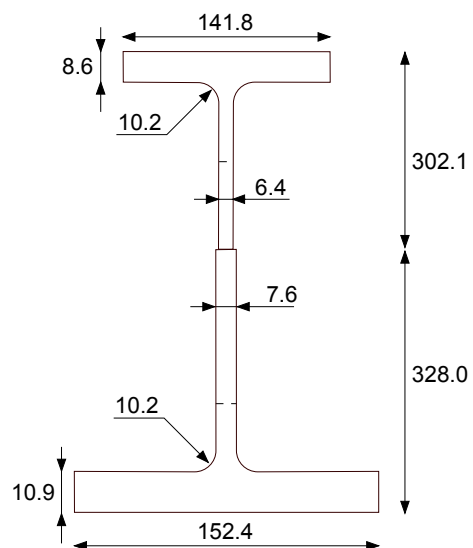


Figure 2-18 : Characteristics of the beam B1

2.5.1 Testing procedure of the beam at ambient temperature

Both tests A1 and B1 were conducted by using portal frames with a loading system of 1600kN capacity. The composite beam specimen was simply supported at both ends. A 600kN hydraulic jack was used to apply the monotonic load. The load was applied to the top concrete flange through a distribution beams exhibited in Figure 2–19 for two concentrated loads. Figure 2–19 demonstrates the equipment used to record the experimental data; load versus deflections and strain gauges readings.

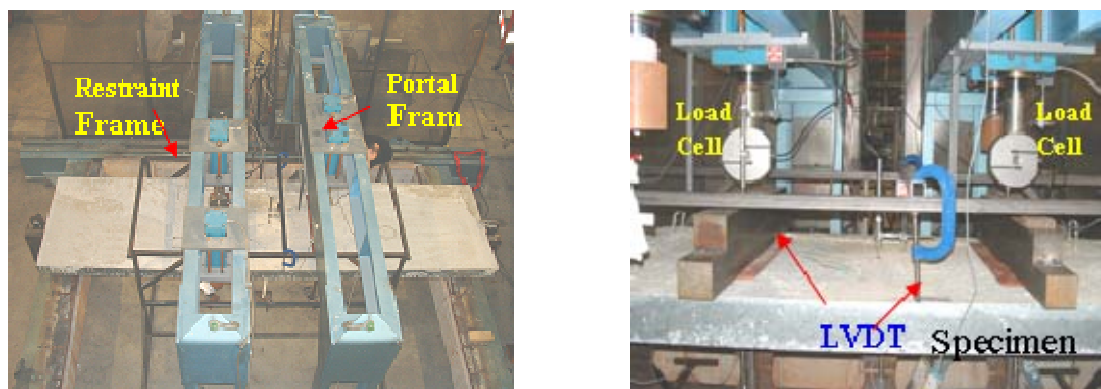


Figure 2–19 : Experimental set up / load introduction of test A1

For both test A1 and B1, load cycles at a load level of 20% and 60% of the pre-design load were applied to ensure that slippage of the load introduction and supports as well as friction in the shear joint and the structure do not perturb the results. All the load cells used for the experiment were calibrated before testing.

After these two cycles, 20% of the pre-design load used by Westok Cellbeam software [58] was kept for one hour before being increased. Each load step with a value of 10 kN/step was carried out at an interval of 3 minutes.

Both ultimate failures of the specimens were associated with web-post buckling. Study of various measures of buckling load led to the conclusion that this maximal load represented the web buckling load. In each case the buckling mode was of the shape of double curvature bending of the post (see Figure 2–20). Before this occurred, high strains had developed following tensile yield of the lower part of the steel beam. Tensile strains developed above the opening indicated that the neutral axis was near to or in the slab.

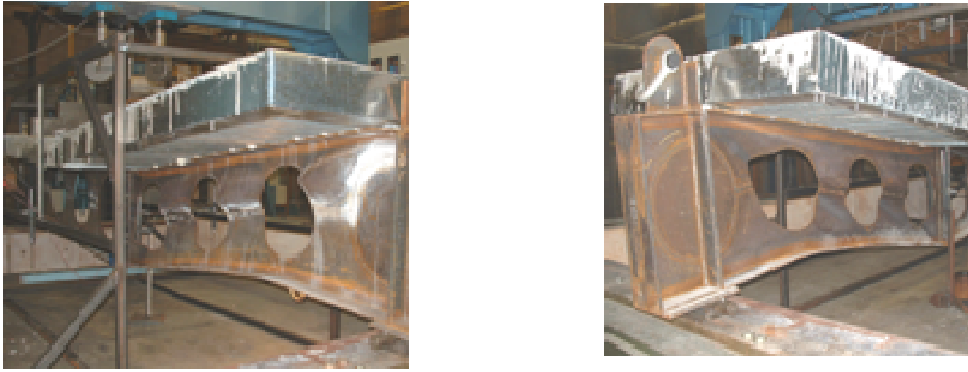


Figure 2–20 : Web post buckling mode failure A1

After the web post buckling took place, the hinges around the openings were developed leading the webs to buckle in form of ‘S’ shape.

2.5.2 Experimental results of tests at elevated temperature

The composite cellular steel beam tests A2 and B2 were performed under the same fire curve shown in Figure 2–13. This fire curve was set up in order to produce lower peak temperatures but longer duration sufficient to permit significant heat conduction. This may generate a large build-up of vapour pressure and create significant thermal expansion which, in turn, may produce a restraint force coming from the concrete slab. The applied loads for tests A2 and B2 are 180kN and 210kN, respectively. They are calculated as 50% of the failure load obtained from the cold tests A1 and B1. Both beams A2 and B2 were kept loaded for over an hour before the furnace was activated. The positions of the thermocouples (Figure 2–21) were located at each web post along its depth of the section and also around the openings.

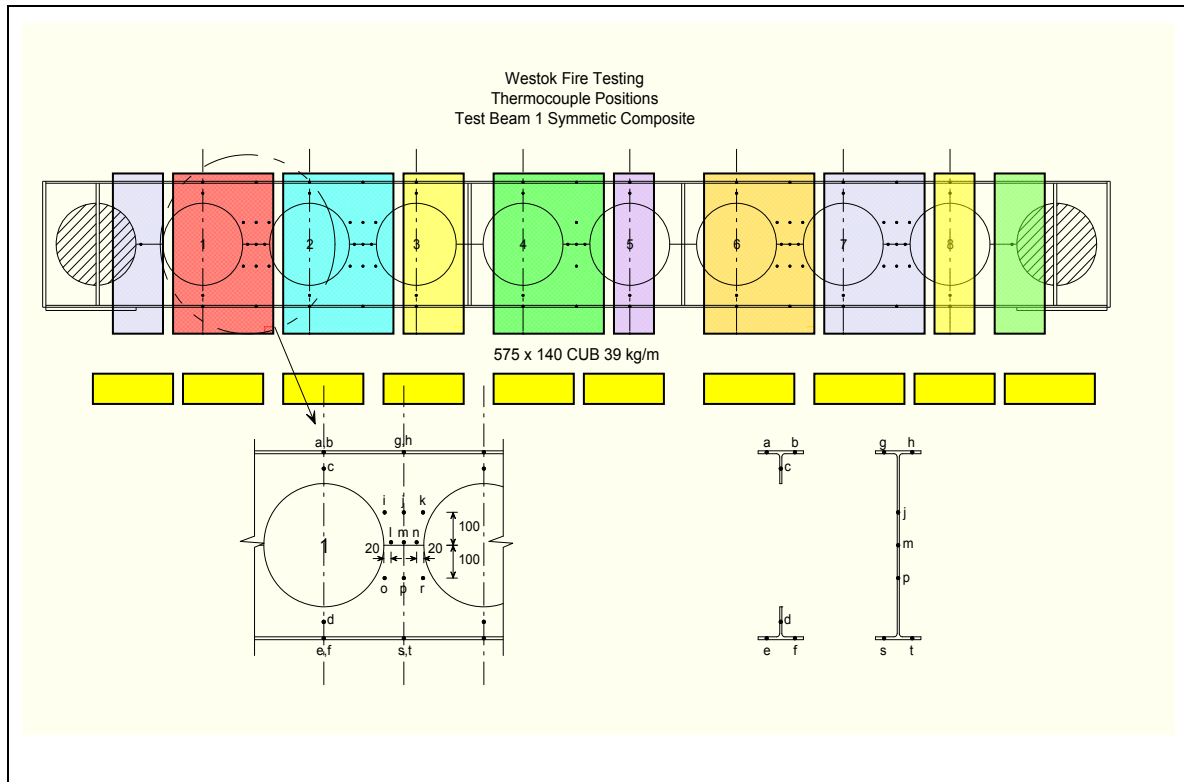


Figure 2-21 : Typical Thermocouples locations

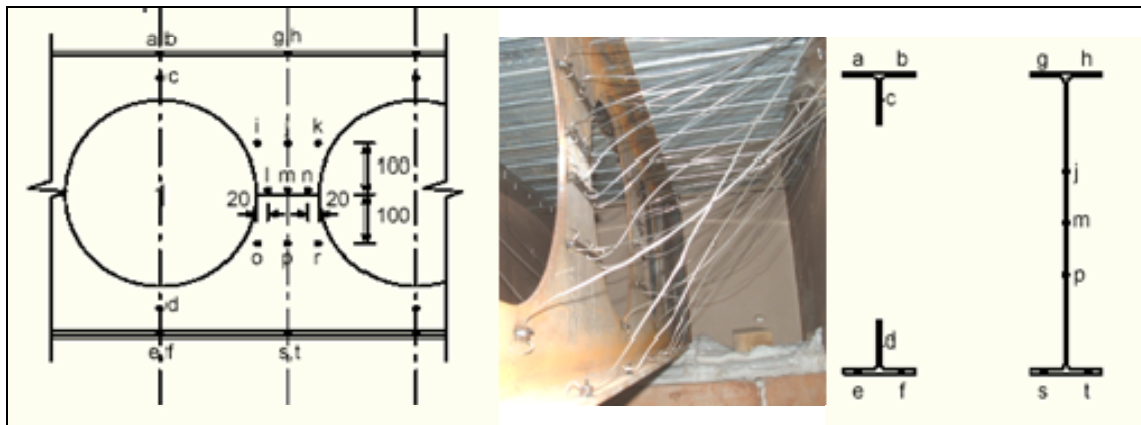


Figure 2-22 : Typical Thermocouples locations

The steel and concrete temperatures were measured at several points in the different beam sections, the graphs hereafter show the recorded results during the fire test.

The steel temperature in a function of time recorded by some thermocouples are given in the following figure for the test B2 (one concentrated load).

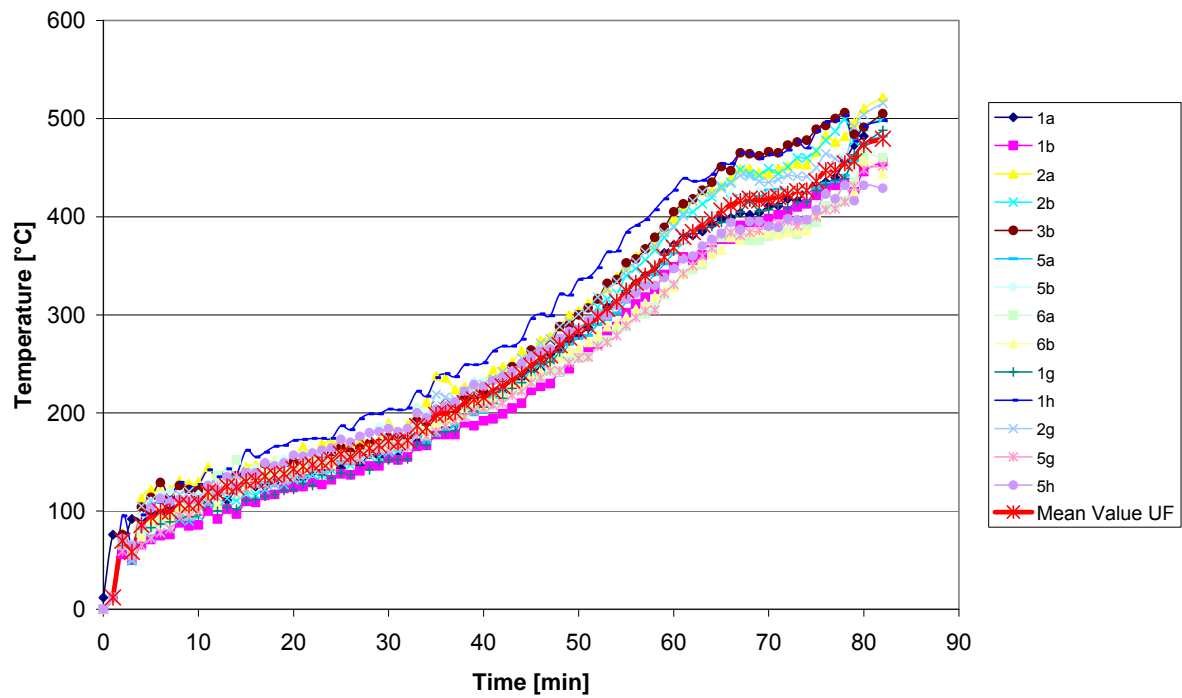


Figure 2-23 : Thermal measurement in the upper flange along the beam

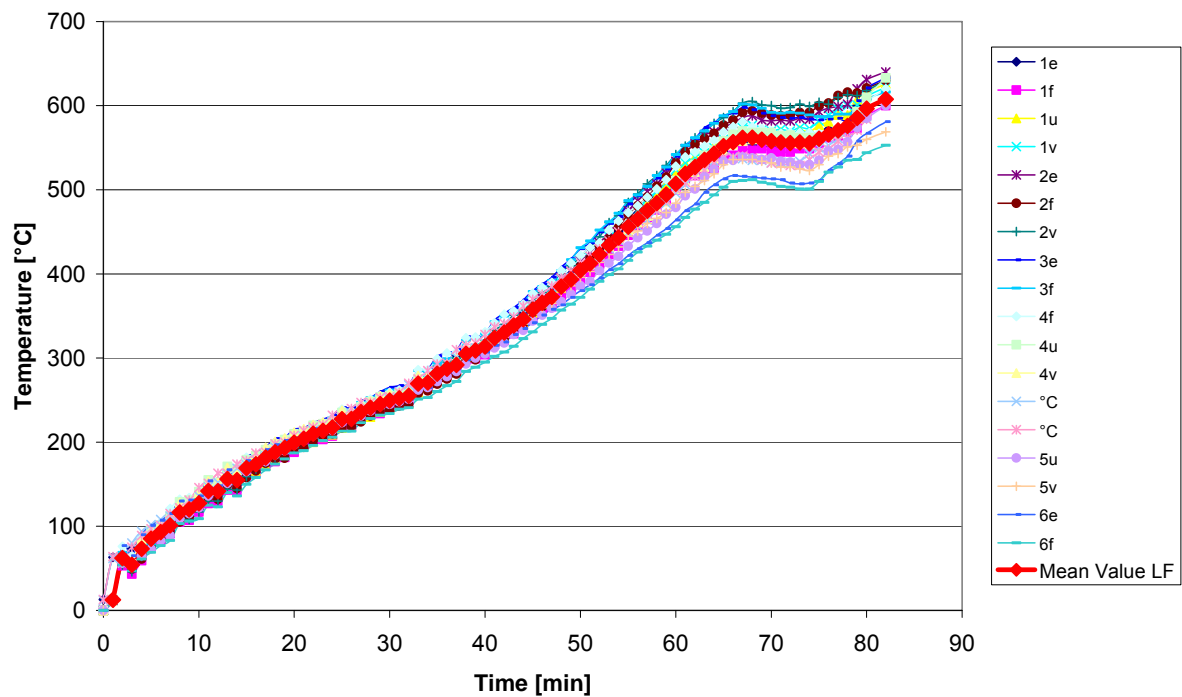


Figure 2-24 : Thermal measurement in the Lower flange along the beam

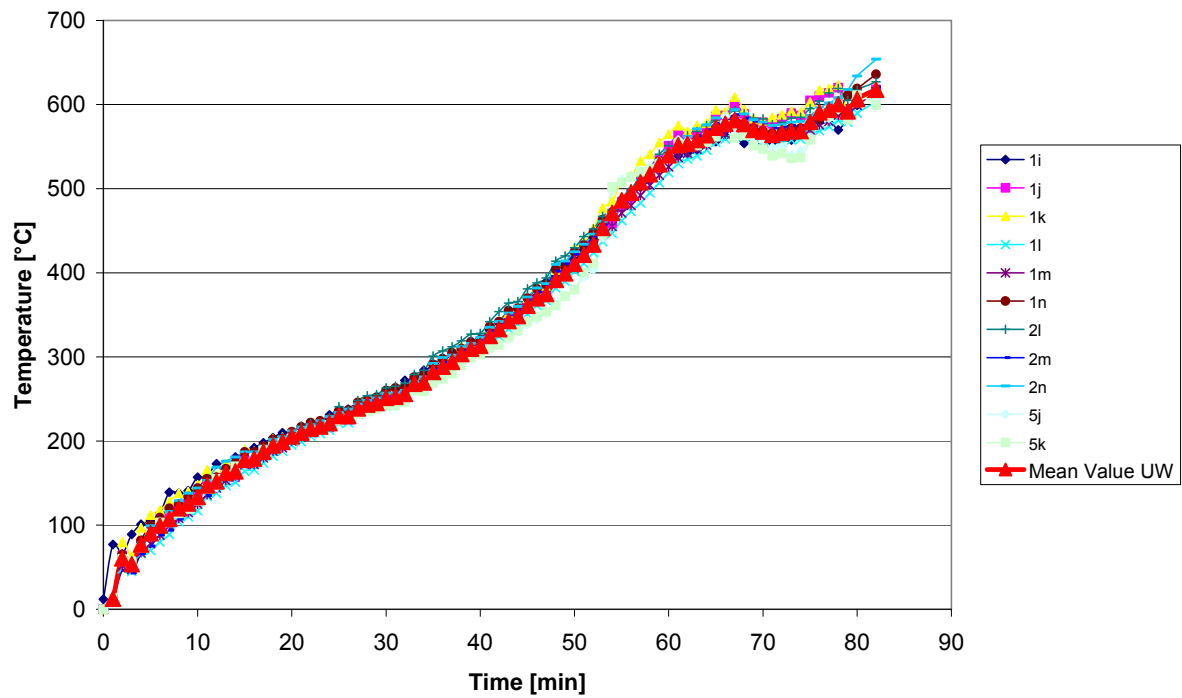


Figure 2–25 : Thermal measurement in the upper web along the beam

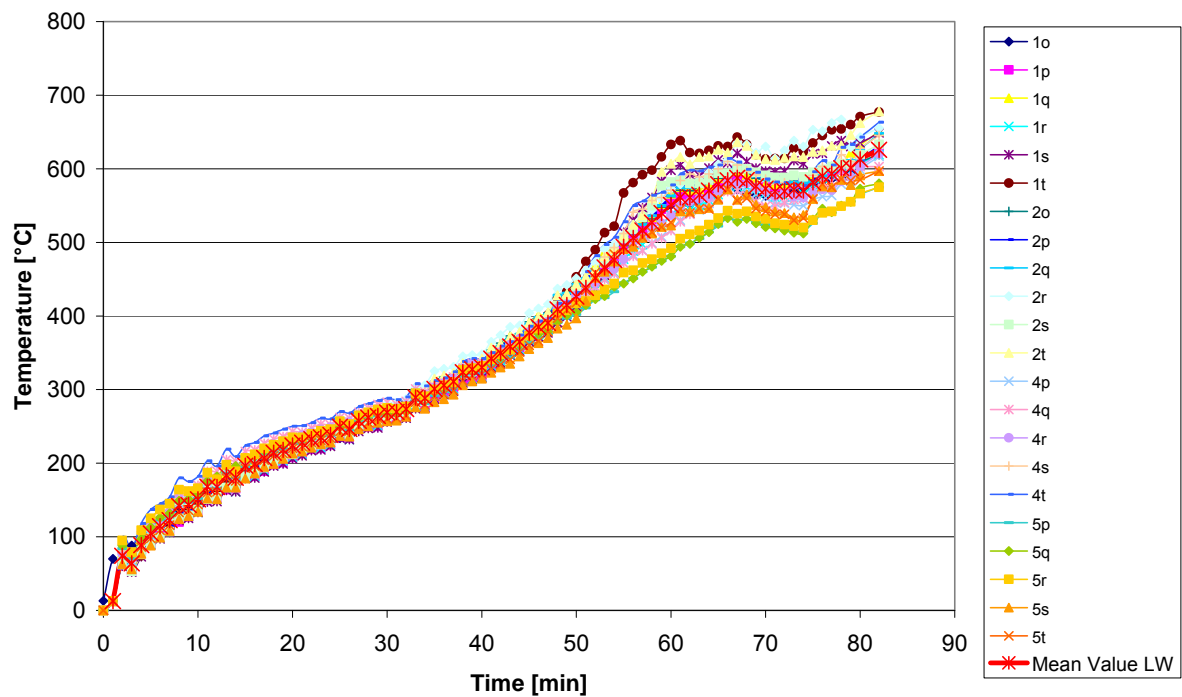


Figure 2–26 : Thermal measurement in the Lower web along the beam

As shown on Figure 2–23 to Figure 2–26, the thermal distribution of the steel temperature along the beam is diverse, especially in the upper flange and the lower web. It is observed

that in the time period from 65 minutes to 85 minutes, the range of temperature can vary about 100°C in the steel for the same type of section.

These discrepancies are not coming from the changes in the geometry (see Figure 2–21), the temperature in points 'a' and 'b' in Figure 2–21 is not higher than in points 'g' and 'h' for neighbouring sections.

The discrepancies are also more relevant for sections subjected to shadow effect (upper flange and lower web). This can be justified by the test setup and the position of the burners in the furnace (see Figure 2–27) where some parts of the beams cannot be directly exposed to the radiative flux of the burners.

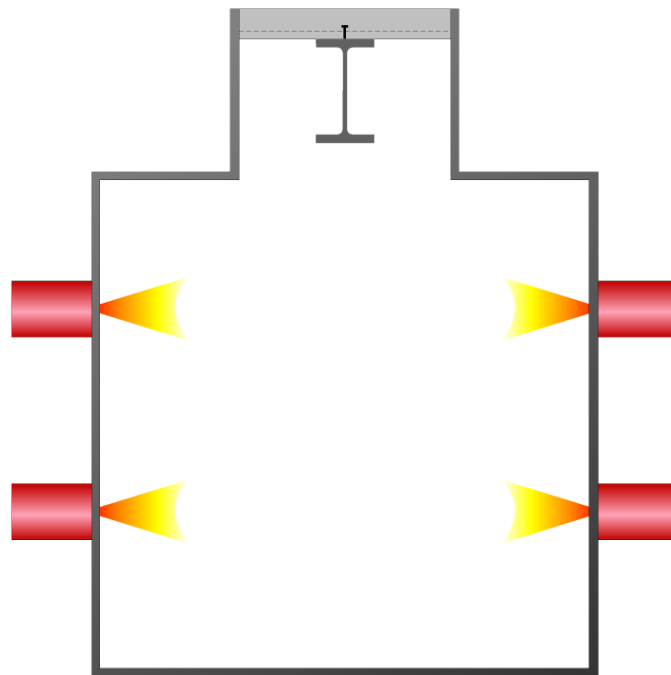


Figure 2–27 : Furnace

With this configuration, the lower part of the web and the upper flange were not subjected directly to the radiation provided by the burners.

The same temperature field and the same discrepancies can be noticed in the second test with low temperature increase on beam A2.

Concerning the displacement and mechanical behaviour, Figure 2–28 and Figure 2–29 illustrate a linear elastic response. In the time deflection curves at 30 minutes time when the temperature is equal to 320°C, almost equal deflections in both beams can be observed. Beam A2 starts to show signs of stiffness loss at time 40 min when the temperature is 432°C

while beams B2 still show no sign of weakness. At 60 min time the deflection is increasing in both beams and the stiffness is decreasing at a temperature equal to 634°C. Between 60 and 70min, deflections of both beams are becoming larger with less stiffness and strength in the members when the temperature climbed up to 712°C. After that time, the beams tried to become 'alive' just for a short time due to the presence of the reinforced concrete slab on the top of the steel members. This instability of the beams is a result of the rapid loss of the web post capacity relative to the loss of capacities in the 'T' sections. This failure mechanism is known as web post buckling and its typical form can be seen in Figure 2–30.

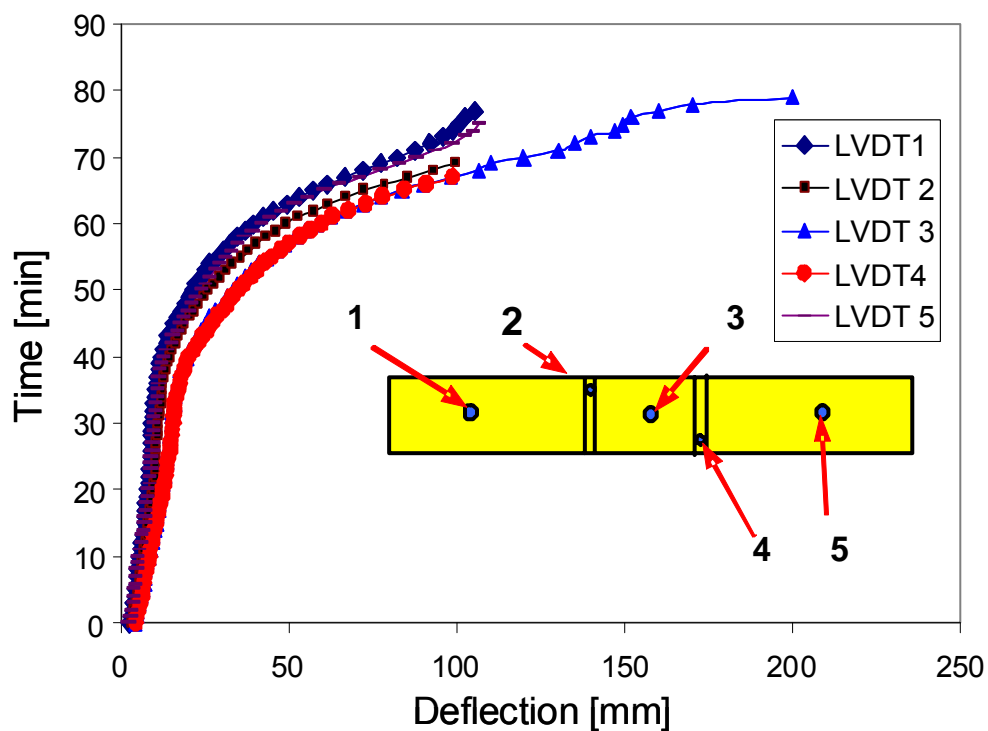


Figure 2–28 : Time versus deflection of test A2.

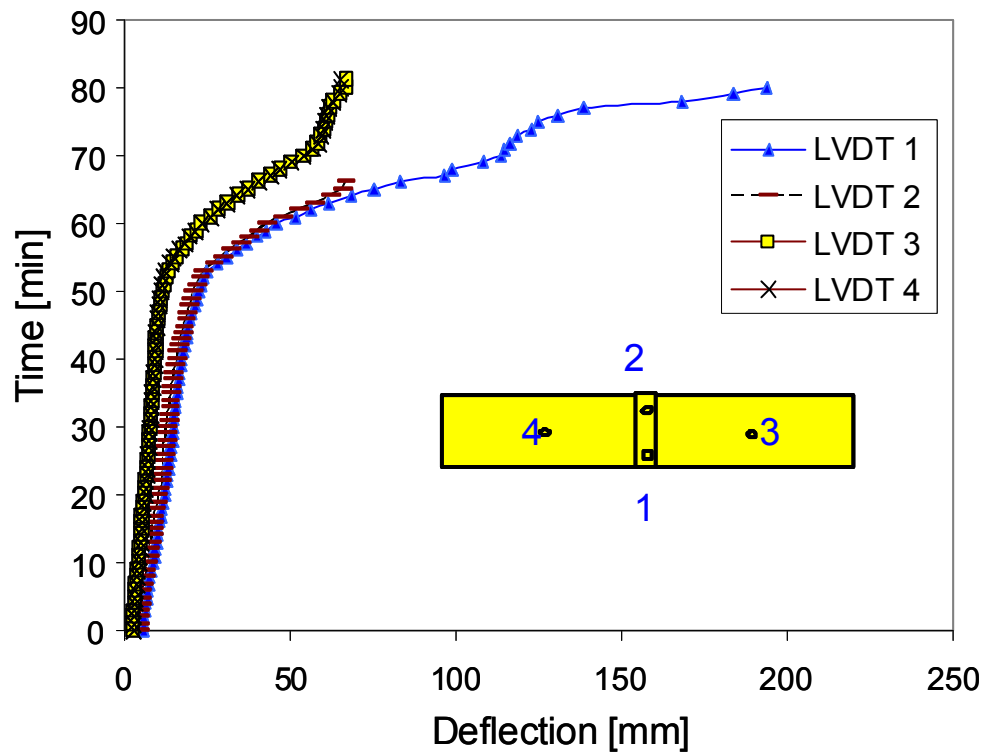


Figure 2-29 : Time versus deflection of test B2.



Figure 2-30 : Web post buckling failure mechanism

2.6 Conclusion on test campaigns

With the available test campaigns before this thesis, it was difficult to understand properly the behaviour of cellular beam in fire conditions. So, in order to assess the behaviour of unprotected cellular beams, a new test campaign was launched at the University of Ulster. This test campaign summarise in this Chapter allow us to have a better understanding of the failure mode of cellular beams in case of fire.

In the next Chapter a Finite Element Model will be built and calibrated on the tests campaign. This FEM model will be used after as reference for the parametrical study.

Chapter 3

Elaboration of a FEM model for cellular beams

3. Elaboration of a FEM model for cellular beams

In order to predict the behaviour of cellular beams in cold and in fire conditions, a FEM model has been built using the software SAFIR elaborated by the University of Liège [16]. This FEM model has been built by S. Majkut under the supervision of J.M. Franssen [66]. A summary of this FEM model is presented hereafter.

3.1 FEM model for pure steel cellular beam

The first step was to develop a FEM model for pure steel cellular beam taking into account global and local instabilities. It was chosen to implement a 3D model using SAFIR SHELL element. The geometry of the SHELL element is described in Figure 3–1.

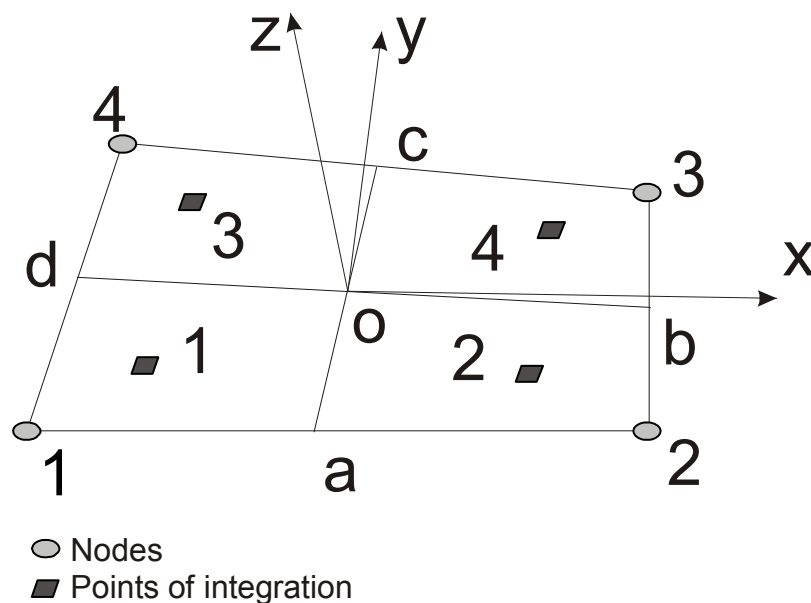


Figure 3–1 : Definition of the geometry and local axes

- The nodes forming the SHELL elements are in the order 1, 2, 3, 4
- a, b, c, d are the middle points of the edges of the elements.
- o, the centre of the local system of co-ordinates, is at the intersection between a-c and b-d.
- z is the normal to the surface of the SHELL element and has the direction of $d-b \wedge a-c$.
- x and y are perpendicular to z and their direction is chosen to have the same angle between o-b and x, on one hand, and o-c and y, on the other hand.

As a particular case, if the element is a plane rectangle, x is the median o-b and y is the median o-c.

This SHELL element is composed of 4 points of integration on the surface of the element, see Figure 3–2. In each direction, the integration is carried out by the Gauss method.

The number of integration points through the thickness is chosen by the user, from 2 to 9, see Figure 3–2. The integration is also carried out by the Gauss method.

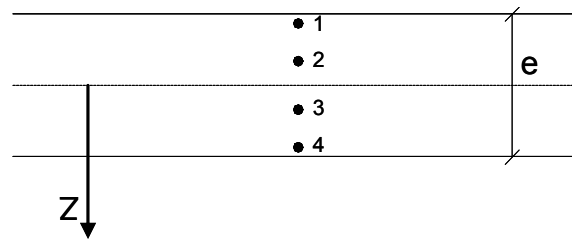


Figure 3–2 : Definition of the integration point on the thickness of the element

It is a 3D model built using the SHELL elements reflecting the exact geometry of the cellular beam (see Figure 3–3).

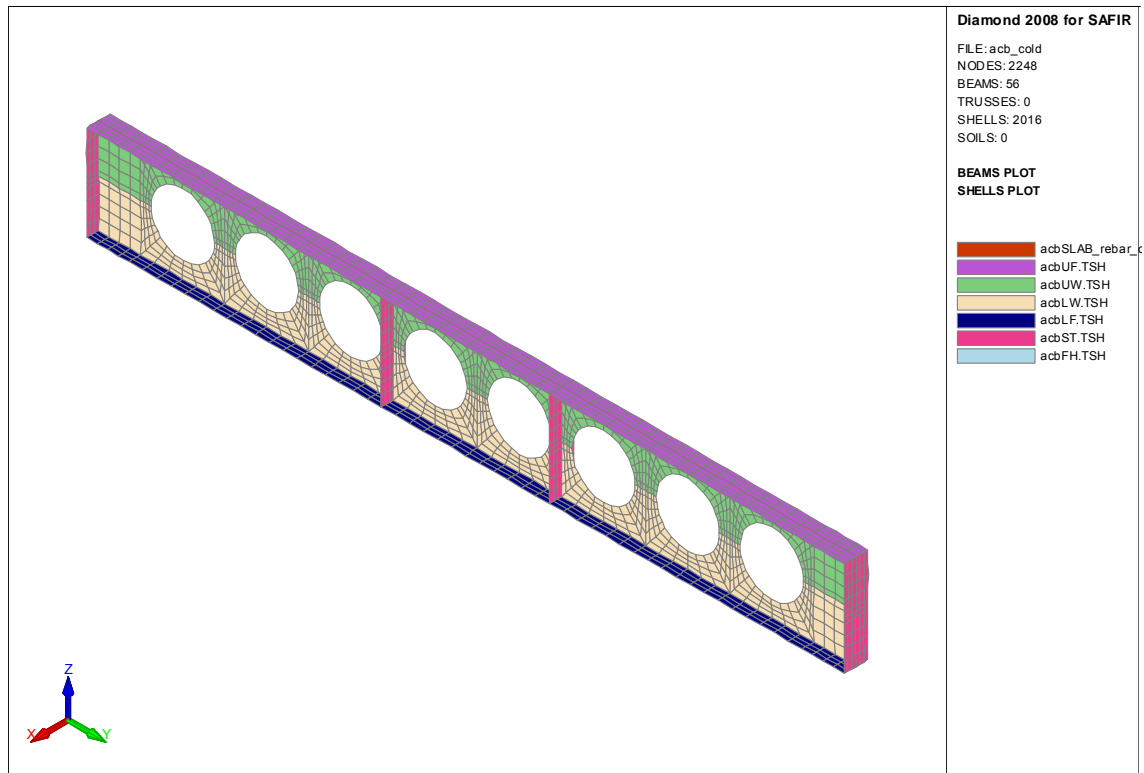


Figure 3–3 : SHELL Finite Element model in SAFIR software

On Figure 3–3, the different geometrical properties (material, thickness, ...) are presented with various colours : Upper Flange, Upper Web, Lower Web, Lower Flange, Stiffener and Filled Hole (that is not used in this case).

The boundary conditions are defined depending on the analysed beam (see Figure 3–4).

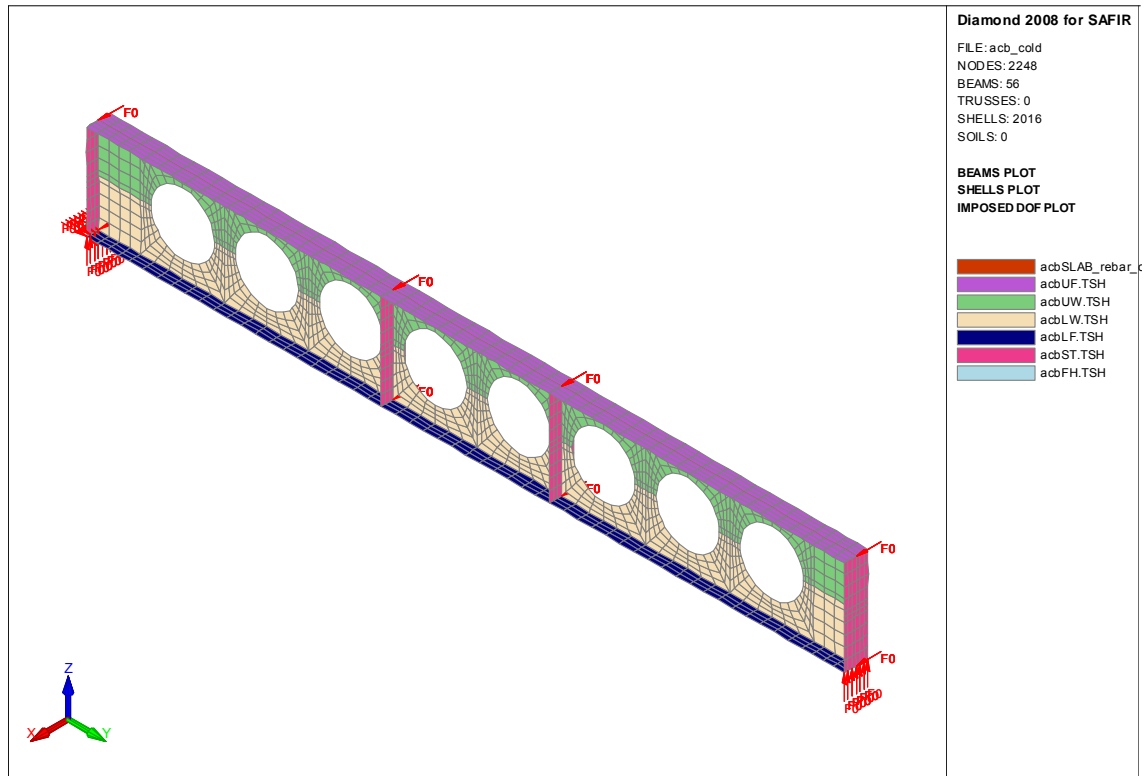


Figure 3–4 : Boundary conditions

The crucial parameter in this type of model is the initial deformation. The initial deformation chosen in this model was defined in the scope of a parametrical study made by CTICM and ArcelorMittal [24]. During one year, the different specimens of cellular beams fabricated in the ArcelorMittal workshop in Differdange were measured and the initial deformations are the mean values of these measurements.

This deformation results from the product of:

- a sine curve on the height of the profile with maximum amplitude reaching $(0.0025 H_{web})$

and

- a cosine curve on half the length of the beam with maximum amplitude equal to 2 mm.

This initial deformation only concerns the web panels and is illustrated on Figure 3–5.

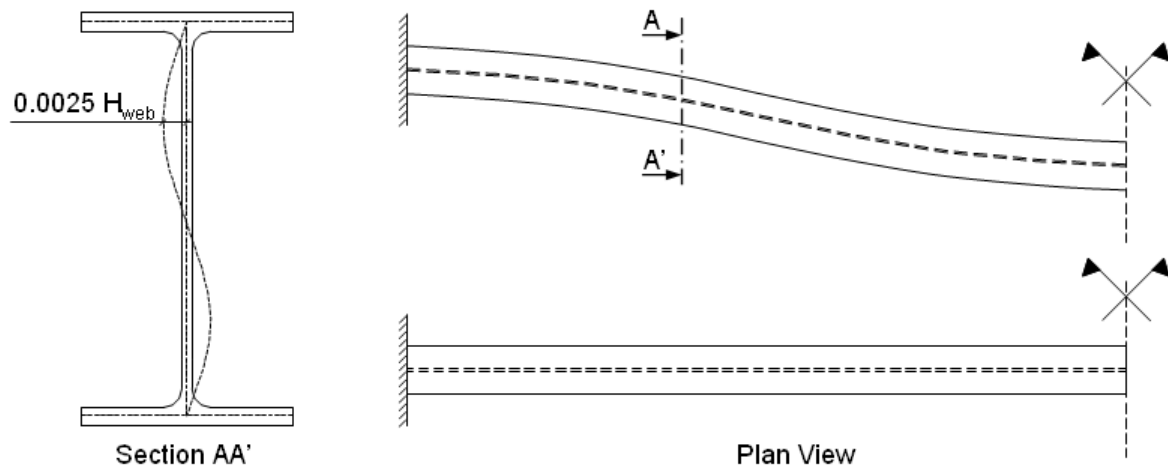


Figure 3-5 : Initial deformation for the SHELL F.E. model

3.2 FEM model for composite cellular beam

In composite cellular beam, the concrete slab must be connected to the upper flange of the beam. In this FEM model, the beam is simulated using SAFIR SHELL elements in order to take into account local instabilities. This FEM model for the cellular beam has only been developed for single member, it is not foreseen to consider the membrane effect of the concrete slab.

So in order to simulate the slab, the SAFIR BEAM Finite Element will be used :

This BEAM element is straight in its undeformed geometry. Its spatial position is defined by the position of three nodes: the two end nodes (N1-N2), and a third node (N4) defining the position of the local y axis of the beam. The node N3 is used to support an additional degree of freedom of freedom.

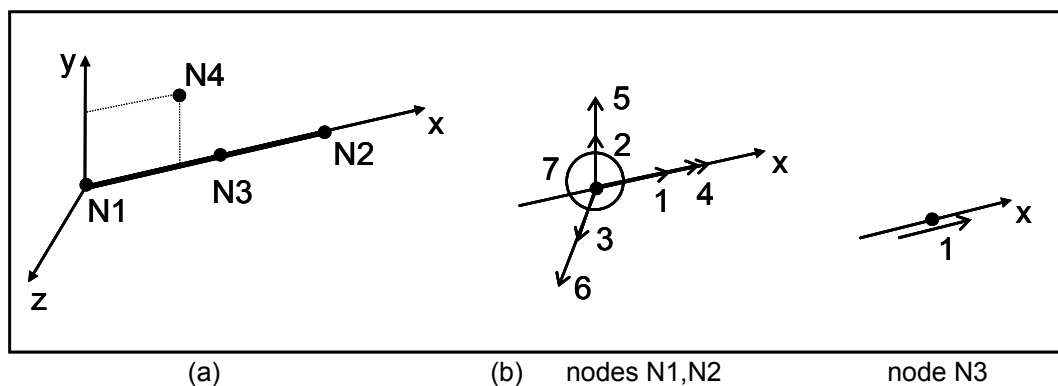


Figure 3-6 : BEAM element: (a) Local axes (b) Degrees of freedom at nodes

To describe the geometry of the cross section, a fibre model is used. The cross section of the beam is subdivided into small fibres (triangles, quadrilaterals or both) see Figure 3–7. The material behaviour of each fibre is calculated at the centre of the fibre and it is constant for the whole fibre.

Each fibre may represent a specific material, so that allows the calculation of composite cross-sections composed e.g. of steel and concrete.

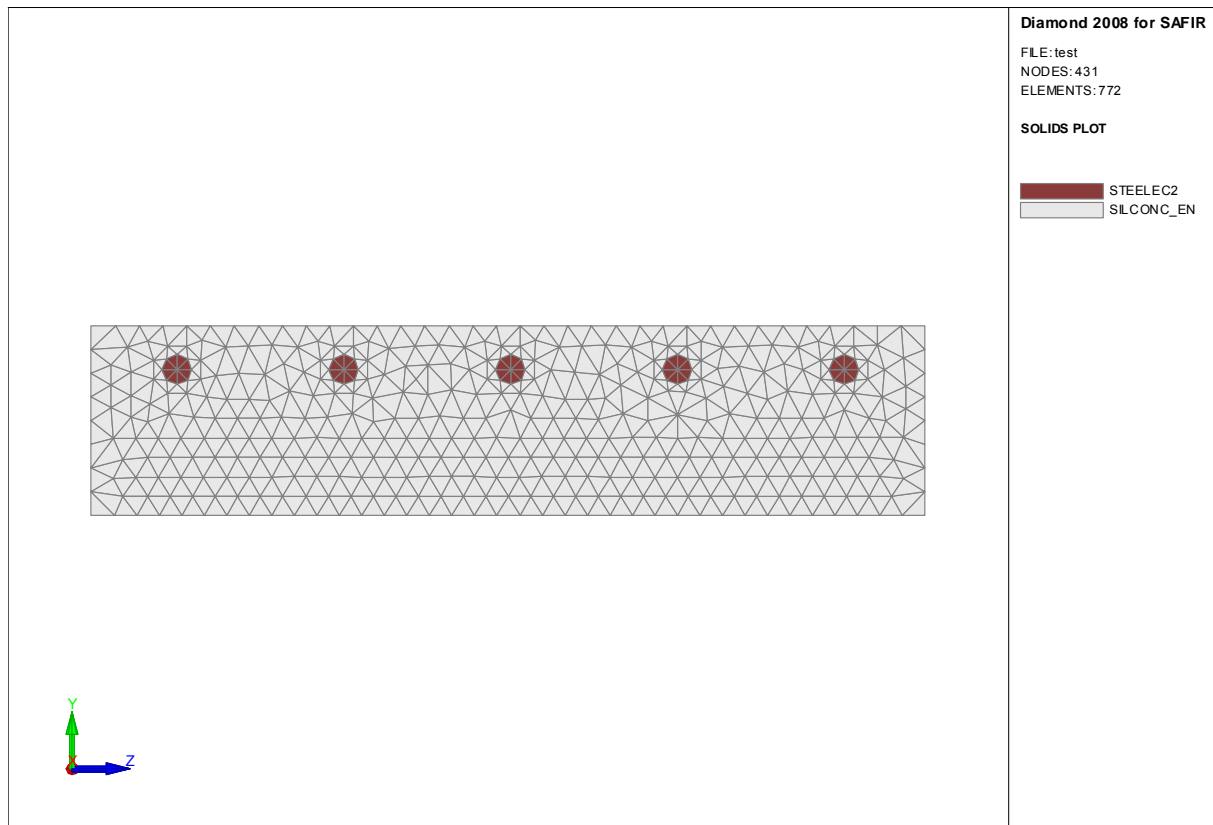


Figure 3–7 : Cross section of a BEAM Finite Element with concrete and rebars

Assumptions for BEAM elements:

- the Bernoulli hypothesis is considered, i.e., the cross section remains plane under bending moment
- yielding is only considered in the longitudinal direction of the member, that is uni-axial constitutive models
- non-uniform torsion is considered

Concerning the connection between the BEAM element and the SHELL element, two possibilities are offered by the SAFIR software :

1. to use the same node to create the SHELL and the BEAM element
2. to build another BEAM element to simulate the steel stud and to connect the upper flange of the beam and the slab.

On the basis of the first possibility, the implementation appears to be easy but the inconvenient is that it is only possible to simulate a full shear connection. The BEAM element forming the slab is connected to the central line of node at the junction between the flange and the web. This assumption can be justified by the fact that in the reality, the slab is connected to beam using a central line of shear connectors. On the Figure 3–8 a description of the numerical model can be seen.

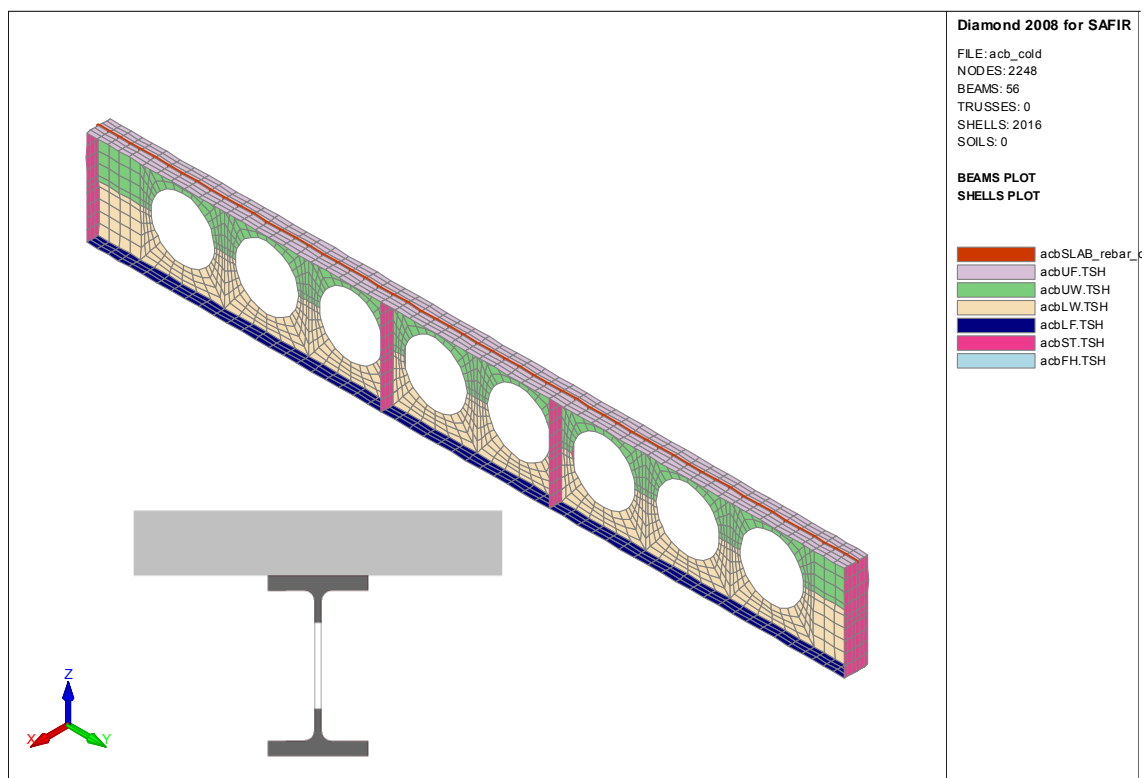


Figure 3–8 : Numerical model taking into account a composite slab with full shear connection.

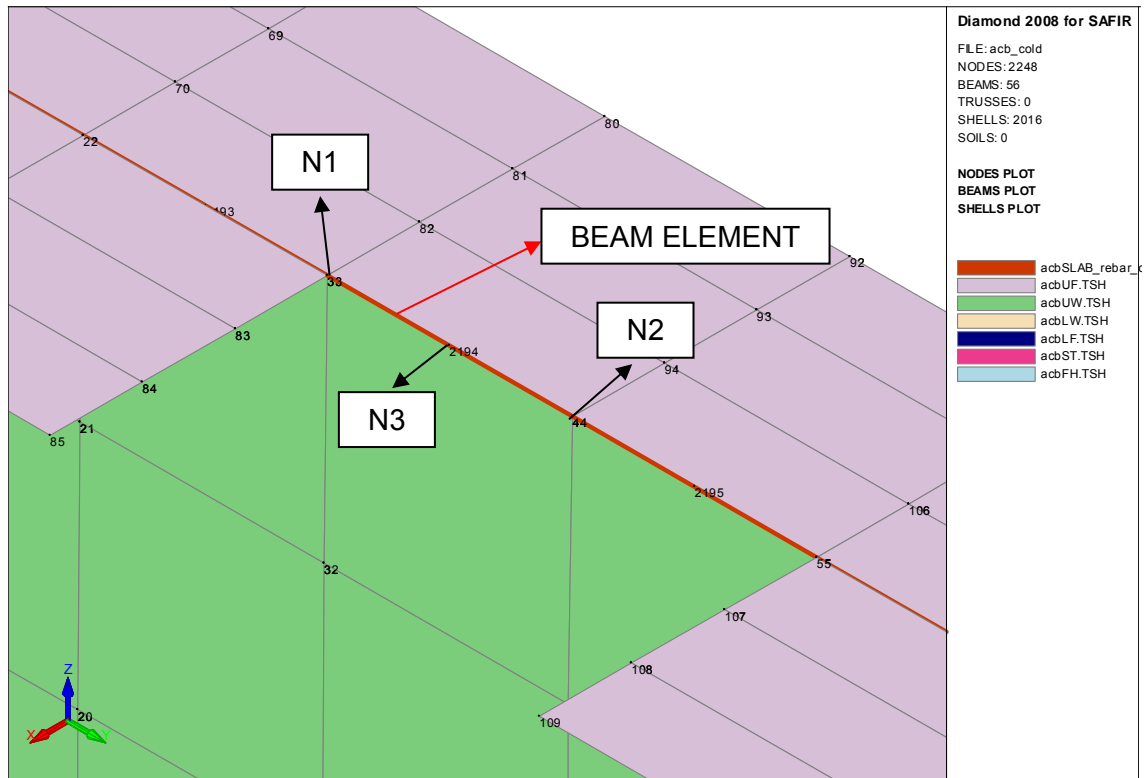


Figure 3–9 : Description in detail of the connection between SHELL and BEAM element.

In respect to the second possibility, the implementation is more complex because it is needed to simulate the steel studs but it is possible to simulate a composite beam with partial shear connection. On the Figure 3–10 a description of the numerical model is illustrated.

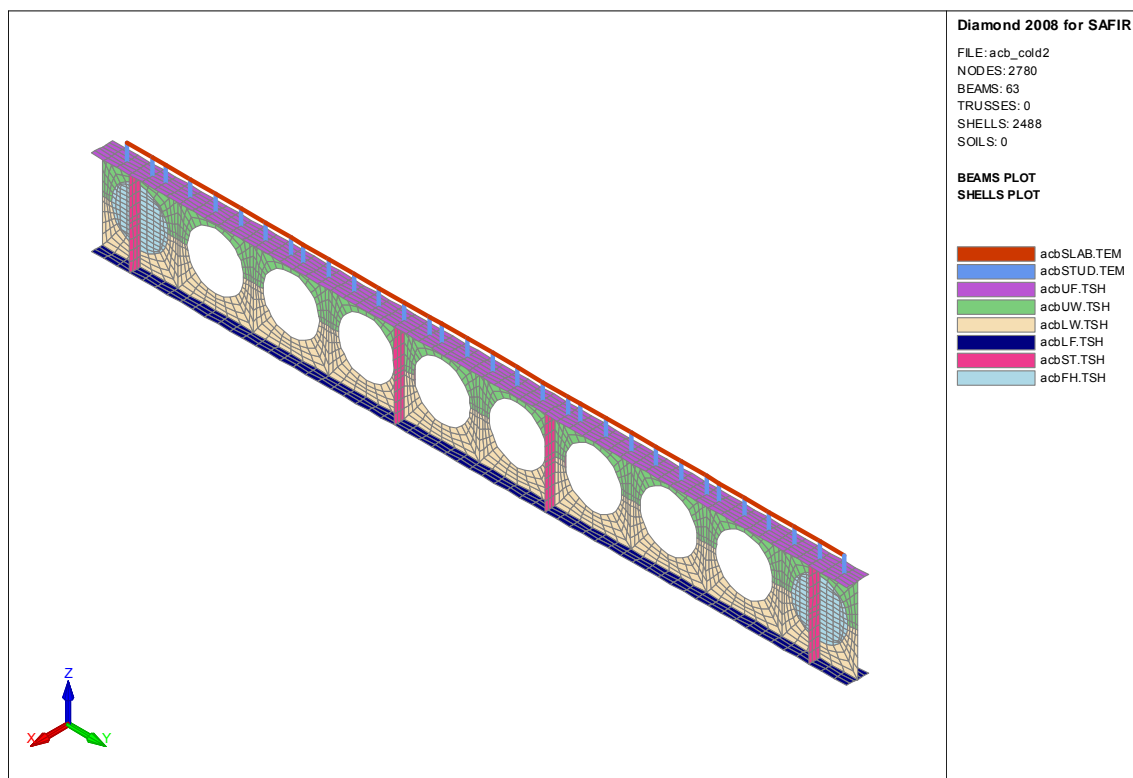


Figure 3–10 : Numerical model taking into account a composite slab with steel studs.

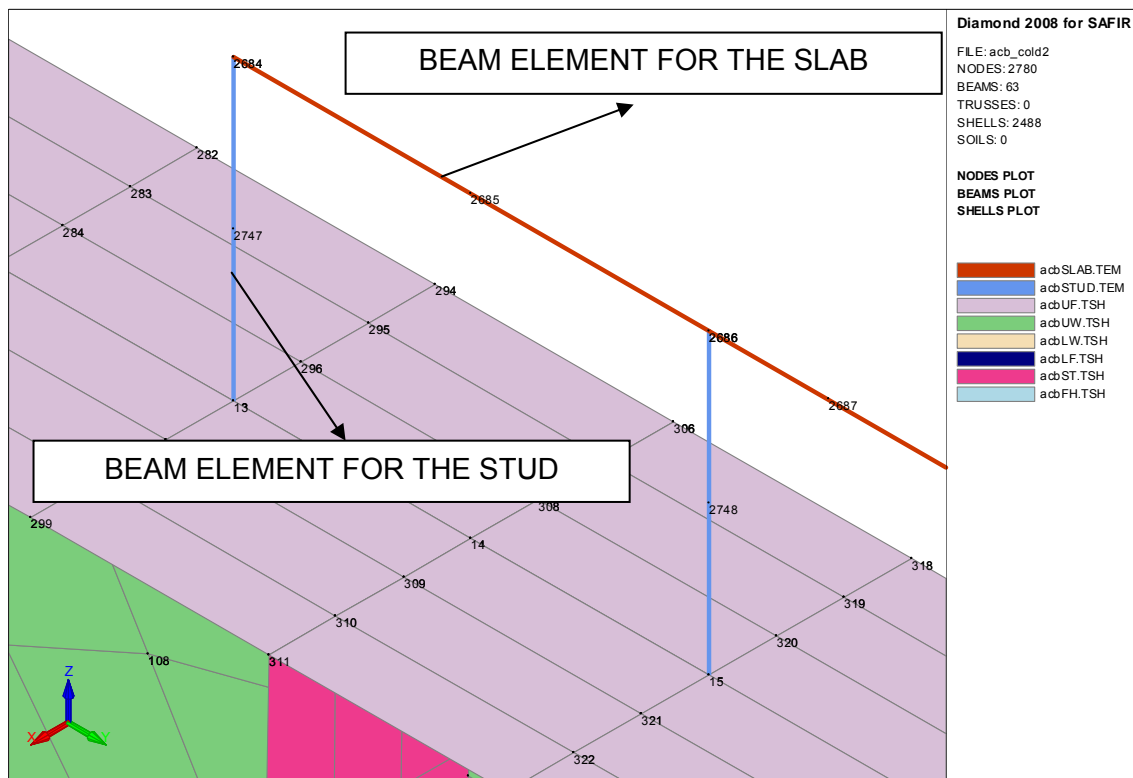


Figure 3–11 : Description in detail of the connection between SHELL and BEAM elements forming the slab and the steel stud.

This stud is represented by a BEAM element reflecting the behaviour of a steel stud. In order to reflect properly the behaviour of the steel studs, two possibilities arise:

- to simulate each steel stud using a circular cross section and the real material properties of the studs
- to simulate equivalent steel studs with adapted cross section and equivalent material properties

The second possibility was chosen in order to have more flexibility in the meshing of the cellular beam. It has been chosen to fix the number of SHELL elements depending on the requested accuracy to have a model able to reproduce the complex behaviour of web post instabilities. The number of “connecting elements” between the BEAM element forming the slab and the SHELL elements forming the beam will be deduced from the available nodes in the model.

In order to create the cross section of the studs, some informations were needed:

- the shear resistance of the steel stud (P_{Rd})
- the stiffness of the steel stud (k)
- torsional stiffness (GJ)

3.2.1 Shear resistance of steel studs

The shear resistance of the steel stud can be estimated by the following approach. The next paragraph is the summary of this approach defined in the EN1994-1-1 [56].

The shear resistance of a steel stud is the minimum between two values:

$$P_{Rd} = \min (P_{Rd1} ; P_{Rd2})$$

P_{Rd1} is the value reflecting the resistance of the steel stud itself (see Figure 3–12).

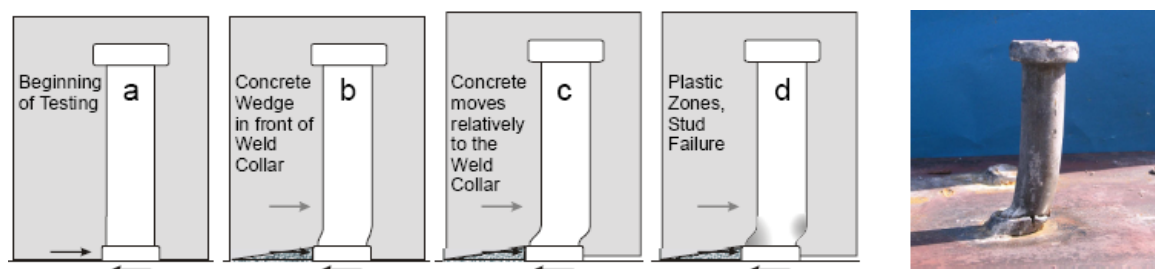


Figure 3–12 : Failure of a steel stud by shear

$$P_{Rd1} = \left(0.8 \cdot f_u \cdot \frac{\pi \cdot d^2}{4} \right) / \gamma_v$$

With :

- f_u = stud ultimate resistance in tension in N/mm²
- d = diameter of the stud in mm
- γ_v = partial safety factor for the stud

P_{Rd2} is reflecting the resistance of the concrete around the stud, see Figure 3–13 :



Concrete crack

Figure 3–13 : Failure of the concrete around the connection

$$P_{Rd2} = \left(0.29 \cdot \alpha \cdot d^2 \cdot \sqrt{f_{ck} \cdot E_{cm}} \right) / \gamma_v$$

With

- if $(h/d) > 4 \quad \Rightarrow \alpha = 1$
- if $3 \leq (h/d) \leq 4 \quad \Rightarrow \alpha = 0.2 \cdot \left(\frac{h}{d} + 1 \right)$
- if $(h/d) < 3 \quad \Rightarrow$ Not covered by EC4
- h = height of the steel stud in mm
- f_{ck} = characteristic resistance of the concrete on cylinder in N/mm²
- E_{cm} = Mean value of the shear modulus of concrete determined by:

$$E_{cm} = 22 \cdot 10^3 \cdot \left(\frac{f_{ck} + 8}{10} \right)^{0.3}$$

The cellular beam can be used with full concrete slab but can also be used using corrugated steel sheet. In this case, it is needed to consider the reduction factor coming from the perpendicular direction of the ribs [56], see Figure 3–14.

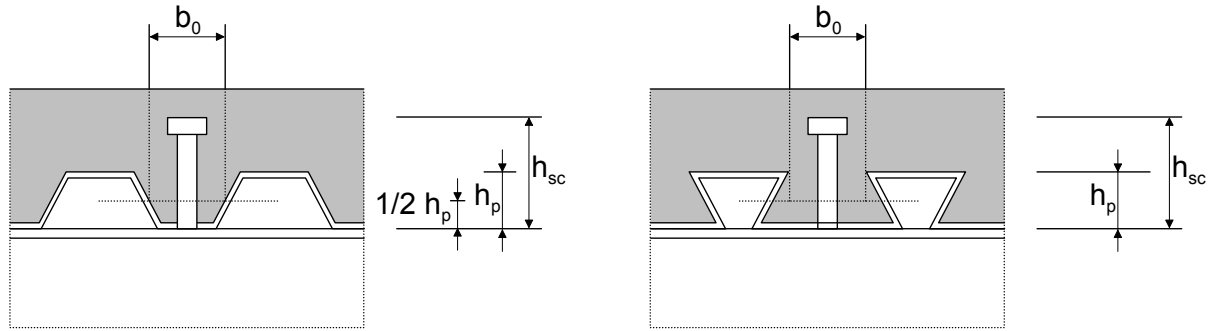


Figure 3–14 : Scheme of a corrugated steel sheet perpendicular to the beam direction

$$k_t = \left(\frac{0.7}{\sqrt{n_{rib}}} \right) \cdot \left(\frac{b_0}{h_p} \right) \cdot \left(\frac{h}{h_p} - 1 \right) \leq (1 \text{ or } 0.8) \text{ if } (n_{rib} = 1 \text{ or } n_{rib} \geq 2)$$

with

- n_{rib} = number of steel studs per rib (max 2)
- b_0 = breath of the rib in mm
- h_p = height of the rib in mm
- h = height of the steel stud in mm

The real number of steel studs per rib must be considered and the final expression can be defined by:

$$P_{Rd} = n_{rib} \cdot k_t \cdot \min (P_{Rd_1} ; P_{Rd_2})$$

with

n_{rib} = number of steel stud per rib

3.2.2 Stiffness of a steel stud (k)

The stud's stiffness is calculated based on the model adopted for the stud's deformation (on the basis of a double fixed stud):

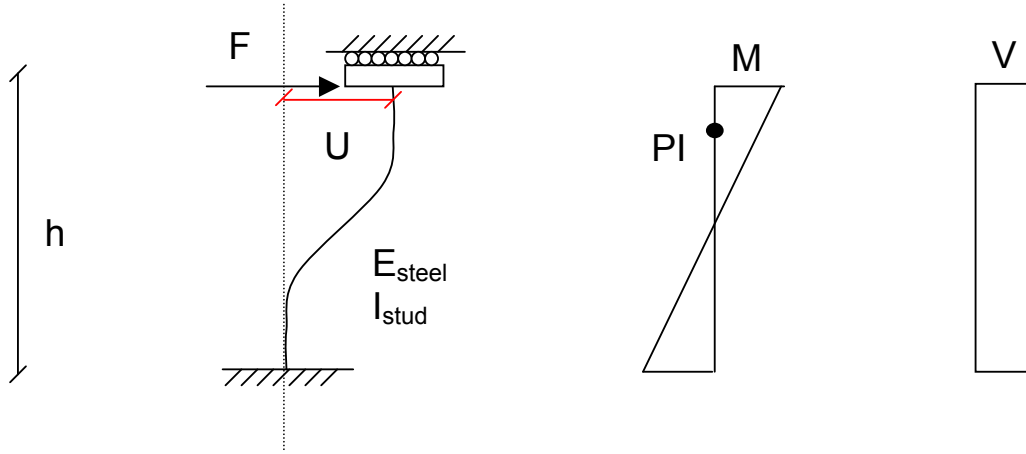


Figure 3-15 : Stud's deformation model

With this assumption and from the reference [61], it can be deduced that the deflection U of the head of the steel stud is given by :

$$U = \frac{F \cdot h^3}{12 \cdot E \cdot I}$$

From this equation, the stiffness of the steel stud can be extracted

$$F = \frac{12 \cdot E \cdot I}{h^3} \cdot U = k \cdot U \Rightarrow k = \frac{12 \cdot E \cdot I}{h^3}$$

with

- E = Young modulus of steel 210000 N/mm²
- h = height of the steel stud in mm
- $I = \frac{\pi \cdot d^4}{64}$ = Inertia of the steel stud

If the number of stud per rib is considered, the stiffness is defined as follows:

$$k = n_{\text{rib}} \cdot \frac{12 \cdot E \cdot I}{h^3}$$

3.2.3 Torsional stiffness (GJ)

The transverse elasticity module can be deduced from the Hooke law [62] :

$$G = \frac{E}{2 \cdot (1 + \nu)}$$

with

- E = Young modulus of steel 210000 N/mm²
- ν = Poisson ratio (0.3)

J represents the polar moment of inertia of the circular section of the stud. For a steel stud with a diameter d, J can be expressed by [63] :

$$J = \frac{\pi \cdot d^4}{32}$$

Finally, if the number of studs per rib is considered, the torsion stiffness can be obtained from:

$$GJ = n_{rib} \cdot GJ$$

3.2.4 Modelling of the steel stud using SAFIR BEAM Finite Element

As explained in the introduction of Chapter 3.2, it was chosen to simulate equivalent steel studs with adapted cross section and equivalent material properties and not to simulate each stud with its own cross section. In the SAFIR BEAM Finite Element, the inertia of the section is calculated by adding the terms of transport ($A \cdot y^2$) for each fibre defined in the cross section (the proper inertia of each fibre is neglected).

Sylvie Majkut decided to model the steel stud [66] using a cross section composed of 4 squared fibres (see Figure 3–16).

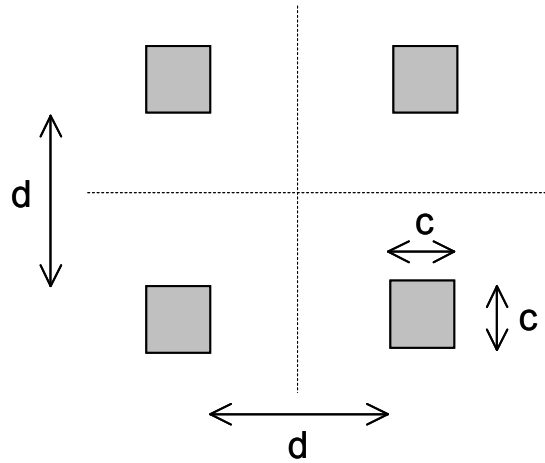


Figure 3–16 : Steel stud composed of 4 squared fibres

The geometrical properties c and d will determine the stiffness and the resistance of the BEAM element.

Determination of the c value

Assuming that cross section of the real stud and cross section of the model are equal :

$$A_{\text{real_stud}} = A_{\text{stud_model}}$$

$$4 \cdot c^2 = \frac{\pi \cdot d^2}{4}$$

If the number of studs per rib is considered, the c value can be obtained from the following relationship :

$$c = \sqrt{n_{\text{rib}} \cdot \frac{\pi \cdot d^2}{16}}$$

Determination of the d value

$$k_{\text{real_stud}} = k_{\text{stud_model}}$$

$$k_{\text{real}} = \frac{12 \cdot E \cdot I}{h_{\text{mod}}^3}$$

Inertia of the stud (I) can be isolated from this equation and expressed by the following relationship:

$$I = k_{\text{real}} \cdot \frac{h_{\text{mod}}^3}{12 \cdot E}$$

with

- $k_{\text{real}} = k$ calculated in the chapter 3.2.2
- I = Inertia of the stud in the model (researched value)
- E = Young modulus of steel 210000 N/mm²
- h_{mod} = height of the stud in the model (from the half thickness of the SHELL element forming the upper flange of the cellular beam to the half thickness of the BEAM element forming the slab)

The modelled stud is composed of 4 squared sections. The inertia of the modelled stud can be defined by the multiplication of the surface and the lever arm of each square section. If the inertia of each fibre itself is neglected, the total inertia of the section can be expressed by the following relationship:

$$I = 4 \cdot c^2 \cdot \left(\frac{d}{2} + \frac{c}{2} \right)^2$$

After development of the formula, d can be described by the following relationship:

$$d = \frac{-2 \cdot c^3 \pm \sqrt{4 \cdot c^2 \cdot I}}{2 \cdot c^2}$$

c is always positive (size of the square section) :

$$d = \frac{-2 \cdot c^3 + \sqrt{4 \cdot c^2 \cdot I}}{2 \cdot c^2} = \frac{-c^2 + \sqrt{I}}{c}$$

The total area of steel in the model must be the same as the surface of steel for the real circular stud.

$$c = \sqrt{n_{\text{rib}} \cdot \frac{\pi \cdot d_{\text{real_stud}}^2}{16}}$$

Finally, d can be determined from the following relationship:

$$d = \frac{-n_{rib} \cdot \frac{\pi \cdot d_{real_stud}^2}{16} + \sqrt{k_{real} \cdot \frac{h_{mod}^3}{12 \cdot E}}}{\sqrt{n_{rib} \cdot \frac{\pi \cdot d_{real_stud}^2}{16}}}$$

Determination of the steel strength limit of the modelled stud (fy)

The failure of the steel stud is obtained when the bending moment at the point of integration is equal to the plastic bending moment of the section.

The point of integration of the BEAM element (PI) is localized at 0.2133*L from the extremity.

The next relationship can be presented as:

$$M_{PI} = \frac{(0.5 - 0.2113)}{0.5} \cdot M_{TOP}$$

Following the chosen deformation model (see Figure 3–15) and the reference [61], it can be written that:

$$M_{TOP} = \frac{6 \cdot E \cdot I}{h_{mod}^2} \cdot U$$

with

- I = Inertia of the stud in the model
- U = displacement of the head of the modelled steel stud taking into account an horizontal force F (see Figure 3–15)

If it is considered that the plastic bending moment is reached when the force F reaches the shear resistance of the stud, the following relationship can be expressed:

$$P_{Rd,real_stud} = k_{real} \cdot U$$

with

- $k_{real} = k$ calculated in the chapter 3.2.2
- $P_{Rd,real_stud} = P_{Rd}$ calculated at the chapter 3.2.1

so:

$$M_{TOP} = \frac{6 \cdot E \cdot I}{h_{mod}^2} \cdot \frac{P_{Rd,real_stud}}{k_{real}}$$

with

- I = inertia of the stud in the model
- E = Young modulus of steel 210000 N/mm²
- h_{mod} = height of the stud in the model (from the half thickness of the SHELL element forming the upper flange of the cellular beam to the half thickness of the BEAM element forming the slab)

Finally:

$$M_{PI} = \frac{(0.5 - 0.2113)}{0.5} \cdot \frac{6 \cdot E \cdot I}{h_{mod}^2} \cdot \frac{P_{Rd,real_stud}}{k_{real}}$$

The plastic bending resistance of the stud can be defined by:

$$M_{plast} = (W_{plast} \cdot f_y) / \gamma_v$$

with

- f_y = steel strength limit of the modelled stud (unknown value in our case)
- γ_v = partial safety factor on steel studs
- As the section of the BEAM element is composed of 4 squared fibres (see Figure 3–16)

W_{plast} is given by the following relationship: $W_{plast} = 4 \cdot c^2 \cdot \left(\frac{d}{2} + \frac{c}{2} \right)$,

$$M_{plast} = \frac{\left(4 \cdot c^2 \cdot \left(\frac{d}{2} + \frac{c}{2} \right) \cdot f_y \right)}{\gamma_v}$$

In order to have the same plastic resistance between the model and the real stud, the following relationship must be satisfied:

$$M_{PI} = M_{plast}$$

And the steel strength limit of the modelled stud can be expressed by:

$$f_y = \left(\frac{(0.5 - 0.2113) \cdot \frac{6 \cdot E \cdot I}{h_{mod}^2} \cdot \frac{P_{Rd,real_stud}}{k_{real}}}{2 \cdot c^2 \cdot (d + c)} \right) \cdot \gamma_v$$

with

- I = inertia of the stud in the model.
- E = Young modulus of steel 210000 N/mm²
- h_{mod} = height of the stud in the model (from the half thickness of the SHELL element forming the upper flange of the cellular beam to the half thickness of the BEAM element forming the slab)
- f_y = steel strength limit of the modelled stud (unknown value in our case)
- γ_v = partial safety factor on steel studs
- P_{Rd,real_stud} = P_{Rd} calculated in the chapter 3.2.1

3.3 Simulation of the test campaigns

This FEM model was first calibrated on tests results available:

- Short span tests in cold conditions
- Protected furnace test
- Ulster test campaign

3.3.1 Short span tests in cold conditions

The modelling of the test was carried out by The Technische Universität Kaiserslautern [25] using the FE-program ANSYS, version 7.0 [17] and was also performed using the FE - program SAFIR. The aim of this study was to calibrate the FEM software SAFIR with the performed tests.

A nonlinear buckling analysis was carried out with ANSYS using the following assumptions:

- use of 4 nodes SHELL element with quadratic deformation approach.
- large displacement approach.
- geometrically as well as materially non-linear calculation.
- solver by iterations according to Newton-Raphson.
- ideal elasto-plastic material behaviour using actual (measured) values.

- the strain hardening was taken into account
- the full (real) stress – strain curve was not included.
- the beam geometry was based on the measured dimensions of the tested beams.
- the little stiffeners at the outer web post were not considered.
- the imperfection of the web was based on the first critical mode (eigenvalue) that was obtained from a linear buckling analysis in the first step.
- the load was applied stepwise on one node in the middle of the upper flange.
- the influence of the mesh and its refinement has been tested out in advance, such that the presented FE-results can be regarded as consolidated [25].

A nonlinear buckling analysis was carried out with the software SAFIR based on the following assumptions:

- implementation of 4 nodes SHELL element with quadratic deformation approach.
- large displacements.
- geometrically as well as materially non-linear calculation (Following EN properties [55]).
- solver by iterations using dynamic calculation according to Newton-Raphson.
- ideal elasto-plastic material behaviour using actual (measured) values.
- the full stress – strain curve of EN was included [55] and is shown on the Figure 3–17.

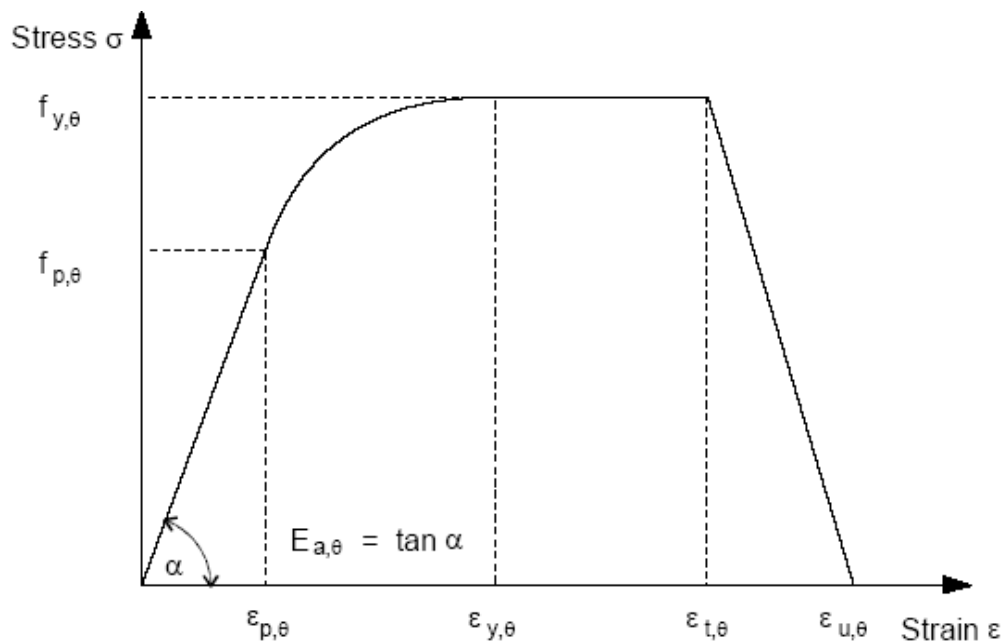


Figure 3–17 : σ - ε relationships for Steel in EC3

- no strain hardening was taken into account
- the beam geometry was based on the measured dimensions of tested beams.
- the small stiffeners at the outer web post were not considered.
- the imperfection of the web was based on the definition of the Finite Element model (see chapter 3.1).
- the load was applied stepwise on all the nodes forming the middle of the upper flange.
- the influence of the mesh and its refinement has been tested out in advance, such that the presented FE-results can be regarded as validated [66].

The results of this FEM study are presented in the Table 3-1:

Specimen N°	Sections		Limit load [kN]			
	Upper part	Lower part	ACB 2.3	Test	ANSYS with hardening	SAFIR without hardening
1-ss	IPE400	IPE400	382	500	480	471
2-hs	HEA300	HEM300	320	606	565	555
3-ss	HEB400	HEB400	326	627	623	611
4-ss	IPE400	IPE400	165	252	261	302
5-hs	IPE300	HEM300	170	393	340	432
6-ss	HEM300	HEM300	421	971	1072	946
7-hs	HEB300	HEM300	508	905	815	786
8-hs	HEA300	HEB300	248	685	601	506

ss corresponds to symmetric section; hs corresponds to hybrid section

Table 3-1 : Results of the FEA

This table shows that both FEM softwares can predict with a reasonable level of accuracy the ultimate limit load of short span cellular beams.

To illustrate the good agreement of the global beam behaviour between the FEA and the real tests, one of the load-deflection-curve is compared in the following Figure 3–18. The load-deflection-curve of each test and their analyse can be found in the final report of LWO⁺ [54].

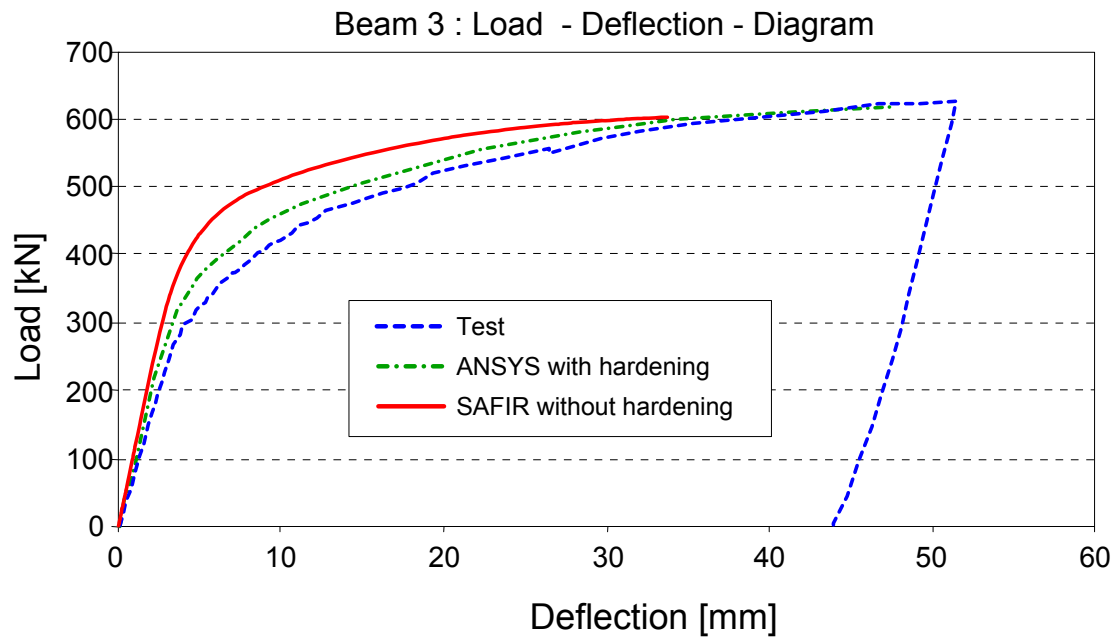


Figure 3–18 : Load-Deflection Diagram (Beam 3)

It should be pointed out that both softwares (ANSYS and SAFIR) are able to predict the load-deformation behaviour of short cellular beams. The results provided by the ANSYS model are more accurate (for this example) than the results provided by the SAFIR model.

However, these tests were performed on really short span specimens that were not reflecting the loading of cellular beams in real conditions. This testing procedure was made to test the behaviour of the section in pure shear and not in bending. Tests with larger span need to be done for the calibration in bending.

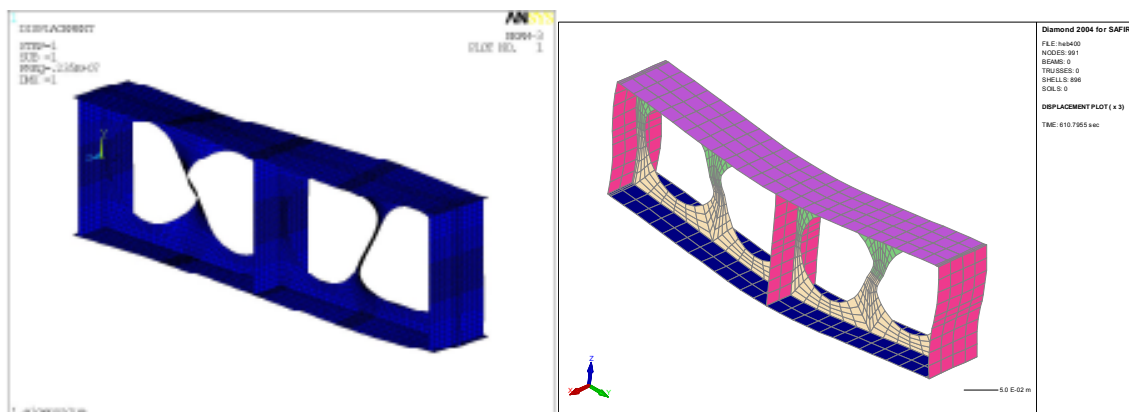


Figure 3–19 : Deformations at the end of the simulation (Beam 3)

Both softwares (ANSYS and SAFIR) predicted the same failure mode at the ultimate limit state, the web post buckling.

The load-deformation behaviour of short beams with large web openings has been investigated. Using this study, it was possible to observe that the Finite Element model that was built in SAFIR is able to reproduce the complex behaviour of such beam. Moreover, the comparison between the ultimate failure load given by SAFIR and the test results appear, in this case, to be satisfactory.

In this first study, it has been shown that ANSYS can also reproduce this complex behaviour with a high level of accuracy. In the scope of this thesis, the fire resistance needs to be investigated and SAFIR has been developed for such calculation.

3.3.2 Protected furnace test

This experimental test was simulated using a model that takes into account the partial shear connection (see Figure 3–20 and Figure 3–21).

The main difficulty in this simulation was to make assumptions on the thermal behaviour of the cellular beam. The thickness of the fire protection in the test was so variant that it has been extremely difficult to replicate it in the model and reproduce the same temperature distribution for each geometrical property.

In order to decrease the influence of the thermal calculation, it has been chosen to introduce directly the measured steel temperature in the numerical model and to focus the work on the thermo-mechanical behaviour.

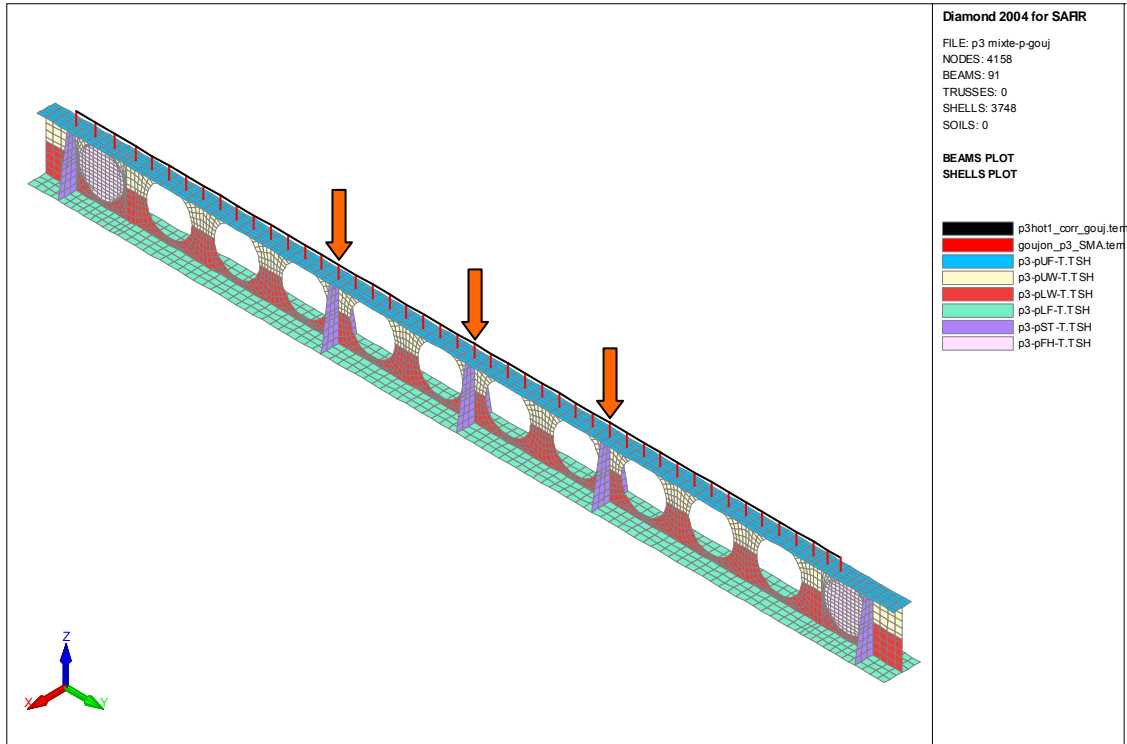


Figure 3–20 : Numerical model of the tested beam

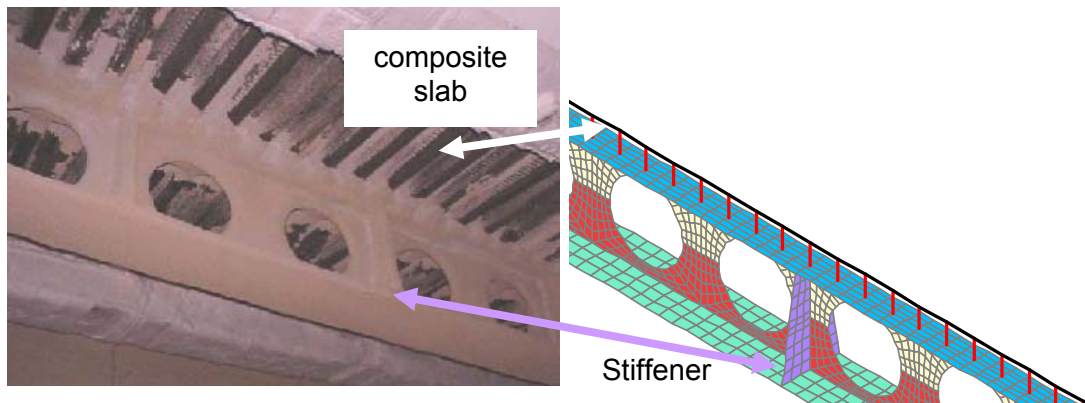


Figure 3–21 : Numerical model of the tested beam

The real measured geometry and the measured material properties were introduced in the model and the results of the simulation are presented in the Figure 3–23.

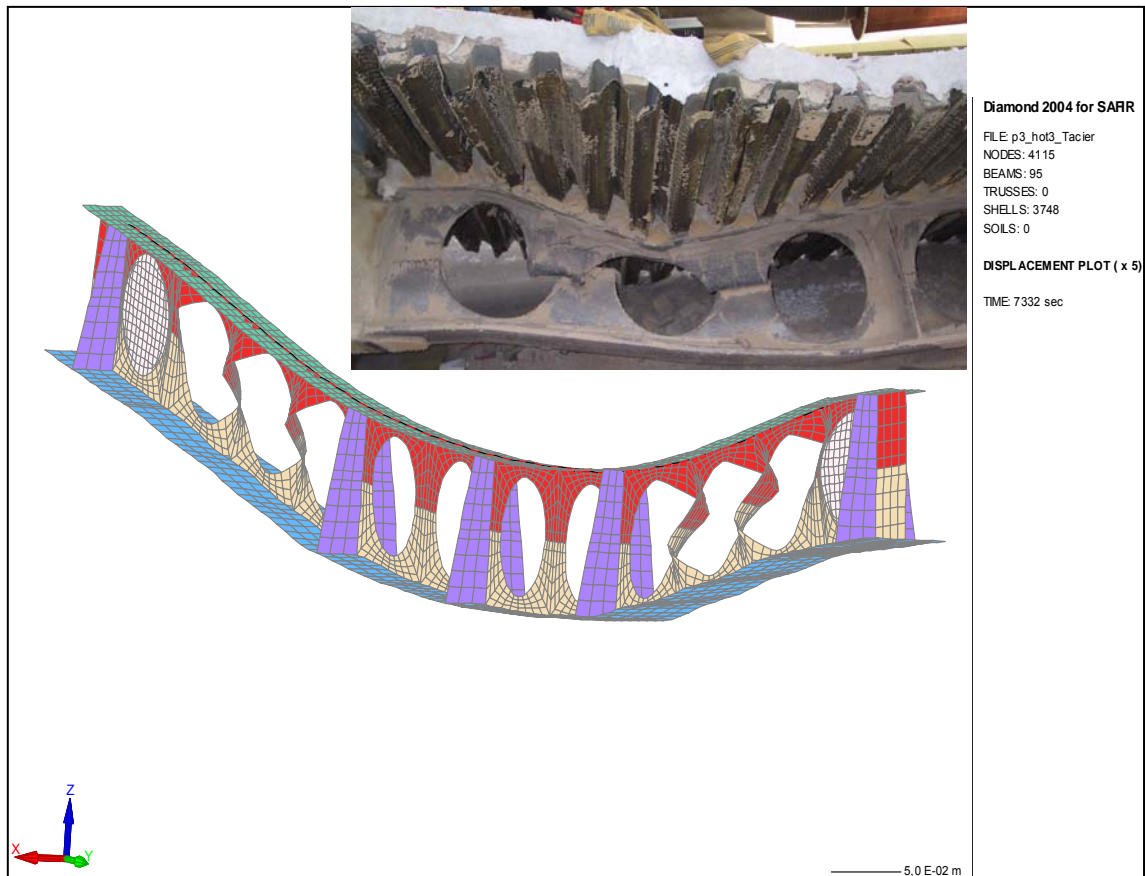


Figure 3-22 : Deformed shape of the structure after the test and at the end of the simulation

The next figure shows the comparison between the deflection obtained at mid span of the beam in the test and predicted by SAFIR simulation.

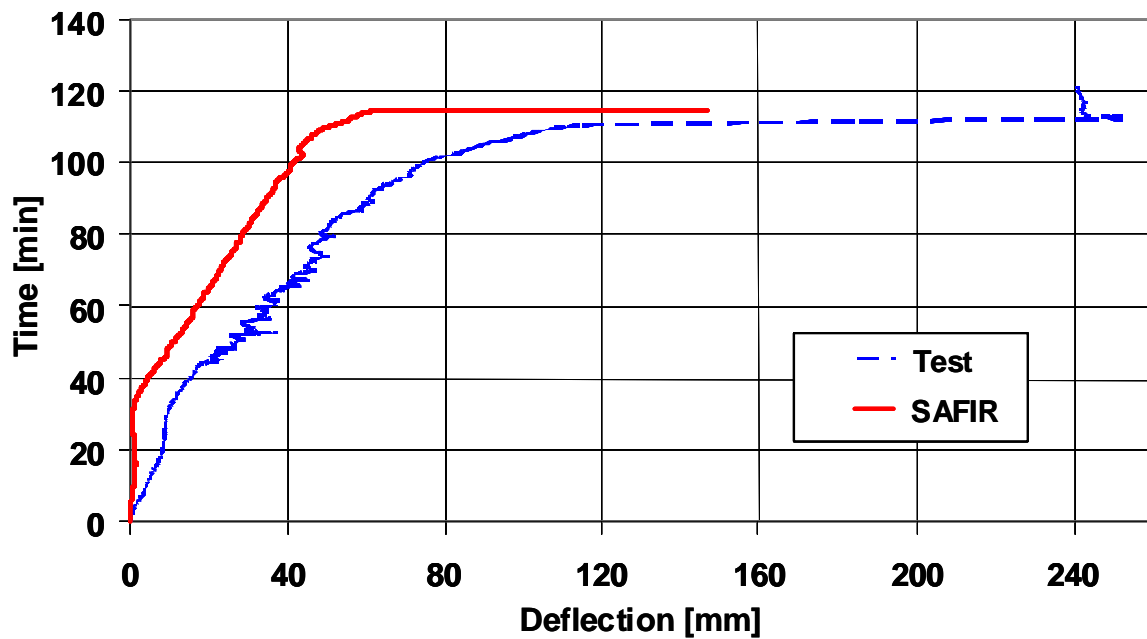


Figure 3-23 : Comparison between the deflections SAFIR/Test

As explained in Chapter 2.3.4, the stability of the thermal results obtained by simulation was not accurate as expected for this fire test. The reason is that the thickness of the fire protection was very variant and consequently the temperature varied a lot for the same section at different positions along the length of the beam. It could be possible to adjust the input of the FEM software, by ‘tuning’ the input temperature, in order to have the numerical simulation more accurately with the test results. However, the aim of this simulation was to demonstrate that the numerical model is capable to reproduce different failure modes of composite cellular beams taking into account local instabilities and variation of material properties.

The reached level of accuracy gives us confidence in the results produced by the FEM software in respect to the reproduction of test results carried out on a protected cellular beam.

3.3.3 Ulster test campaign

These experimental tests were simulated using a model that takes into account the full shear connection.

The following Figure 3–24 shows the SHELL Finite Element model built to simulate the tests A and B.

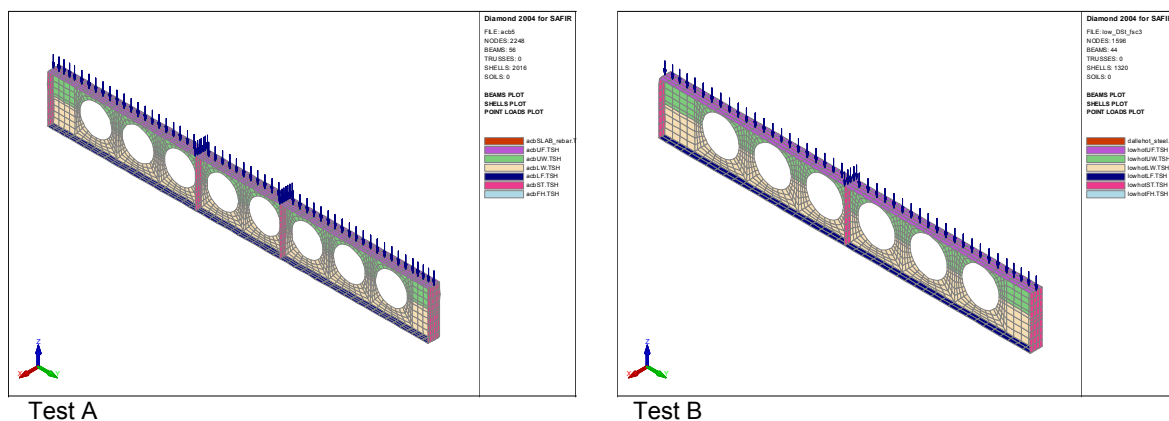


Figure 3–24 : FEM model of test A and test B

Exactly the same model was used to simulate the cold tests and the tests at elevated temperature. For the purpose of comparison, Figure 3–25 and Figure 3–26 show variation of central deflection in a function of load as a result of model and test.

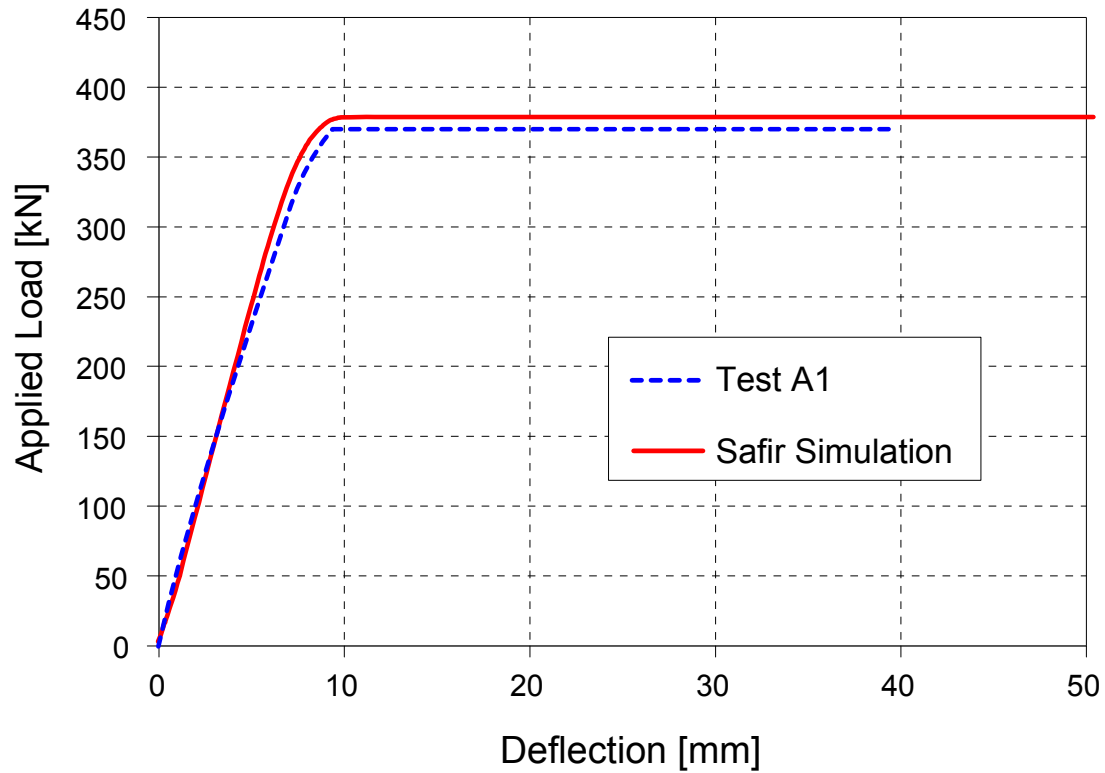


Figure 3–25 : FEM vs test A1

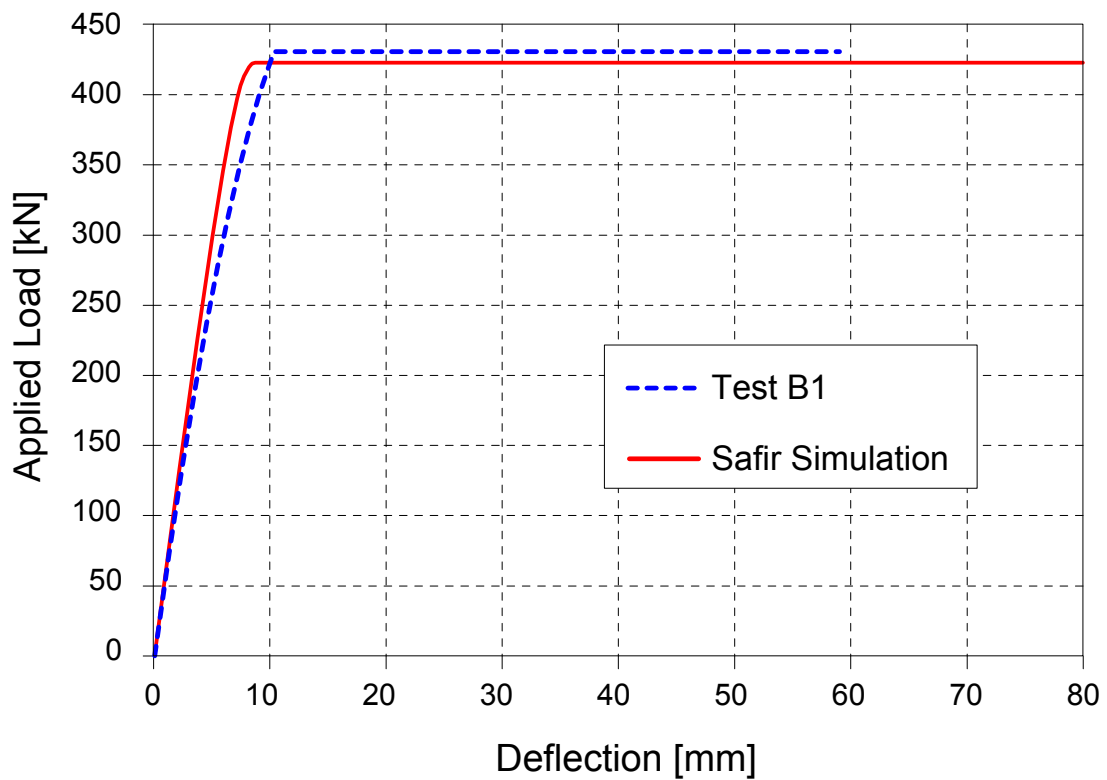


Figure 3–26 : FEM vs test B1

In order to separate the thermal behaviour from the thermo-mechanical behaviour of the cellular beams, the different temperatures measured during the two tests at elevated temperature were directly introduced in the FEM model to simulate the behaviour of the cellular beams in hot conditions. But, as shown in Figure 2–23 to Figure 2–26, the evolution of the temperature along the beam is not constant for a given section. Therefore, an average value for the temperature was applied for each geometrical property, different Time/Temperature curves were introduced for the bottom flange, web, upper flange and concrete slab. The Figure 3–27 shows the repartition of the stresses in the steel section of the cellular beam for test B2.

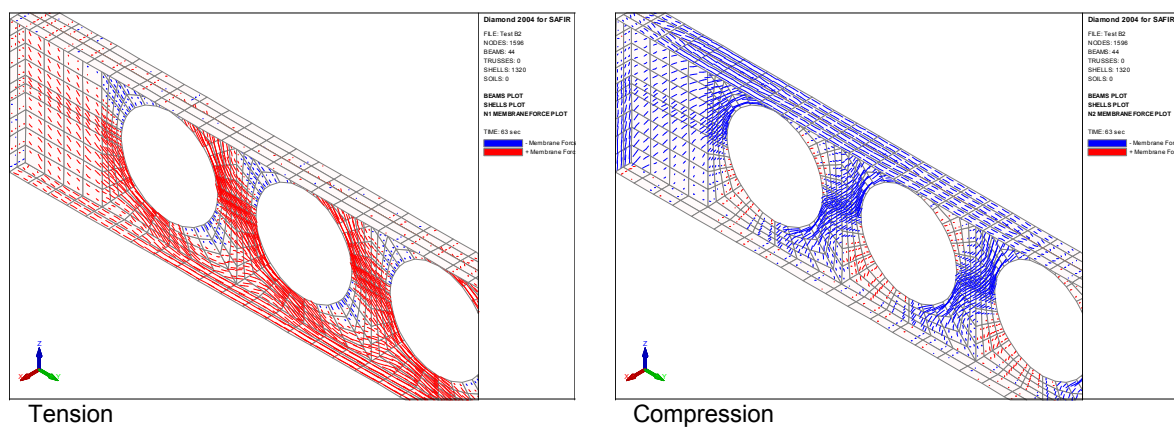


Figure 3–27 : Membrane force in tension

The deformed shape (without amplification) in function of time is given at some relevant steps for the test at elevated temperature B2 in the following Figure 3–28 to Figure 3–30.

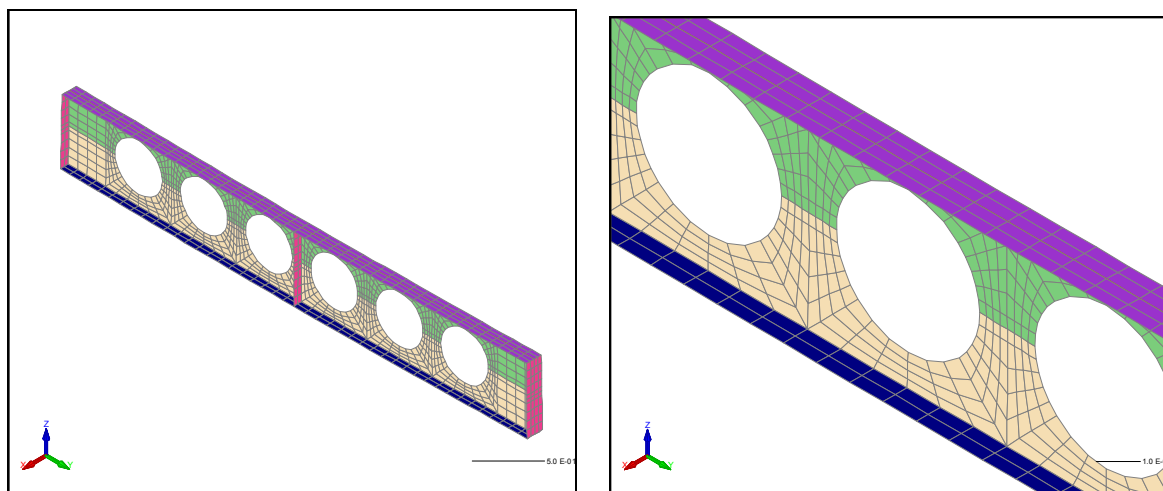


Figure 3–28 : Deformed shape after 3000 sec of heating

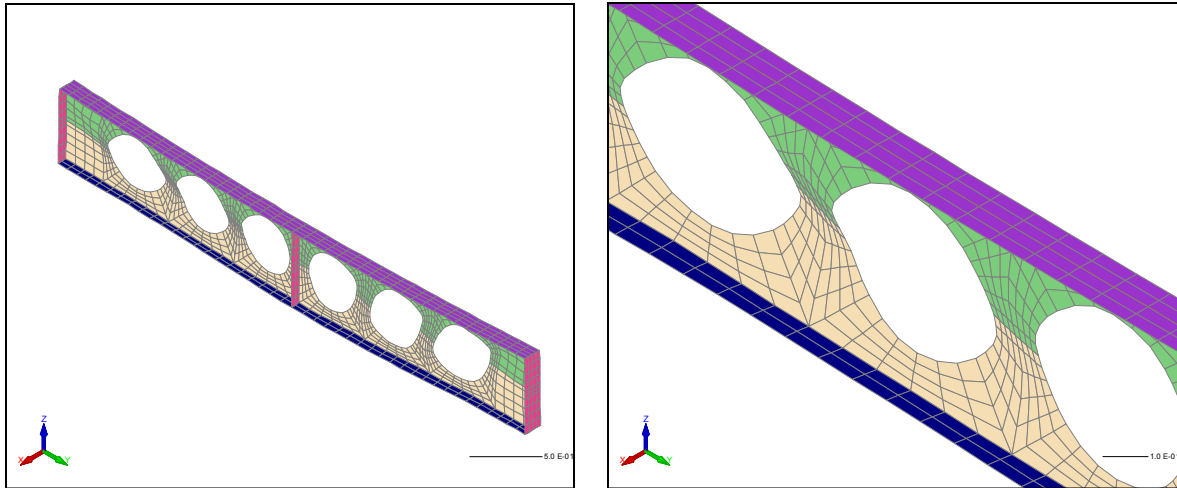


Figure 3–29 : Deformed shape at the beginning of the web post buckling

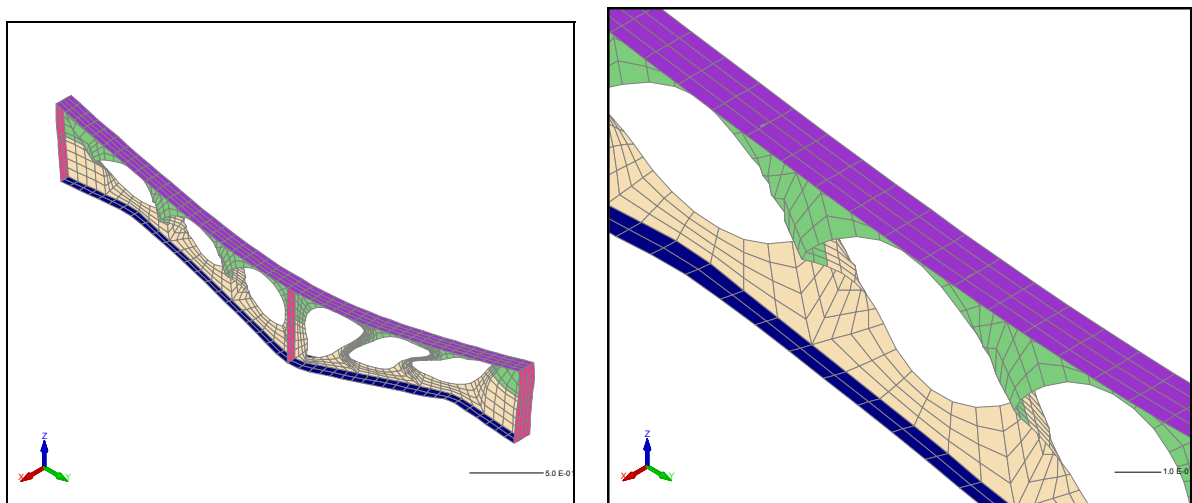


Figure 3–30 : Deformed shape at the end of the test

The Figure 3–31 and Figure 3–32 show the comparison between the displacements at mid span obtained both from the tests (A2 and B2) and the FEM model in SAFIR.

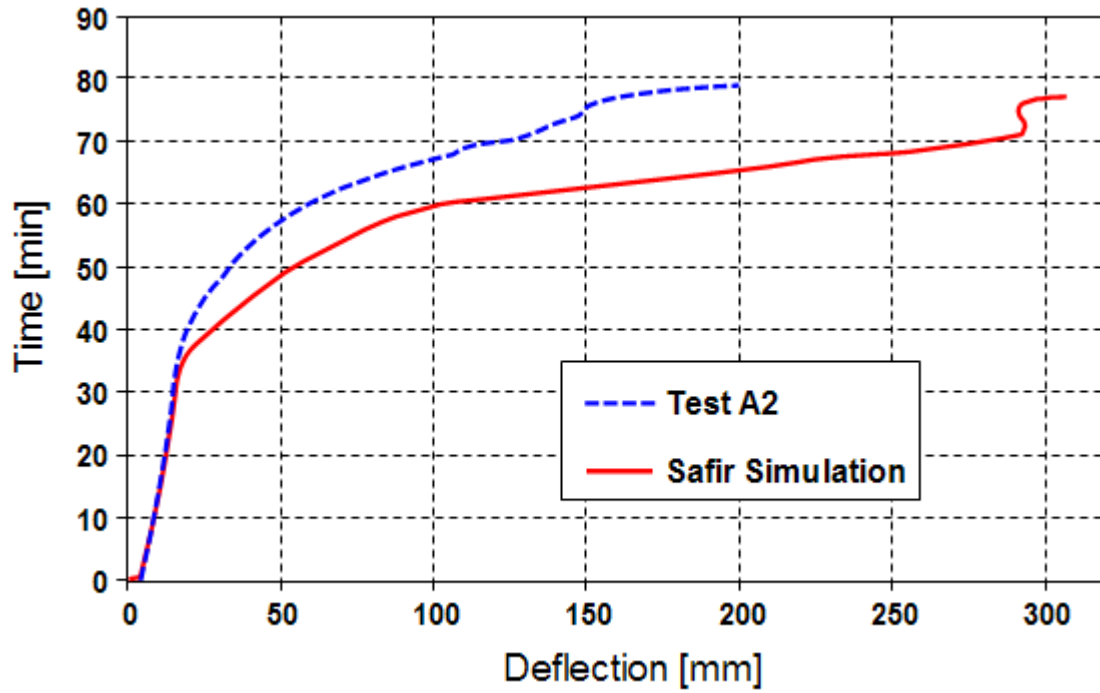


Figure 3-31 : FEM vs test A2

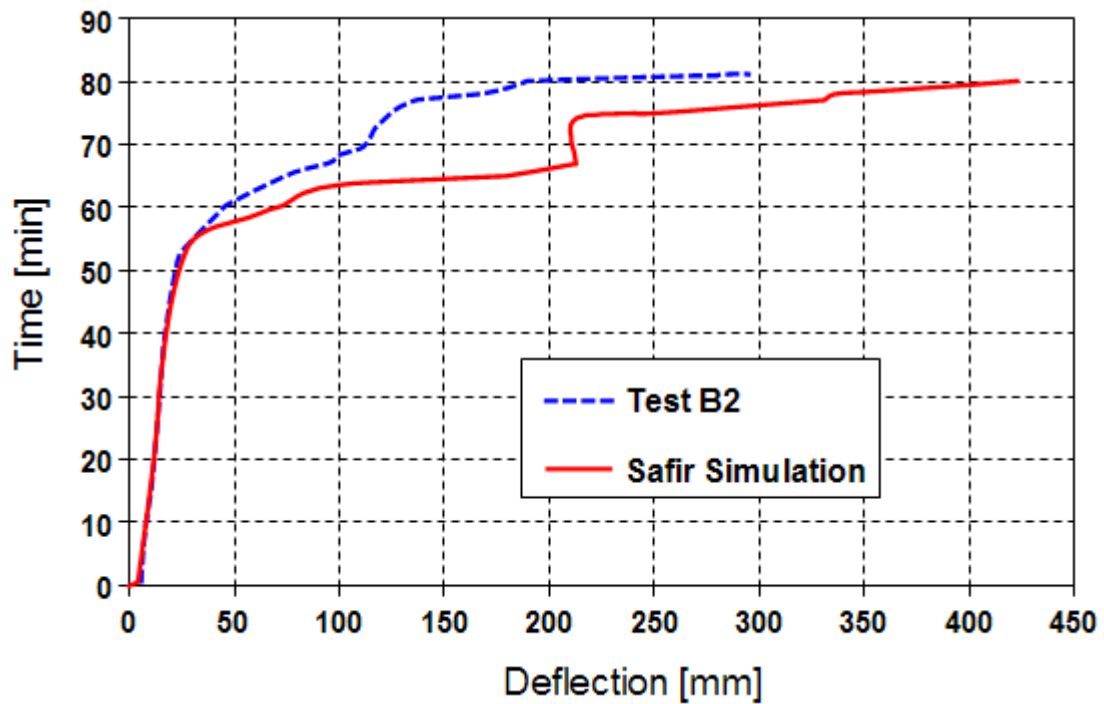


Figure 3-32 : FEM vs test B2

The Figure 3-33 to Figure 3-35 show a picture of the beam B2 after the fire test and the shape of the beam at the end of the numerical simulation using the FEM model in SAFIR.



Figure 3–33 : Cellular beam after the test B2

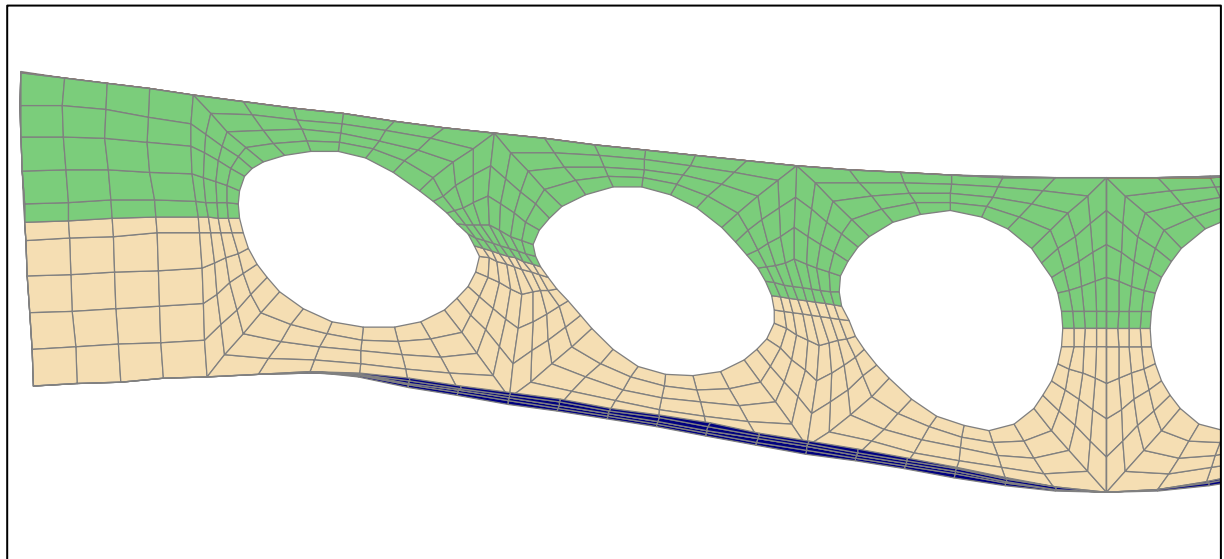


Figure 3–34 : Cellular beam after the numerical simulation of the test B2

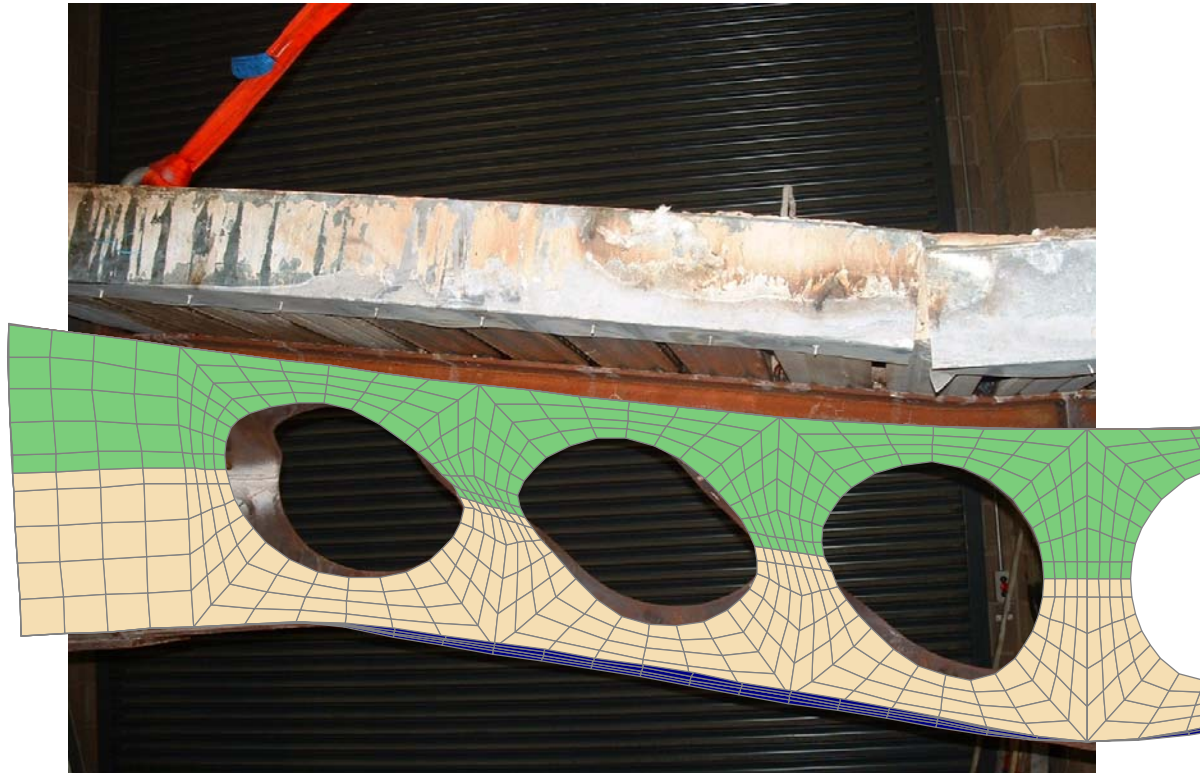


Figure 3–35 : Comparison between the deformed shape of the test B2 (furnace test vs numerical simulation)

For both simulations, the software SAFIR was able to predict with an acceptable accuracy the complex behaviour of the cellular beams in case of fire. On the first part of the graphs, the elastic behaviour of the beams is reproduced with accuracy. In a second step, the SAFIR model predicts the web-post buckling earlier than expected but the model is still able to follow the displacements of the beams until the end of the tests.

In conclusion, the experimental data have been compared with the results obtained from the Finite Element modelling with an acceptable level of accuracy. The deflection is over-evaluated by the FEM calculation but it is on the safe side and the simulated beam is a perfect beam on two supports.

An improved correlation between the Finite Element model and test results could be produced by ‘tuning’ the input data of the software. The temperature distribution along the beam varies significantly and it would be possible to define a better combination of temperature for the model.

Moreover, it would also be possible to change material properties of the steel sections.

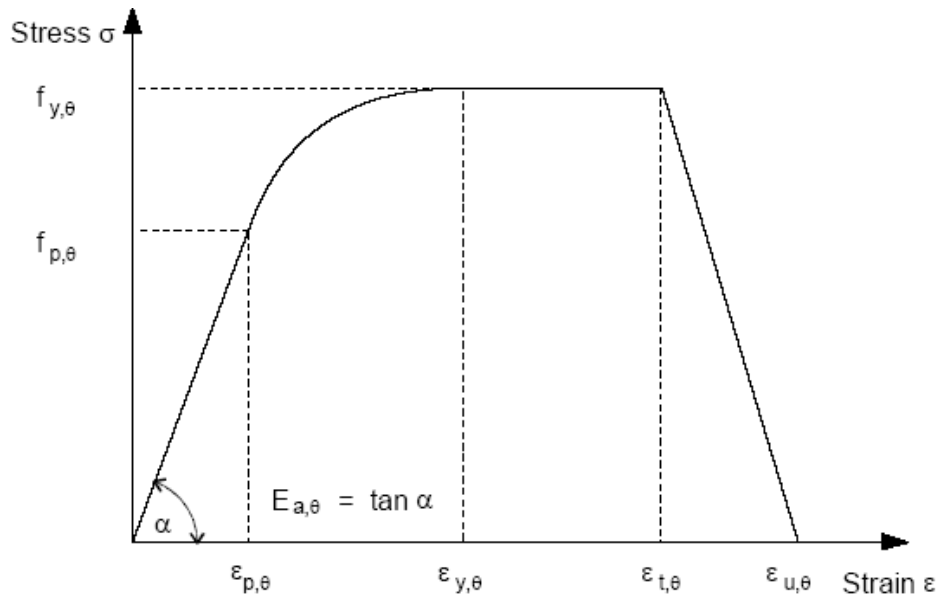


Figure 3–36 : σ - ε relationships for steel in EC3

Using a modified σ - ε relationships for steel (see Figure 3–37), it would be possible to have a better correlation between the test results and the results of the model.

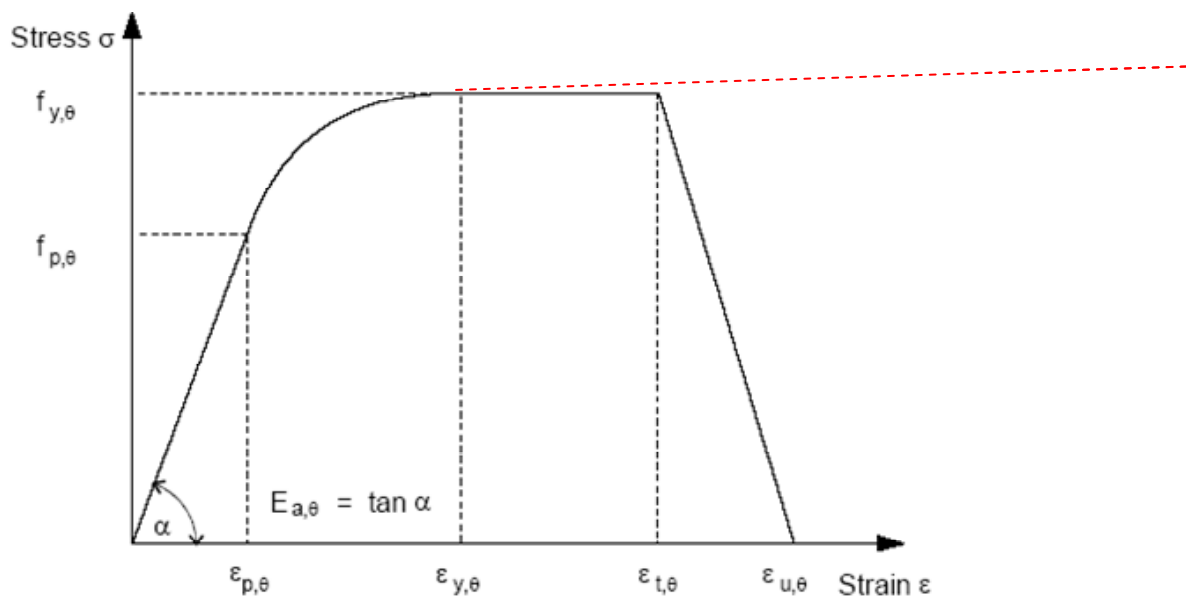


Figure 3–37 : Modified σ - ε relationships for steel

However, the aim of the simulation was to show that the Finite Element model built in SAFIR is able to predict with a relative accuracy the thermo-mechanical behaviour of cellular beam in fire conditions taking into account the Eurocode material properties. The material

properties for steel in the software SAFIR fit perfectly with the Eurocodes rules (see Figure 3–36). The $\varepsilon_{t,\theta}$ has a value of 15% and $\varepsilon_{u,\theta}$ has a value of 20%.

Consequently, these results show that the FEM model can be used for further parametric studies. The numerical model is capable of simulating the mechanical behaviour of composite cellular beam sections in both cold and elevated temperature conditions with a relatively high accuracy.

Chapter 4

Analytical calculation model for cellular beam in fire conditions

4. Analytical calculation model for cellular beam in fire conditions

This chapter presents an analytical model for the evaluation of the resistance of cellular beam in fire condition. The two failure modes that will be studied are the web post buckling and the Vierendeel bending.

For both a complete analytical model will be elaborated taking into account the decrease of steel properties with the elevation of temperature (Steel Strength limit, Young modulus...).

4.1 Web post buckling analytical model

The analytical method for the web post buckling in cold condition has been developed by CTICM on behalf of ArcelorMittal, as part of the ACB Design Optimisation study. It is described in many references [24], [49] to [53].

This method was adapted for the cellular beam calculation in fire conditions. It is presented hereafter.

Following the observations and the analysis of all the tests performed on cellular beam in cold and in fire situation, it was decided that the analytical model must be based on the principal stress resistance at the border of the opening (see Figure 4–1).

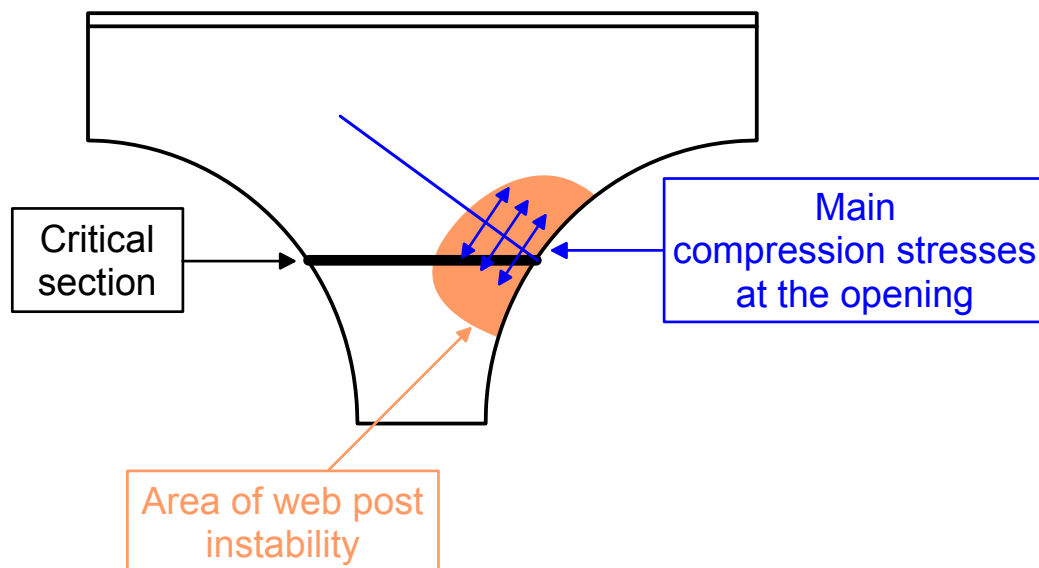


Figure 4–1 : Principle of the check of the web post stability

The criterion for resistance to buckling of an intermediate web post at elevated temperature is given by the following equation :

$$\Gamma_b = \frac{|\sigma_{w,fi,Ed}|}{\kappa \sigma_{w,fi,Rd}}$$

It is based on the calculation of the principal stress resistance in fire situation for the half post being studied $\sigma_{w,fi,Rd}$ and the principal compressive stress in fire situation in the half post being studied $\sigma_{w,fi,Ed}$ ($\sigma_{w,fi,Ed,up}$ for the upper half post and $\sigma_{w,fi,Ed,low}$ for the lower half post). These stresses are calculated for the critical section of the member being verified, adjacent to the opening where the compression is at a maximum (see Figure 4–2) :

Factor κ in the equation is the factor for post critical reserve of strength, taking into account failure by a mechanism that occurs after the appearance of local buckling of the web post given in Chapter 4.1.8.

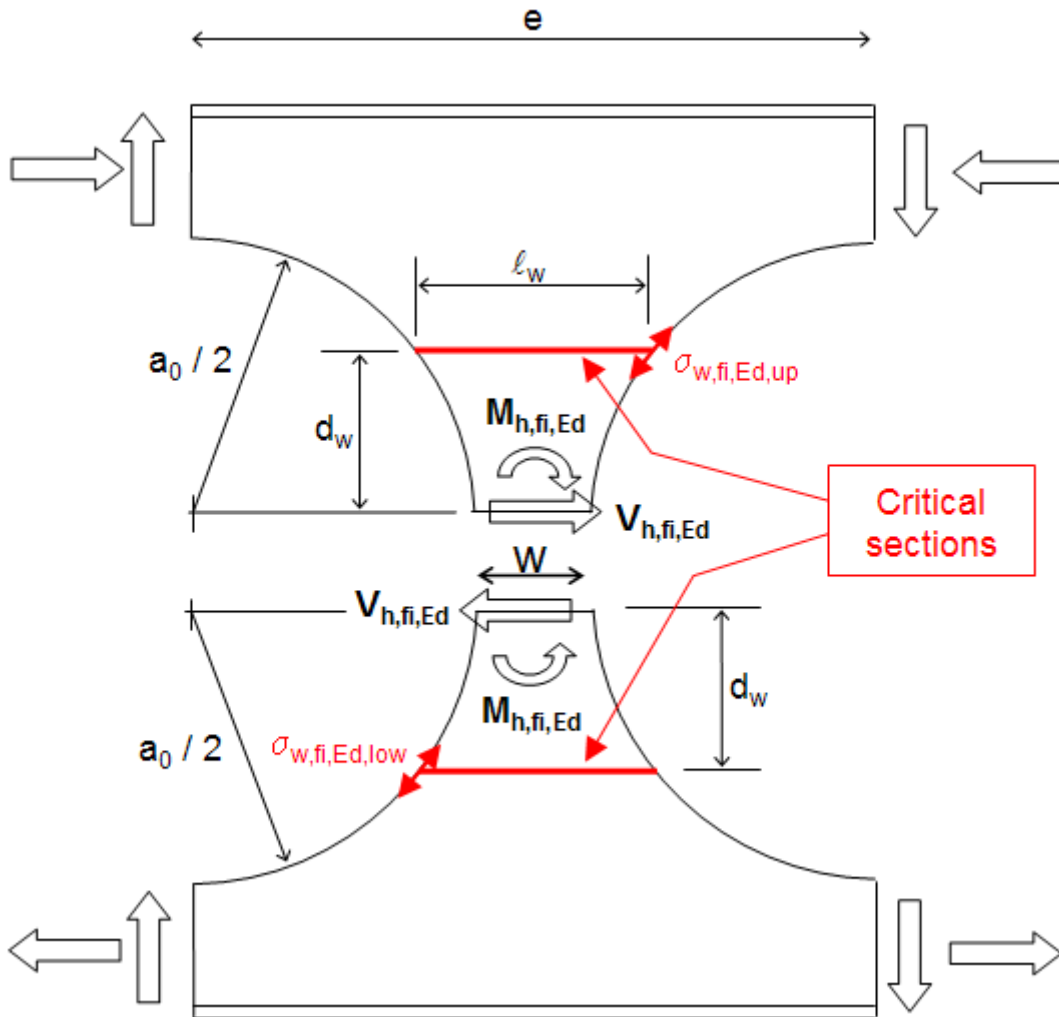


Figure 4–2 : Definition of critical section for stability of an intermediate web post

This approach based on the principal stresses came from the analysis of the multiple laboratory tests realised by ArcelorMittal and on the localisation of the compression stresses in the cellular beam web post using Finite Element modelling (see Figure 4–3).

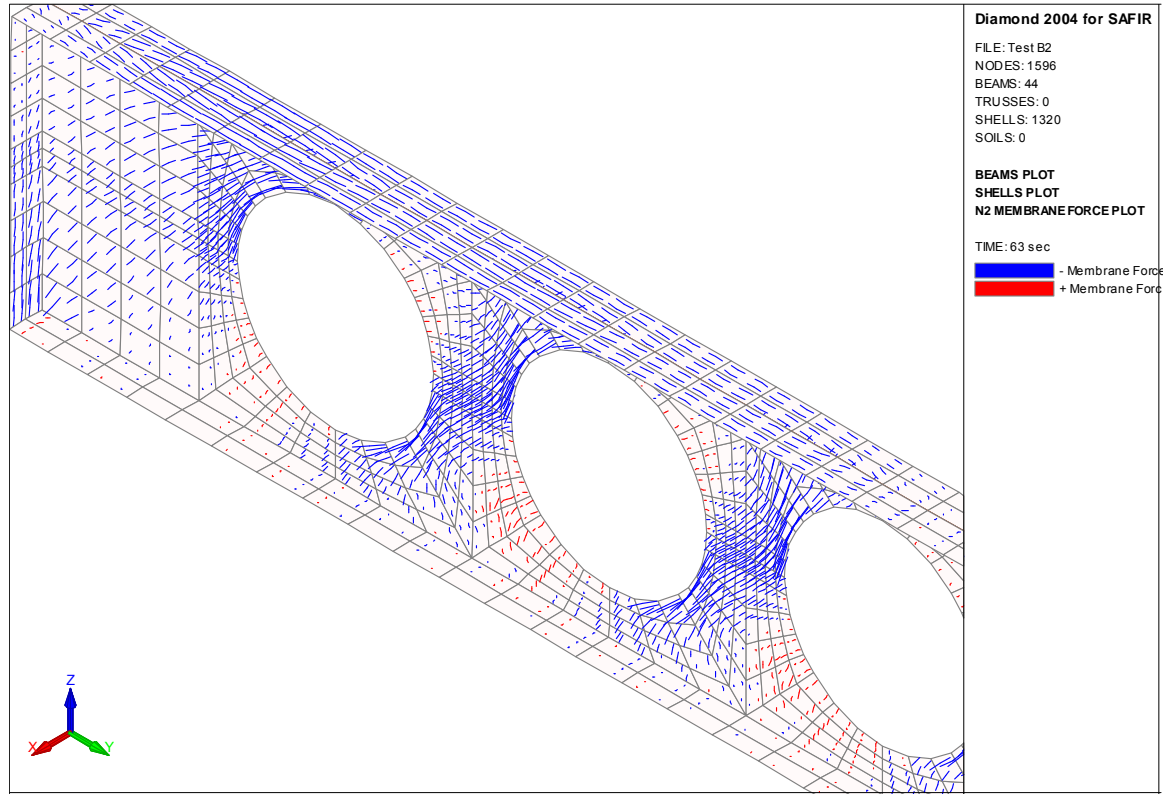


Figure 4–3 : Compression stresses in the cellular beam

Throughout the following parts of this thesis, the parameter α is defined as the width of the web post in terms of the following relationship:

$$\alpha = 1 + w / a_0$$

4.1.1 Position of the critical section in the web post

The critical section of a half post is the section where the horizontal shear $V_{h,fi,Ed}$ gives the maximum bending stress in the plane of the web. This section is defined in terms of its distance d_w from the joint between the two half posts, given by the following relationship based on geometrical relationship:

$$d_w = \frac{a_0}{2} \sqrt{\frac{\alpha^4 + 8\alpha^2 - 2 - \alpha^2}{2}}$$

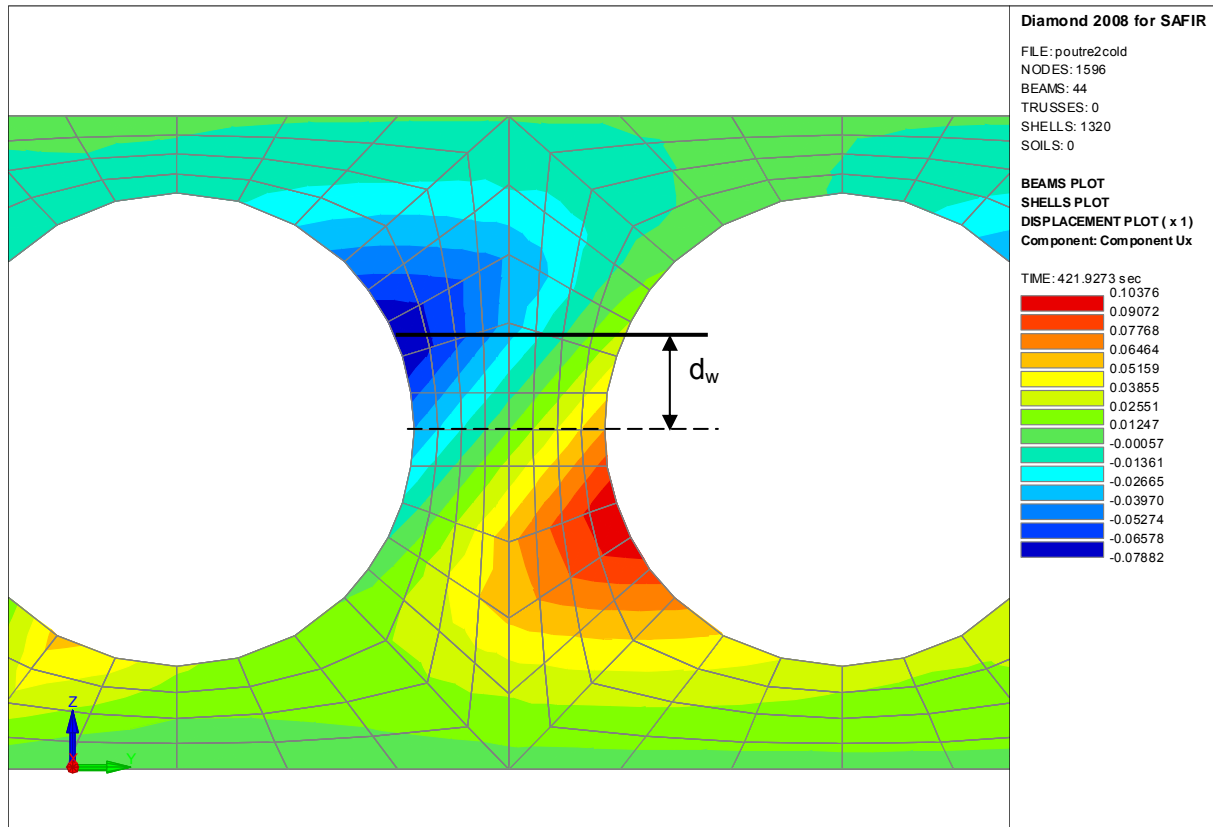


Figure 4–4 : Out of plane displacement and position of the critical section

The width ℓ_w of the critical section is obtained by considering the following relationship:

$$\ell_w = a_0 \left(\alpha - \sqrt{1 - \left(\frac{2 d_w}{a_0} \right)^2} \right)$$

4.1.2 Principal compressive stress

The principal compressive stress in case of fire at the critical section due to local bending moment (Figure 4–5) is given by :

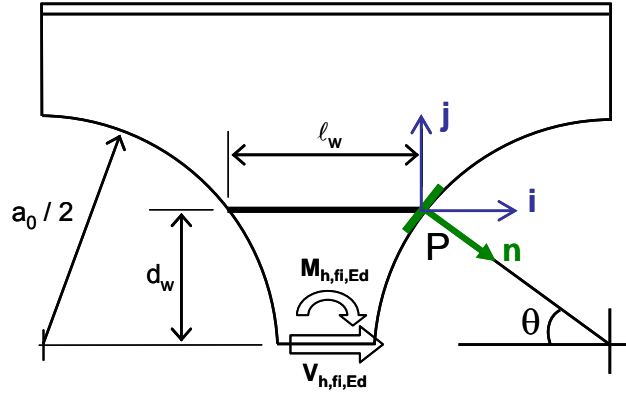


Figure 4-5 : Orientation of the face tangent to the border of the opening

The stress distribution in the point P of the critical section due to the horizontal shear $V_{h,fi,Ed}$ and bending moment $M_{h,fi,Ed}$ can be expressed by the following relationship on the axes system (i, j) (see Figure 4-5) :

$$\begin{bmatrix} -\sigma_x & \tau_v \\ \tau_v & -\sigma_f \end{bmatrix}$$

$\sigma_{w,fi,Ed}$ is the principal stress in the plane of the web and can be expressed by the following relation:

$$\sigma_f = \frac{6 M_c}{\ell_w^2 t_w}$$

For the face tangent to the opening, the normal 'n' can be expressed in the axes system (i, j) taking into account the angle θ :

$$\sigma_{i\theta} = -\sigma_x \cos\theta - \tau_v \sin\theta$$

$$\sigma_{j\theta} = \tau_v \cos\theta + \sigma_f \sin\theta$$

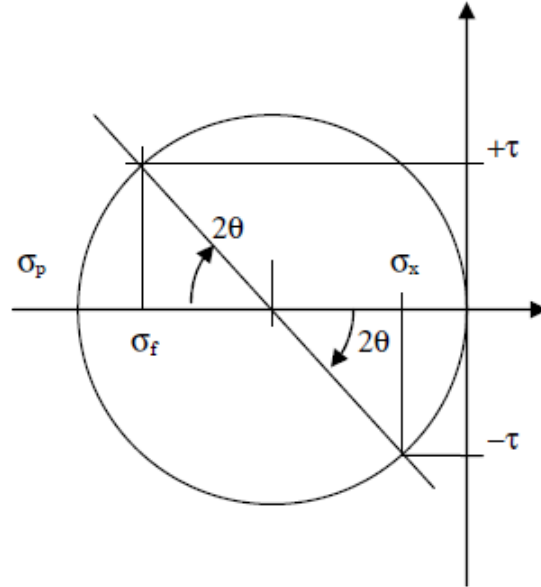


Figure 4-6 : Stresses at point P (Mohr circle)

The boundary conditions impose $\sigma_{i\theta} = \sigma_{j\theta} = 0$, and we found the following expression for the principal stress $\sigma_{w,fi,Ed} = \sigma_x + \sigma_f$:

$$\sigma_{w,fi,Ed} = \frac{6 M_{c,fi,Ed}}{\ell_w^2 t_w \left(1 - 4 (d_w / a_0)^2\right)}$$

where $M_{c,fi,Ed}$ is the bending moment in the critical section in fire situation.

Upper member : $M_{c,fi,Ed,up} = V_{h,fi,Ed} d_w - M_{h,fi,Ed}$

Lower member : $M_{c,fi,Ed,low} = V_{h,fi,Ed} d_w + M_{h,fi,Ed}$

4.1.3 Forces acting on a pure steel 'T' section

The forces acting on the 'T' at the location of an opening are obtained using the following relationships. They are a function of the global forces $M_{fi,Ed}$ and $V_{fi,Ed}$ calculated at the openings to the left (subscript i) and right (subscript i+1) of the web post.

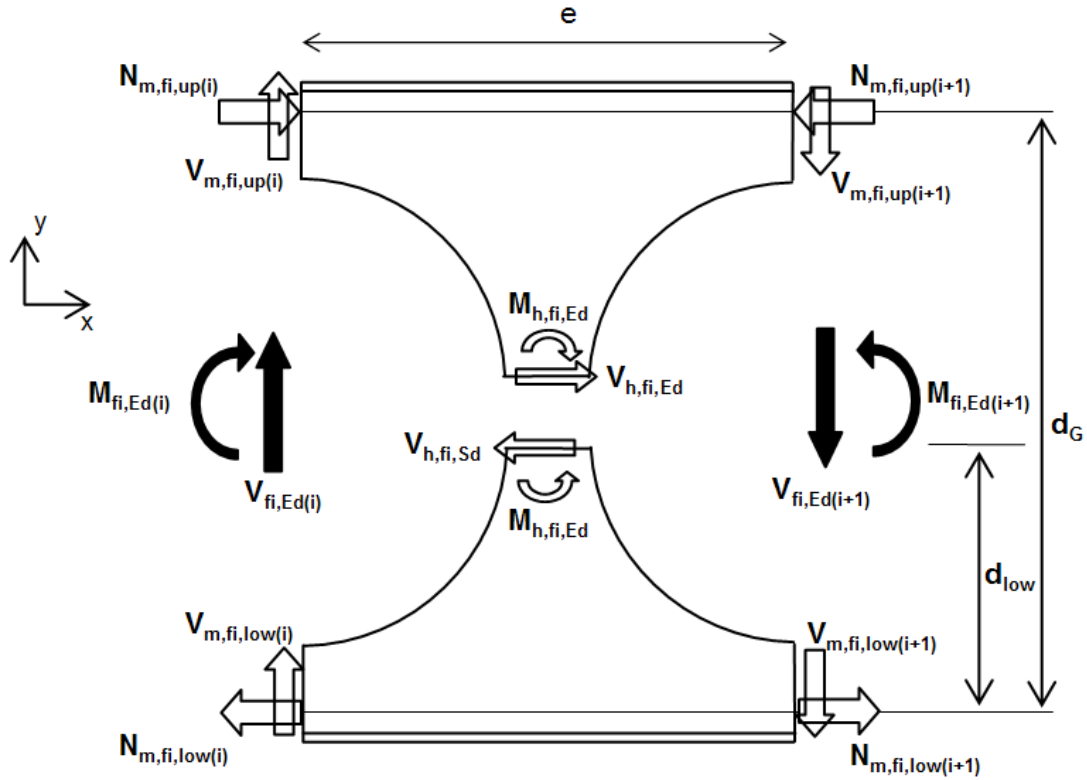


Figure 4-7 : Forces acting on 'T's

If the hypothesis of an inflection point (point where the bending moment is null) in the 'T' sections at maximum opening, validated by numerical simulations [24], the global bending moment can be expressed by two axial forces in each 'T' member:

$$N_{m,fi,low(i)} = N_{m,fi,up(i)} = M_{fi,Ed(i)} / d_G$$

$$N_{m,fi,low(i+1)} = N_{m,fi,up(i+1)} = M_{fi,Ed(i+1)} / d_G$$

The shear force in each 'T' member is determined on the basis of the global shear values $V_{fi,Ed(i)}$ and $V_{fi,Ed(i+1)}$.

The repartition of the shear force was studied by Daniel Bitar [24] and is summarised in the next paragraph.

The forces in the web post are given by :

$$V_{h,fi,Ed} = N_{m,fi,up(i+1)} - N_{m,fi,up(i)} = N_{m,fi,low(i+1)} - N_{m,fi,low(i)}$$

$$M_{h,fi,Ed} = (V_{m,fi,low(i+1)} + V_{m,fi,low(i)}) \cdot \frac{e}{2} - V_{h,m,fi} \cdot d_{low}$$

Remark: for a symmetrical profile, $M_{h,m,fi} = 0$

where d_{low} is the distance between the centre of gravity of the lower 'T' (at the opening centre line) and the line of the joint between the half posts (see Figure 4–8).

4.1.4 Repartition of the shear between the 'T' members

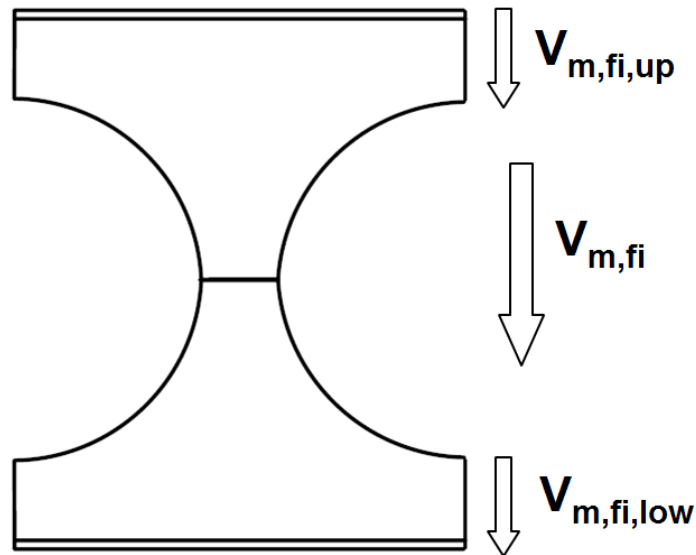


Figure 4–8 : Shear forces repartition

$V_{m,fi}$: Global Shear force in the steel beam at the maximum opening position

$V_{m,fi,low}$: Shear force in the lower 'T' section

$V_{m,fi,up}$: Shear force in the upper 'T' section

$A_{v,0,up}$: Shear area of the upper 'T'

$A_{v,0,low}$: Shear area of the lower 'T'

The shear forces are linked by the following equation :

$$V_{m,fi} = V_{m,fi,low} + V_{m,fi,up}$$

A first approach consisted in the repartition of the global shear force in function of the shear area.

After the analysis of the different test results and the numerical simulation [24], it was observed that this hypothesis was not the most suitable for asymmetric sections. A new

model was proposed by Bitar in order to reflect the reality better. On the Figure 4–9, you can find a comparison between the old method, the new method and the test results.

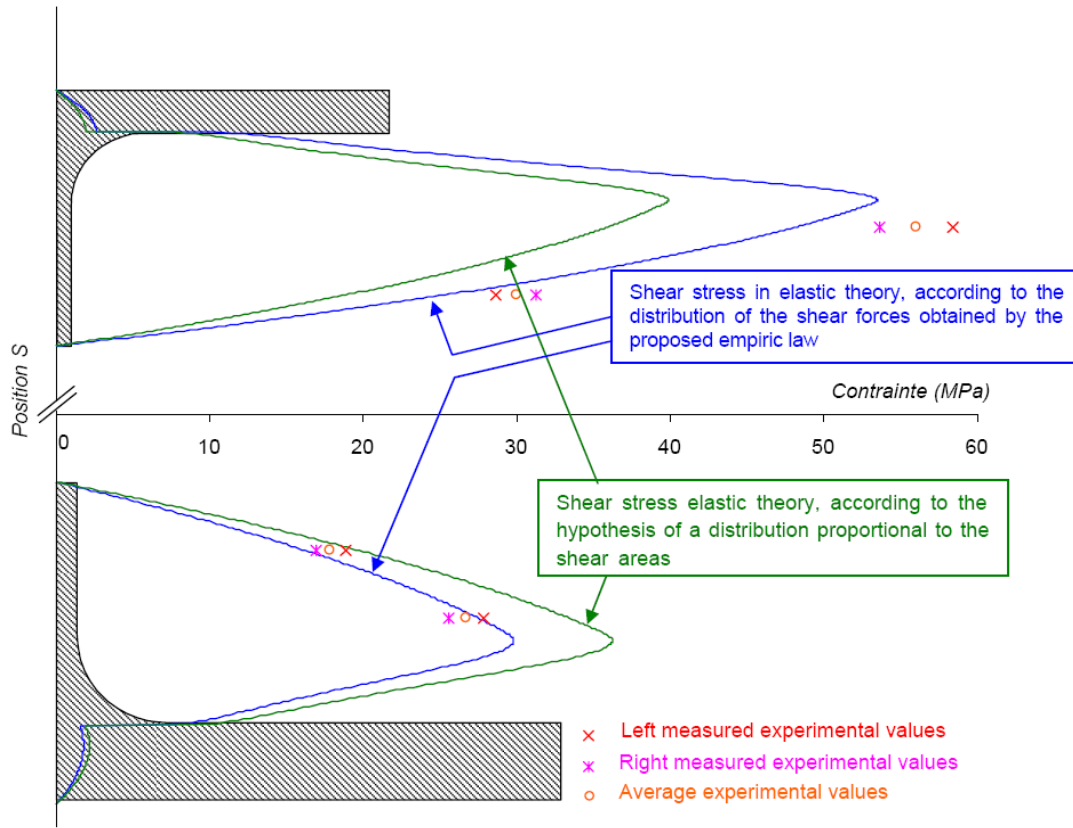


Figure 4–9 : Steel beam test 3a - Shear stresses comparison

This new empirical model can be expressed by the following relationship:

$$V_{m,fi,low(i)} = (1 - k_{Av}) V_{fi,Ed(i)} \quad V_{m,fi,up(i)} = k_{Av} V_{fi,Ed(i)}$$

$$V_{m,fi,low(i+1)} = (1 - k_{Av}) V_{fi,Ed(i+1)} \quad V_{m,fi,up(i+1)} = k_{Av} V_{fi,Ed(i+1)}$$

where : k_{Av} is the coefficient for distribution of the shear force, given by :

$$k_{Av} = \frac{A_{v,0,low}^{\eta}}{A_{v,0,up}^{\eta} + A_{v,0,low}^{\eta}}$$

η is empirical coefficient calibrated using numerical simulations given by :

$$\eta = \frac{1}{9.48 - 4.84 \alpha}$$

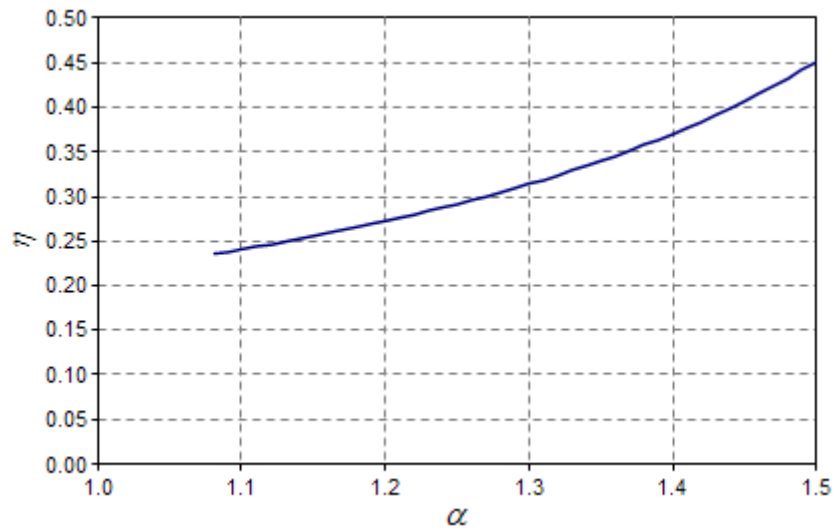


Figure 4-10 : Form of the variable η as a function of α

The shear area of a 'T' is given by :

$$A_{v,0} = \left(h_m - \frac{a_0}{2} - \frac{t_f}{2} \right) t_w + r_c t_f + \frac{4 - \pi}{2} r_c^2$$

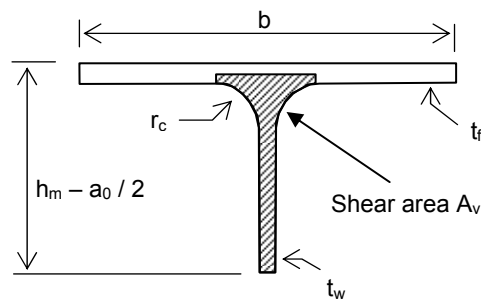


Figure 4-11 : Shear area of a 'T' at the location of an opening

4.1.5 Forces acting on a 'T' shape composite section

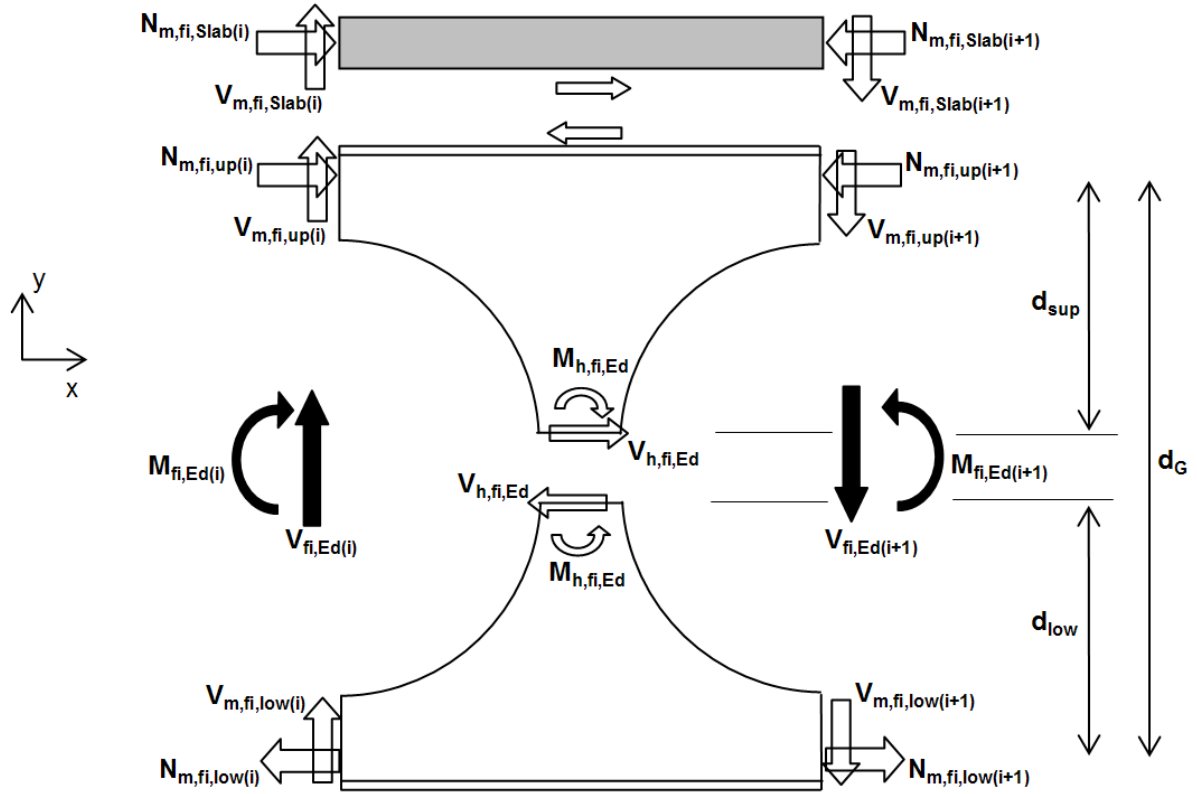


Figure 4–12 : Forces in the steel 'T's and the slab

At an opening the axial forces applied at the centres of gravity of the 'T' shaped steel members and the slab are considered as being equal to the forces deduced from the diagram of stresses at the ULS of plastic resistance of the section, reduced in proportion to the ratio $M_{fi,Ed} / M_{fi,Rd}$. This leads to the following relationships:

$$N_{m,fi,up} = N_{m,ULS,up} \frac{M_{fi,Ed}}{M_{fi,Rd}}$$

$$N_{m,fi,low} = N_{m,ULS,low} \frac{M_{fi,Ed}}{M_{fi,Rd}}$$

$$N_{m,fi,slab} = N_{m,ULS,slab} \frac{M_{fi,Ed}}{M_{fi,Rd}}$$

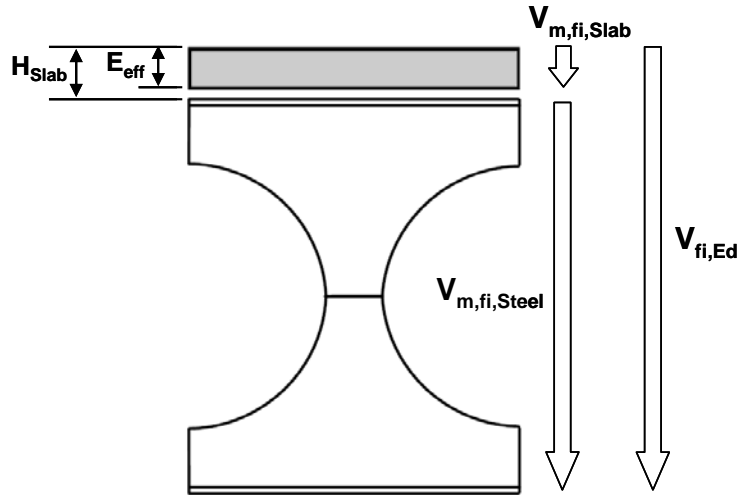


Figure 4–13 : Shear force distribution between concrete slab and steel beam

At an opening, the global shear force $V_{fi,Ed}$ is divided by the shear force in the slab and the shear force in the steel beam (see Figure 4–13). The shear forces applied at the centres of gravity of the ‘T’s and the slab are determined using the following relationships :

$$V_{m,fi,Slab} = k_{Slab} V_{fi,Ed}$$

$$V_{m,fi,Steel} = (1 - k_{Slab}) V_{fi,Ed}$$

$$V_{m,fi,up} = k_{Av} V_{m,fi,Steel}$$

$$V_{m,fi,low} = (1 - k_{Av}) V_{m,fi,Steel}$$

with :

$$k_{Slab} = \min \left(\frac{A_{v,Slab}}{A_{v,Slab} + A_{v,up} + A_{v,low}}; \frac{V_{fi,Rd,Slab}}{V_{fi,Ed}} \right)$$

$$k_{Av} = \frac{A_{v,0,up}^{\eta}}{A_{v,0,up}^{\eta} + A_{v,0,low}^{\eta}} \text{ and } \eta = \frac{1}{9.48 - 4.84 \alpha} \text{ (demonstrated in chapter 4.1.4)}$$

where

$A_{v,0,up}$ is the shear area of upper ‘T’

$A_{v,0,low}$ is the shear area of lower ‘T’

$A_{v,Slab}$ is homogenised shear area of the slab. The value of this shear area has been determined by experience in the scope of Soon Ho Cho’s thesis [59]. It can be calculated using the following expression:

$$A_{v,slab} = \frac{L_{Slab} E_{eff}}{m}$$

Hence;

E_{eff} is an effective thickness of the slab adjacent to the opening (see Figure 4–13)

L_{Slab} is an effective width of the slab adjacent to the opening being considered. The value of this length has been determined by experience in the scope of Soo Ho Cho's thesis [59]. It can be calculated using the following expression:

$$L_{Slab} = \text{Min} (1.5 E_{eff} ; L_{disp,l}) + \text{Min} (1.5 E_{eff} ; L_{disp,r})$$

$L_{disp,r}$ and $L_{disp,l}$ are available length of slab (right and left)

m is a coefficient of equivalence steel/concrete for short term loading.

$V_{Rd,Slab}$ is shear resistance of the concrete slab, calculated according to :

$$V_{Rd,Slab} = 3.6 \tau_{Rd,Slab} E_{eff} L_{Slab}$$

$\tau_{Rd,Slab}$ is design shear resistance of the slab

$$\tau_{Rd,slab} = 0.25 \cdot 0.7 \cdot \frac{f_{ctm}}{\gamma_{c,fi}}$$

f_{ctm} is an average tension resistance of the concrete forming the slab

$$f_{ctm} = 0.3 \cdot (f_{ck})^{2/3}$$

f_{ck} is the characteristic compressive resistance of the concrete after 28 days.

4.1.6 Principal stress resistance

The principal stress resistance is calculated using the following formula based on EN1993-1-2 [64]:

$$\sigma_{w,fi,Rd} = \frac{\chi_{fi} \cdot \xi \cdot k_{y,\theta} \cdot f_y}{\gamma_{M,fi}}$$

where:

χ_{fi} is a reduction factor for out-of-plane buckling of the web post adapted for fire situation following EN1993-1-2 [64], and calculated using the following formulae :

$$\chi_{fi} = \frac{1}{\phi_{\theta} + \left(\phi_{\theta}^2 - \bar{\lambda}_{\theta}^2 \right)^{0.5}} \text{ and } \chi_{fi} \leq 1.0$$

$$\phi_{\theta} = 0.5[1 + \alpha \bar{\lambda}_{\theta} + \bar{\lambda}_{\theta}^2]$$

$$\alpha = 0.65 \sqrt{\frac{235}{f_y}}$$

ξ is a shape factor for the critical section calibrated using the Finite Element modelling and is given by :

$$\xi = 1.5 + \frac{2 \cdot 10^{-5}}{(1 - \alpha)^4}$$

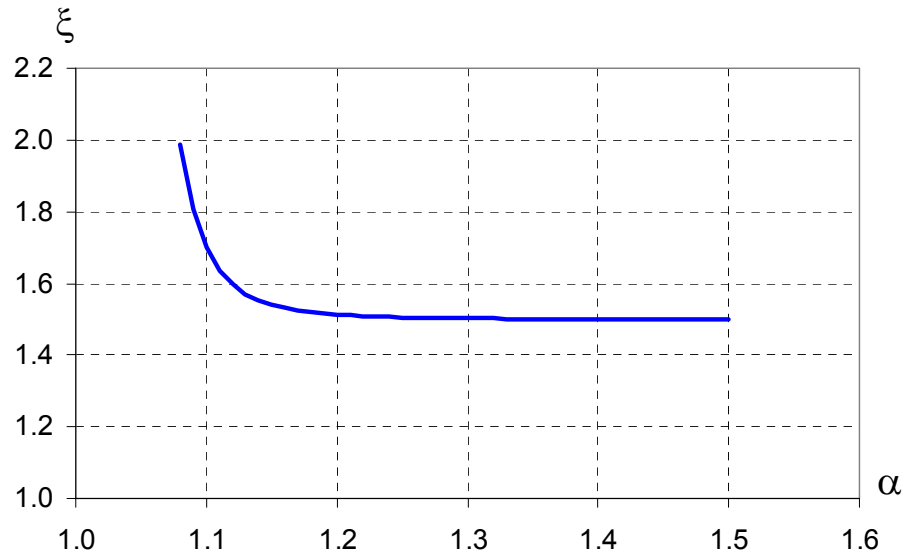


Figure 4-14 : Curve ξ in function of α

For the large web posts, the shape factor ξ is equal to 1.5. It is equal to the ratio between the plastic and the elastic modulus of a rectangle section. It reflects the fact that the failure mode due to the shear V_h , without taking into account the instability, is obtained by a plastic hinge in the critical section.

For smaller web posts, the shape factor ξ varies from 1.5 to 2. It reflects the ability of the web post to work as a connecting rod in tension after the yielding of the critical section.

The reduced slenderness $\bar{\lambda}_{\theta}$ of the web post being considered in case of fire is given by :

$$\bar{\lambda}_{\theta} = \bar{\lambda} \sqrt{\frac{k_{y,\theta}}{k_{E,\theta}}} = \sqrt{\frac{\xi f_{yw}}{\sigma_{w,fi,cr}}} \sqrt{\frac{k_{y,\theta}}{k_{E,\theta}}}$$

Where $k_{y,\theta}$ and $k_{E,\theta}$ are the reduction factors for steel strength limit and Young modulus, respectively, at elevated temperature.

4.1.7 Principal stress resistance for instability

The critical principal stress for instability $\sigma_{w,fi,cr}$ is determined taking into account the two possible instabilities :

- the buckling of the web caused by the shear force V_h (left part of Figure 4–15)
- the buckling of the web caused by the axial force in the 'T's (right part of Figure 4–15)

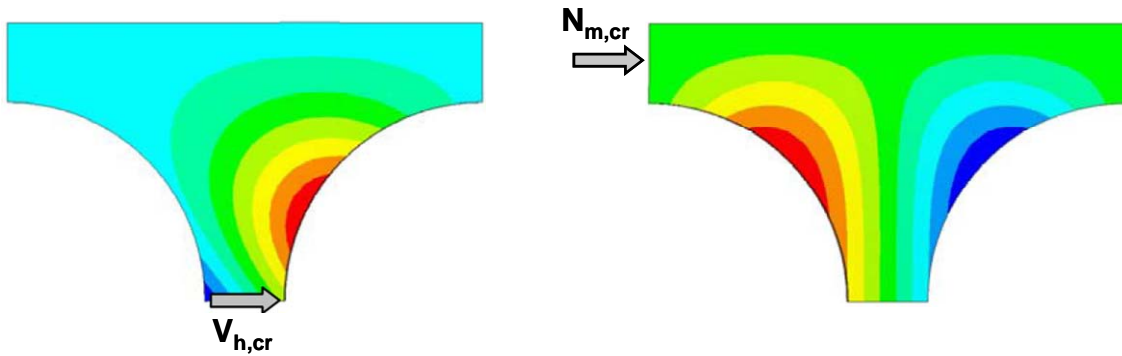


Figure 4–15 : Instability mode of the 'T's

The critical principal stress for instability $\sigma_{w,fi,cr}$ in fire condition is given by :

Upper half post : $\sigma_{w,fi,cr,up} = \alpha_{cr,fi,up} \sigma_{w,fi,up}$

Lower half post : $\sigma_{w,fi,cr,low} = \alpha_{cr,fi,low} \sigma_{w,fi,low}$

$\sigma_{w,fi,up}$, $\sigma_{w,fi,low}$ are the principal stresses in fire situation in the upper and lower half posts respectively, caused by the shear force $V_{h,m,fi}$ alone and calculated using the formula given in the Chapter 4.1.2.

$\alpha_{cr,fi,up}$, $\alpha_{cr,fi,low}$: are critical coefficients for the upper and lower half posts respectively, taking into account interaction between the two members and given by :

$$\alpha_{cr,fi,up} = \max \left(\beta_{cr,fi,up} ; \frac{2 \beta_{cr,fi,up} \beta_{cr,fi,low}}{\beta_{cr,fi,up} + \beta_{cr,fi,low}} \right)$$

$$\alpha_{cr,fi,low} = \max \left(\beta_{cr,fi,low} ; \frac{2 \beta_{cr,fi,up} \beta_{cr,fi,low}}{\beta_{cr,fi,up} + \beta_{cr,fi,low}} \right)$$

$\beta_{cr,fi,up}$, $\beta_{cr,fi,low}$: are critical coefficients for the upper and lower half posts respectively, taking into account only compression in the member and shear in the web post.

It must be noticed that the buckling of the web due to the shear force V_h is the dominating failure mode. The influence of the axial force in the 'T's is taken into account by the linear interaction of Dunkerly. The two types of action were separated; the unfavourable action of the compression member and the favourable action of the tensile member. The stabilisation of the web post by the member in tension is less important than the instability effect of the compression. So a factor of 0.5 was taken into account in the interaction for the member in tension.

$$\beta_{cr,fi,up} = \frac{1}{\frac{V_{h,fi,Rd}}{V_{h,cr,fi,up}} + \frac{N_{m,fi,up}}{N_{m,cr,fi,up}}}$$

$$\beta_{cr,fi,low} = \frac{1}{\frac{V_{h,fi,Rd}}{V_{h,cr,fi,low}} - 0.5 \frac{N_{m,fi,low}}{N_{m,cr,fi,low}}}$$

It is important to note that these coefficients are calculated assuming that the lower member is in tension and the upper member is in compression.

$V_{h,cr,fi,up}$, $V_{h,cr,fi,low}$: Critical shear forces in fire condition for out-of-plane buckling of the upper and lower half posts respectively (see definition hereafter).

$N_{m,cr,fi,up}$, $N_{m,cr,fi,low}$: Critical axial forces in fire condition for local buckling of the web of the upper and lower members respectively (see definition hereafter).

$N_{m,fi,up}$, $N_{m,fi,low}$: Axial forces in fire condition in the webs of the upper and lower members respectively, given by :

$$N_{m,fi,up} = \frac{A_{w,up}}{A_{0,up}} \min(N_{m,fi,up(i)} ; N_{m,fi,up(i+1)})$$

$$N_{m,fi,low} = \frac{A_{w,low}}{A_{0,low}} \min(N_{m,fi,low(i)} ; N_{m,fi,low(i+1)})$$

$A_{0,up}$, $A_{0,low}$: Areas of the upper and lower 'T' sections respectively, at the location of the openings.

$A_{w,up}$, $A_{w,low}$: Areas of the webs of the upper and lower 'T' sections respectively, at the location of the openings, given by :

$$A_{w,up} = A_{0,up} - b_{up} t_{f,up}$$

$$A_{w,low} = A_{0,low} - b_{low} t_{f,low}$$

This calculation of axial force consists in the repartition of the global axial force as a function of the shear area of the members. A similar approach to the repartition of the shear force between the members could be used. This approach has not yet been validated for the cold situation and will not be used in the scope of this thesis.

CTICM performed more than 600 numerical simulations [24] in order to determine the critical forces $V_{h,cr,fi}$ for shear in the web post and $N_{m,cr,fi}$ for compression in a member. These simulations covered all the value of α between 1.08 and 1.5 and all the values of δ ($\delta = \frac{h_w}{a_0}$)

from 0.6 and 2 (see Figure 4–16).

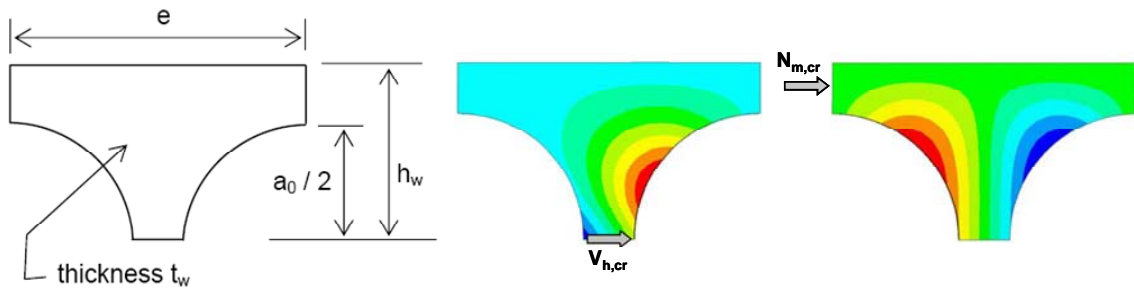


Figure 4–16 : Critical forces for a member

The web of the 'T' member was considered fully encased in the flange. This assumption is always correct for hot rolled profiles but it is really complex to ensure it in case of welded sections.

Consequently, this calibration is only valid for hot rolled section and must be completely recalibrated in case of welded sections.

After analysing the results of the 600 numerical simulations, the following relations were established:

$$V_{h,cr,fi} = P_E (C_0 + C_1 t_w)$$

$$N_{m,cr,fi} = P_E (D_0 + D_1 t_w)$$

where

P_E is the reference Euler buckling load.

Euler has demonstrated that this buckling load can be mathematically expressed by the following equation:

$$P_E = EI \frac{\pi^2}{4\ell^2} \text{ for a beam encased on one support and hinged on the other support.}$$

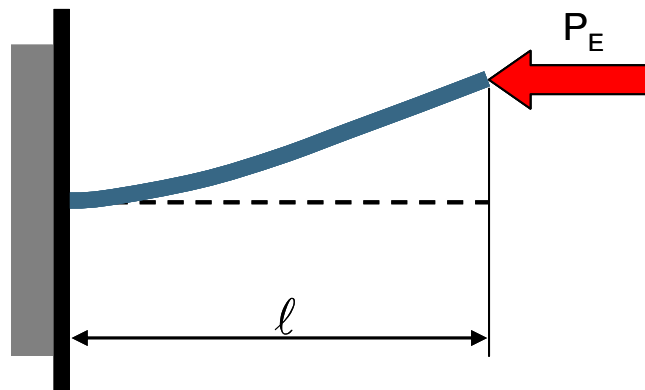


Figure 4–17 : Euler buckling forces

Following the assumption that we are only taking into account the rectangular part of the web post (see Figure 4–18), the reference Euler buckling load can be expressed by the equation where the constant values were removed :

$$P_E = \frac{\pi^2 E_a}{a_0^2} w t_w^3$$

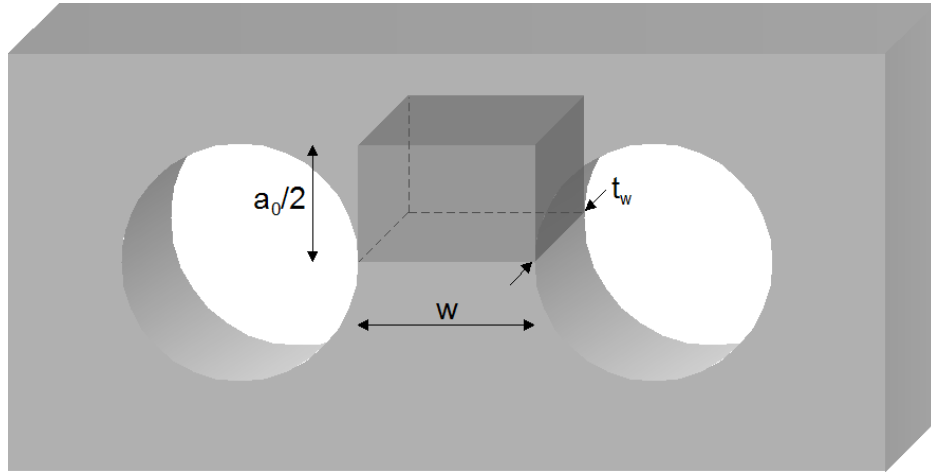


Figure 4-18 : Rectangular part of the web post

Expressions for the coefficients C_0 , C_1 , D_0 and D_1 , based on experimental and numerical calibration, are represented as a function of the following non-dimensional parameters and can be found in reference [24] :

$$\delta = \frac{h_w}{a_0}$$

$$\zeta = \frac{1}{\sqrt{\delta} - 0.5}$$

$$\mu = \frac{1}{\sqrt{\alpha} - 1}$$

4.1.8 Post critical reserve of strength

During the laboratory tests and numerical simulations in cold conditions, it was noted that the web-post buckling of the first web post can be a local failure without causing the global failure of the beam. The beam will act like a beam with elongated opening.

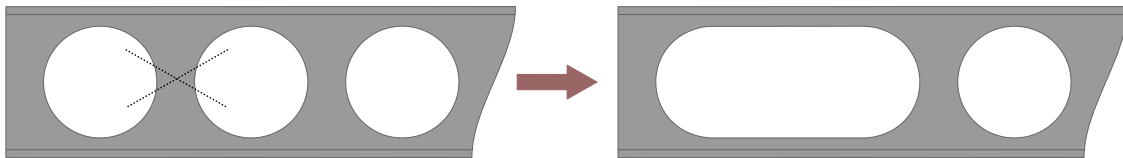


Figure 4-19 : Elongated opening

The factor for post critical reserve of strength κ has been determined on the basis of the numerical simulations and is given by :

$$\kappa = 1 + 0.625 (\psi - 0.3)$$

$$\text{while } 1 < \kappa < 1.25$$

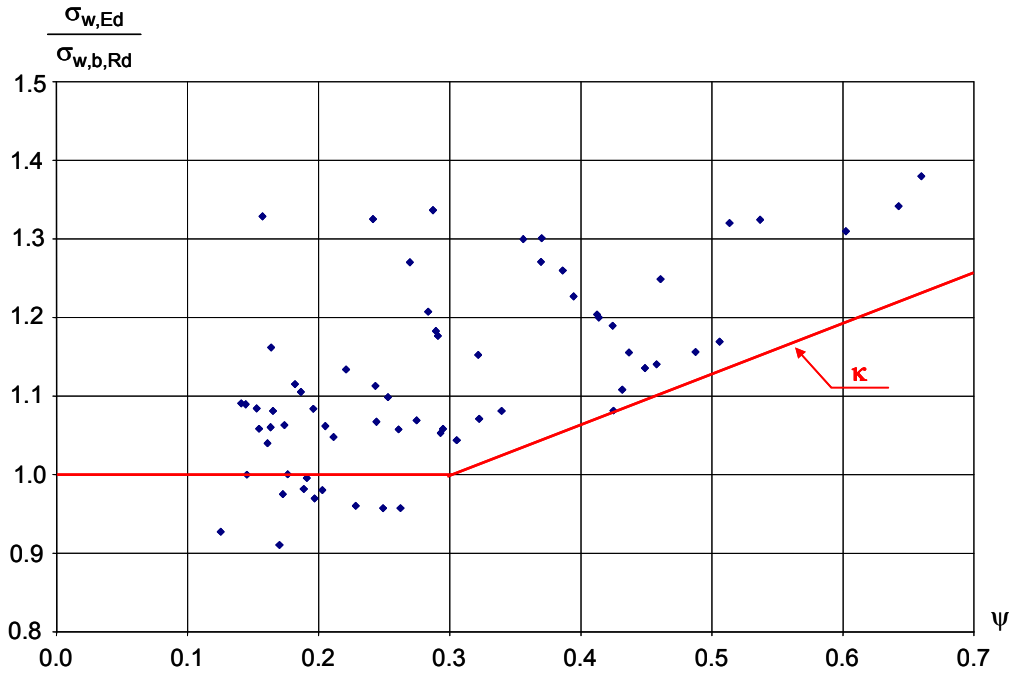


Figure 4–20 : Value of κ factor respecting to ψ value

ψ is a non-dimensional factor given by :

$$\text{Upper T : } \psi = \frac{M_{pl,Rd,up}}{e \cdot V_{fi,up}}$$

$$\text{Lower T : } \psi = \frac{M_{pl,Rd,low}}{e \cdot V_{fi,low}}$$

where

$M_{pl,Rd,up}$, $M_{pl,Rd,low}$ are the plastic moment resistances of the upper and lower ‘T’ respectively, at the location of an opening.

$V_{fi,up}$, $V_{fi,low}$ are the shear forces in the upper and lower members respectively. The lower of the values for ψ obtained to the right and left of the web post is used.

e is the length of panel (see Figure 4–21).

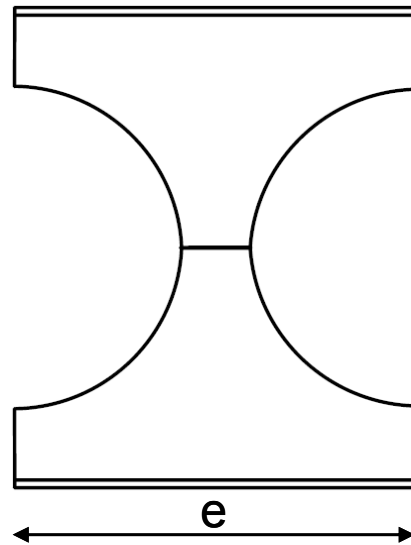


Figure 4-21 : Standard panel

4.2 Resistance of the net section at the location of a web opening (Vierendeel model)

Another failure mode of cellular beams is the yielding of the members caused by Vierendeel effect with the appearance of plastic hinges. (see Figure 4-22)



Figure 4-22 : Failure caused by Vierendeel effect

These plastic hinges appear in the beam where the solicitations of forces are the biggest, and the combination of axial force, shear force and bending moment is the most important.

A calculation method is available in the Annex N of the ENV version of EC3 [60]. It has been validated by Bitar [49] in the test campaign and numerical simulation made to determine the analytical web post buckling in cold conditions.

This model in cold condition was adapted to fire conditions and was modified to take into account the difference of elongation between the web and the flange.

4.2.1 Determination of the geometry

The transverse cross-section of a cellular beam is symmetrical in the mid-plane of the web. A cross section is shown in Figure 4–23(a). The section is decomposed into elementary parts when calculating its characteristics; for the gross section and for the net section as shown in Figure 4–23(b) and Figure 4–23(c) respectively.

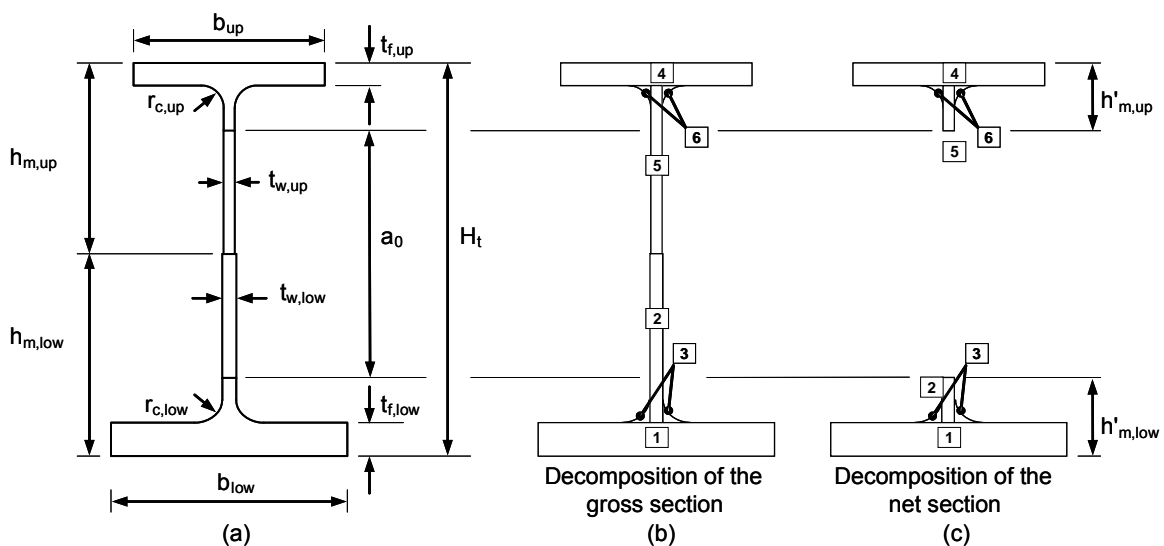


Figure 4–23 : Geometrical description of a transverse cross-section

For each elementary part, the following values are calculated:

- its area a_i ,
- the position of its centre of gravity z_i relative to the bottom fibre,
- the second moment of area $I_{oy,i}$ about the axis which is parallel to the major axis of the section,
- the second moment of area $I_{oz,i}$ about the axis which is parallel to the minor axis of the section,

The analytical expression of each parameter 1-6 from Figure 4–23 is expressed in the Table 4-1 for the gross section.

i	a_i	z_i	$I_{oy,i}$	$I_{oz,i}$
1	$b_{low} t_{f,low}$	$t_{f,low} / 2$	$b_{low} t_{f,low}^3 / 12$	$t_{f,low} b_{low}^3 / 12$
2	$(h_{m,low} - t_{f,low}) t_{w,low}$	$(h_{m,low} + t_{f,low}) / 2$	$t_{w,low} (h_{m,low} - t_{f,low})^3 / 12$	$(h_{m,low} - t_{f,low}) t_{w,low}^3 / 12$
3	$(4 - \pi) r_{c,low}^2 / 2$	$t_{f,low} + k_c r_{c,low}$	$0.0151 r_{c,low}^4$	$0.0151 r_{c,low}^4$
4	$b_{up} t_{f,up}$	$H_t - t_{f,up} / 2$	$b_{up} t_{f,up}^3 / 12$	$t_{f,up} b_{up}^3 / 12$
5	$(h_{m,up} - t_{f,up}) t_{w,up}$	$H_t - (t_{f,up} + h_{m,up}) / 2$	$t_{w,up} (h_{m,up} - t_{f,up})^3 / 12$	$(h_{m,up} - t_{f,up}) t_{w,up}^3 / 12$
6	$(4 - \pi) r_{c,up}^2 / 2$	$H_t - t_{f,up} - k_c r_{c,up}$	$0.0151 r_{c,up}^4$	$0.0151 r_{c,up}^4$
with $k_c = 1 - 2 / (12 - 3 \pi)$				

Table 4-1 : Characteristics of the elementary areas of a gross section

The total area of the gross section is obtained by the summation of each elementary part and it can be expressed by the following equation:

$$A_{gross} = \sum_{i=1}^6 a_i$$

The ‘static moment’ of the gross section relative to the bottom fibre is obtained by :

$$\mu_{gross} = \sum_{i=1}^6 z_i a_i$$

The position of the centre of gravity relative to the bottom fibre is given by :

$$z_{G,gross} = \mu_{gross} / A_{gross}$$

The second moment of area of the section about the major axis through the centre of gravity is given by :

$$I_{y,gross} = \sum_{i=1}^6 (I_{oy,i} + (z_i - z_{G,gross})^2 a_i)$$

The elastic modulus of the gross section is calculated for both the bottom ($W_{el,y,low}$) and top ($W_{el,y,up}$) fibres using :

$$W_{el,y,low} = \frac{I_{y,gross}}{z_{G,gross}}$$

$$W_{el,y,up} = \frac{I_{y,gross}}{H_t - z_{G,gross}}$$

The second moment of area of the section about the minor axis through the centre of gravity is given by:

$$I_{z,gross} = \sum_{i=1}^6 (I_{oz,i}) + a_3 (0.5 t_{w,low} + k_c r_{c,low})^2 + a_6 (0.5 t_{w,up} + k_c r_{c,up})^2$$

4.2.2 Geometry of the net section

The net section is defined at the location of an opening in a cellular beam (see Figure 4–24).

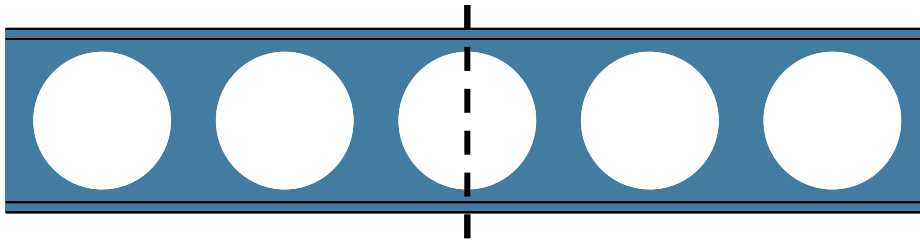


Figure 4–24 : Net section location

The elemental decomposition of the net section is shown in Figure 4–23(c). The characteristics of the elementary parts are these given in Table 4-1 of a gross section except those for the web (areas 2 and 5), for which the characteristics are defined as follows (see Figure 4–25 and Table 4-2):

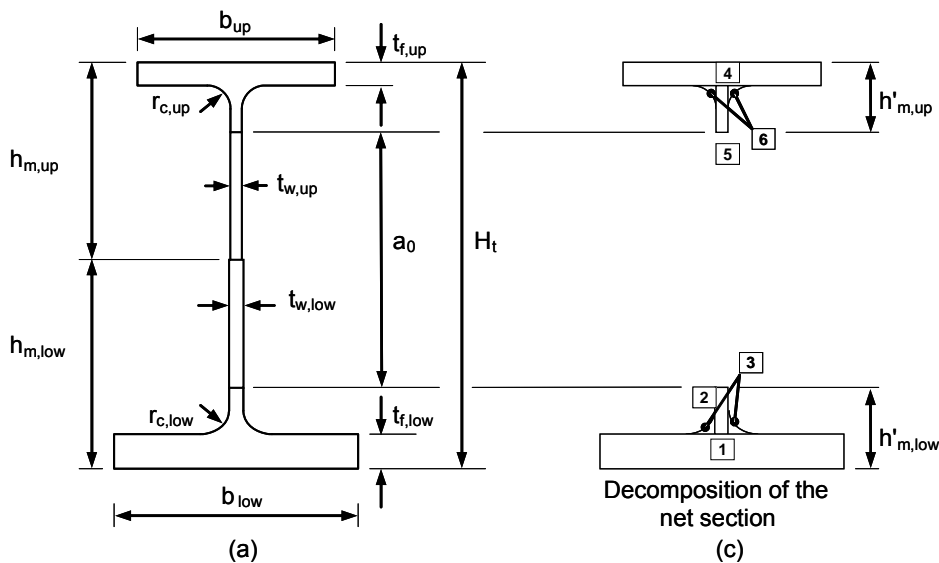


Figure 4–25 : Decomposition of the net section

i	a_i	z_i	$I_{oy,i}$	$I_{oz,i}$
2	$(h'_{m,low}-t_{f,low}) t_{w,low}$	$(h'_{m,low}+t_{f,low}) / 2$	$t_{w,low} (h'_{m,low}-t_{f,low})^3 / 12$	$(h'_{m,low}-t_{f,low}) t_{w,low}^3 / 12$
5	$(h'_{m,up}-t_{f,up}) t_{w,up}$	$H_t - (t_{f,up}+h'_{m,up})/2$	$t_{w,up} (h'_{m,up}-t_{f,up})^3 / 12$	$(h'_{m,up}-t_{f,up}) t_{w,up}^3 / 12$
with $h'_{m,low} = h_{m,low} - a_0/2$ and $h'_{m,up} = h_{m,up} - a_0/2$				

Table 4-2 : Characteristics of the elementary areas of the web of a net section

The total area of the net section is obtained by the summation of each elementary part and can be expressed by the following equation:

$$A_{net} = \sum_{i=1}^6 a_i$$

The 'static moment' of the net section relative to the bottom fibre is given by :

$$\mu_{net} = \sum_{i=1}^6 z_i a_i$$

The position of the centre of gravity of the net section relative to the bottom fibre is given by :

$$z_{G,net} = \mu_{net} / A_{net}$$

The second moment of area of the net section relative to the major axis through the centre of gravity is given by :

$$I_{y,net} = \sum_{i=1}^6 (I_{oy,i} + (z_i - z_{G,net})^2 a_i)$$

The second moment of area of the net section relative to the minor axis through the centre of gravity is given by:

$$I_{z,net} = \sum_{i=1}^6 (I_{oz,i}) + a_3 (0.5 t_{w,low} + k_c r_{c,low})^2 + a_6 (0.5 t_{w,up} + k_c r_{c,up})^2$$

4.2.3 Cross sectional characteristics of the members

At the location of a gross cross-section the area of the transverse sections is defined as :

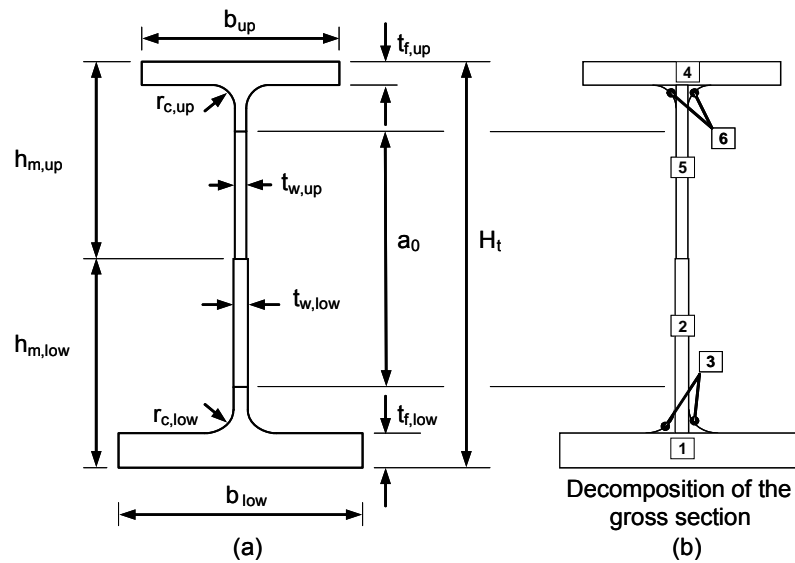


Figure 4-26 : Decomposition of the gross section

for the lower member :
$$A_{m,low} = \sum_{i=1}^3 a_i$$

for the upper member :
$$A_{m,up} = \sum_{i=4}^6 a_i$$

At the location of a gross cross-section the shear area is illustrated in Figure 4-27 and can be expressed by the following equations:

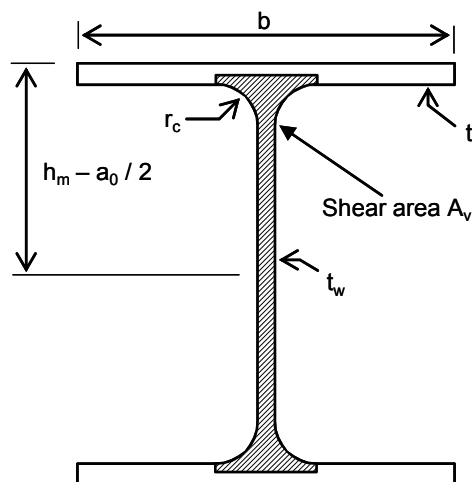


Figure 4-27 : Shear area of a 'T' at the location of a web post

- for the lower member,

$$A_{v,low} = t_{w,low} (h_{m,low} - t_{f,low}) + (2 - \pi/2) r_{c,low}^2 + t_{f,low} (t_{w,low} + 2 r_{c,low}) / 2$$

- for the upper member,

$$A_{v,up} = t_{w,up} (h_{m,up} - t_{f,up}) + (2 - \pi/2) r_{c,up}^2 + t_{f,up} (t_{w,up} + 2 r_{c,up}) / 2$$

4.2.4 Characteristics of an inclined section at the location of an opening

At the location of an opening the characteristics of a cross section inclined of an angle ϕ (see Figure 4–28) with respect to the vertical are determined considering the verification of resistance of this section, allowing for Vierendeel effects. This is done for either the upper or lower member.

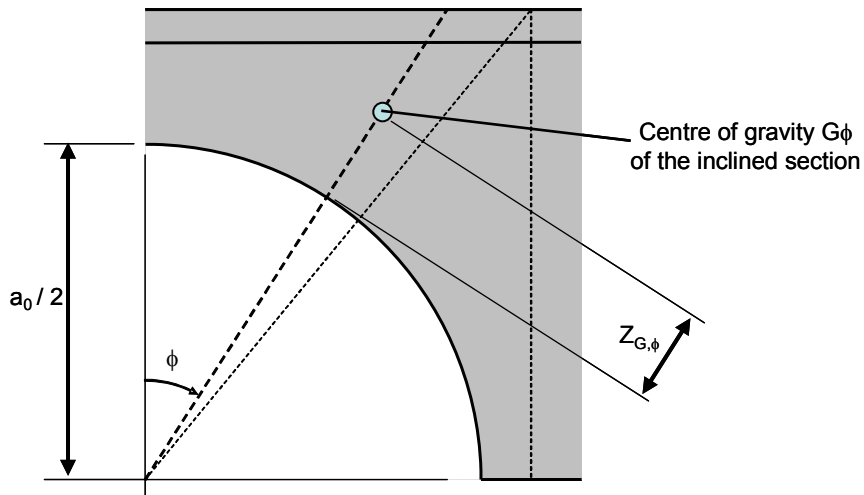


Figure 4–28 : Inclined section at the location of an opening

The expressions given below apply to both the upper and lower members.

The height of the inclined section is :

$$h_{\phi} = h_m / \cos\phi - a_0 / 2$$

The inclined section is decomposed into elements as shown in Figure 4–29. The characteristics of the elementary areas forming this cross-section are given in Table 4-3.

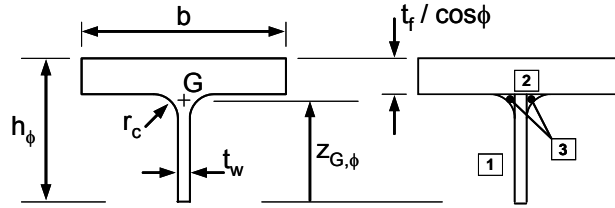


Figure 4-29 : Decomposition of a 'T' section

i	a_i	z_i	$I_{oy,i}$
1	$t_w (h_\phi - t_f / \cos \phi)$	$(h_\phi - t_f / \cos \phi) / 2$	$t_w (h_\phi - t_f / \cos \phi)^3 / 12$
2	$b t_f / \cos \phi$	$h_\phi - (t_f / \cos \phi) / 2$	$b (t_f / \cos \phi)^3 / 12$
3	$(4 - \pi) r_c^2 / 2$	$h_\phi - t_f / \cos \phi - k_c r_c$	$0.0151 r_c^4$
with $k_c = 1 - 2 / (12 - 3 \pi)$			

Table 4-3 : Characteristics of the elementary areas of an inclined section

The following parameters may be calculated

- the area of the section :

$$A_\phi = \sum_{i=1}^3 a_i$$

- the shear area :

$$A_{v,\phi} = a_1 + a_3 + 0.5 (t_w + 2 r_c) t_f / \cos \phi$$

- the 'static moment' of the net section relative to the edge of the opening :

$$\mu_\phi = \sum_{i=1}^6 z_i a_i$$

- the position of the centre of gravity of the section relative to the edge of the opening:

$$z_{G,\phi} = \mu_\phi / A_\phi$$

- the second moment of area relative to the centre of gravity of the section :

$$I_{y,\phi} = \sum_{i=1}^6 (I_{oy,i} + (z_i - z_{G,\phi})^2 a_i)$$

- the elastic moduli:

$$\text{for the bottom fibre,} \quad W_{el,\phi,low} = \frac{I_{y,\phi}}{z_{G,\phi} + t_r}$$

$$\text{for the top fibre,} \quad W_{el,\phi,up} = \frac{I_{y,\phi}}{h_\phi - z_{G,\phi}}$$

For the cross sectional characteristics of the members at the location of an opening corresponding to the specific case of $\phi = 0$, the following notation is used with the appropriate subscript “low” or “up” :

- area : A_0
- shear area: $A_{v,0}$
- position of the centre of gravity : $z_{G,0}$
- second moment of area : $I_{y,0}$

4.2.5 Calculation of forces considering Vierendeel action

The resistance of the section at the location of each opening is checked taking into account Vierendeel action (§ N.3.3.2.3 and Annex N of Eurocode 3) [60], for both the lower and upper members.

At the location of an opening the forces $N_{fi,Ed}$, $V_{fi,Ed}$ and $M_{fi,Ed}$ are distributed between the upper and lower members as follows :

- for the lower member,

$$N_{m,fi,Ed,low} = N_{fi,Ed} \frac{A_{0,low}}{A_{0,low} + A_{0,up}} - \frac{M_{fi,Ed}}{z_{G,0,up} + a_0 + z_{G,0,low}}$$

$$V_{m,fi,Ed,low} = V_{fi,Ed} \frac{A_{v,0,low}}{A_{v,0,low} + A_{v,0,up}}$$

- for the upper member,

$$N_{m,fi,Ed,up} = N_{fi,Ed} \frac{A_{0,up}}{A_{0,low} + A_{0,up}} + \frac{M_{fi,Ed}}{z_{G,0,up} + a_0 + z_{G,0,low}}$$

$$V_{m,fi,Ed,up} = V_{fi,Ed} \frac{A_{v,0,up}}{A_{v,0,low} + A_{v,0,up}}$$

The characteristics A_0 , $A_{v,0}$ and $z_{G,0}$ of the section of a member adjacent to an opening are calculated as indicated in Chapters 4.2.1 to 4.2.4.

The resistance of each section inclined at an angle ϕ is verified varying this angle from $-\phi_{\max}$ to $+\phi_{\max}$ by increment of 1° (see Figure 4–30).

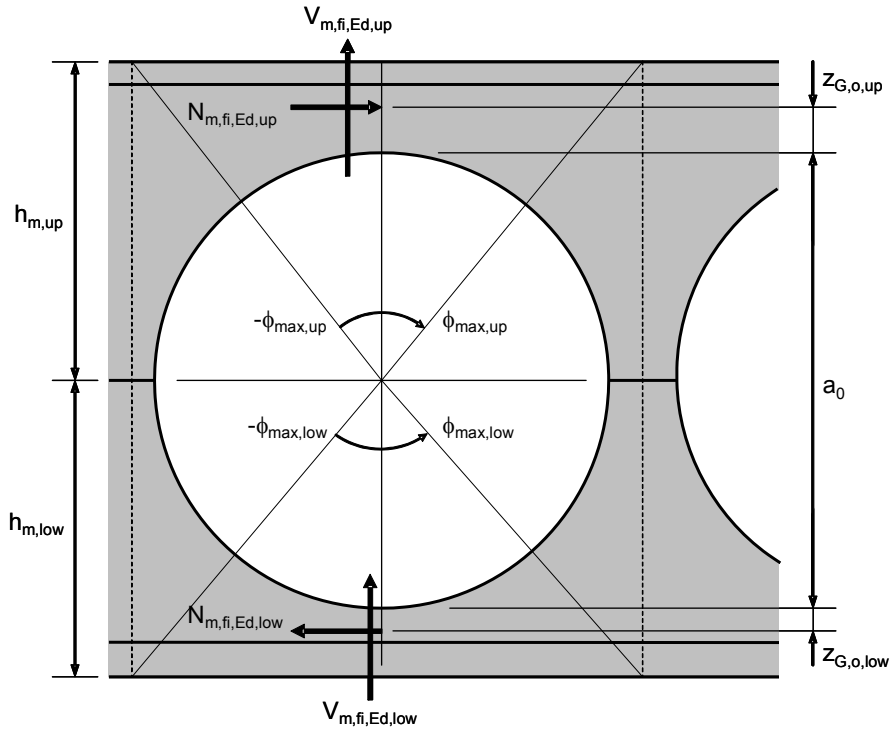


Figure 4–30 : Section of an opening with angle ϕ_{\max}

- for the lower member :
$$\phi_{\max} = \text{Arctg} \left(\frac{a_0 + w}{2 h_{m,\text{low}}} \right)$$
- for the upper member :
$$\phi_{\max} = \text{Arctg} \left(\frac{a_0 + w}{2 h_{m,\text{up}}} \right)$$

In the following expressions there is no distinction made between the upper and lower members. The forces acting on a section inclined at an angle ϕ are illustrated on the Figure 4–31.

$$N_{\phi,\text{fi},\text{Ed}} = N_{m,\text{fi},\text{Ed}} \cos \phi - V_{m,\text{fi},\text{Ed}} \sin \phi$$

$$V_{\phi,\text{fi},\text{Ed}} = N_{m,\text{fi},\text{Ed}} \sin \phi (A_{v,\phi} / A_{\phi}) + V_{m,\text{fi},\text{Ed}} \cos \phi$$

$$M_{\phi,fi,Ed} = N_{m,fi,Ed} (0.5 a_0 + z_{G,0} - (0.5 a_0 + z_{G,\phi}) \cos\phi) + V_{m,Ed} (0.5 a_0 + z_{G,\phi}) \sin\phi$$

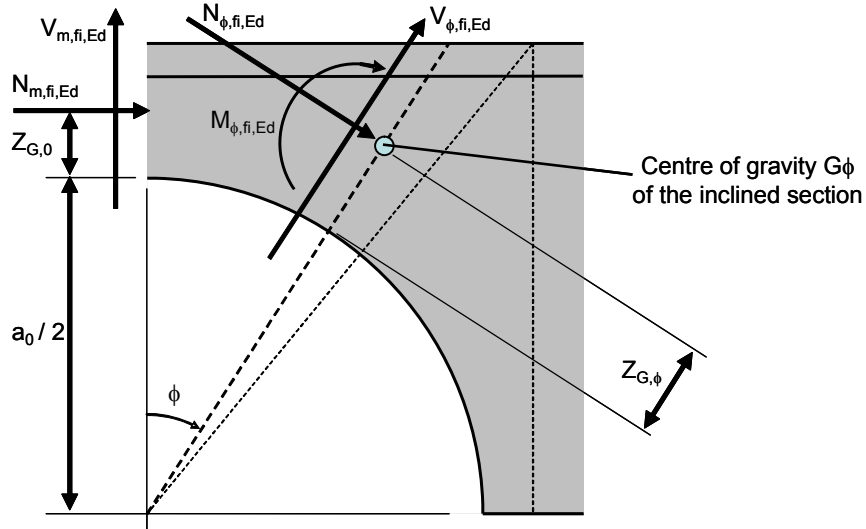


Figure 4-31 : Forces acting on an inclined section

4.2.6 Calculation of forces considering the thermal expansion of the flange and the web

In the UK, there is a rather rough prescriptive “rule” specified in BS5950 Part 8:1990 [20] for beams with web openings, stating that 20% of extra coating thickness is required in comparison with solid-web beams. This rough prescriptive rule was justified by the fact that the temperature of the web is higher than the temperature of the flange.

If the temperature of the web is higher than the temperature of the flanges, compression stresses will appear in the web, which will cause the web post buckling earlier than foreseen.

In order to verify this phenomenon, numerical simulations were performed using the software SAFIR (previously calibrated on furnace tests as described in Chapters 2 and 3).

The first numerical simulation was made using the geometry and measured temperature in the fire test A2 performed at the University of Ulster. In order to avoid influence of any boundary condition on the thermal calculation, the temperatures measured in various points during the tests at elevated temperature were directly introduced in the FEM model to simulate the behaviour of the cellular beams in hot conditions. The statical analysis was made without any loading on the beam (see Figure 4-32).

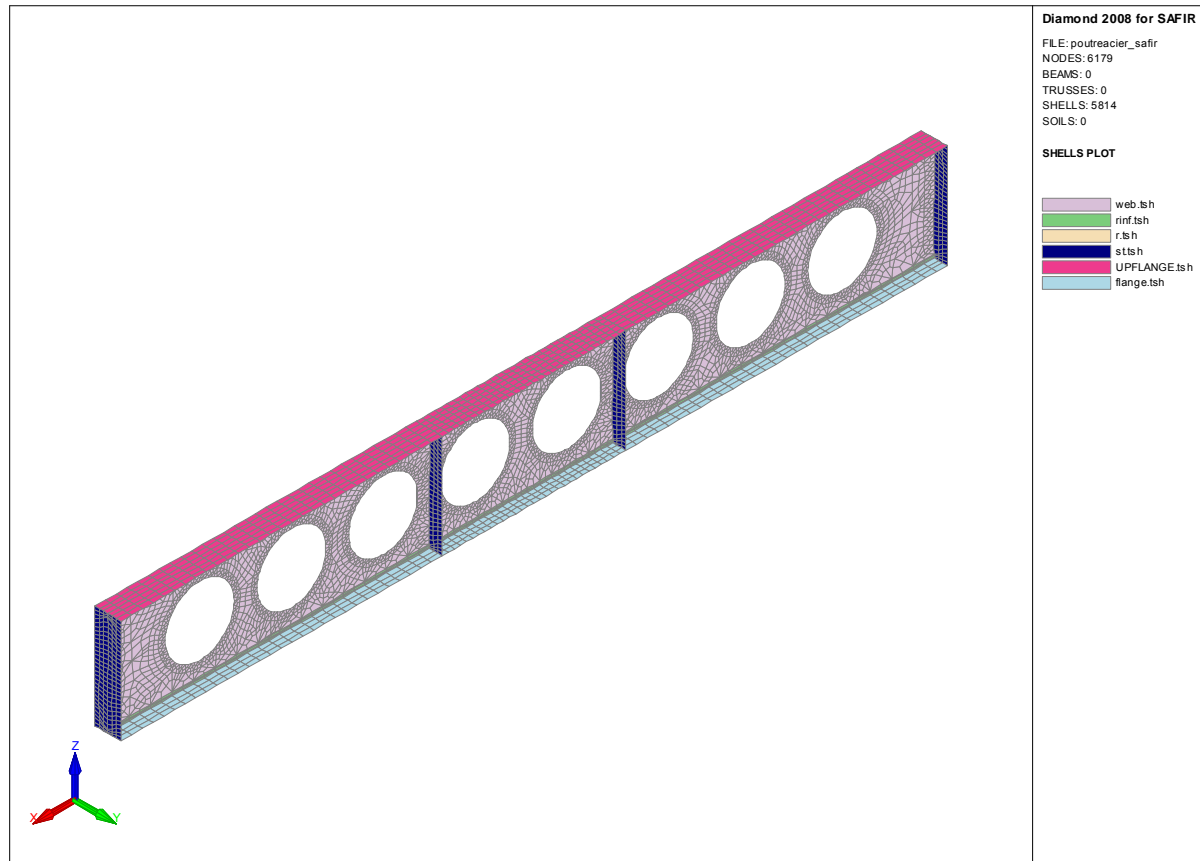


Figure 4–32 : Numerical model without loading

Such arrangement of the simulation enables isolation of the stresses that appeared in the beam due to the differences in thermal elongation between the flange and the web.

The results of the calculation show that compression stresses appeared in the web while tension stresses appeared in the flanges (see Figure 4–33).

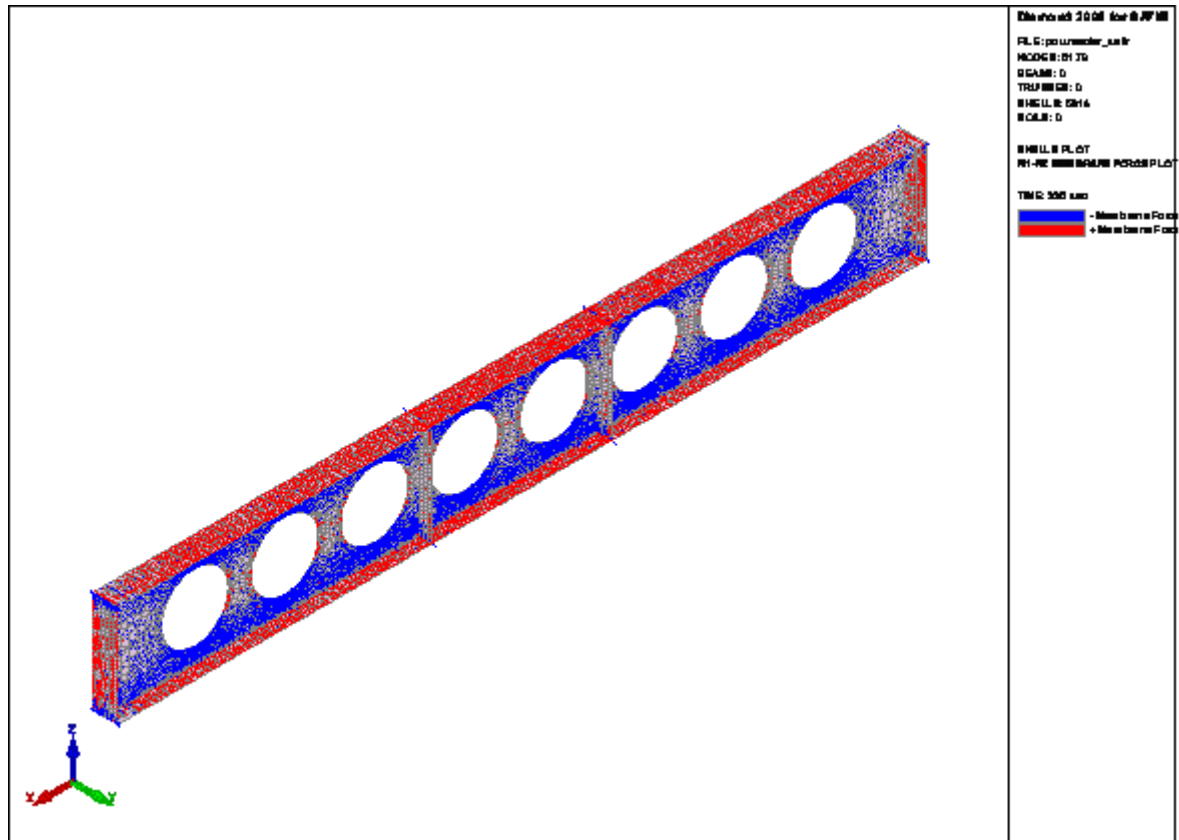


Figure 4-33 : Thermal stresses in cellular beam

Analysing the intensity and the position of the stresses, it could be concluded that, for this simulation made on the basis of the furnace test A2, the first thermal stresses appearing in the web of the beam are:

- not concentrated in the critical section for the web post buckling (see Figure 4–34)
- the stresses that appear in the critical section for the web post buckling are neglectable compared to the stresses induced by the statical loads.

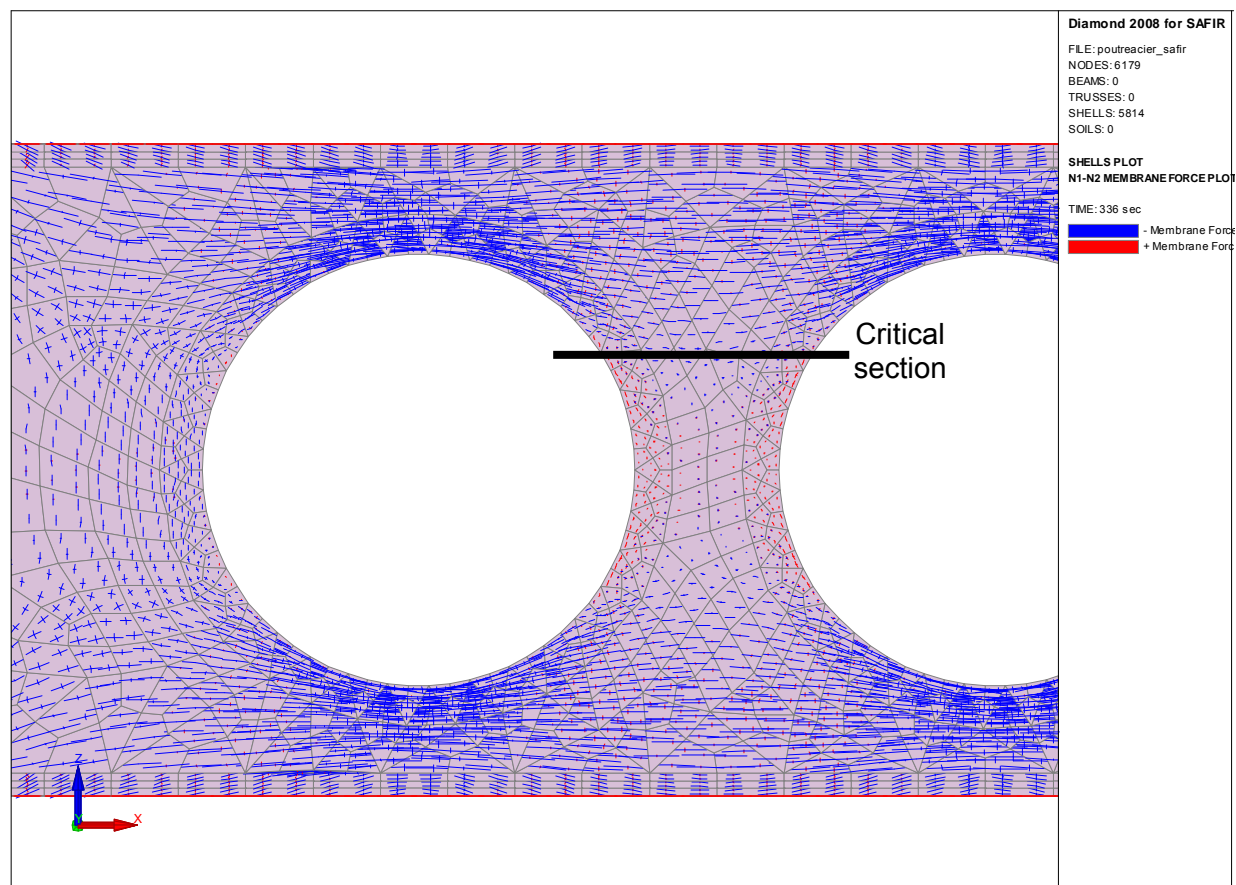


Figure 4–34 : Concentration of thermal stresses in cellular beam

This numerical simulation was performed on the basis of the thermal measurement made during the test A2 (test performed with a time-temperature curve that was not corresponding to the ISO curve).

It was decided that different numerical simulations will be made on the same basis but take into account a heating curve corresponding to the ISO-834 curve (see Figure 4–35).

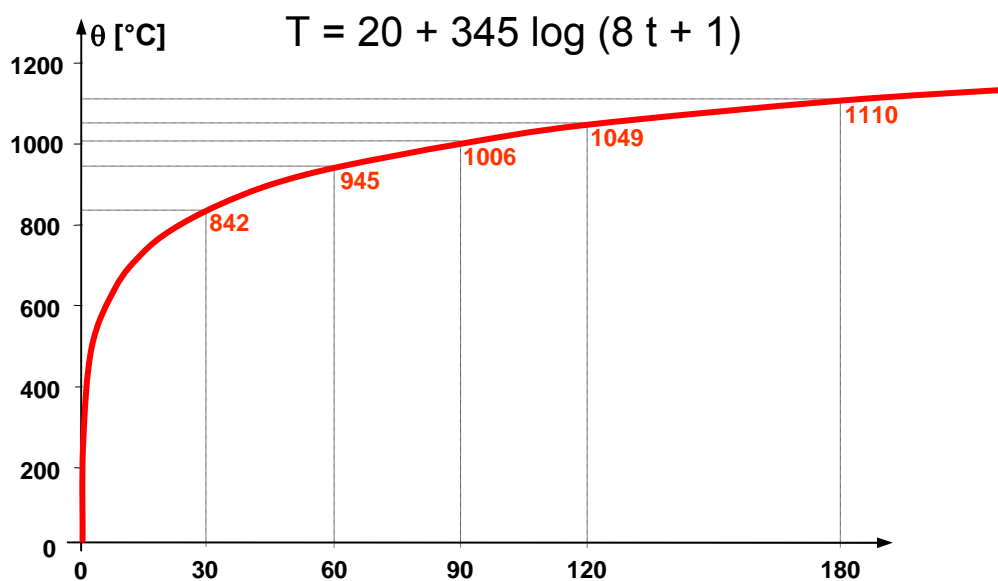


Figure 4–35 : ISO-834 curve

The heating calculation of the SHELL element was made by SAFIR with heating on both sides of the element (see Figure 4–36).

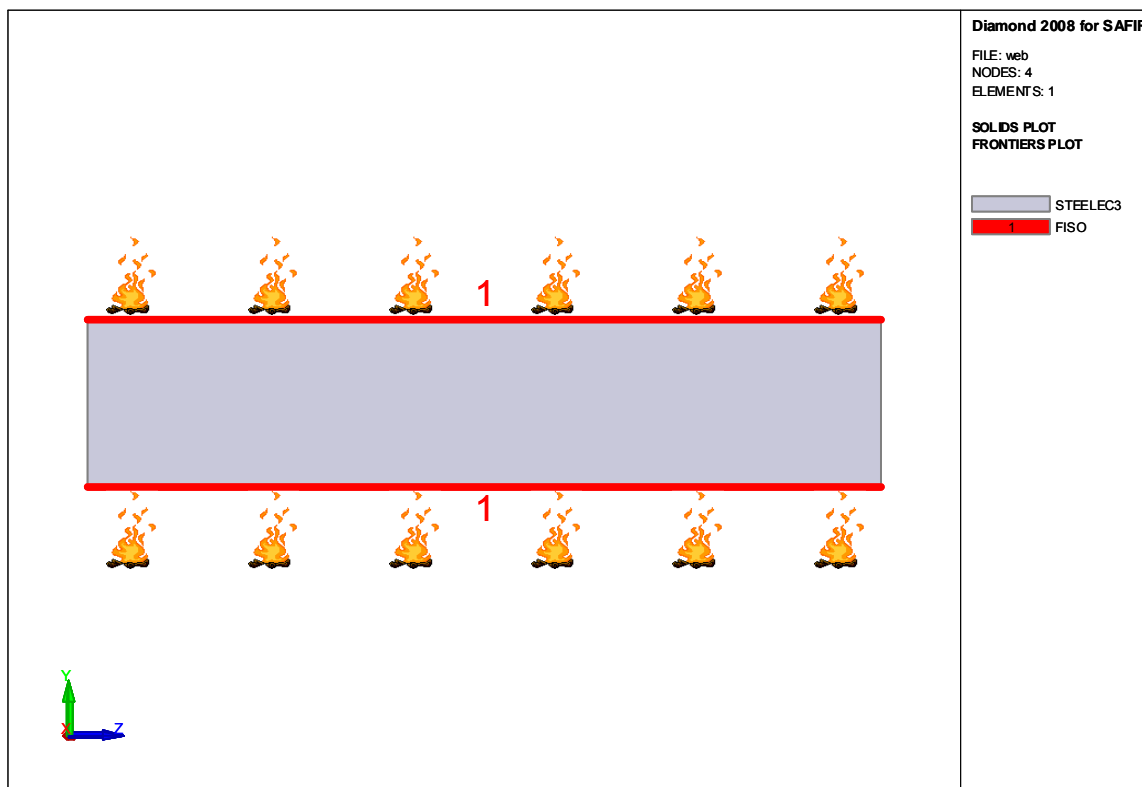


Figure 4–36 : Boundary condition of the SAFIR SHELL element

The exercise was made on a range of beam covering the limits of the ratio $\frac{\text{WebThickness}}{\text{FlangeThickness}}$.

The numerical simulations were made on the basis of :

- UB UB406X140X39 with a ratio of 0.74
- HD 400X421 with a ratio of 0.62
- HEM 360 with a ratio of 0.525 (smallest ration of the entire ArcelorMittal catalogue for hot rolled sections)

The results of these different numerical simulations indicated the same tendency as the first simulation. The compression stresses that appeared in the web at the location of the critical section for web post buckling are neglectable.

But it can be seen that significant stresses appeared in the section of the 'T's. The amount of stresses in this area can be critical for the Vierendeel bending (see Figure 4–37, Figure 4–38 and Figure 4–39)

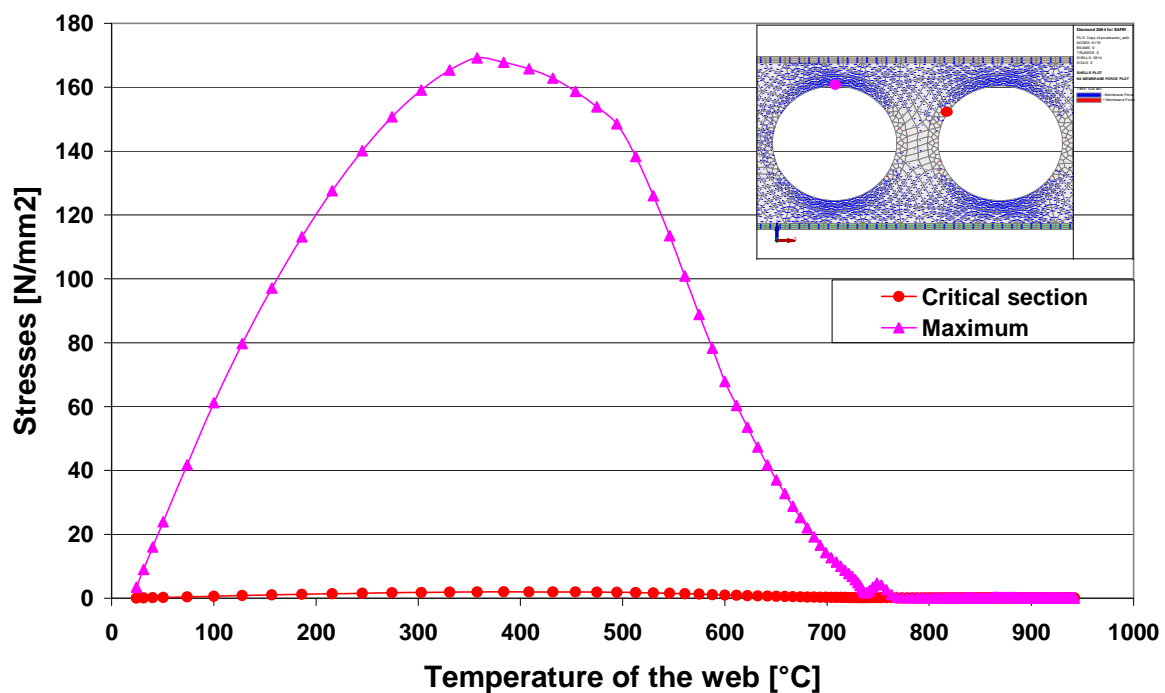


Figure 4–37 : Stresses results for the UB section

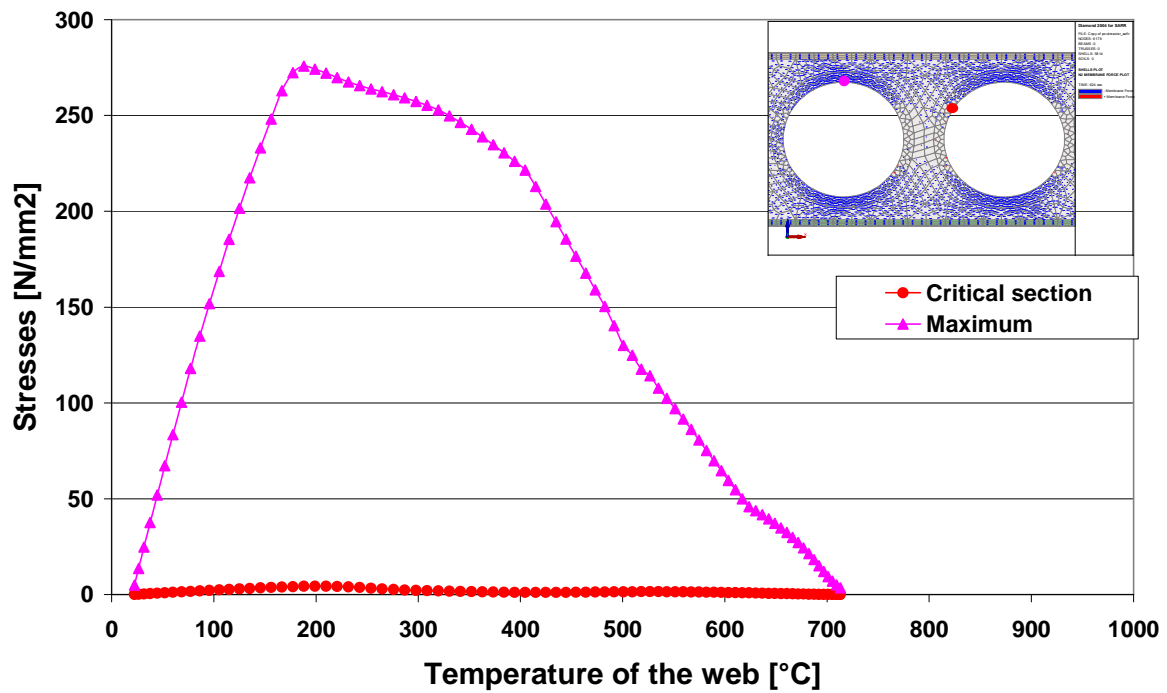


Figure 4–38 : Stresses results for the HD section

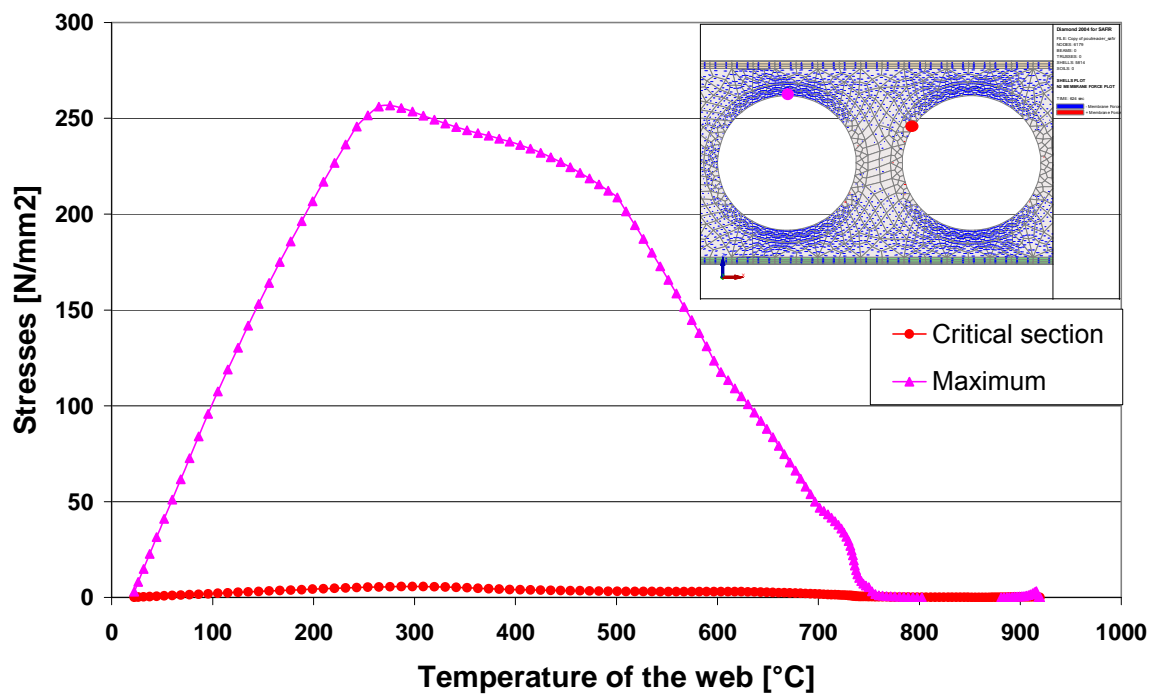


Figure 4–39 : Stresses results for the HEM section

4.2.7 Development of an analytical model for the evaluation of stresses due to thermal expansion

Some hypothesis have been done for the elaboration of this analytical model :

- simplification of the geometry

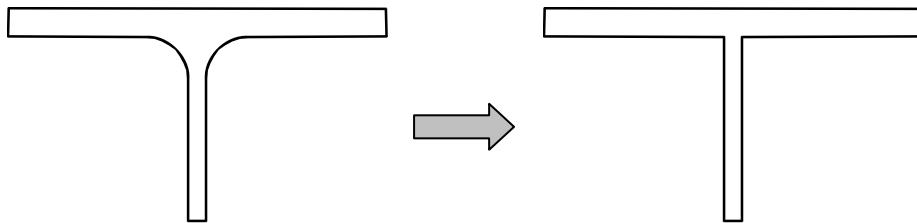


Figure 4-40 : Simplified geometry

- the model will be fully elastic without instability.

In order to evaluate the thermal stresses that are caused by the thermal expansion, it is necessary to understand what physically happens in the 'T' section during heating :

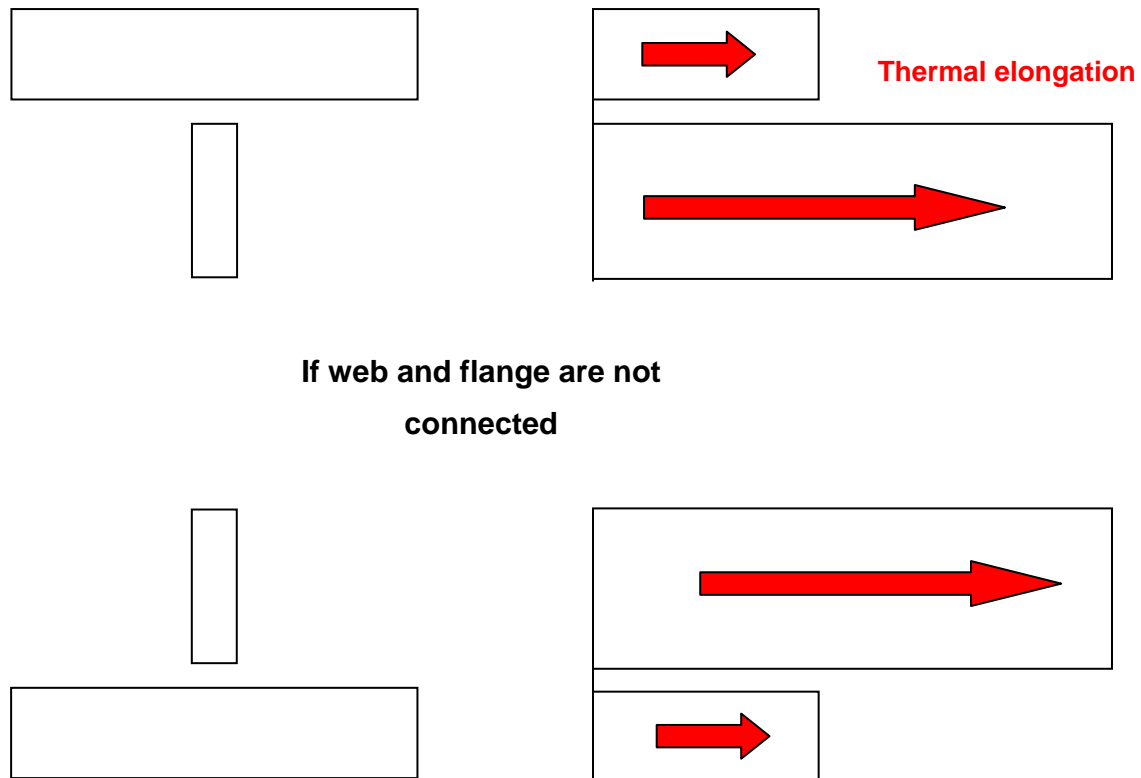
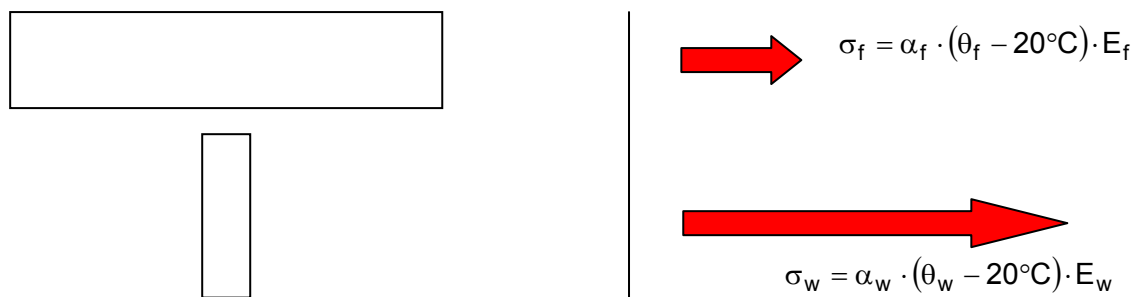


Figure 4-41 : Free thermal elongation

In a hot rolled section, the thickness of the flange is always bigger than the thickness of the web. So, when the profile is heated, the temperature of the web is higher than the temperature of the flange.

If the web and the flange are fully restrained, the axial force increases proportionally with the variation of temperature in the steel. Compression stresses appear in the steel members.



If web and flange are fully restrained

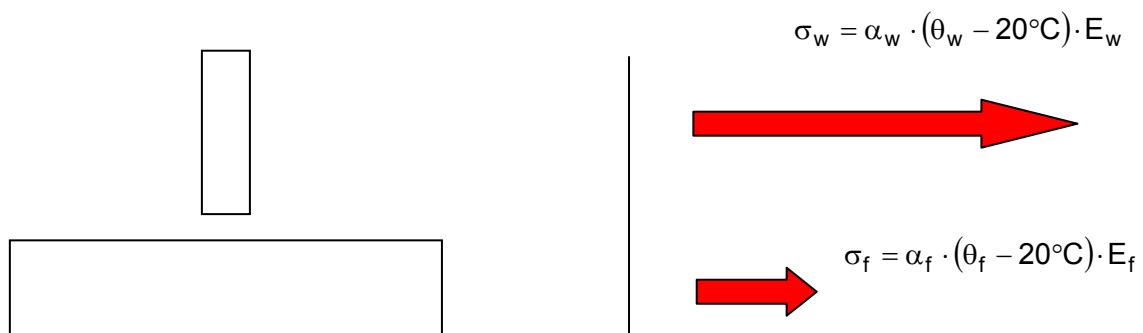


Figure 4–42 : Axial force due to fully restrained web and flange

$$\sigma_f = \alpha_f \cdot (\theta_f - 20^\circ\text{C}) \cdot E_f \quad (\text{Compression stresses in the flange})$$

$$\sigma_w = \alpha_w \cdot (\theta_w - 20^\circ\text{C}) \cdot E_w \quad (\text{Compression stresses in the web})$$

With :

α = coefficient of thermal elongation for the steel

θ = temperature of the steel member (flange or web)

E = Young modulus

Now if the flange and the web are connected and if the assumption that the entire section (the 'T') can expand freely is made, a position of equilibrium will be found between the free elongation of the flange and the free elongation of the web (see Figure 4–43).

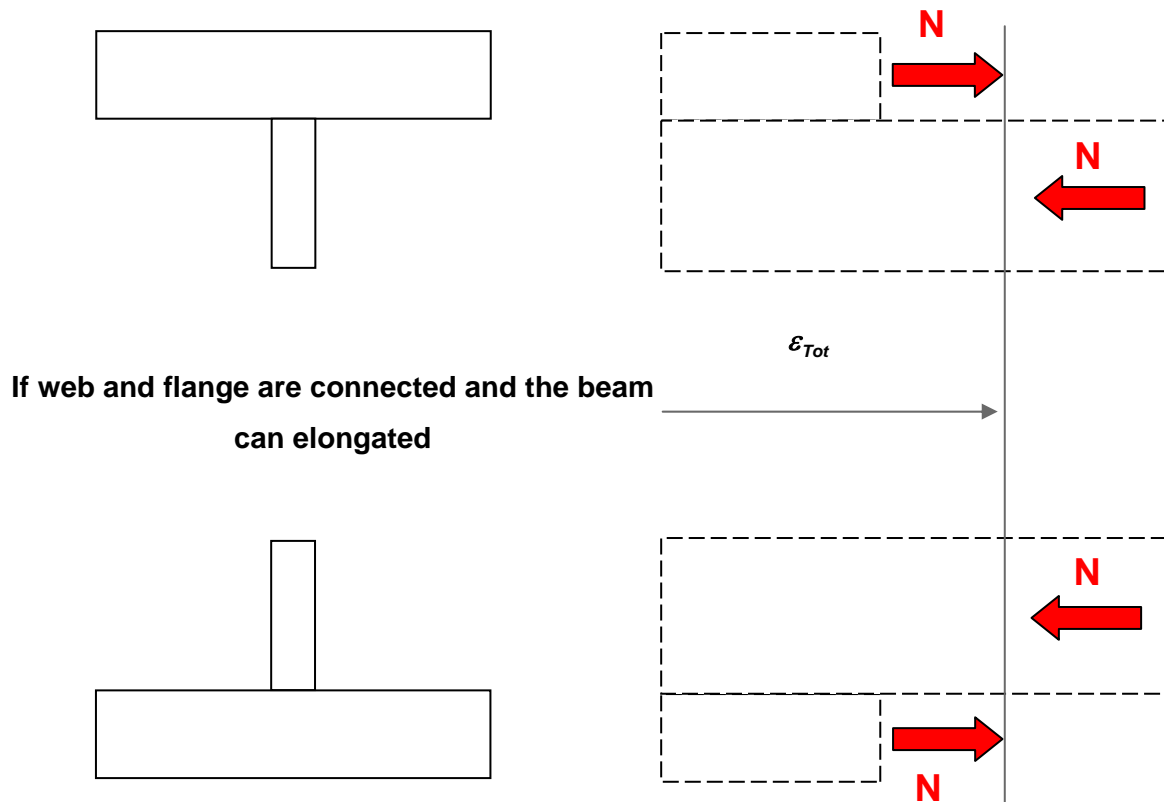


Figure 4–43 : Elongation of the 'T' taking into account web and flange

An axial force will appear in the web and in the flange. The equilibrium will be obtained when the axial force in the web is equal to the axial force in the flange.

The objective of this model is the evaluation of the stresses in the lower part of the web (see Figure 4–44) :

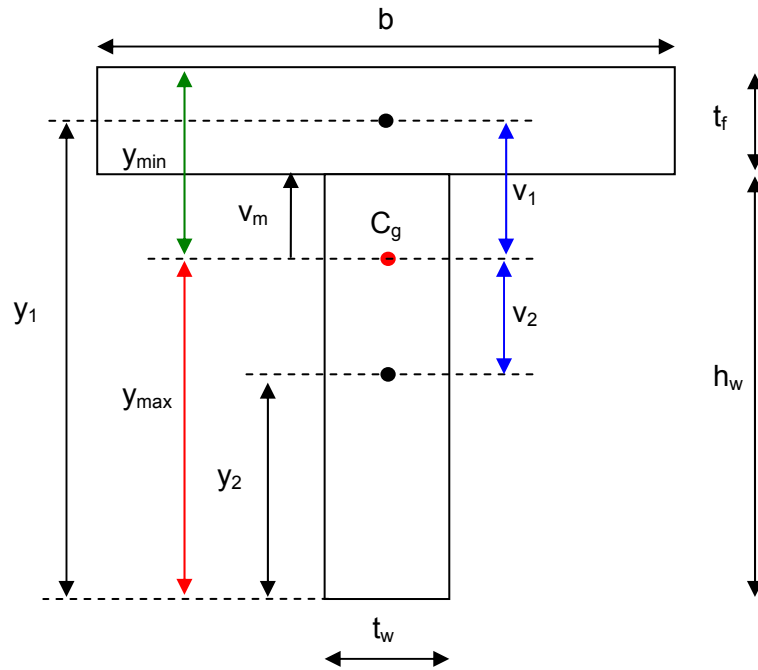


Figure 4-44 : Geometrical description of the 'T' section

At the interface between the flange and the web, the elongation in the flange is equal to the elongation in the web.

$$\varepsilon_{Tot} = \frac{A_f \cdot E_f \cdot \varepsilon_f + A_w \cdot E_w \cdot \varepsilon_w}{A_f \cdot E_f + A_w \cdot E_w}$$

From this value of ε_{Tot} , it is now easy to deduce the stresses in the lower part of the web :

$$\sigma_w = (\varepsilon_w - \varepsilon_{Tot}) \cdot E_w$$

$$\sigma_w = \left(\varepsilon_w - \frac{A_f \cdot E_f \cdot \varepsilon_f + A_w \cdot E_w \cdot \varepsilon_w}{A_f \cdot E_f + A_w \cdot E_w} \right) \cdot E_w$$

This analytical model, for the evaluation of the thermal stresses, has been compared to the stresses extracted from the numerical simulations performed in the Chapter 4.2.6.

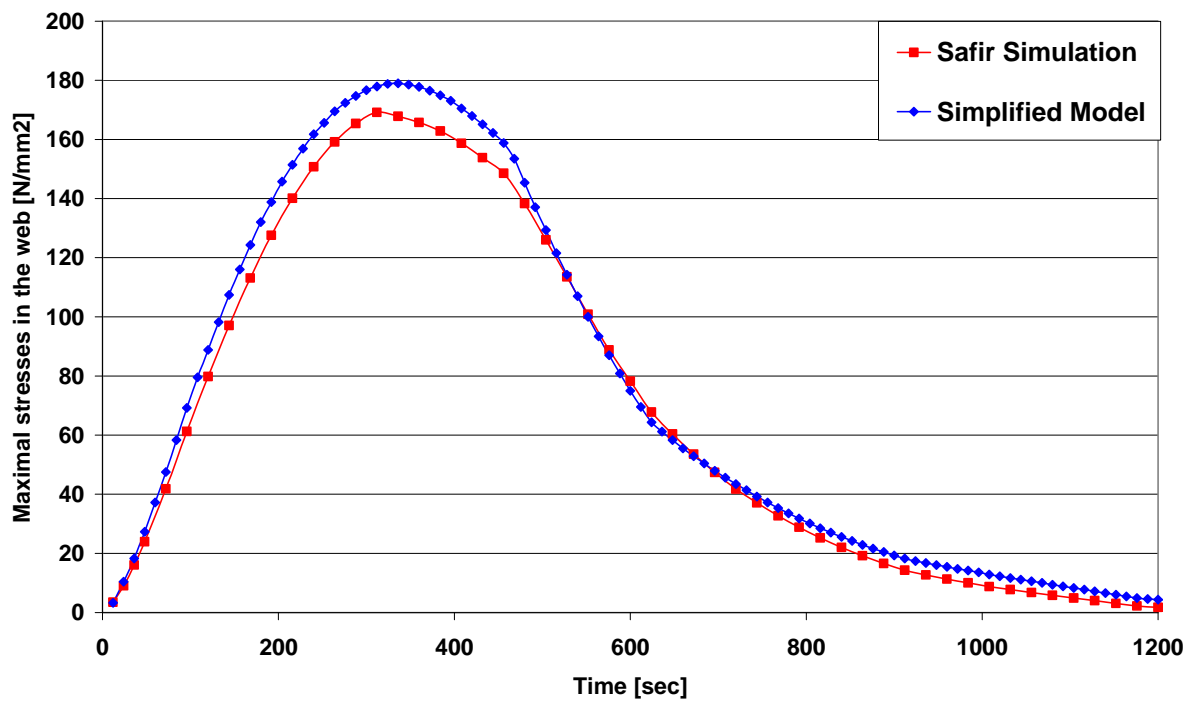


Figure 4–45 : Thermal stresses for UB section

As it can be seen on the Figure 4–45 here above, the analytical model predicts accurately the maximum stress intensity that is induced in the web by thermal expansion in “normal” profiles.

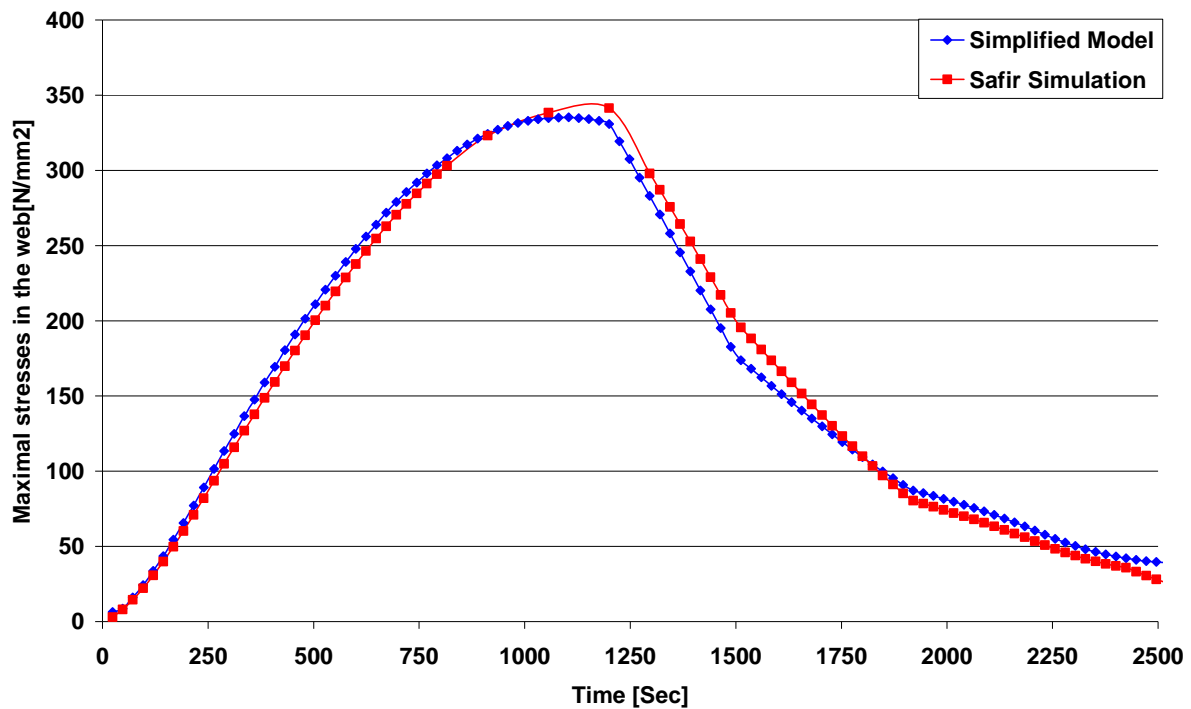


Figure 4-46 : Thermal stresses for a critical HD section

As shown in the Figure 4-46 here above, the analytical model can predict accurately the maximum stress intensity that is induced in the web by thermal expansion of thick profiles.

After the analyses of this phenomenon and quantification of the stress intensity, it can be concluded that:

- the value of the stresses that appear in the web can be equal to the steel strength limit
- the intensity of the stresses depends on the ratio web/flange
- the intensity increases with the heating velocity

For “normal profiles”, profiles used commonly as beam in the construction market for roofing and slabs (IPE, HEA, HEB), the intensity of these stresses can be high even in a low range of temperature.

This thermal elongation intensity varies with the value of the Young modulus. The Young modulus decreases quickly with the temperature (see Figure 4-47) :

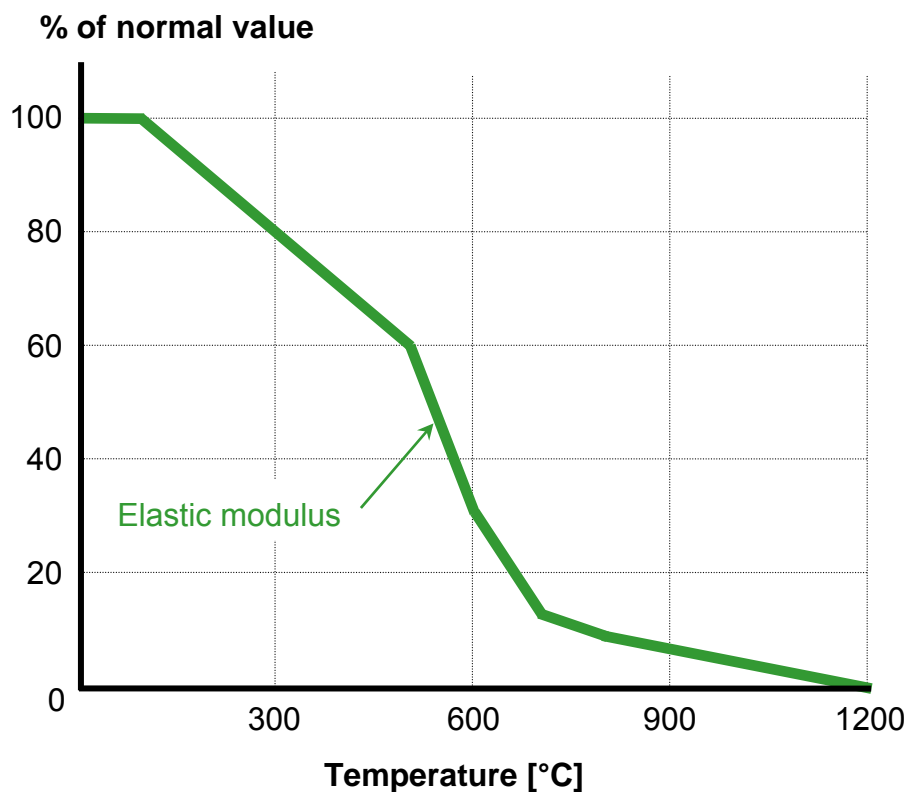


Figure 4–47 : Decrease of the Young modulus with the temperature

In the case of the Vierendeel bending, the critical temperatures are often higher than 600°C. So, the interaction between the thermal stresses and the stresses developed due to the loading, is really small in this range of temperature. Additionally, this simplifies the model for thermal stresses is an elastic model. In a 'T' section, the difference between M_{el} and M_{pl} is important.

In conclusion, for “normal profiles” (IPE, HEA and HEB), the intensity of the thermal stresses is too small to induce the failure of the beam in a low range of temperature. It is also too small to be combined with the stresses developed around the critical temperature due to the loading.

This effect of the thermal stresses could nevertheless damage locally the beam and some local yielding could appear between (100°C and 300°C) if the velocity of heating is high (ISO or Hydrocarbon fire curve). This local yielding will not affect the global stability of the beam but could be an issue for the rehabilitation of the building after a fire.

For “heavy profiles”, profiles that are not used commonly as beam in the construction market for roofing and slab (HEM, HD,...), the intensity of this stresses can be really high in a low

range of temperature. It is common to reach the steel strength limit at the lower part of the web around 250°C in case of ISO fire curve.

But these profiles are thick sections and their web is always Class 1 or Class 2. In this case, we can always reach M_{pl} in the 'T' section before endanger the stability of the beam. In such 'T', the difference between M_{pl} and M_{el} is so big that the thermal stresses could never cause the failure of the beam.

As for the "normal profiles", this thermal elongation intensity varies with the value of the Young modulus. The Young modulus decreases quickly with the temperature and the stresses are small around the critical temperature.

In conclusion, for "heavy profiles" (HEM, HD...), the intensity of the thermal stresses is too small to induce the failure of the beam in a low range of temperature and it is also too small to be combined with stresses developed around the critical temperature due to the loading.

It is important to highlight the fact that these conclusions are only valid for hot rolled sections. Moreover, in hot rolled sections, the root fillet ensures a better transition between the temperature of the flange and the temperature of the web, decreasing this effect at the interface between the web and the flange.

It can also be noted that in case of a welded section; an important shear force will appear in the welding between the web and the flange. This shear force is equal to the value of N calculated in Chapter 4.2.7.

In EC3 part 1-2 [64], it is described that the decrease of steel strength properties in the welding is quicker than in the carbon steel properties.

A failure mode by thermal shear in the welding between the web and the flange could be the most critical failure mode in welded cellular beams. This failure mode is not covered and will not be studied in the scope of this research focused on hot rolled sections.

4.2.8 Cross section classification of a member at a web opening

For the purpose of simplified rules the cross sections may be classified as for a normal temperature design with a reduce value for ε as given in [64].

$$\varepsilon = 0.85 \cdot \sqrt{\frac{235}{f_y}}$$

At the location of an opening the section classification for each member is determined for an angle $\phi = 0^\circ$.

For a steel beam each member cross section is either totally in tension, or totally in compression. In the first case, the plastic resistance is used. In the latter case, the classification is determined for pure compression, being the highest class of either the flange, the web or, if applicable, the stiffener.

According to EN1993-1-1 [55] :

$$c = 0.5 \cdot (b - t_w) - r_c$$

For a member in compression the flange is :

- Class 1 if $c / t_f \leq 9 \varepsilon$
- Class 2 if $c / t_f \leq 10 \varepsilon$
- Class 3 if $c / t_f \leq 14 \varepsilon$
- Class 4 if $c / t_f > 14 \varepsilon$

In case of an opening, which is not stiffened, the class of the web is determined according to paragraph N.1.7.2(3) of Annex N of Eurocode 3 [60]. The web is :

- Class 2 if $0.7 a_0 \leq 32 \varepsilon t_w$

$$\text{where } h_{\phi=0} - t_f \leq \frac{10 \varepsilon t_w}{\sqrt{1 - \left(\frac{32 \varepsilon t_w}{0.7 a_0} \right)^2}}$$

- Class 3 if $0.7 a_0 \leq 36 \varepsilon t_w$

$$\text{where } h_{\phi=0} - t_f \leq \frac{14 \varepsilon t_w}{\sqrt{1 - \left(\frac{36 \varepsilon t_w}{0.7 a_0} \right)^2}}$$

- Class 4 if the conditions for Class 3 are not satisfied.

Cellular beams having a member at an opening that has a Class 4 web are outside the scope of application of the model. Consequently, only the flange may be Class 4 for a steel beam.

4.2.9 Verification of the resistance of an inclined section

The resistance of each inclined section is verified (as a function of the classification of the member determined for $\phi = 0^\circ$) under axial force $N_{\phi,fi,Ed}$ and bending moment $M_{\phi,fi,Ed}$, considering that :

- the plastic resistance for sections are Class 1 or 2,
- the elastic resistance for sections are Class 3,
- the elastic resistance of the effective section for sections are Class 4.

The characteristics of the inclined section are calculated using the expressions given in Chapter 4.2.4.

If the flange is Class 4, the effective width is calculated as for $\phi = 0^\circ$ when calculating these characteristics. In EN 1993-1-2:2005 [55] it is advised that the effective cross section area and the effective section modulus should be determined based on the material properties at 20°C.

Following this assumption, this effective width is :

$$b_{eff} = \rho b$$

$$\text{with : } \rho = (\lambda - 0.22) / \lambda^2$$

$$\lambda = \frac{b / 2}{28.4 \varepsilon t_f \sqrt{k_\sigma}}$$

$$k_\sigma = 0.43$$

$$\text{With } \varepsilon = \sqrt{\frac{235}{f_y}} \text{ as in cold situation.}$$

The reduction factor for the design yield strength of carbon steel relative to the yield strength at 20°C may be taken from Table 4-4 as illustrated in Figure 4-48:

Temperature [°C]	Reduction factor $k_{p0,2,\theta}$ class 4
20	1.000
100	1.000
150	0.890
200	0.780
300	0.650
400	0.530
500	0.300
600	0.130
700	0.070
800	0.050
900	0.030
1000	0.020

Table 4-4 : Strength reduction factors for the design of class 4

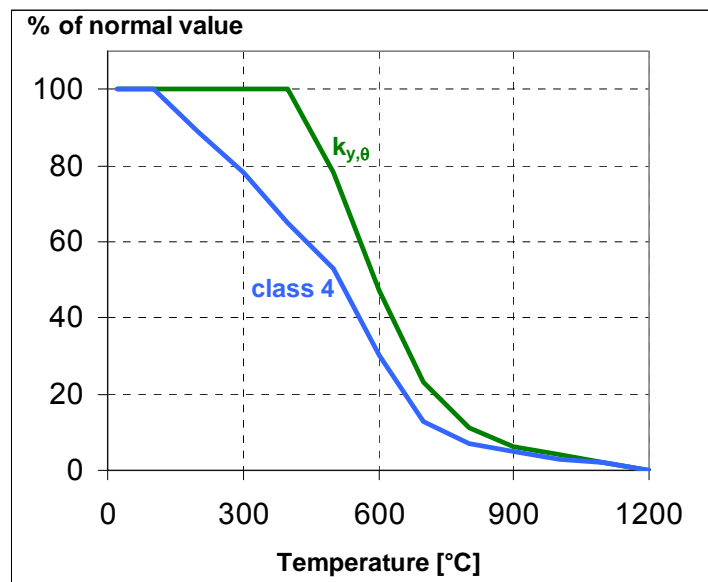


Figure 4-48 : Strength reduction factors for the design of class 4 vs effective yield strength

The influence of shear force on the bending resistance is taken into account only when the applied shear force $V_{\phi,fi,Ed}$ exceeds half of the plastic shear resistance $V_{pl,fi,Rd}$.

For a section inclined at an angle ϕ the expression for the axial load design resistance is :

- for sections of Class 1, 2 or 3 : $N_{c,fi,Rd} = A_{\phi} \cdot k_{y,\theta} \cdot f_y / \gamma_{M,fi}$
- for sections of Class 4 : $N_{c,fi,Rd} = A_{\phi,eff} \cdot k_{p0,2,\theta} \cdot f_y / \gamma_{M,fi}$

The criterion for resistance to axial load is defined by : $\Gamma_N = \frac{|N_{\phi,fi,Ed}|}{N_{c,fi,Rd}}$

For a section inclined at an angle ϕ the expression for the shear force design resistance is :

$$V_{pl,fi,Rd} = 0.577 A_{v,\phi} \cdot k_{y,\theta} \cdot f_y / \gamma_{M,fi}$$

The criterion for resistance to shear force is defined by : $\Gamma_V = \frac{|V_{\phi,fi,Ed}|}{V_{pl,fi,Rd}}$

For a section inclined at an angle ϕ the expression for the flexural bending design resistance is:

- for sections of Class 1 or 2, $M_{c,fi,Rd} = W_{pl,\phi} \cdot k_{y,\theta} \cdot f_y / \gamma_{M,fi}$
- for sections of Class 3, $M_{c,fi,Rd} = \min (W_{el,\phi,low} ; W_{el,\phi,up}) \cdot k_{y,\theta} \cdot f_y / \gamma_{M,fi}$
- for sections of Class 4, $M_{c,fi,Rd} = \min (W_{eff,\phi,low} ; W_{eff,\phi,up}) \cdot k_{p0,2,\theta} \cdot f_y / \gamma_{M,fi}$

The criterion for resistance to flexural bending is defined by: $\Gamma_M = \frac{|M_{\phi,fi,Ed}|}{M_{c,fi,Rd}}$

For a section inclined at an angle ϕ the expression for the combined axial load and bending design resistance is:

- for sections Class 1 or 2 linear interaction is considered,

$$\Gamma_{MN} = \frac{|N_{\phi,fi,Ed}|}{A_{\phi} k_{y,\theta} f_y / \gamma_{M,fi}} + \frac{|M_{\phi,fi,Ed}|}{W_{pl,\phi} k_{y,\theta} f_y / \gamma_{M,fi}}$$

- for sections Class 3,

$$\Gamma_{MN} = \frac{\max(|\sigma_{fi,low}| ; |\sigma_{fi,up}|)}{k_{y,\theta} f_y / \gamma_{M,fi}}$$

with : $\sigma_{fi,low} = \frac{N_{\phi,fi,Ed}}{A_{\phi}} - \frac{M_{\phi,fi,Ed}}{W_{el,\phi,low}}$ and $\sigma_{fi,up} = \frac{N_{\phi,fi,Ed}}{A_{\phi}} + \frac{M_{\phi,fi,Ed}}{W_{el,\phi,up}}$

- for sections Class 4,

$$\Gamma_{MN} = \frac{\max(|\sigma_{fi,low}| ; |\sigma_{fi,up}|)}{k_{p0,2,\theta} f_y / \gamma_{M,fi}}$$

$$\text{with : } \sigma_{fi,low} = \frac{N_{\phi,fi,Ed}}{A_{\phi,eff}} - \frac{M_{\phi,fi,Ed}}{W_{eff,\phi,low}} \quad \text{and} \quad \sigma_{fi,up} = \frac{N_{\phi,fi,Ed}}{A_{\phi,eff}} + \frac{M_{\phi,fi,Ed}}{W_{eff,\phi,up}}$$

The influence of shear force on moment resistance is taken into account when the applied shear $V_{fi,Ed}$ exceeds half of the plastic shear resistance :

$$|V_{fi,Ed}| > 0.5 V_{pl,fi,Rd}$$

In such a case, the moment resistance $M_{NV,fi,Rd}$ of the section is calculated taking into account the presence of both axial force $N_{fi,Ed}$ and shear force $V_{fi,Ed}$. A plastic distribution of stresses is assumed. The effect of the shear force is considered by adopting a reduced yield strength over the shear area, which is assumed to be limited to the web and root radii.

A reduced yield strength is calculated for both the lower and upper members, assuming that the applied shear is distributed between the two in proportion to the relative shear areas :

$$\text{- for the lower member,} \quad (1 - \rho_{low}) k_{y,\theta} f_{y,low}$$

$$\text{with : } \rho_{low} = \left(\frac{2 |V_{fi,Ed}| A_{v,low} / (A_{v,low} + A_{v,up})}{0.577 A_{v,low} k_{y,\theta} f_{y,low} / \gamma_{M,fi}} - 1 \right)^2$$

$$\text{- for the upper member,} \quad (1 - \rho_{up}) k_{y,\theta} f_{y,up}$$

$$\text{with : } \rho_{up} = \left(\frac{2 |V_{fi,Ed}| A_{v,up} / (A_{v,low} + A_{v,up})}{0.577 A_{v,up} k_{y,\theta} f_{y,up} / \gamma_{M,fi}} - 1 \right)^2$$

When it is necessary to consider the influence of shear force on the section resistance the following interaction criteria are determined:

$$\text{- axial force – shear } \Gamma_{NV} ,$$

$$\Gamma_{NV} = \frac{|N_{\phi,fi,Ed}|}{N_{V,fi,Rd}}$$

where $N_{V,fi,Rd}$ is the axial resistance reduced due to the presence of shear force.

$$\text{- bending moment – shear force } \Gamma_{MV} ,$$

$$\Gamma_{MV} = \frac{|M_{\phi,fi,Ed}|}{M_{V,fi,Rd}}$$

where $M_{V,fi,Rd}$ is the plastic moment resistance reduced due to the presence of shear force.

- bending moment – axial force – shear force Γ_{MNV} ,

$$\Gamma_{MNV} = \Gamma_{NV} + \Gamma_{MV}$$

Note: when the shear force is less than 50% of the plastic shear resistance, the following occurs:

- $\Gamma_{NV} = \Gamma_N$,
- $\Gamma_{MV} = \Gamma_M$,
- $\Gamma_{MNV} = \Gamma_{MN}$.

Chapter 5

Validation of the analytical model

5. Validation of the analytical model

In order to validate the web post buckling model and the models for other failure mode, a parametrical study will be made on different cellular beams and the results of the models will be compared with the results of the FEM software SAFIR.

The numerical model created in SAFIR has been calibrated as described in Chapters 2 and 3. The results obtained from this model will be therefore used as reference.

The simplified models are based on Eurocodes principles and will be validated using a fire curve based on the ISO-834 curve (see Figure 5–1).

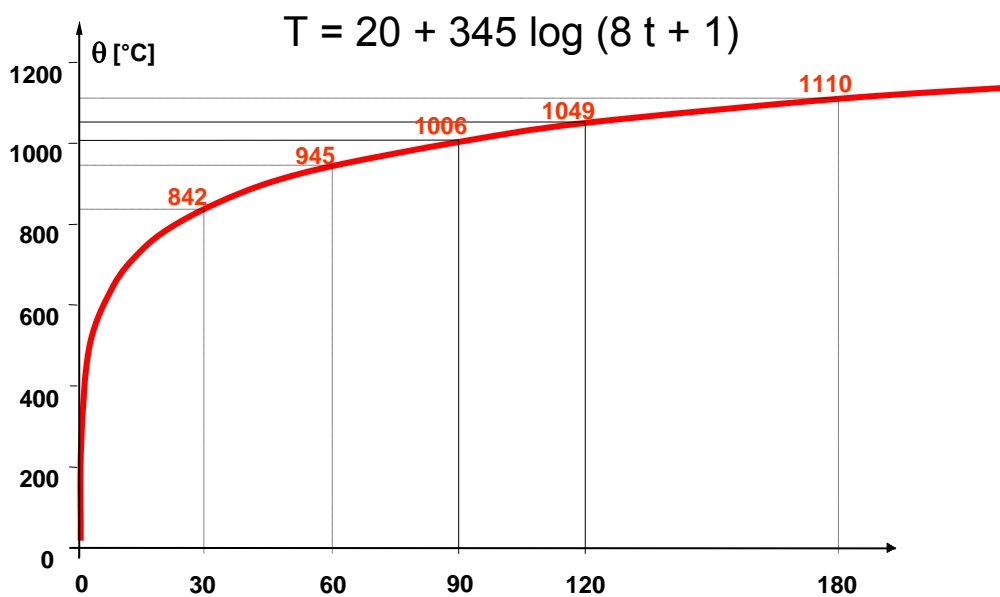


Figure 5–1 : ISO 834-curve

The validation was made using an ISO curve but the results of the simplified models are critical temperatures of the analysed sections ; so these models are also valid for other type of heating curves.

5.1 Web post buckling model

5.1.1 Web post buckling in pure steel section

Before starting the parametrical study, it is needed to define what will be considered as a web post buckling failure for the FEM software SAFIR.

The web post buckling failure can be identified by:

- the shape of the beam of the numerical simulation (see Figure 5–2 and Figure 5–3)

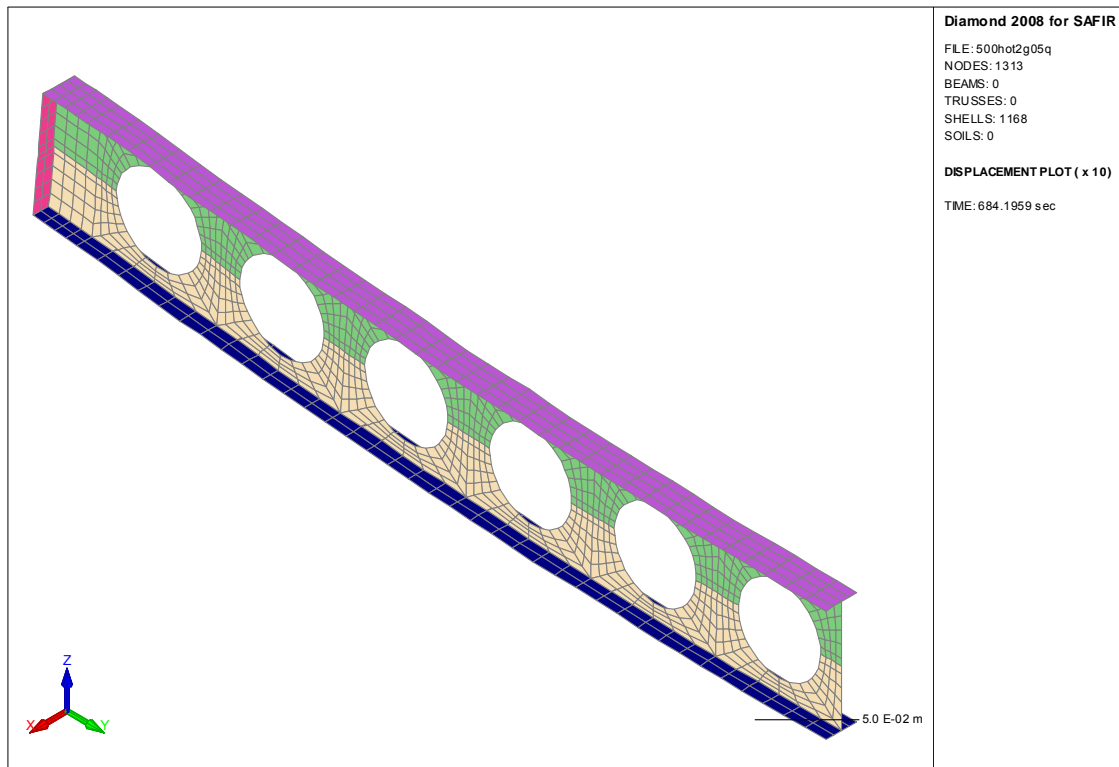


Figure 5–2 : Displaced shape of a beam without web post buckling

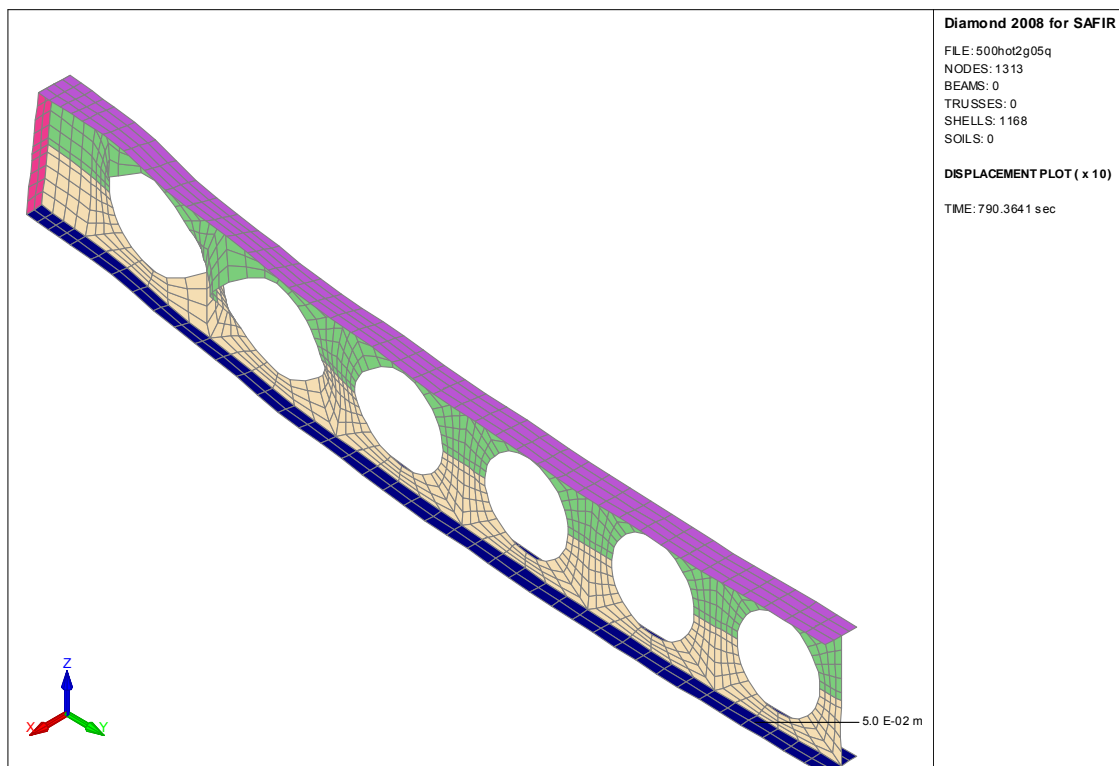


Figure 5–3 : Displaced shape of a beam with web post buckling

- the out of plane displacement of the critical section (see Figure 5–4 and Figure 5–5)

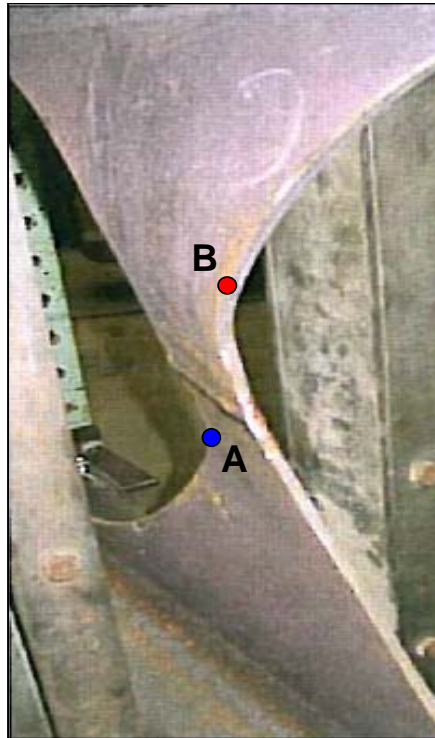


Figure 5–4 : Out of plane displacement of the web post for symetric steel profile

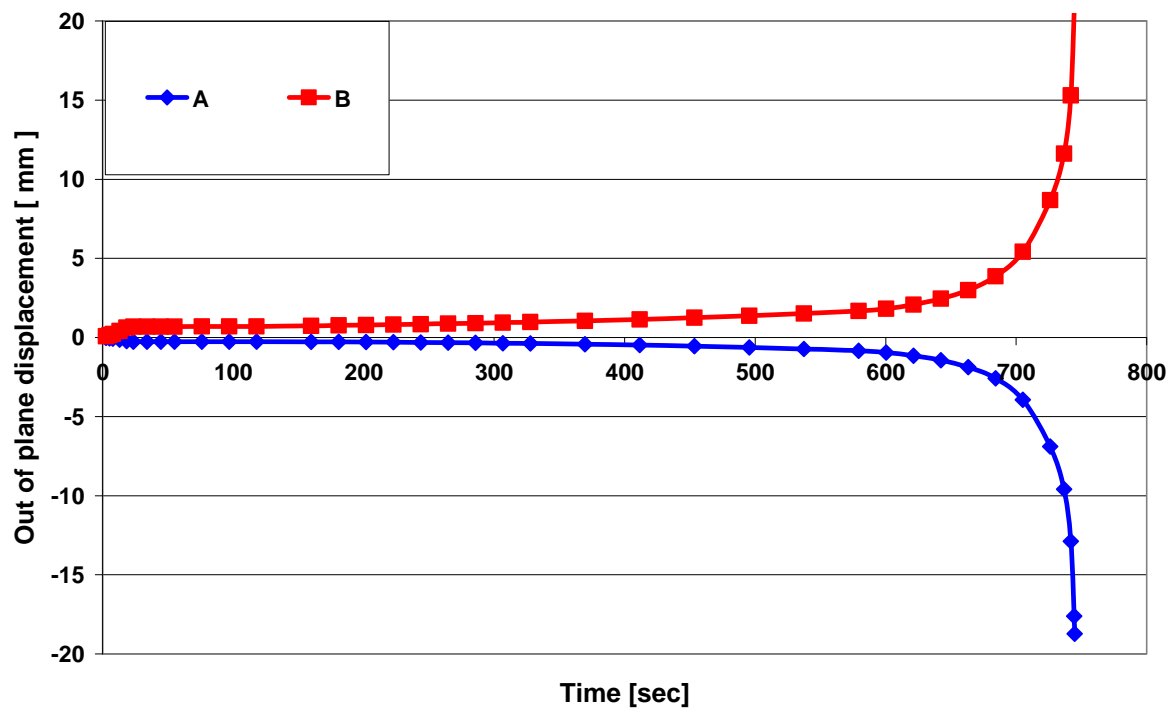


Figure 5–5 : Out of plane displacement of the web post

5.1.2 Web post buckling in composite section

As it has been done for steel sections in previous sections, it is necessary to define what will be considered as a web-post buckling failure for the FEM software SAFIR before starting the parametrical study on composite sections.

The web-post buckling failure can be identified by:

- the shape of the beam of the numerical simulation (see Figure 5–6 and Figure 5–7)

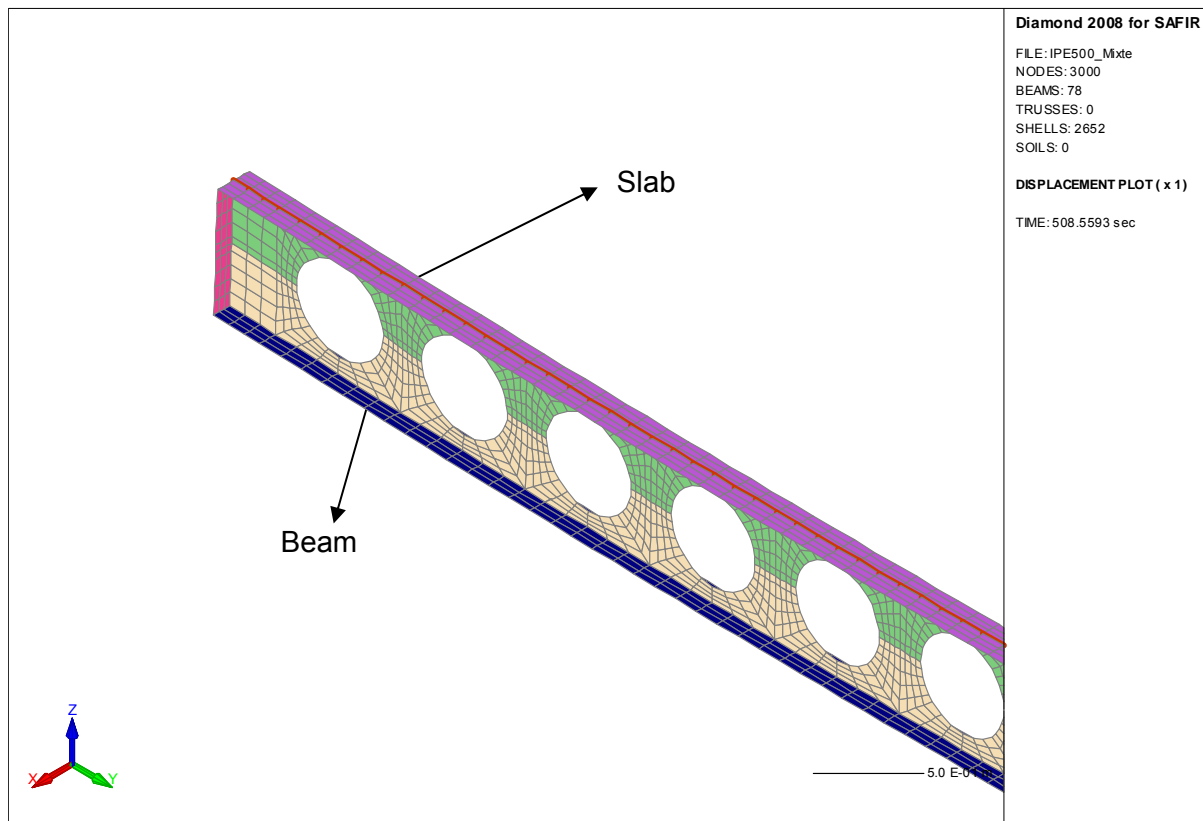


Figure 5–6 : Displaced shape of a beam without web post buckling

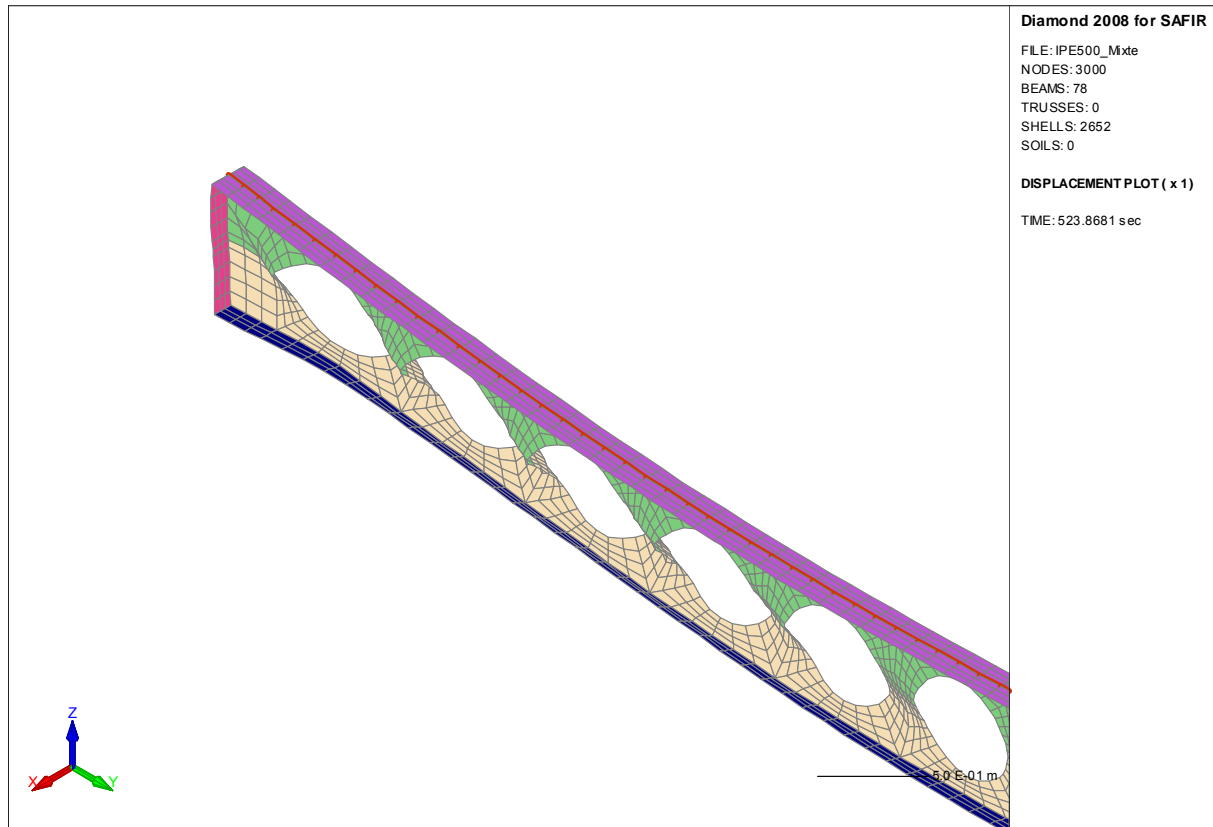


Figure 5–7 : Displaced shape of a beam with web post buckling

- the out of plane displacement of the critical section (see Figure 5–8 and Figure 5–9)

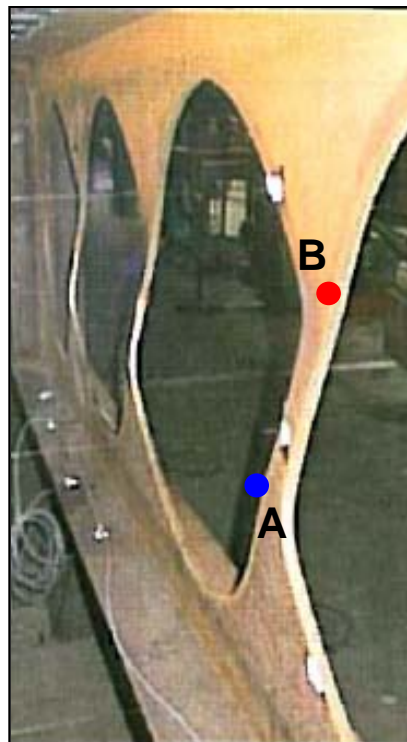


Figure 5–8 : Out of plane displacement of the web post for composite section

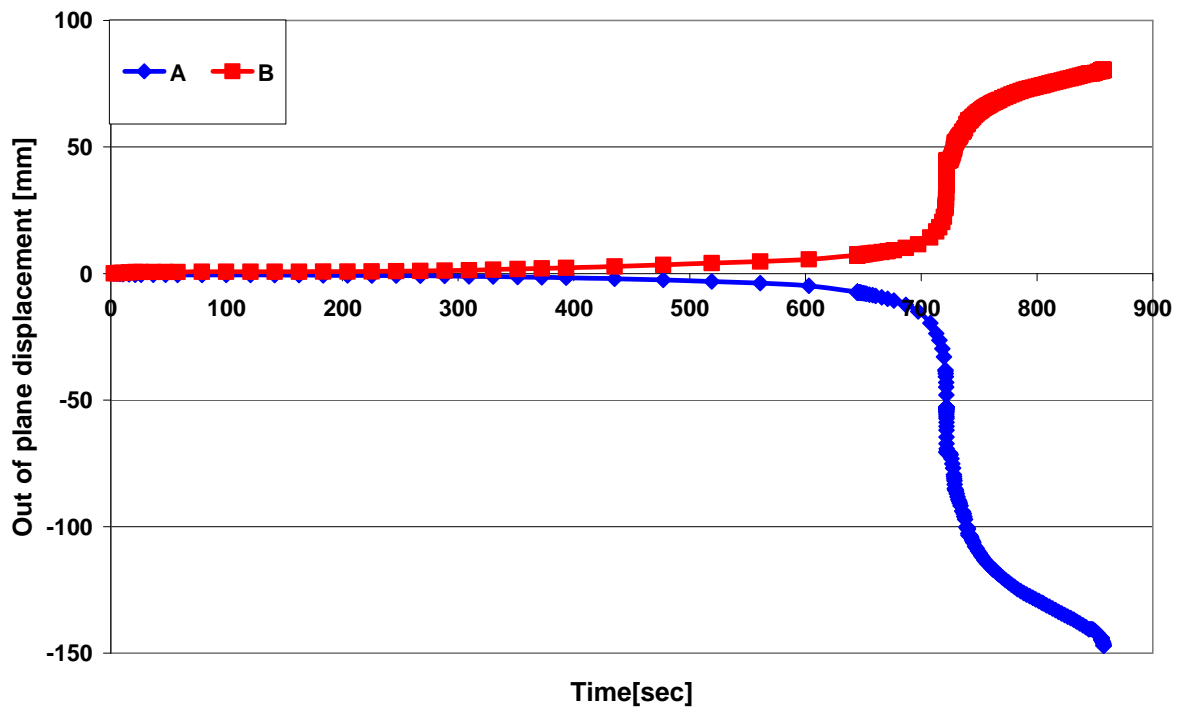


Figure 5–9 : Out of plane displacement of the web post for composite section

Analysing Figure 5–9, it is observed that the upper web post is rigidified by the presence of the composite slab.

5.1.3 Web post buckling in composite non-symmetrical section

In composite sections, it is possible to use smaller profiles for the upper part of the beam as explained in Chapter 1.

The web-post buckling failure can be identified by:

- the shape of the beam of the numerical simulation (see Figure 5–10 and Figure 5–11)

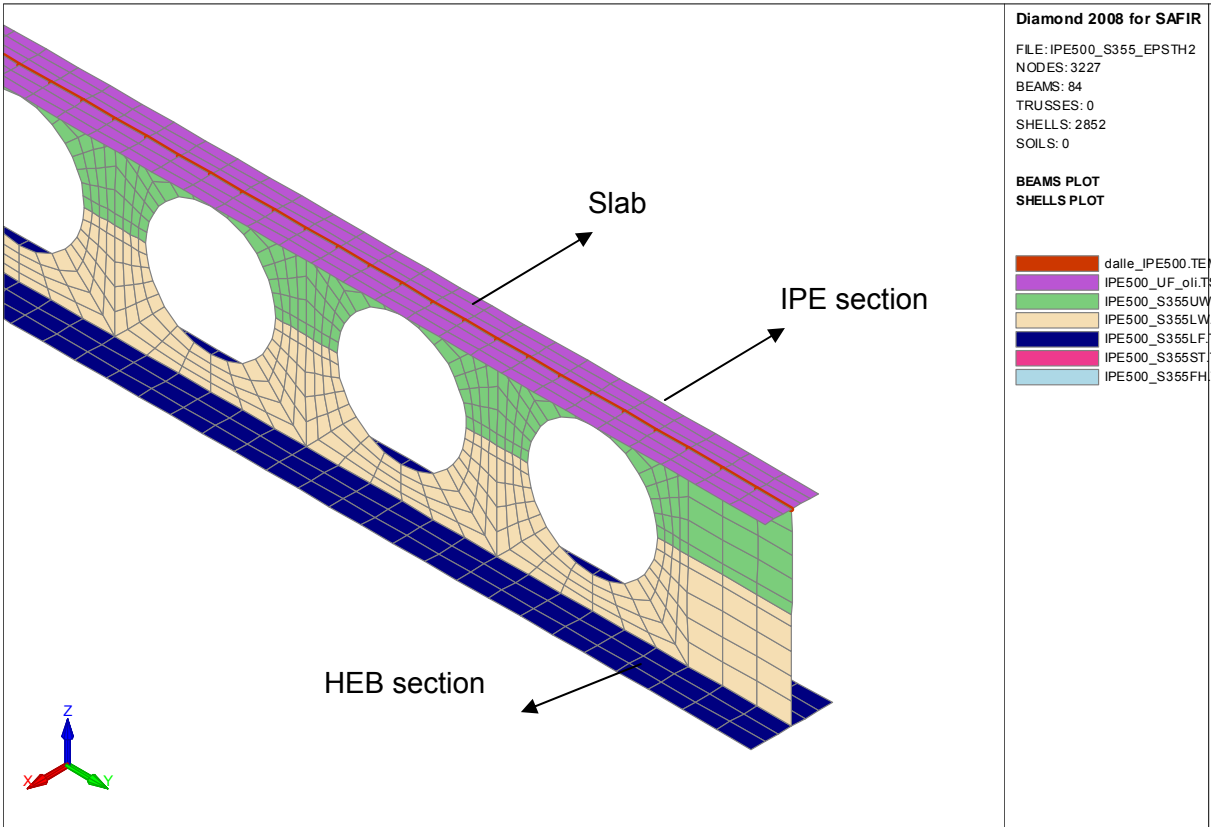


Figure 5–10 : Displaced shape of a beam without web post buckling

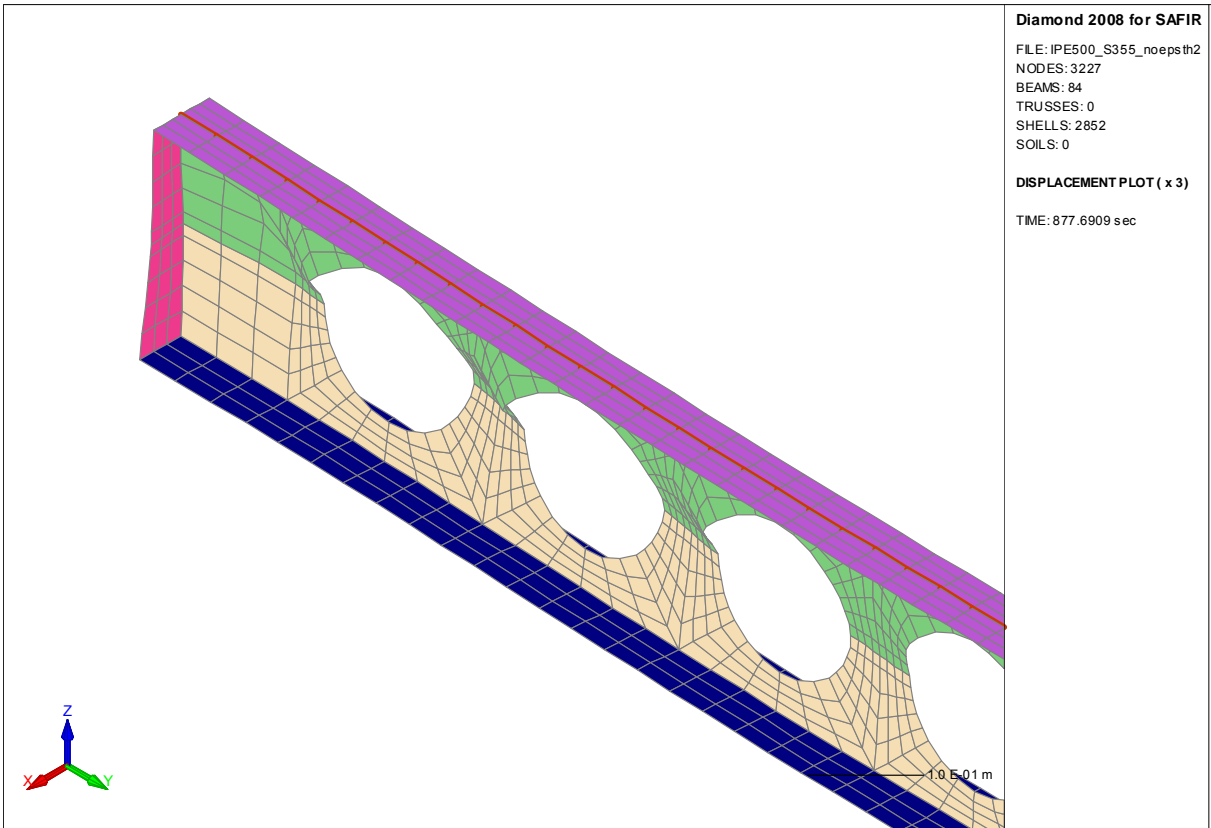


Figure 5–11 : Displaced shape of a beam with web post buckling

- the out of plane displacement of the critical section (see Figure 5–12 and Figure 5–13)

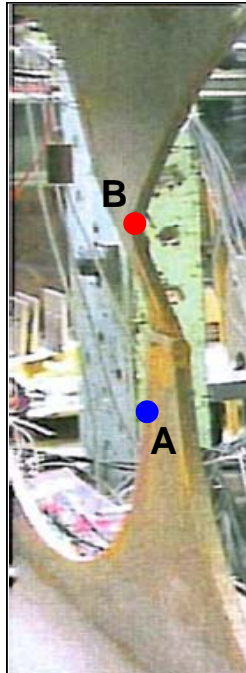


Figure 5–12 : Out of plane displacement of the web post for composite hybrid section

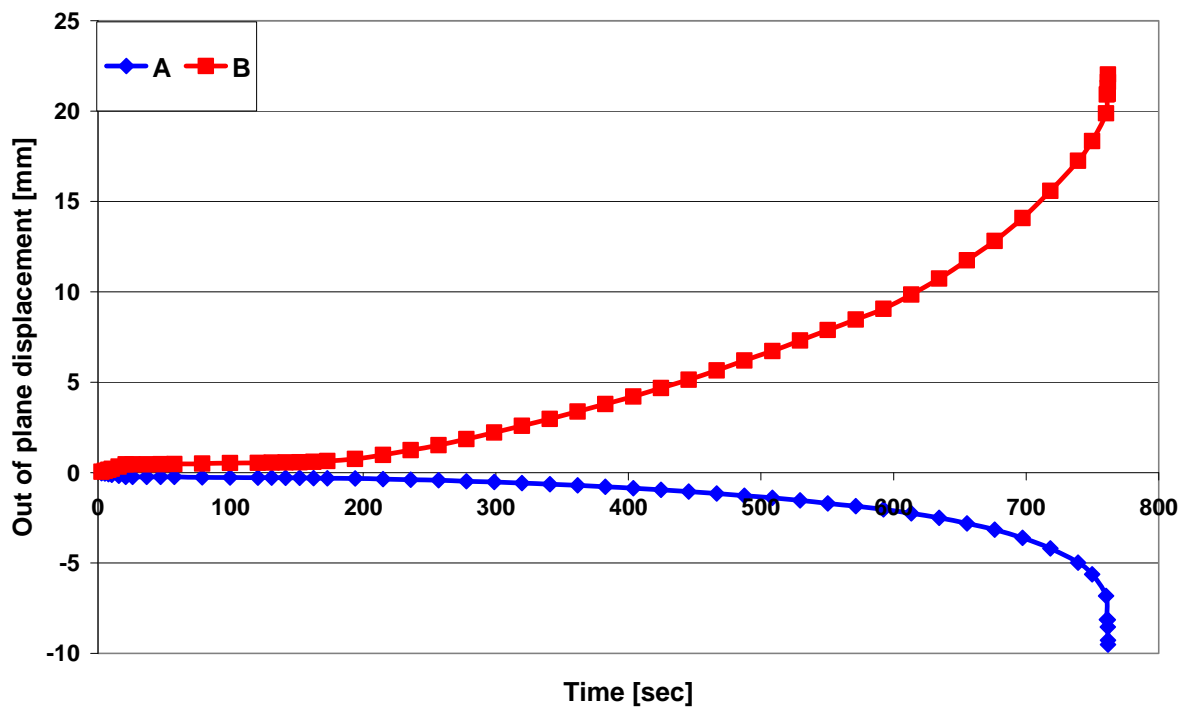


Figure 5–13 : Out of plane displacement of the web post for composite hybrid section

Analysing Figure 5–13, it can be noticed that the upper part of the web (IPE section) is stabilised by the lower part of the web (HEB).

5.1.4 Parametrical study

The aim of this chapter is to show the validity of the analytical model in a given range of application. The range of application of the model is the same as the range of application of the CTICM model in cold conditions. The numerical simulations were made using the software SAFIR and the failure time was defined using the procedure here after.

After identifying the failure time of the structural 3D model in SAFIR, the critical temperature is taken as the temperature of the critical section (in our case, the web). This temperature is extracted from the thermal calculation of SAFIR (see Figure 5–14 and Figure 5–15).

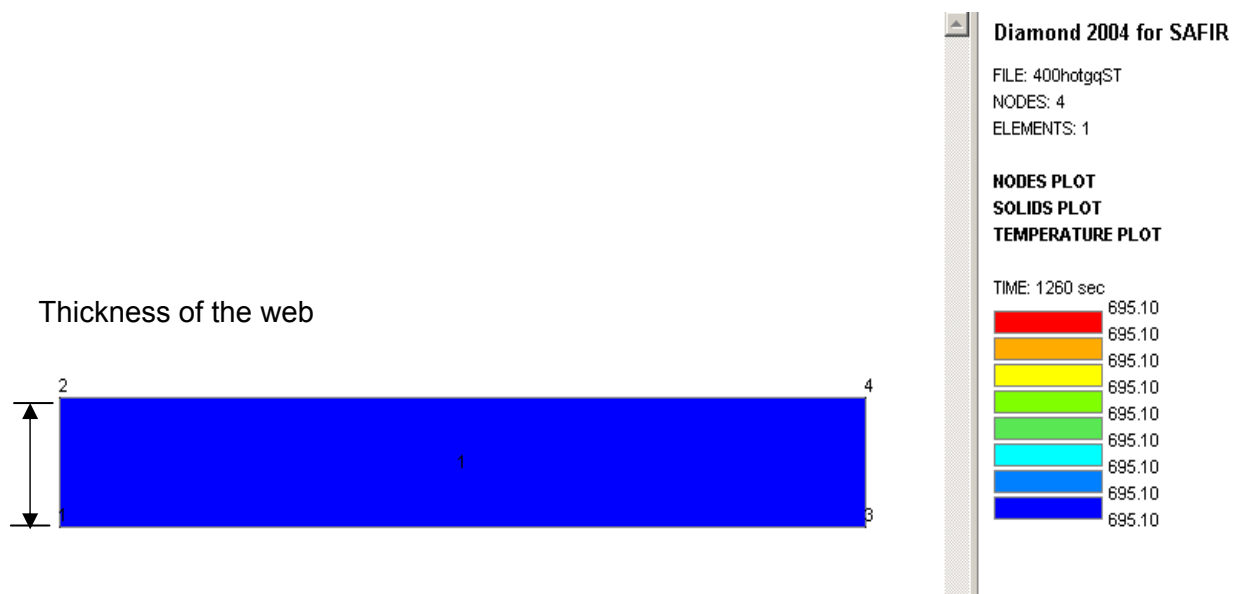


Figure 5–14 : Thermal calculation of the SHELL element forming the web

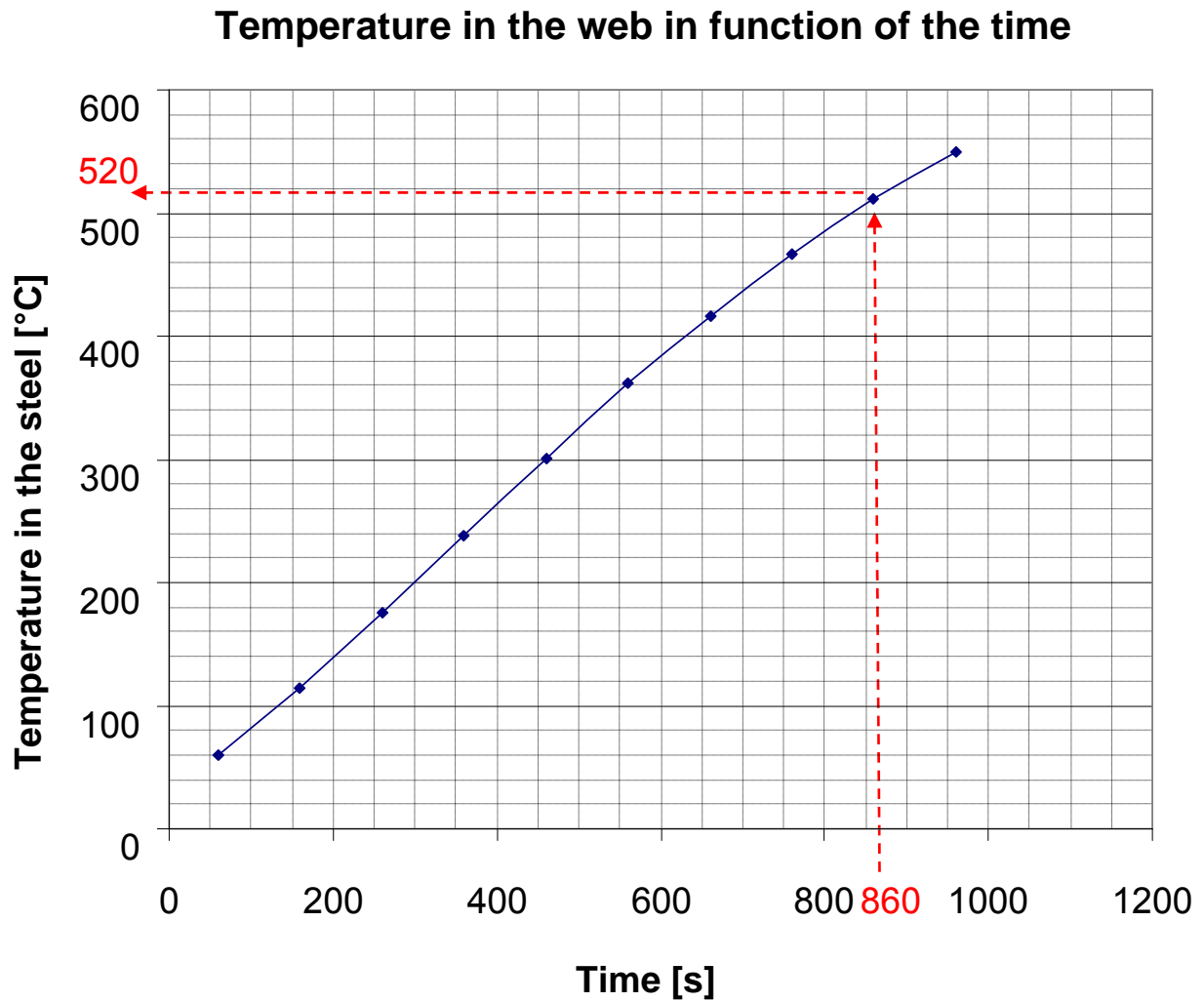


Figure 5–15 : Web temperature

The different parameters that varied in the study are :

- the type of sections,
- the steel strength limit,
- the length of the beam,
- the utilisation factor,
- the geometry of the beam (height, diameter of the opening, size of the web-post).

The type of sections

Profiles have a very different section factor, thus the heating velocity is very variant from one section to another.

This massivity influences the temperature in the steel e.g. an IPE500 has a massivity of the full section 151m^{-1} , if it is heated by an ISO fire, it will reach approximatively 600°C in 15 minutes, while a HEB400 that has a massivity of 97m^{-1} will only reach 500°C after the same time of 15 minutes.

So, different profiles from the ArcelorMittal hot rolled section catalogue will be used for the parametrical study.

The steel strength limit

Indeed, the yield point of the steel influences considerably the fire resistance; to increase the steel grade of a beam without increasing the section can be enough to satisfy the requirements of fire resistance. If the plastic or the elastic resistance of a section is taking into account, the fire resistance is directly a function of the steel strength limit f_y . For example, if the chosen steel strength limit is 460N/mm^2 instead of 355N/mm^2 , the fire resistance will be increased by 30%.

It is different in case of the web-post buckling. The web post buckling resistance depends not only on the steel strength limit but also on the Young modulus. More the web post will be “sensible” to instability, less the steel strength increase will be efficient. In order to study the influence of the steel strength limit, the different steel grades have been used:

- S235
- S355
- S460

The length of the beam

Depending on the nature of the building, the length of beams is different. The web-post buckling is mainly caused by shear force, the length of the beam can be influenced by the behaviour of the web-post.

The applied load

The fire resistance of a profile will be related to the utilisation factor of the section. For section with a really low utilisation factor, the fire resistant rate can be high.

The same profile may be used in office building or in roofing of industrial building. The utilisation factor can be different in fire condition depending on his application. The influence of this parameter will be taken into account in the parametrical study.

The geometry of the beam

As explained in Chapter 4, the web post buckling is influenced by the geometry of the beam. The model in cold conditions has been validated by a parametrical study taking into account different geometry [24]. Hereafter, an example of results on the variation of the size of the web-post buckling on a given steel profile is presented.

The chosen steel profile is an IPE500 in S355 Histar.

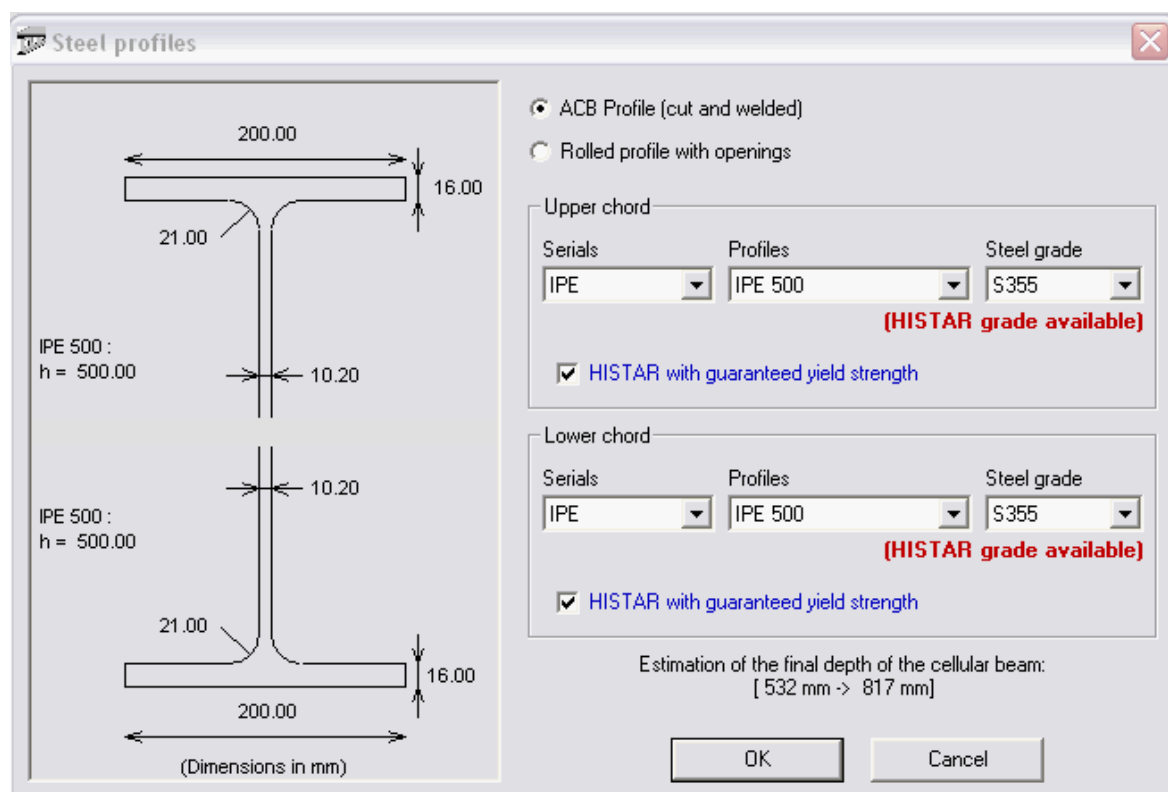


Figure 5–16 : Dimensions of the steel profile

The diameter of the opening has been fixed to 0.5m and the span of the beam has been fixed at 15m.

A variation has been made on the size of the web post in order to cover all the possible web post in this beam specification. The web-post can vary from 50mm to 375mm (see Figure 5–17 and Figure 5–18).

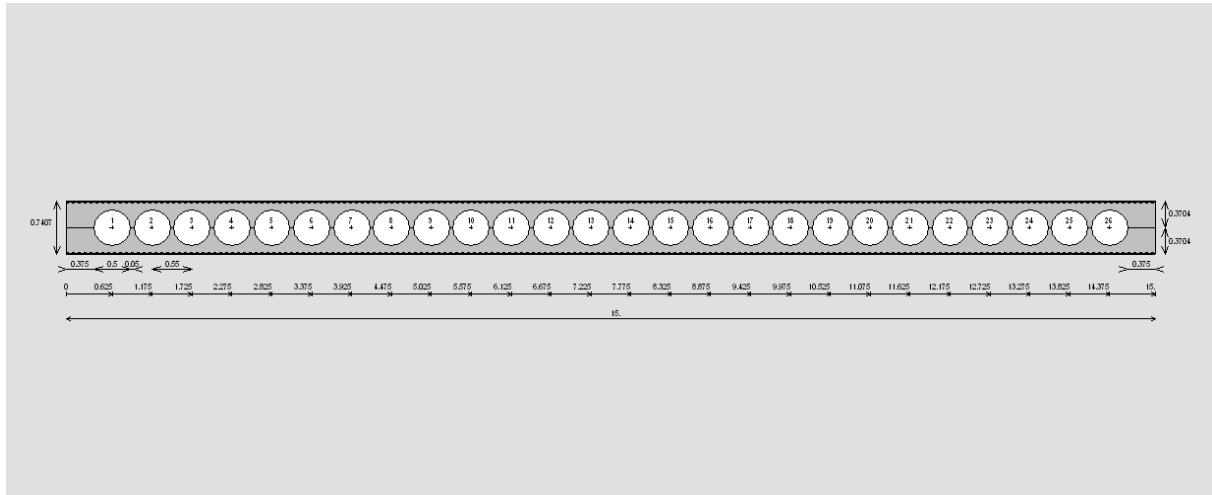


Figure 5–17 : Geometry of the IPE500 with $w = 50\text{mm}$

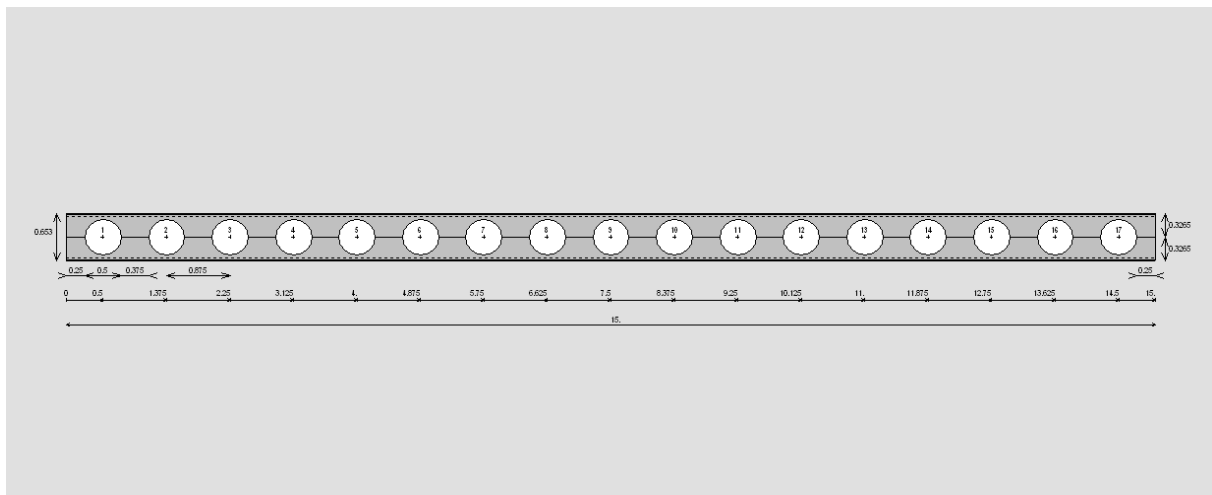


Figure 5–18 : Geometry of the IPE500 with $w = 375\text{mm}$

First of all, the web post buckling model in cold condition was compared to the results of the SAFIR FEM software not only for load bearing capacity but also for failure modes (see Figure 5–19).

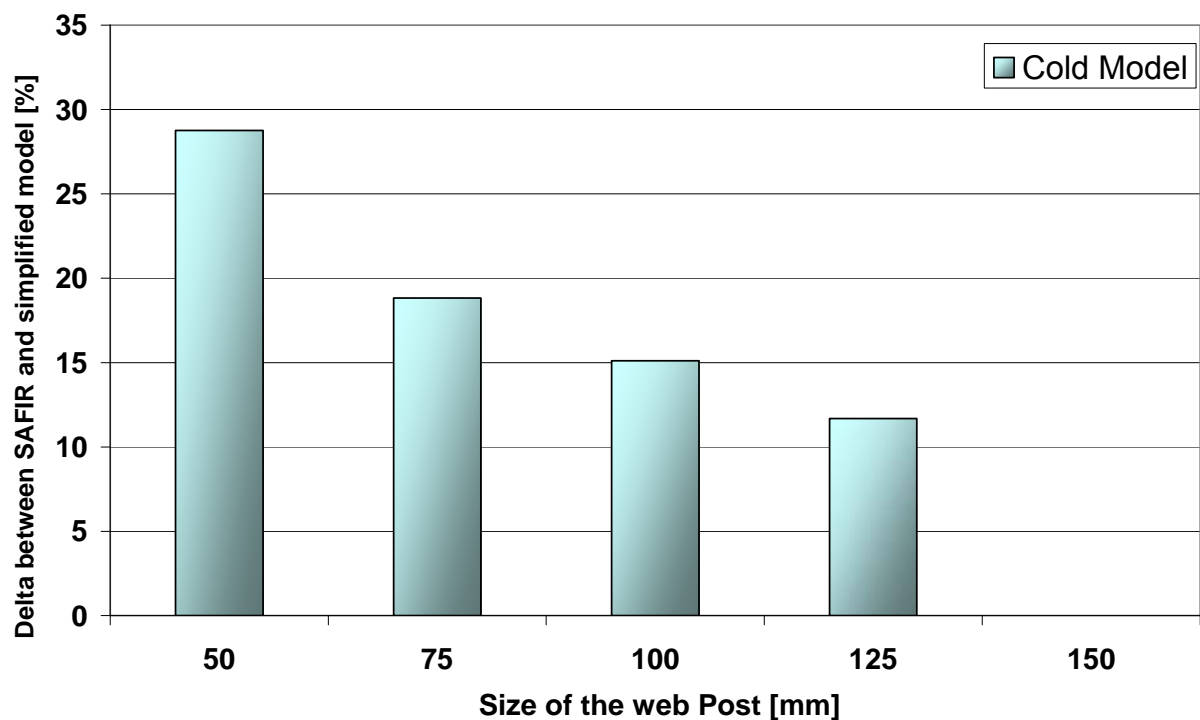


Figure 5–19 : Delta between SAFIR and simplified model for the failure load in cold conditions

The difference between the FEM model and the simplified method is in line with the parametrical study performed by P.O. Martin using ANSYS FEM software [24]. A positive delta in Figure 5–19 indicates the results obtained from simplified model are on safe side. The comparison between FEM and simplified model is only possible for web posts smaller than 150mm. This is because for these sizes the failure mode changes to Vierendeel failure for both calculation models.

The same study has been made at elevated temperature; the results are illustrates in Figure 5–20.

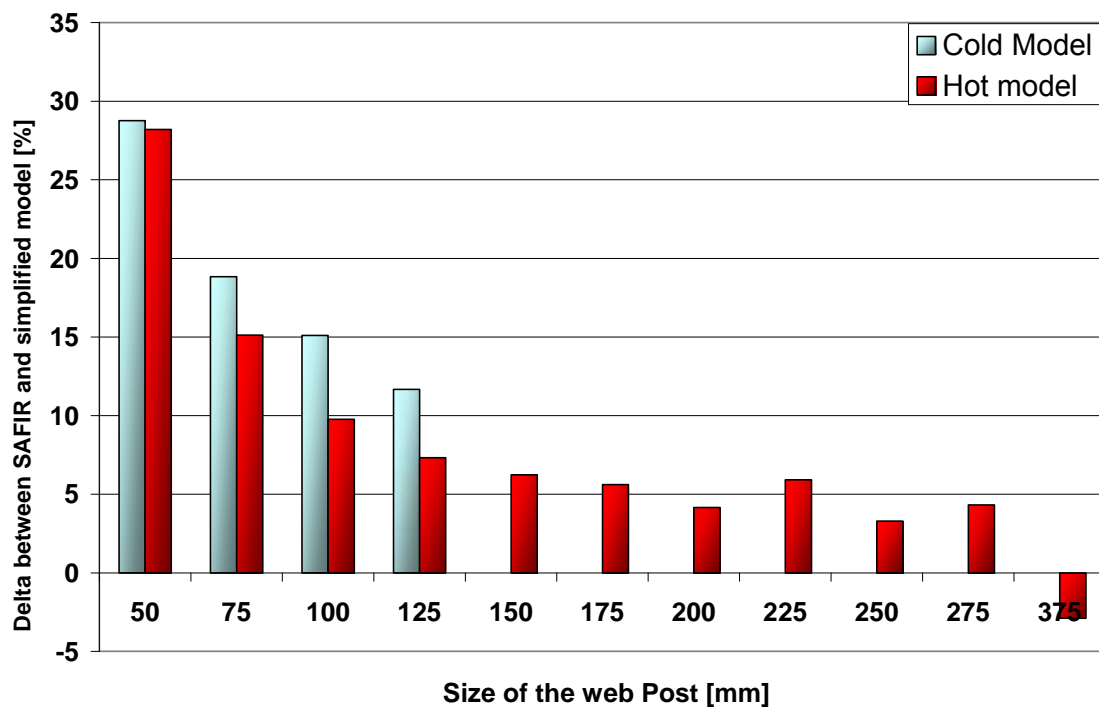


Figure 5–20 : Delta between SAFIR and simplified model for the failure load in cold and hot conditions

Figure 5–20 shows that the web post buckling is the only possible failure mode for this group of geometry. The largest feasible web post (375mm) is not resistant enough to survive in case of fire. It is concluded that for this very large web-post, the analytical model gives unsafe results but lower than 5% which is also in line with the calibration of the cold model performed by P. O. Martin [24].

5.1.5 Implementation of a tool for the simplified model

In order to realise a parametrical study, the simplified analytical model was implemented in an Excel spreadsheet.

The inputs are:

- the geometry of the beam
- the steel strength
- the applied load in case of fire.

The outputs are:

- the geometry and the massivity of the critical section for each web-post
- the critical temperature of each web-post

5.1.6 Results of the parametrical study

Taking into account the different parameters explained here above, about 100 numerical simulations were performed on pure steel and composite sections. The results are summarised in Figure 5–21 :

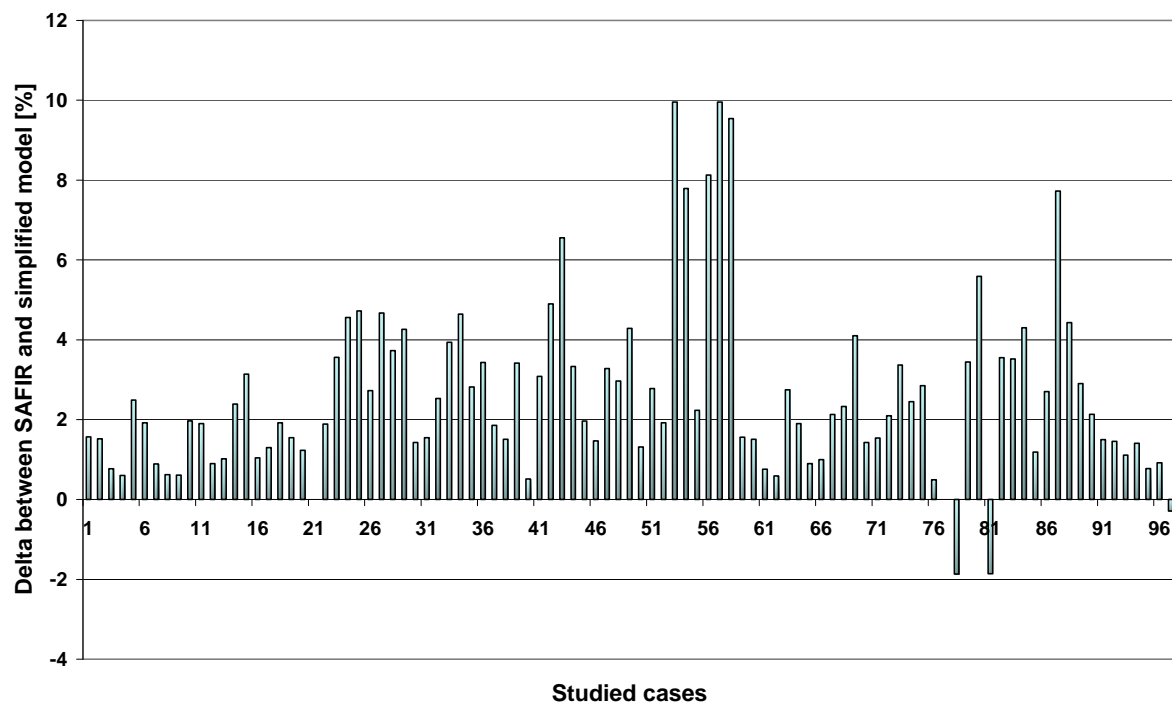


Figure 5–21 : Summary of the results for the parametrical study on the web post buckling.

This figure shows that the model predicts with a good accuracy the critical temperature of the web-post. The study leads to a conclusion that the model provides safe results for 97% of the analysed cases. The unsafe results are extreme cases in steel (explained in chapter 5.1.4) and the two composite unsafe cases are composite asymmetrical sections with a big discrepancy between the sizes of the members (IPE & HEB).

The biggest discrepancies between the simplified model and the FEM are around 10% in respect to the critical temperature. These bigger differences are coming from cases in pure steel with really small web-post. This phenomenon was also reported by P. O. Martin [24], who analysed cold situation.

In the case of composite section, the difference is coming from the fact that the shear force, taken by the composite slab, is underestimated in the model.

The value of this shear force (see Chapter 4.1.5) is already underestimated in the cold model. In hot situation, the simplified model does not allow for a redistribution of shear force in the slab when the temperature of the beam increases; so the critical temperature of the web-post can be underestimated.

5.2 Vierendeel bending

Before starting the parametrical study, it is needed to define Vierendeel failure for the FEM software SAFIR.

The Vierendeel failure can be identified by:

- the shape of the beam of the numerical simulation (see Figure 5–22 and Figure 5–23)

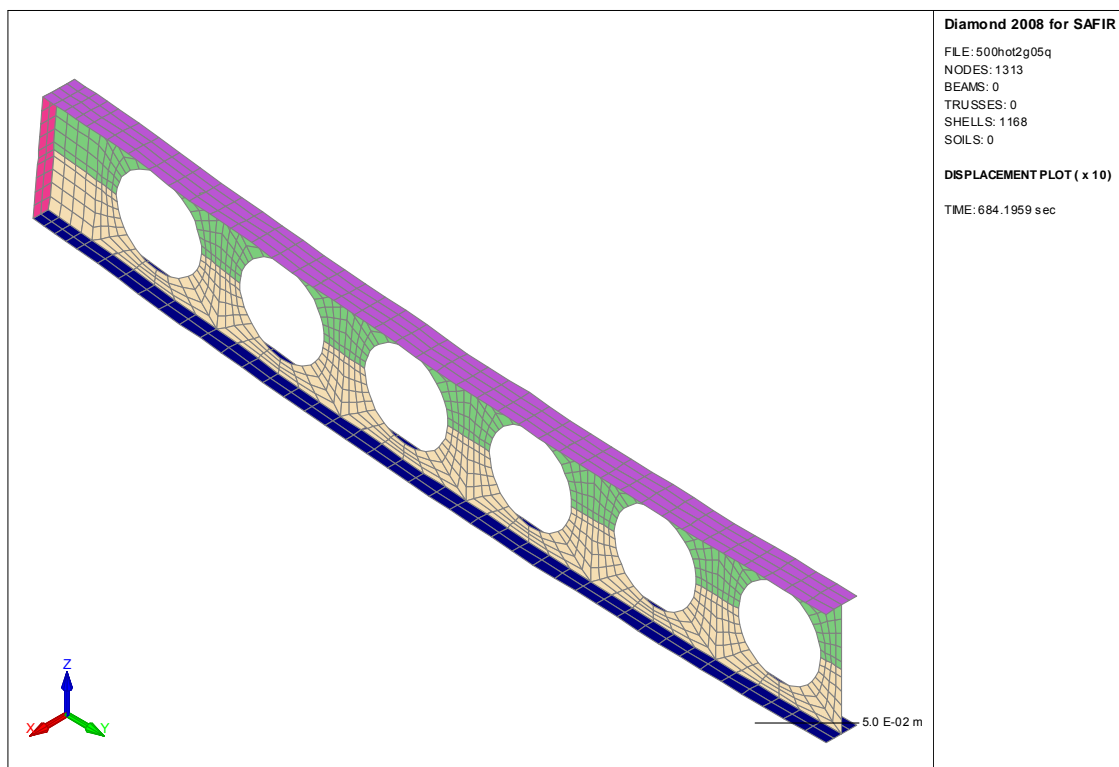


Figure 5–22 : Displaced shape of a beam without Vierendeel failure

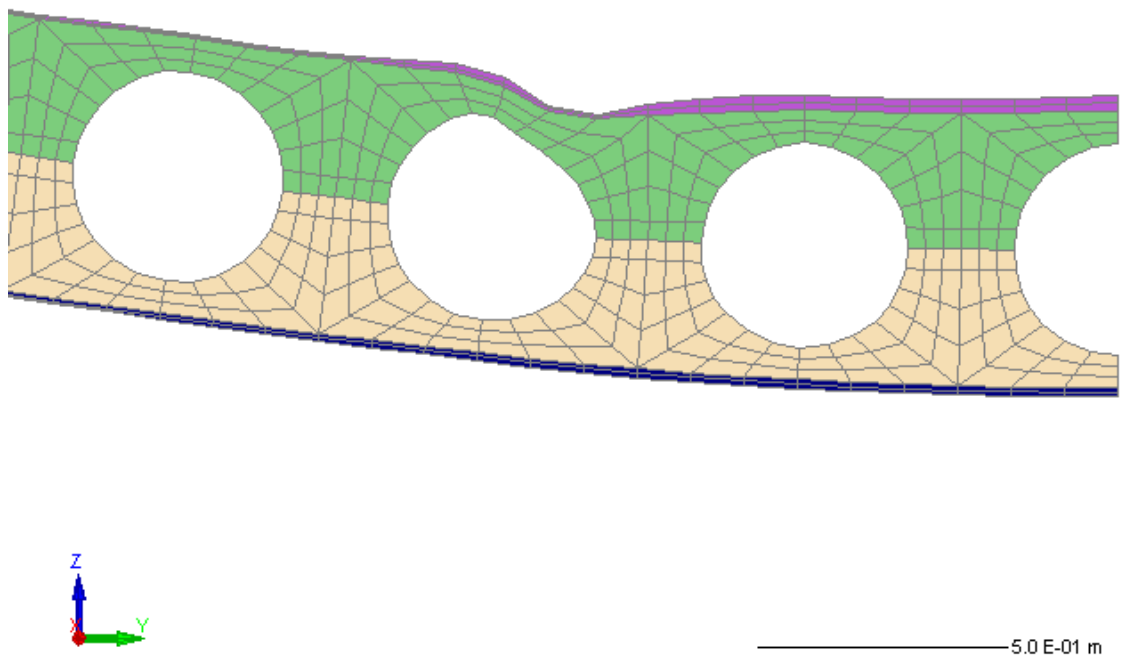


Figure 5-23 : Displaced shape of a beam with Vierendeel failure

An analysis of the vertical displacement in the centre of the beam (see Figure 5-24) and the out of plane displacement of the first web post are sufficient to show that the failure of the beam was reached, without any out of plane movement of the web post.

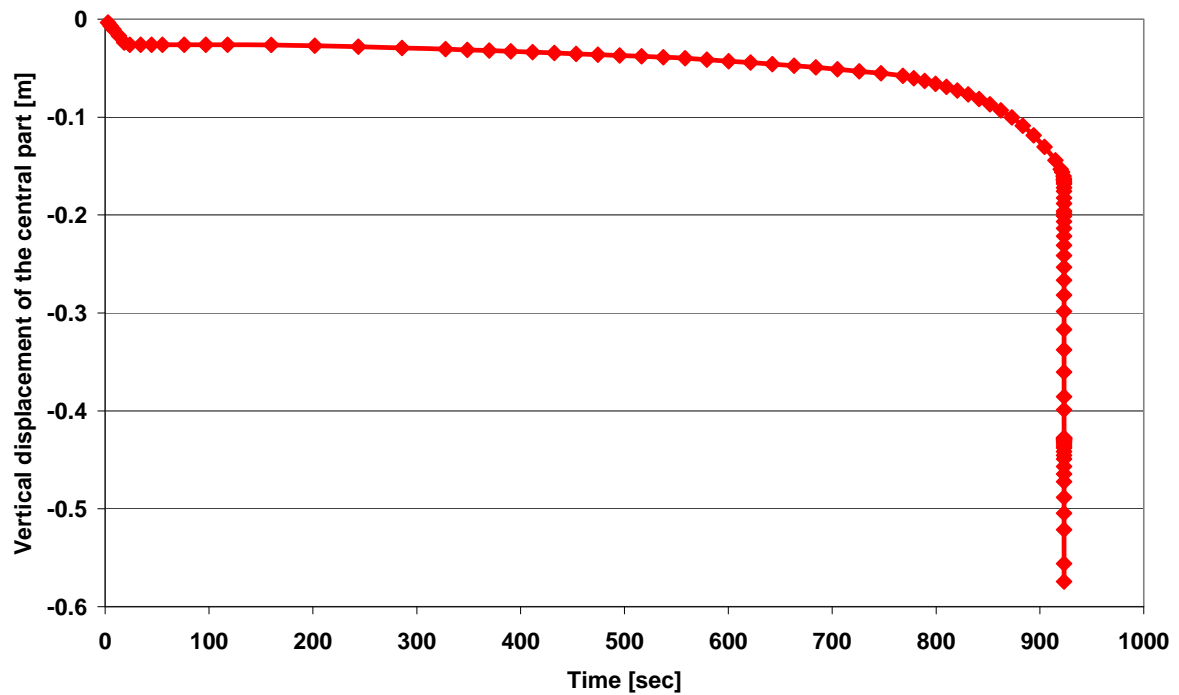


Figure 5-24 : Vertical displacement of the central part of the beam in function of the time

5.2.1 Parametrical study for Vierendeel bending

The aim of this section is to show the validity of the analytical model for Vierendeel bending in a given range of application. The range of application of the model is the same than the range of application of the CTICM model in cold conditions. The numerical simulations were made using the software SAFIR and the failure time was defined using the procedure hereafter.

Failure time of the structural 3D model in SAFIR will allow identifying the critical temperature of the critical section (in our case, the upper or the lower 'T'). It can be extracted from the thermal calculation of SAFIR as for the web post. However, the procedure is much more complex. In fact, the 'T' section is composed of the entire flange of the steel profile and a part of the web (see Figure 5–25).

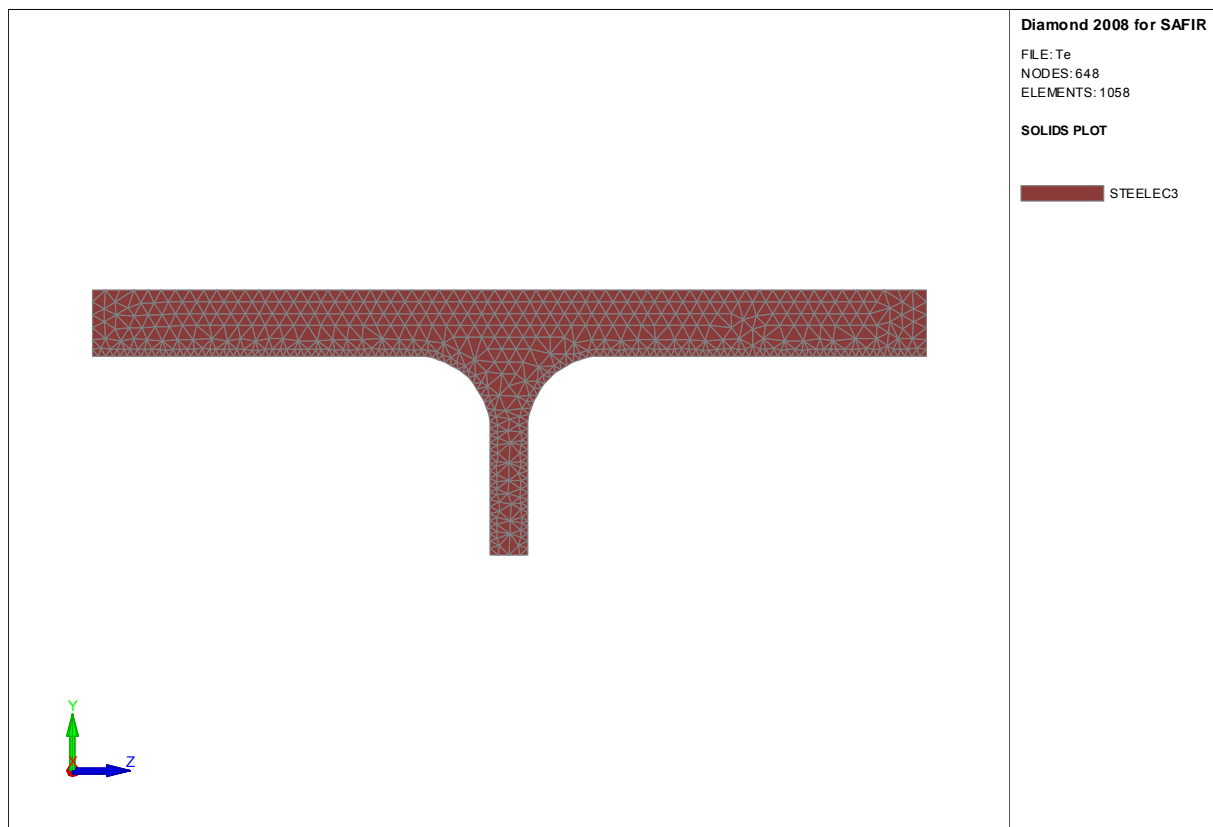


Figure 5–25 : FEM model of a 'T' section using a BEAM element

This profile exposed to an ISO fire all around its perimeter, the temperature is not constant in each part of section (web and flange) (see Figure 5–26).

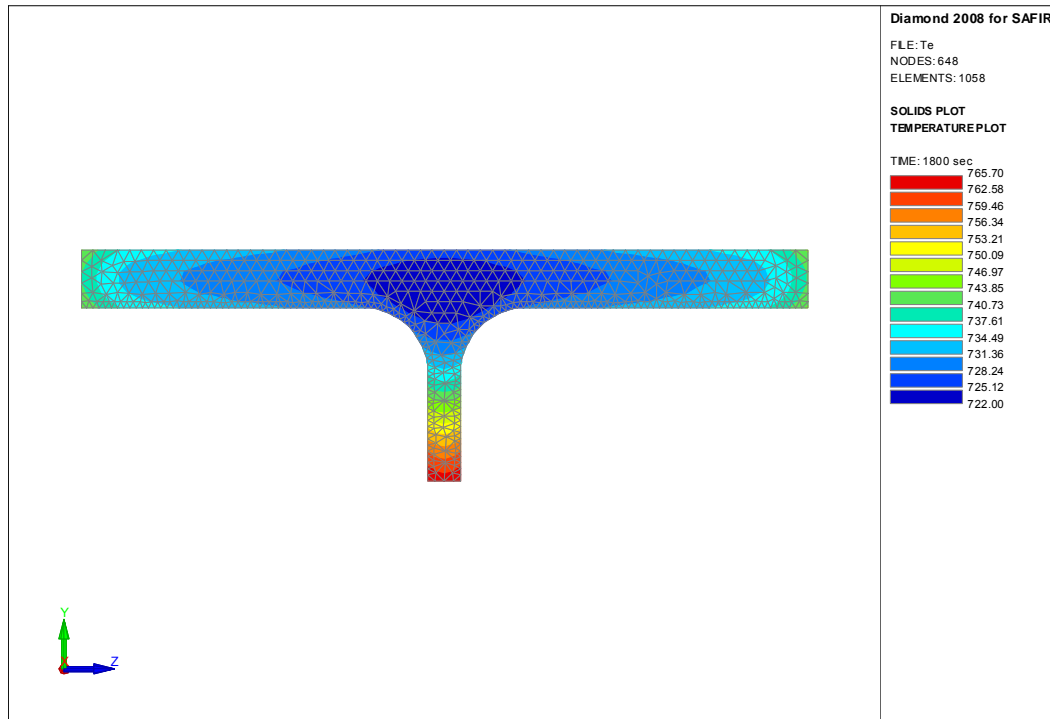


Figure 5-26 : Temperature in the section after 1800 sec

In the numerical simulation performed in this parametrical study applying the FEM model developed and calibrated in Chapters 2 and 3, the steel beam is modeled using SHELL Finite Element. The temperature field in this case is shown in Figure 5-27.

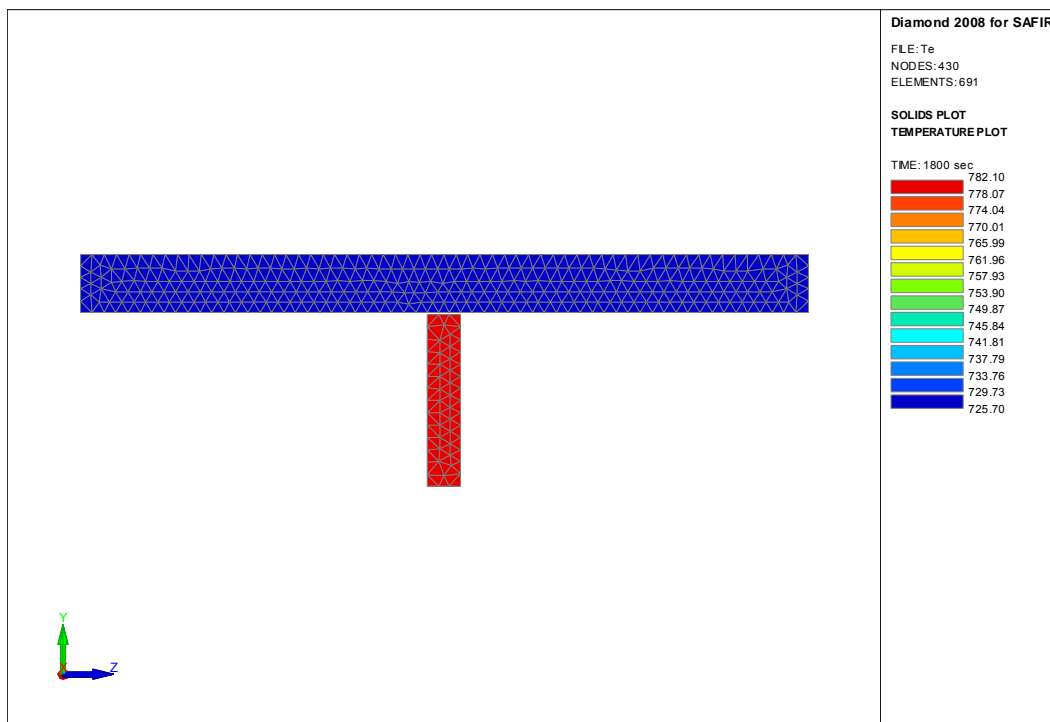


Figure 5-27 : Temperature distribution equivalent to the SHELL FEM model

This simplification is the only way to apply SHELL elements in SAFIR. It has been proved in Chapters 2 and 3 that this procedure will not affect the results of the simulation.

In order to obtain a global critical temperature in the section for the SAFIR simulation, the temperature of the flange and the temperature of the web were extracted from the numerical simulation (Figure 5–28):

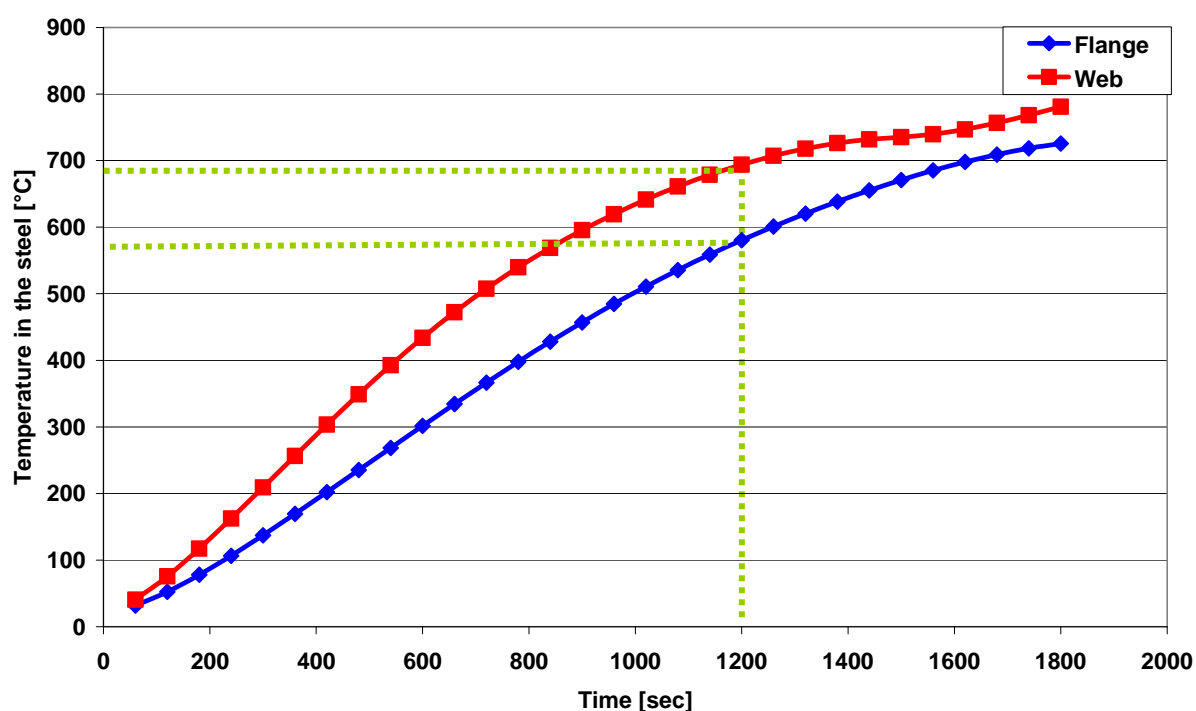


Figure 5–28 : Web and flange temperature distribution

An average temperature of the section is obtained using the temperature of each section weighted by their surface. This approximation is exactly the same as the one used in EC3 1-2 [55] for the simplified calculation of a steel profile taking into account the section factor.

For the Vierendeel failure, the parametrical study was performed on smaller sample than the one for the web post buckling. It was demonstrated in Sections 4.2.6 and 4.2.7 that the induced thermal stresses can be neglected for the calculation in case of fire and the results provided by FEM confirmed this point.

On the contrary, there is no controversy on the calculation of the Vierendeel bending of the web post buckling in case of fire.

Moreover, it was very difficult to find examples where the Vierendeel failure occurs before the web post buckling. This phenomenon is explained in the paragraph hereafter:

In cold situation, it is often possible to optimise the geometry in such a way to reach simultaneously the ultimate limit state in the web posts and in the 'T' parts of the section and consequently fully optimise the design.

In hot situation it can be easily shown that the web post buckling failure is the dominant failure mode.

An example has been chosen to illustrate and explain the dominant failure mode.

In case of fire, once the beam starts to be heated, the temperature increases in the steel and the steel properties decreases in the 'T' section and in the web post. If the simplified models are applied to a given geometry, the bearing capacities in a function of the temperature in the section can be extracted (Figure 5–29).

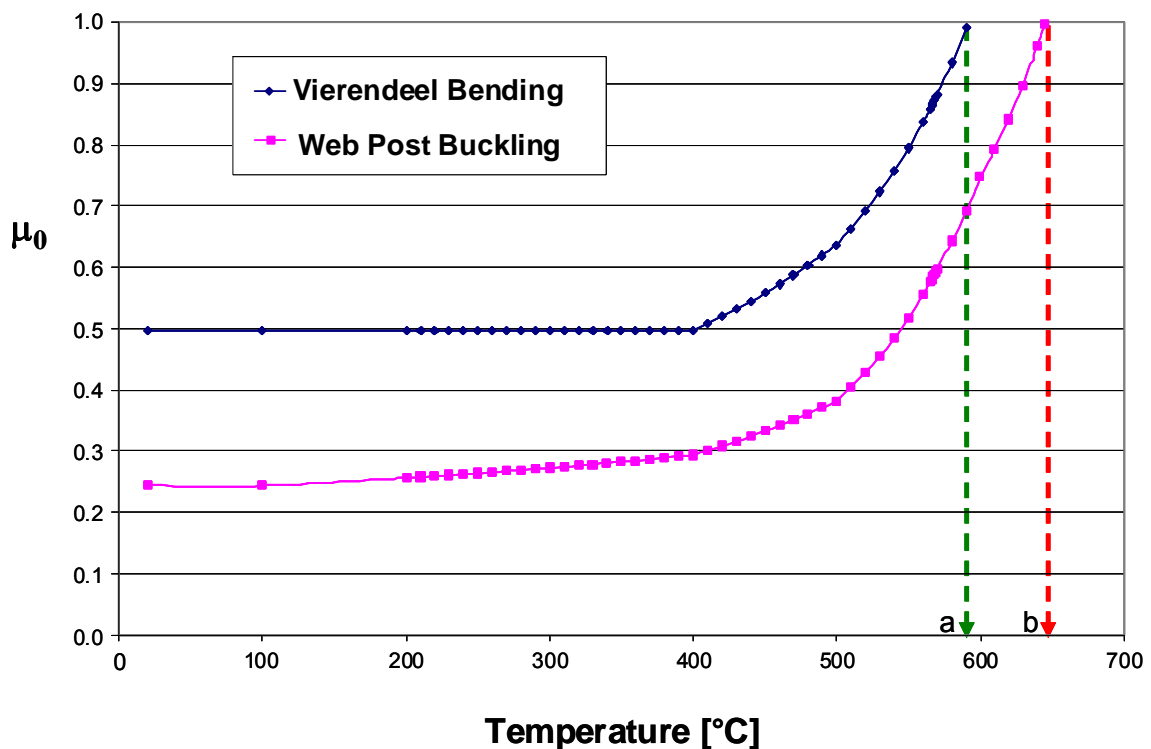


Figure 5–29 : Bearing capacities in function of the temperature in the section

Analysing Figure 5–29, it could be concluded that the Vierendeel bending will occur before the web post buckling as the critical temperature is significantly smaller (point 'a'). But the failure mode in this example is still the web post buckling because the temperature in the web increases faster than the temperature in the flange (see Figure 5–30).

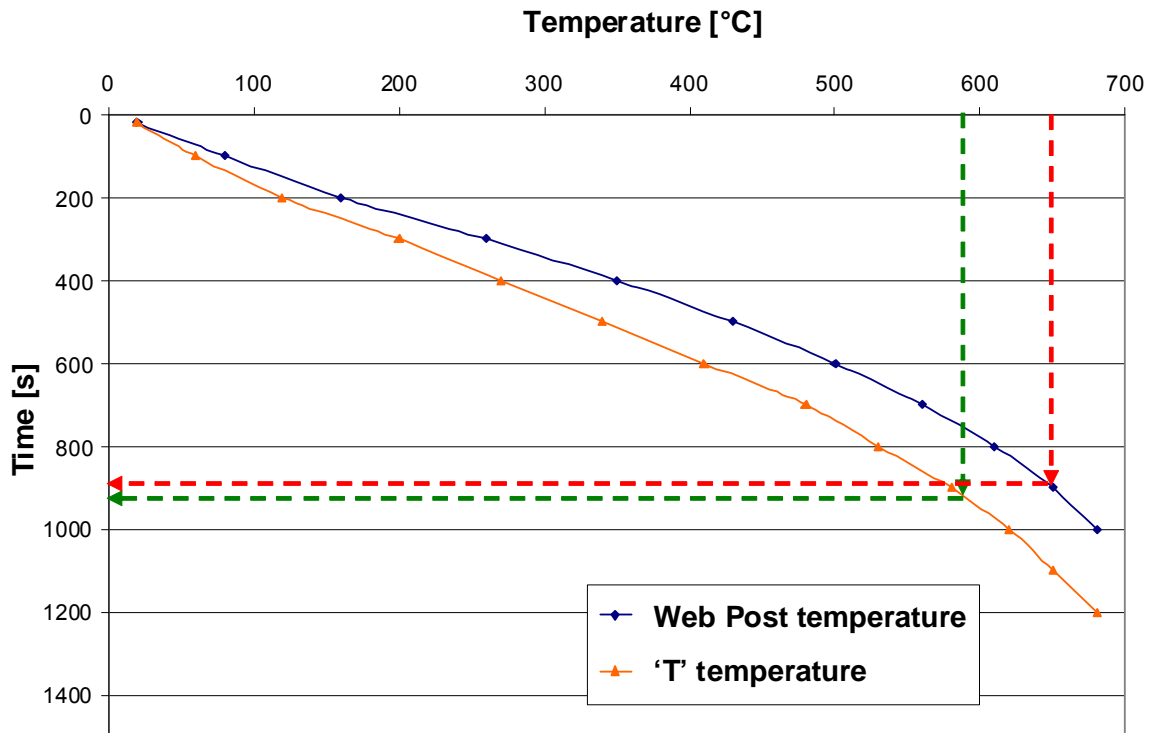


Figure 5–30 : Temperature in the different sections

This example indicates the fact that it is really difficult to find a reasonable example where the Vierendeel failure is the dominant failure mode.

For the parametrical study, it was decided to perform simulation avoiding the web post buckling failure mode in order to reach a failure by Vierendeel.

Different system's modifications are possible to avoid the web-post buckling :

- **Filling of openings** (Figure 5–31).

This is done by inserting discs made of steel plates welded from both sides. The thickness of the plate and the weld seam are optimised according to the local stresses.

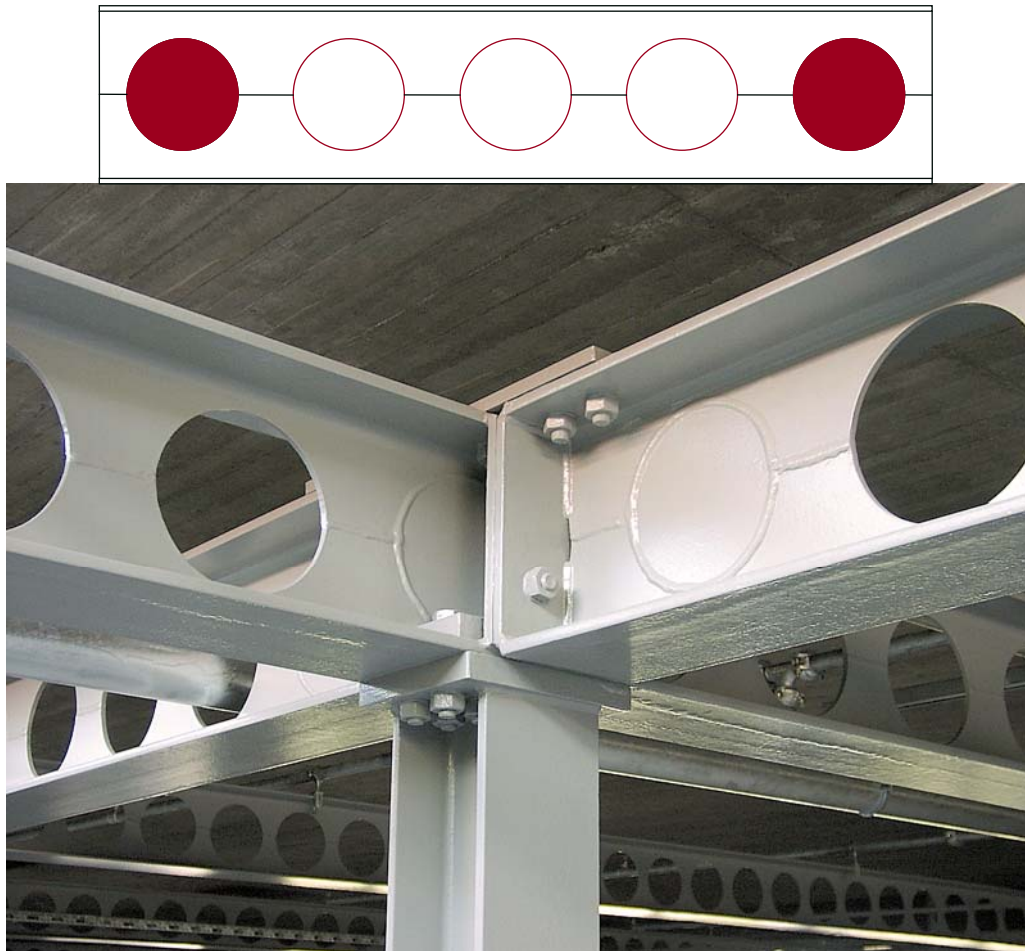


Figure 5–31 : Example of ACB® beam with filled openings

- **Circular reinforcement** (Figure 5–32)

If, for aesthetic reasons, the opening must be maintained, a hoop welded around the opening can be used

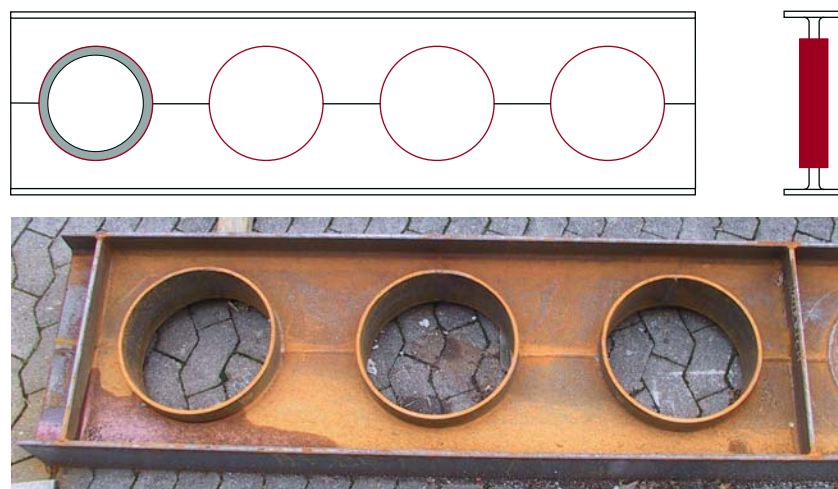
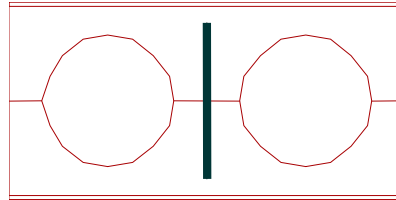


Figure 5–32 : Example of ACB® beam with reinforced opening

- **Reinforcement of the web post** (Figure 5–33)

Alternatively, experimental investigations have shown that a simple rigid plate, welded on the web post, is effective. Two part hoops can also be used.



Simple flat



Figure 5–33 : Measures to avoid buckling of the web post

In order to simplify the implementation and for an optimal use of the available meshing tools in SAFIR, it was decided to use the filled opening in the FEM software (see Figure 5–34).

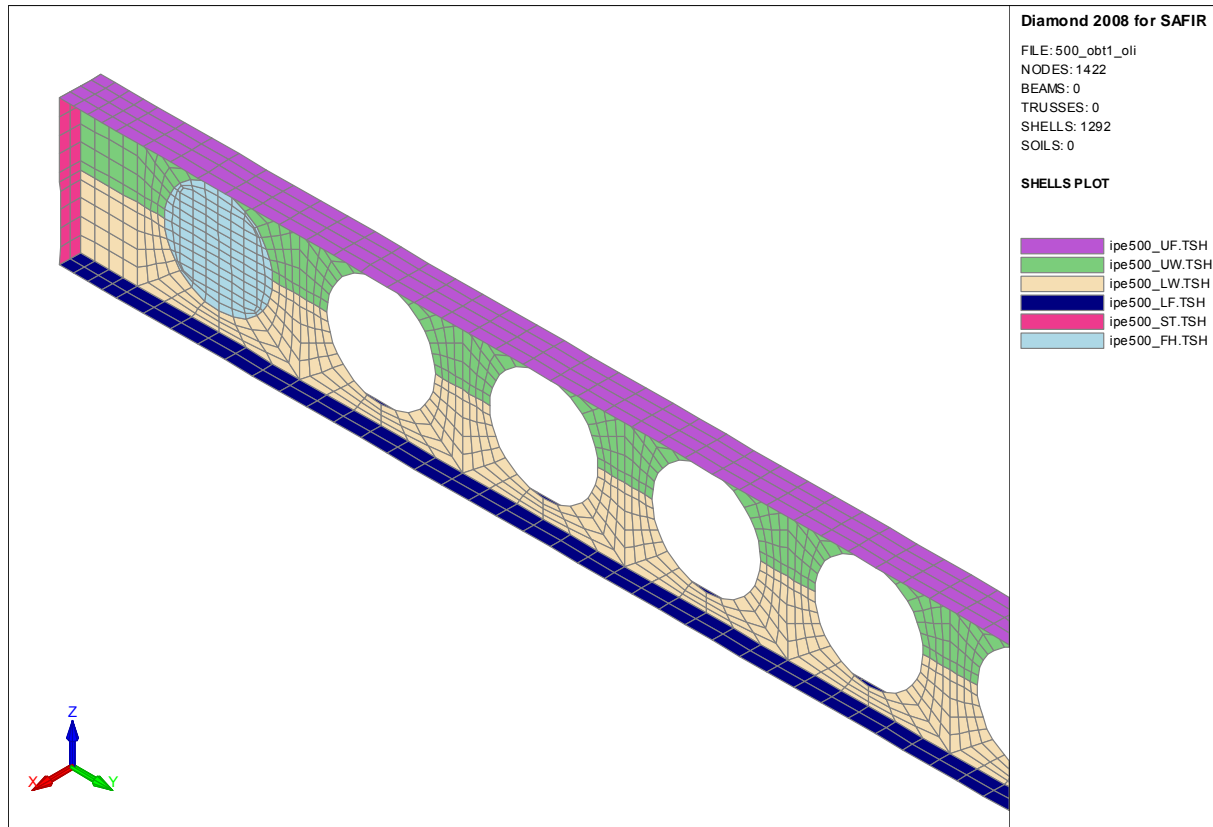


Figure 5–34 : FEM model of the filled opening in SAFIR

For each chosen profile, the numerical simulation has been made filling the first opening, then the second,... until having a failure by Vierendeel bending (see Figure 5–35 and Figure 5–36).

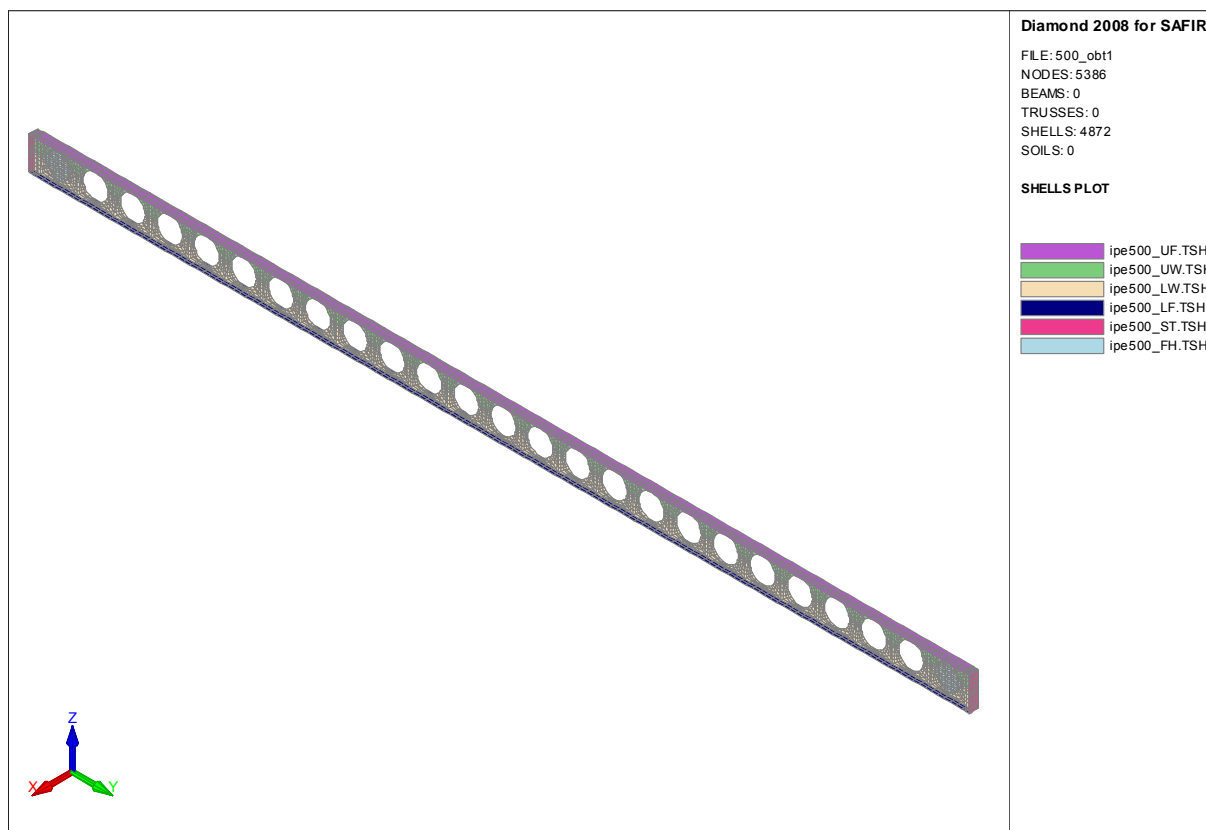


Figure 5–35 : FEM model with one filled opening in SAFIR

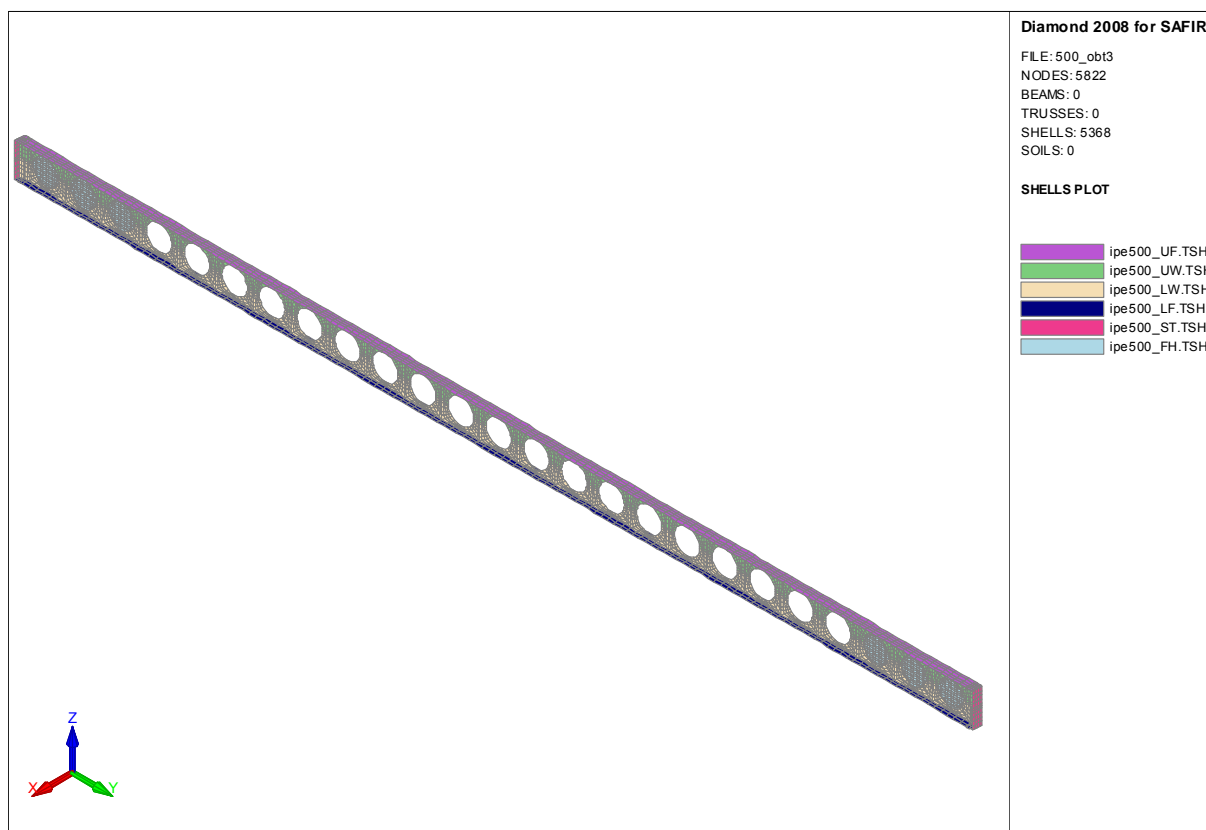


Figure 5–36 : FEM model with three filled openings in SAFIR

For some profiles, it was very difficult to obtain a Vierendeel failure, more than 4 openings needed to be filled. Such scenario will never happen in the normal design of a cellular beam.

5.2.2 Results of the parametrical study

Taking into account the different parameters defined at the beginning of this chapter, numerical simulations were performed on pure steel sections. The results are summarised on Figure 5–37.

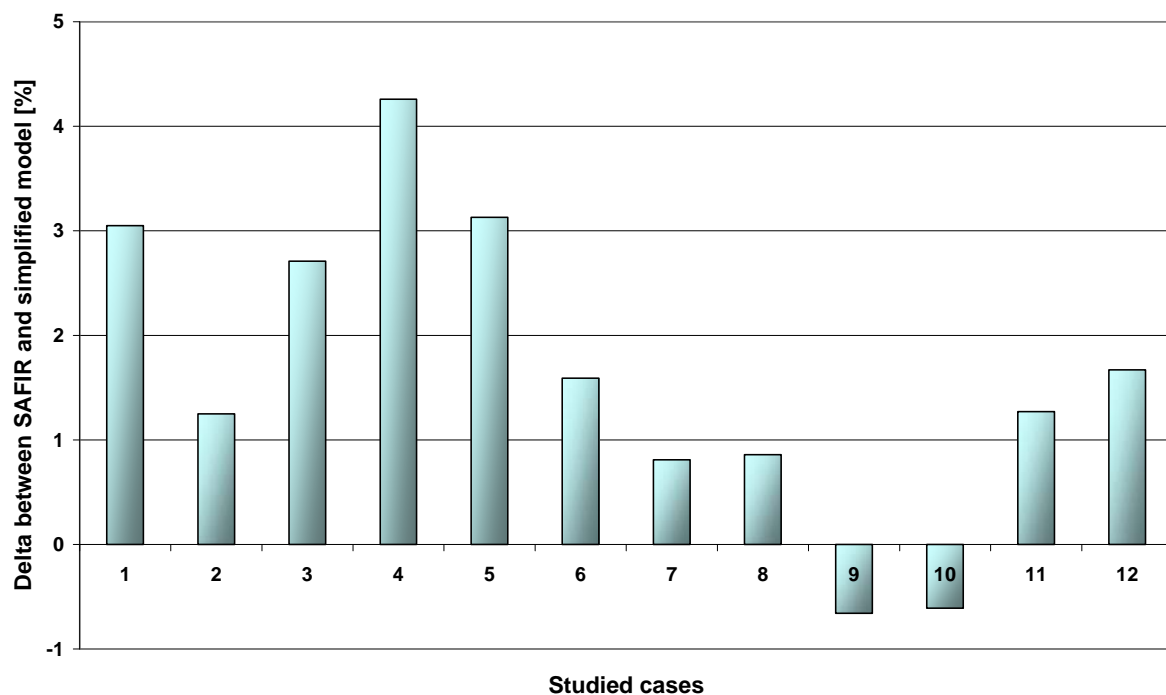


Figure 5–37 : Summary of the results for the parametrical study on the Vierendeel bending

This figure shows that the model predicts with a good accuracy the critical temperature of the 'T' sections. The unsafe results are coming from simulations where the number of filled openings is significant (min 4), and consequently the model reaches the limits because the model was developed for cellular beam and not for beam with isolated openings.

In composite sections, it was impossible, even with 4 filled openings, to obtain a Vierendeel failure. This is coming from the fact that the critical temperature of the lower 'T' is really bigger than the critical temperature of the web. It could be possible to find one geometry with nearly all the openings closed where the Vierendeel failure could be reached in case of fire. But the obtained profile would not be anymore a cellular beam but a beam with isolated opening and such beams are not covered by this thesis.

Conclusion

Conclusion

Conclusion

6. Conclusion

This thesis aimed to provide an analytical model enabling prediction of the critical temperature of cellular beam in case of fire.

The first chapter introduced the background of this thesis and explained the necessity to perform this study.

The second step was the implementation of a numerical model in the FEM software SAFIR. This model must take into account the complex behaviour of cellular beam with local instabilities and composite connection between the slab and the steel profile. This model was built using SHELL elements in 3D to assess the local behaviour and the instability of the web post.

The third step was a comparison between this Finite Element model and the existing data's on tests performed on cellular beams. All the previously available tests on cellular beams were made in cold situation. It was shown in a first step that the Finite Element model built in SAFIR was able to predict with a good accuracy the complex behaviour of cellular beam in cold conditions. Only one test was performed on a cellular beam in fire situation, it was the test made in the scope of the RFCS project Large Web Opening for Service Integration. This test was also simulated using the Finite Element model. However in this case, the beam was thermally protected by spray material. No tests on unprotected cellular beams were available.

In order to have a better understanding of the behaviour of unprotected cellular beam in case of fire, a test campaign was launched at the University of Ulster in Northern Ireland where unprotected cellular beams were tested in cold and in fire conditions. On the basis of these new tests, it was possible to show that the Finite Element model built in SAFIR was able to provide satisfactory prediction of the complex behaviour of cellular beam in fire conditions.

The next step of the study was the development of an analytical model for the prediction of the critical temperature of cellular beam in case of fire. This analytical model was based on the model developed for the cellular beam in cold conditions. Different failure modes were taken into account in this analytical model (web post buckling and Vierendeel bending). It was also shown that the induced thermal stresses could affect the mechanical behaviour of the cellular beam. In case of cellular beam made of hot rolled sections this effect is too small to endanger the stability of the beam.

The last step was the realisation of parametrical studies made with the Finite Element model built in SAFIR in order to validate the results of the analytical models. The same calculations

were performed using Finite Element and using the analytical model. The results were compared and it can be concluded that the model predicts with a good accuracy the critical temperature of the different sections.

In conclusion, this analytical model was validated by a parametrical study and can now be used for the prediction of the critical temperature of cellular beam in case of fire. This model takes into account the complex behaviour of cellular beams in fire conditions and is based on the Eurocodes principles taking into account the loss of material properties and stiffness required in the Eurocodes.

In future research, this model could be developed further for cellular beam having more complex geometries like tapered or curved cellular beams.

It was also indicated by new tests that a vertical stiffener welded on one side of the web post could be sufficient to avoid the web post buckling in fire conditions. This new technique could increase a lot the fire resistance of cellular beam in an economical way avoiding the web post buckling that is the main failure mode in fire conditions.

Bibliography

Bibliography

Bibliography

- [1] REFAO-I, Computer assisted Analysis of the Fire Resistance of Steel and Composite Concrete-Steel Structures / C.E.C. Research 7210 SA/502
- [2] REFAO-II, Practical Design Tools for Composite Steel Concrete Construction Elements Submitted to ISO-FIRE, Considering the Interaction Between Axial Load N and Bending Moment M / C.E.C. Research 7210-SA/504
- [3] REFAO-III, Practical Design Tools for Unprotected Steel Columns Submitted to ISO-Fire / C.E.C. Research 7210-SA/505
- [4] Buckling Curves in Case of Fire / C.E.C. Research 7210-SA/515
- [5] Development of design rules for steel structures subjected to natural fires in LARGE COMPARTMENTS / C.E.C. Research 7210-SA/517
- [6] Development of design rules for steel structures subjected to natural fires in CLOSED CAR PARKS / C.E.C. Research 7210-SA/518
- [7] Competitive Steel Building through Natural Fire Safety Concept / C.E.C. Research 7210-SA/522
- [8] Natural Fire Safety Concept - Full Scale Tests, Implementation in the Eurocodes and Development of a User-friendly Design Tool / C.E.C. Research 7210-PR-060.
- [9] Fire safety of Industrial Halls and Low-rise Buildings: Realistic Fire Design, Active Safety Measures, Post-local failure simulation and Performance Based Requirements / C.E.C. Research 7210-PR-378.
- [10] Natural Fire Safety Concept – the Development and Validation of a CFD-based Engineering Methodology for Evaluating Thermal Action on Steel and Composite Structures / C.E.C. Research 7210-PR-184
- [11] Risk-Based Fire resistance Requirements / C.E.C. Research 7210-PR-251
- [12] Design tools for the behaviour of multi-storey steel framed buildings exposed to natural fire conditions, "Cardington 2" / C.E.C. 7210-PR-112
- [13] Behaviour of a multi-storey steel framed building subject to natural fires C.E.C. 7215-CA/306/603/806
- [14] Dissemination of Fire Safety Engineering Knowledge "DIFISEK" RFS-C2-03048
- [15] Integrating advanced three-dimensional modelling methodologies for predicting thermo-mechanical behaviour of steel and composite structures subjected to natural fires "FIRESTRUC" RFS-PR-2110)
- [16] Franssen J.-M, SAFIR. A Thermal/Structural Program Modelling Structures under Fire, Engineering Journal, A.I.S.C., Vol 42, No. 3 (2005),143-158
- [17] Ansys, Inc. (2006). "ANSYS Academic version, Release 10.0, Help System".
- [18] ABAQUS, 1998, Hibbitt, Karlsson, and Sorensen, Inc., 100 Medway St., Providence,Rhode Island.
- [19] O. Vassart, L.G. Cajot, M. O'Connor, Y. Shenkai, C. Fraud, B. Zhao, J. De La Quintatna, J. Martinez De Aragon, J.M. Franssen, F. Gens " 3D simulation of Industrial Hall in case of fire. Benchmark between ABAQUS, ANSYS and SAFIR " 10th International Fire Science & Engineering Conference ; Interflam ; Edinburgh 2004

- [20] BS5950 Part 8 - Code of Practice for Fire Resistant Design : 1990
- [21] Advisory Desk Notes - AD 269: The use of intumescent coatings for the fire protection of beam with web openings- Steel Construction Institute.
- [22] "RT1006 Version 02: Fire Design of Cellular Beams with Slender Web Posts", SCI, Ascot, (2004).
- [23] ARBED Cellular Beams – "Descriptif Technique Détaillé", 2002
- [24] P.-O. Martin - Rapport de recherche CTICM "ACB Design optimisation – Flambement du Montant" – CTICM – Novembre 2003.
- [25] Large Web Openings for Service Integration in Composite Floor C.E.C. 7210 PR315, 2004
- [26] "Properties and strength of castellated beams. Consideration of previous tests", Report D.GE. 71/262, The United Steel Companies Ltd, Swinden Laboratories, Rotherham, (1957).
- [27] Gibson & Jenkins, The Structural Engineer, 35 (12), (1957) pp467-479.
- [28] Sherbourne, Proc. 2nd Commonwealth Welding Conference, Institute of Welding, London, C2 (1966) pp1-5.
- [29] R. Delesques : Stabilité des montants de poutres ajourées, revue Construction métallique n°3-1968, CTICM, 1968, p.26-33
- [30] A. Bazile et J. Texier, Essais de poutres ajourées, revue Construction métallique n°3-1968, CTICM, 1968, p.12-25.
- [31] Hosain & Speirs, J. American Welding Society, Welding Res. Supp., 52 (8), (1973) pp329-342.
- [32] Mandel et al., J. Structural Division, ASCE, 97 (ST7), (1971) pp1947-1967.
- [33] Shoukry, J. American Welding Society, Welding Res. Supp., 44 (5), (1965) pp231- 240.
- [34] RG Redwood, Analyse et dimensionnement des poutres ayant des ouvertures dans les âmes, revue Construction métallique n°3-1978, CTICM, 1978, p.15-27
- [35] D. Mateesco et G. Mercea, Un nouveau type de poutres ajourées, revue Construction Métallique, n°3-1981, CTICM, 1981, p.3-14
- [36] Srimani, & Das, Computers and Structures, 9, (1978) pp169-174.
- [37] Gotoh, Trans. JSCE, 7, (1976) pp37-38.
- [38] Nethercot & Rockey, The Structural Engineer, 49 (7), (1971) pp312-330.
- [39] Nethercot & Trahair, The Structural Engineer, 54 (6), (1976) pp197-204.
- [40] Kerdal & Nethercot, J. Construct. Steel Research, 4, (1984) pp295-315.
- [41] Okubo & Nethercot, Proc. Instn. Civ. Engrs., Part 2, (79), (1985) pp533-557.
- [42] Knowles, Proc. Instn. Civ. Engrs., Part 1, 90, (1991) pp521-536.
- [43] Dougherty, J. South African Institution of Civil Engineers, 35 (2), (1993) pp12-20.
- [44] Zaarour & Redwood, Journal of Structural Engineering, (1996) pp860-866.
- [45] Megharief & Redwood, Proc. Annual conference, Canadian Society for Civil Engineering, (1997) pp239-248.
- [46] "Fire Protection for Structural Steel in Buildings", Second Edition, ASFP/SCI/FTSG, (1992).

- [47] Bailey C.G. Indicative Fire Tests to Investigate the Behaviour of Cellular Beams Protected with Intumescent Coatings. Fire Safety Journal. Fire Safety Journal. 39 2004 pp 689-709.
- [48] Newman G.M., Robinson J.T. and Bailey C.G., Fire Safe design: A New Approach to Multi-Storey Steel-Framed Buildings (Second Edition). SCI Publication P288. The Steel Construction Institute, Ascot. 2006.
- [49] D. Bitar, T. Demarco, P.O. Martin, Steel and non composite cellular beams – Novel approach for design based on experimental studies and numerical investigations, brochure EUROSTEEL, june 2005
- [50] A. Nadjai, O. Vassart, A. Faris, D. Talamona, A. Allam and M. Hawes Performance of cellular composite floor beams at elevated temperatures , SIF 2006
- [51] "Fire Protection for Structural Steel in Buildings", Second Edition, ASFP/SCI/FTSG, (1992).
- [52] Y. Galéa, P.-O. Martin - Rapport de recherche CTICM "ACB Design optimisation – Calcul des flèches" – CTICM – Décembre 2003.
- [53] D. Bitar, P.-O. Martin, Y. Galéa, T. Demarco - Poutres cellulaires acier et mixtes - Partie 1 : proposition d'un modèle pour la résistance des montants. Revue Construction Métallique n°1-2006. CTICM.
- [54] Large Web Openings for Service Integration in Composite Floor Valorisation project , Research Fund for Coal and Steel, 2006
- [55] EN1993-1-1 "Eurocode 3: Design of steel structures - Part 1-1: General rules and rules for buildings"
- [56] EN1994-1-1 "Eurocode 4: Design of composite steel and concrete structures - Part 1-1: General rules and rules for buildings"
- [57] Rapport d'essai CTICM n° 02-6-332-2000.
- [58] Westok Cell Beam Software, V 3.01, Steel Construction Institute
- [59] Soon Ho Cho "Slab behaviour in composite beams of web openings", Mc Gill University, London, June 1990.
- [60] ENV1993-1-1 "Eurocode 3: Design of steel structures - Part 1-1: General rules and rules for buildings"
- [61] Ch. Massonnet, S. Cescotto "Mécanique des Matériaux" page 255
- [62] Ch. Massonnet, S. Cescotto "Mécanique des Matériaux" page 48
- [63] Ch. Massonnet, S. Cescotto "Mécanique des Matériaux" page 142
- [64] EN1993-1-2 "Eurocode 3: Design of steel structures - Part 1-2: General rules - Structural fire design"
- [65] EN1994-1-2 2 "Eurocode 4: Design of composite steel and concrete structures - Part 1-2: General rules - Structural fire design"
- [66] S. Majkut, J.-M. Franssen "Poutrelles métalliques courtes de type ACB testées en Allemagne. Rapport des simulations numériques effectuées à Liège", 2003

Bibliography

Analytical model for cellular beams made of hot rolled sections in case of fire

This thesis allows developing an analytical model for the prediction of the critical temperature of cellular beams made of hot rolled sections subjected to fire.

This target is carried out through research focused on tests and simulations of isolated cellular beam submitted to fire. Based on this study a new analytical model is developed.

In order to ensure the reliability of the developed model, different steps are followed:

- realisation of large scale fire tests in laboratory
- implementation of a Finite Element model in the software SAFIR
- calibration of the FEM model in comparison with laboratory tests
- development of the simplified analytical model
- validation of this analytical method through a parametrical study using FEM software SAFIR.

The developed Finite Element and analytical models are able to reproduce with a satisfactory level of accuracy the complex behaviour of cellular beam in fire conditions.

Key words

Construction, steel, composite, cellular beam, instability, fire resistance.

Modèle analytique en cas d'incendie pour poutres cellulaires fabriquées à base de profilés laminés à chaud

Cette thèse a permis de développer un modèle analytique pour la prédiction de la température critique de poutrelles cellulaires fabriquées à base de profilés laminés en situation d'incendie. Ces résultats seront basés sur la mise au point d'un nouveau modèle analytique de poutrelle cellulaire isostatique soumise au feu. Pour assurer la fiabilité du modèle développé, les étapes suivantes ont été considérées :

- la réalisation de tests en grande échelle en laboratoire
- la mise au point d'un Modèle Éléments Finis dans le logiciel SAFIR
- la validation du Modèle Éléments Finis en comparaison des essais en laboratoire
- le développement du modèle analytique simplifié
- la validation de cette méthode analytique par une étude paramétrique utilisant le modèle Éléments Finis

Le modèle éléments finis et le modèle analytique qui ont été développés sont capables de reproduire le comportement complexe des poutrelles cellulaires en cas d'incendie avec un niveau de précision satisfaisant.

Mots clés

Construction, acier, mixte acier béton, poutre cellulaire, instabilité, incendie.